

Time-Resolved Spectroscopy of Selective Catalytic Reduction (SCR) Catalysts under Transient Conditions

Présentée le 23 décembre 2021

Faculté des sciences de base
Groupe Kröcher
Programme doctoral en chimie et génie chimique

pour l'obtention du grade de Docteur ès Sciences

par

Rob Jeremiah G. NUGUID

Acceptée sur proposition du jury

Prof. K. Sivula, président du jury
Prof. O. Kröcher, Dr D. Ferri, directeurs de thèse
Dr A. Marberger, rapporteur
Prof. E. Tronconi, rapporteur
Prof. W. L. Queen, rapporteuse

“Otiositas inimica est animae.”

– Benedictus Nursiae

Abstract

Understanding the mechanisms behind chemical transformations is key to developing improved catalytic systems. To this end, operando spectroscopy has contributed significantly to the advancement of our molecular view of many reactions at the heart of the chemical industry. In this work, we show the application of time-resolved spectroscopic techniques to elucidate the mechanism of a reaction that has always occupied a central role in emission control research – the selective catalytic reduction (SCR) of NO_x with NH_3 .

Chapter 1 introduces the SCR reaction in the context of the different industrially relevant catalysts and the generally accepted reaction mechanisms in the literature. It also gives an overview of the principles of transient experimentation and modulated excitation (ME) as well as the aims of the thesis.

Chapter 2 describes the design and performance characteristics of a custom-built spectroscopic cell that was used extensively in the entire project. The low void volume of the cell allowed the implementation of transient and ME experiments. Furthermore, it was versatile enough to be used in time-resolved infrared, Raman, and visible spectroscopy.

Chapter 3 reports the increased level of mechanistic information that Raman spectroscopy can provide when combined with ME. Through this approach, the VO_x active phase and the TiO_2 support were shown to play a role in the SCR process. Only the coordinatively unsaturated portion of the VO_x species act as catalytic active centers while the majority remains largely unresponsive. Although TiO_2 is not directly involved in the SCR reaction, it was shown to act as a reservoir of NH_3 molecules that can be mobilized to the active sites.

Chapter 4 shows the influence of temperature, gas feed, and catalyst composition on the interconversion between the Lewis and Brønsted-Lowry acid sites of $\text{V}_2\text{O}_5/\text{WO}_3\text{-TiO}_2$.

Water could increase Brønsted-Lowry functionality not just by converting pre-existing Lewis centers, but also by generating spontaneously new acid sites. Phase-sensitive detection revealed the presence of three Lewis acid sites that have different kinetic behaviors and degrees of resistance against hydroxylation.

Chapter 5 details the study of hydrogen cyanide (HCN) production from formaldehyde-containing gas streams over $V_2O_5/WO_3\text{-TiO}_2$ as well as Fe-ZSM-5, Cu-BEA, and Cu-SSZ-13. Due to this side reaction, NH_3 is consumed parasitically and the NO_x conversion decreases, even after compensating for the fraction of lost NH_3 .

Chapter 6 presents a mechanistic investigation of HCN formation from the reaction of NH_3 with formaldehyde over vanadia-based SCR catalysts. The detection of the key cyanide intermediate was accomplished by operando infrared spectroscopy combined with ME experimentation, thereby providing unambiguous evidence that the HCN-forming reaction occurs on the catalyst surface. In this side reaction, formaldehyde reacts directly from the gas phase with adsorbed NH_3 to form amide species and then HCN.

Chapter 7 discusses the low-temperature NH_3 inhibition effect on the SCR reaction over Cu-SSZ-13. Transient X-ray absorption spectroscopy results showed that excess NH_3 halts the SCR process by locking the Cu species in the reduced solvated state, which are very stable in the low-temperature regime. Intermittent pulsing of NH_3 was shown to improve the SCR activity significantly.

Chapter 8 provides a summary of the results and an outlook for further research in this field.

Keywords: Catalysis; Selective catalytic reduction; Time-resolved spectroscopy; Infrared spectroscopy; Raman spectroscopy; UV-visible spectroscopy; X-ray absorption spectroscopy; Transient experimentation; Modulated excitation

Zusammenfassung

Das Verständnis chemischen Reaktionen ermöglicht die Entwicklung verbesserter Katalysatoren. Zu diesem Zweck hat die Operando-Spektroskopie wesentlich dazu beigetragen, unsere molekulare Sicht auf viele Reaktionen im Herzen der chemischen Industrie zu verbessern. In diesem Forschungsprojekt zeigen wir die Verwendung zeitaufgelöster spektroskopischer Techniken zur Aufklärung des Mechanismus der selektiven katalytischen Reduktion («selective catalytic reduction» auf Englisch oder SCR) von NO_x mit NH_3 , eine Reaktion, die eine zentrale Rolle in der Abgasnachbehandlung einnimmt.

Kapitel 1 stellt die SCR-Reaktion im Kontext der verschiedenen industriell relevanten Katalysatoren und der allgemein akzeptierten Reaktionsmechanismen vor. Es gibt auch einen Überblick über die Prinzipien transienter Experimentiere und der modulierten Anregung («modulated excitation» auf Englisch oder ME) sowie die Ziele der Doktorarbeit.

Kapitel 2 beschreibt das Design und die Leistungsmerkmale einer sonderangefertigten Spektroskopie-Zelle, die in den folgenden Arbeiten verwendet wurde. Das kleine Hohlraumvolumen der Zelle hat die Durchführung von Experimenten mit transienten Reaktionen und ME ermöglicht. Die Vielseitigkeit der Zelle wurde bestätigt, denn sie wurde erfolgreich in der zeitaufgelösten Infrarot-, Raman- und sichtbaren Spektroskopie verwendet.

Kapitel 3 berichtet über die mechanistischen Informationen, welche die Raman-Spektroskopie nur in Kombination mit ME liefern kann. Durch diesen Ansatz wurde gezeigt, dass die VO_x -Aktivphase und das TiO_2 -Trägermaterial entscheidende Rollen im SCR-Prozess spielen. Nur der koordinativ ungesättigte Teil der VO_x -Spezies agiert als aktive Zentren, während der Grossteil weitgehend an der Reaktion unbeteiligt bleibt. TiO_2

nicht direkt an der SCR-Reaktion beteiligt ist, fungiert es als Reservoir für NH_3 , das zu den aktiven Zentren diffundieren kann.

Kapitel 4 zeigt den Einfluss von Temperatur, Gaskomposition und Materialzusammensetzung auf die Umwandlung von Lewis- und Brønsted-Lowry-säure Zentren von $\text{V}_2\text{O}_5/\text{WO}_3\text{-TiO}_2$ -Katalysatoren. Wasser könnte die Anzahl der Brønsted-Lowry-säure Zentren erhöhen, nicht nur durch die Umwandlung bereits vorhandener Lewis-säure Zentren, sondern auch durch spontane Bildung neuer saurer Zentren. Die phasenabhängige Demodulation hat auch gezeigt, dass es drei Lewis-säure Zentren gibt, die sich unterschiedlich entwickeln und variierende Resistenz gegen Hydroxylierung aufweisen.

Kapitel 5 detailliert die Untersuchung der Herstellung von Cyanwasserstoff (HCN) aus formaldehydhaltigen Gasströmen über $\text{V}_2\text{O}_5/\text{WO}_3\text{-TiO}_2$ sowie Fe-ZSM-5, Cu-BEA und Cu-SSZ-13. Durch diese Nebenreaktion wird NH_3 parasitär verbraucht und der NO_x -Umsatz nimmt ab, auch wenn der Anteil an verlorenem NH_3 kompensiert wird.

Kapitel 6 präsentiert eine mechanistische Untersuchung der Bildung von HCN aus der Reaktion von NH_3 mit Formaldehyd an $\text{V}_2\text{O}_5/\text{WO}_3\text{-TiO}_2$ -Katalysatoren. Der Nachweis des Schlüsselzwischenprodukts Cyanid wurde durch Operando-IR-Spektroskopie in Kombination mit ME-Experimenten erreicht, was eindeutige Beweise dafür liefert, dass die HCN-bildende Reaktion auf der Katalysatoroberfläche abläuft. Formaldehyd reagiert wahrscheinlich direkt aus der Gasphase mit voradsorbiertem NH_3 , um Amid und dann HCN zu bilden.

Kapitel 7 diskutiert die Hemmung von NH_3 bei niedriger Temperatur auf die SCR-Reaktion über Cu-SSZ-13. Die Resultate der transienten Röntgenabsorptionsspektroskopie zeigen, dass überschüssiges NH_3 den SCR-Prozess verlangsamt, indem die Cu-Spezies im reduzierten solvatisierten Zustand fixiert wird, die in niedriger Temperatur sehr stabil sind. Es wurde gezeigt, dass intermittierendes Pulsieren von NH_3 die SCR-Aktivität deutlich verbessert.

Kapitel 8 gibt eine Zusammenfassung der Ergebnisse und einen Ausblick auf mögliche weitere Forschungen auf diesem Gebiet.

Schlüsselwörter: Katalyse; Selektive katalytische Reduktion; Zeitaufgelöste Spektroskopie; Infrarotspektroskopie; Raman-Spektroskopie; UV-Vis-Spektroskopie; Röntgenabsorptionsspektroskopie; Transientes Experimentieren; Modulierte Anregung

Acknowledgments

Embarking on a PhD has turned out to be as much of a sociocultural odyssey as a scientific journey for me. Aside from receiving a holistic academic training, I have also developed a deep cultural understanding of the world, improved my interpersonal skills, and widened my social circle exponentially during these last four years. I could not have achieved these without the help of special persons whom I would like to acknowledge profusely in the following paragraphs. Hence, although this section is the least scientific part of my whole thesis, I consider it to be the most important one.

I would like to thank Prof. Oliver Kröcher, my thesis director, for giving me the opportunity to work on this study. He has granted me full freedom and flexibility to pursue my research interests within the framework of the project while guiding me with his knowledge and expertise through our meetings and beyond. The goal of a doctorate is to make the student into an independent researcher, and I am glad to have become one under his seasoned tutelage.

I extend my gratitude to Dr. Davide Ferri, my direct supervisor, who epitomizes the word “mentor” in every respect. I could not overstate his contribution to my academic upbringing as he has helped me design my experiments, taught me how to give a presentation effectively, and corrected my drafts with enthusiasm and pedantry. I truly admire his work ethic and erudition. Fond memories of having *dolce far niente*-themed Sunday brunches with him and his family will stay with me.

I also thank Dr. Maarten Nachtegaal, who completes the triumvirate of my PhD advisors. He has not only guided me in every experiment that I conducted at SuperXAS, but also helped me polish my beamtime proposals and scientific manuscripts. My summers would

have been less fun without the traditional Swiss activity of *Heuen* in his backyard and the sumptuous dinner afterwards.

I would like to express my appreciation to Prof. Kevin Sivula, Prof. Wendy Lee Queen, and Prof. Enrico Tronconi for kindly accepting my invitation to serve as part of my thesis panel and for providing valuable feedback.

I consider myself extremely blessed for having had the opportunity to work with great colleagues in the Applied Catalysis and Spectroscopy (ACS) and SuperXAS groups. I am indebted to Martin Elsener for always lending a hand whenever I encounter a problem in the laboratory and for incidentally aiding me to improve my German skills during our jogging sessions. I am thankful to Gisela Herlein for the administrative support, coffee break discussions about culture, and opening her home to me on more than one occasion. I am immensely grateful to Dr. Adrian Marberger, my senior colleague, who introduced me to many practical things in the laboratory. He has certainly left big shoes to fill, and I hope that I have covered at least half. I thank Dr. Miren Agote-Arán for being the best beamtime buddy and baking partner. I also thank Dr. Ivo Alxneit, Dr. Olga Safonova, Dr. Adam Clark, Dr. Tanja Franken, Dr. Dominik Wierzbicki, Dr. Andrey Petrov, Dr. Patrick Simon Steiger, Dr. Thibault Fovanna, Dr. Jerick Imbao, Dr. Dzulija Kuzmenko, Maneka Claire Roger, Filippo Buttignol, Luca Maggiulli, Ilia Sadykov, Anna Zabilska, Urs Vogelsang, Stephan Hitz, Gaultier Lefay, and Vilde Jacobsen as well as the master and international students that I have had the pleasure of working with: Lorenzo Ortino Ghini, Samuel Regli, Hiroe Kubota, and Jie Yang.

I should not forget to mention the persons whom I have had the privilege of collaborating with during my PhD. These include Prof. Atsushi Urakawa, Prof. Izabela Czekaj, Dr. Vitaly L. Suskevich, Dr. Ali Bahmanpour, and Ole H. Bjørkedal. I am also grateful to Marcel Hottiger, Andri Hirt, Thomas Scherer, and Erich de Boni for the technical help that I received whenever I have to modify or repair my experimental setup.

I would like to thank Prof. Tae Joo Park and his team for hosting me at Hanyang University in the framework of the Swiss-Korean Young Researchers' Exchange Program. Likewise,

I am truly humbled by the support that I received from Ms. Elise Nardin, Ms. Lucia Arpagaus, and Dr. Alessandra Apicella during this time.

As someone who arrived in Switzerland with absolute zero German skills, I am proud to have achieved conversational fluency in four years' time thanks to my teachers at ECAP Aargau, VHS Waldshut-Tiengen, and EPFL Centre de Langues. Additionally, I would like to acknowledge the facilitators of the language meetings organized by Sprachenzentrum der UZH und der ETH Zürich, Sprachcafé Basel, Stadtbibliothek Baden, Stadtbibliothek Chur, Sprachencafé Bad Zurzach, IIK Düsseldorf, Sprachinstitut Berlin, Kreativhaus Berlin, Die Lernwerkstatt Berlin, Stadtteilzentrum Siemensstadt, Give Something Back to Berlin, Münchner Stadtbibliothek, Weltmuseum Wien, StartWien, Station Wien, Stand 129, and Verein Begegnung-Arcobaleno. Participating in these online meetups helped me not just to hone my German skills, but also to have something to look forward to during the pandemic.

I will forever be indebted to Prof. Isabelle Ledoux, Prof. Ngoc Diep Lai, Prof. Guillermo Orellana, Prof. Katarzyna Matczyszyn, and Prof. Andrzej Miniewicz for giving me the opportunity to undertake my master studies under an Erasmus Mundus scholarship. This once-in-a-lifetime opportunity kick-started my European journey and is directly responsible for everything that followed. Thanks are also due to Prof. Cedric Po-Wen Chung, Prof. Ryan Wang, Prof. Jacek Skarżewski, and Prof. Naomi J. Halas, who have supervised my master research projects. I would also like to convey my appreciation to my professors in the Philippines, especially Prof. Jennifer C. Sy, Prof. Nemias T. Dacumos, Prof. Emelinda P. Sabando, Prof. Lynne M. Labaclado, Prof. Anilyn M. Falcatan, Prof. Roderick E. de Luna, Prof. Alex A. Tardaguila, and Prof. Albert P. Mirani for teaching me the foundational aspects of chemistry and for keeping in touch through the years.

Teaching is something that I cherish as much as research. Hence, I would also like to express my gratitude to the Kapisanang Kimika ng Pilipinas for recruiting me to serve as a coach for inorganic chemistry for our country's official delegation to the International

Chemistry Olympiad (IChO). It is always fun to interact with talented and passionate young people in line with our “*para sa bayan*” motto.

At this juncture, I would also like to thank my friends and my *kababayans* whom I have met abroad: Luvylyn A. Sevileno, Julius Andrew P. Nuñez, Frances Anne Marie S. Vicente, Flores family, Dublin family, Valenzuela family, Monje family, Manjares family, Ronquillo family, Daulat family, Foz-Metcalf family, Floria family, Ortiz family, Dela Cruz family, Abad family, Arancon family, and Banzon family. They truly personify our country’s shared culture of *malasakit*.

My penultimate thanks goes to my family: my parents, Roberto and Aurelia, who have always encouraged me to dream big; my brothers, Rosjon, Ronn, and Kevin, with whom I shared my idyllic childhood and teenage years; my grandparents Nanay Let, Lolo Clem, Nanay Levi, and Lolo Zaro, who have always shared their wisdom with me through anecdotes and stories; and my uncle, Raphael, my aunt, Evy, as well as my cousins, Carlo and Danelle, who have always been there for me. Living apart in five different time zones across four continents is not always easy, but we somehow manage to make it work.

Lastly but most importantly, I thank God for the gift of life and knowledge. It is to Him that I solely dedicate not only this doctoral thesis, but also everything that I have achieved in the past and will accomplish in the future, however big or small.

Contents

Abstract.....	v
Zusammenfassung	vii
Acknowledgments	xi
 Chapter 1 – Background of the Study	 19
1.1. Nitrogen oxide emissions and selective catalytic reduction (SCR)	19
1.2. Transient experimentation and modulated excitation spectroscopy	34
1.3. Scope of the thesis	40
 Chapter 2 – Design of a Reactor Cell for Transient Response and Modulated Excitation Studies	 41
2.1. Introduction	41
2.2. Materials and methods.....	42
2.3. Results and discussion.....	48
2.4. Conclusions	56
 Chapter 3 – Modulated Excitation Raman Spectroscopy of V₂O₅/TiO₂: Mechanistic Insights into the Selective Catalytic Reduction of NO by NH₃	 59
3.1. Introduction	59

3.2. Materials and methods.....	60
3.3. Results and discussion.....	62
3.4. Conclusions	73
Chapter 4 – Interconversion between Lewis and Brønsted-Lowry Acid Sites on Vanadia-Based Materials	75
4.1. Introduction	75
4.2. Materials and methods.....	75
4.3. Results and discussion.....	78
4.4. Conclusions	87
Chapter 5 – Hydrogen Cyanide Production from Formaldehyde over Vanadia-, Copper-, and Iron-Based Catalysts under Selective Catalytic Reduction Conditions.....	89
5.1. Introduction	89
5.2. Materials and methods.....	91
5.3. Results and discussion.....	96
5.4. Conclusions	105
Chapter 6 – Operando Detection of Cyanide Intermediate Species during the Reaction of Formaldehyde with Ammonia over V₂O₅/WO₃-TiO₂.....	107
6.1. Introduction	107
6.2. Materials and methods.....	108
6.3. Results and discussion.....	110

6.4. Conclusions	130
------------------------	-----

Chapter 7 – NH₃-Mediated Inhibition of the SCR Reaction over Cu-SSZ-13 at Low Temperature.....131

7.1. Introduction	131
-------------------------	-----

7.2. Materials and methods.....	131
---------------------------------	-----

7.3. Results and discussion.....	133
----------------------------------	-----

7.4. Conclusions	146
------------------------	-----

Chapter 8 – Conclusions and Outlook.....147

Annex – Teaching Infrared Spectroscopy in the Context of SCR: A Learning Activity for In-Person and Virtual Laboratory Classes149

A.1. Introduction.....	149
------------------------	-----

A.2. Learning outcomes	150
------------------------------	-----

A.3. Experimental overview	151
----------------------------------	-----

A.4. Safety hazards	153
---------------------------	-----

A.5. Results and discussion.....	153
----------------------------------	-----

A.6. Conclusions	163
------------------------	-----

Appendix.....165

References.....201

Contents

List of Scientific Contributions.....	215
Curriculum Vitae	219

Chapter 1 – Background of the Study

1.1. Nitrogen oxide emissions and selective catalytic reduction (SCR)

Nitrogen oxide (NO_x) pollution ranks among the biggest problems of the 21st century, especially in highly industrialized cities [1, 2]. Formed as a byproduct of fuel combustion, NO_x can have negative implications not just for the environment, but for human health as well. Through a series of complex chemical reactions with ozone and hydrocarbons, untreated NO_x can cause photochemical smog formation and reduce visibility [3]. NO_x can also react with water in the atmosphere and contribute to acid rain, which can damage vegetation and crops [4]. Finally, it can give rise to a myriad of health problems and respiratory diseases [5, 6]. Therefore, the abatement of harmful NO_x is a chief component of all modern pollution control strategies worldwide.

Selective catalytic reduction (SCR) is currently the most efficient technology to curb NO_x emissions from diesel-powered vehicles and thermal power plants. First introduced in Japan in the 1970's [7], SCR quickly gained global recognition as an integral part of stationary exhaust gas after-treatment. In the late 1980's, the first experiments were conducted to transfer the SCR process to mobile applications as well, for which it was established as the best option for NO_x abatement in engines that operate under excess oxygen.

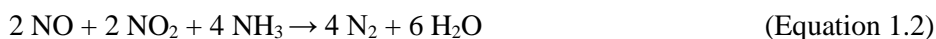
As the term implies, SCR requires a reductant that will preferentially react with NO_x to form environmentally benign products. During the early stages of SCR development, several chemical substances were extensively investigated as potential reducing agents. The most studied ones are hydrocarbons, hydrogen (H_2), and ammonia (NH_3). Hydrocarbon-SCR is particularly convenient because the fuel itself and/or the unburned hydrocarbons in the exhaust can serve as the reducing agent directly [8]. However, the overall efficiency of the process was found to be low because most of the hydrocarbons are

actually oxidized to carbon dioxide (CO₂) instead of selectively reacting with NO_x. Side reactions can also form HCN, an extremely poisonous gas, at concentrations above the threshold limit value [9]. H₂-SCR was proposed as a much “greener” alternative, but it requires a large excess of H₂ to achieve sufficient conversions and expensive Pt-based catalysts [10]. Due to these serious limitations, hydrocarbon-SCR and H₂-SCR did not achieve widespread use. Indeed, most modern SCR installations use NH₃ as a reducing agent for the conversion of NO_x. While this technology is more expensive to implement, its efficiency and selectivity make up for the added cost. To solve the problem of toxicity and storage of NH₃, urea was proposed as a safe NH₃ precursor compound. Under SCR-relevant conditions, urea easily decomposes in situ yielding two equivalents of NH₃. With the introduction of the SCR system in diesel vehicles, AdBlue® (32.5 wt% urea solution) became the most used NH₃ precursor worldwide [11].

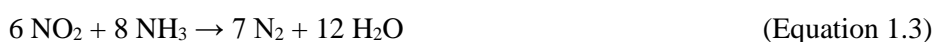
There are three main types of NH₃-SCR reactions that lead to the reduction of NO_x, depending on the feed composition and the reaction temperature. Under normal conditions, nitric oxide (NO) accounts for nearly 90% of the total NO_x in the exhaust [12], and the chemical equation corresponding to its reduction is known as the standard SCR reaction (Equation 1.1).



It should be noted that the reaction also requires oxygen, which is available in excess in the exhaust gas of diesel engines. From the perspective of the active site, the SCR process can be thought of as a redox cycle. The first half involves the reduction of the metal centers in the presence of NO and NH₃, and the catalytic cycle is closed in the second half by oxygen that regenerates the active sites through reoxidation. The presence of nitrogen dioxide (NO₂) can accelerate the NO_x conversion through a different reaction pathway, known as the fast SCR reaction (Equation 1.2).



The rate enhancement is thought to occur from the faster reoxidation of the active sites in the second half of the catalytic cycle. This is because NO_2 is a much stronger oxidizing agent than O_2 [13]. For this reason, diesel oxidation catalysts are usually installed upstream of the SCR system in order to partially oxidize NO to NO_2 and induce the fast SCR reaction. However, too much NO_2 in the gas feed is not beneficial for SCR. When NO_2 is present above the equimolar amount of NO , the SCR process is hampered through the occurrence of Equation 1.3.



This equation is known as NO_2 -SCR or slow SCR due to its sluggish kinetics [14].

Side reactions also compete with the main SCR reactions during non-optimal conditions. At high temperatures, NH_3 could be directly oxidized to N_2 (and to a lesser degree, N_2O and NO), thereby limiting the amount of reductant that can selectively react with NO_x [15]. Some catalyst formulations are also susceptible to forming significant amounts of N_2O , which has approximately 300 times higher greenhouse warming potential than CO_2 . In the presence of sulfur compounds in the exhaust, $(\text{NH}_4)_2\text{SO}_4$ can precipitate at low temperatures and cause catalyst fouling [16]. Preventing the occurrence of these undesirable reactions is a major objective of ongoing studies.

The last four decades of SCR development yielded different classes of catalysts with diverse formulations. Vanadium-based catalysts are the first to be commercialized for SCR, and they have remained to be the preferred materials for stationary and marine applications [17]. On the other hand, copper- and iron-exchanged zeolites have emerged as a commercial solution for mobile SCR, for which a wider operating window is required. Although the composition of SCR catalysts can be completely different, they all have the following two key characteristics: (1) the presence of acidic sites that adsorb NH_3 from the gas phase; and (2) a redox site where the actual reaction between NH_3 and NO_x occurs.

The variety of SCR catalysts today reflects the diversity of diesel and gas engines used in the field. Indeed, engines for on-road applications (e.g. passenger car, trucks or buses) and

non-road applications (e.g. mining trucks, harvesters, trains, ships or power-generating applications) differ in engine size, working speed, and quality of fuel [18].

1.1.1. Vanadia-based SCR catalysts

Vanadia-based catalysts typically consist of 1-3 wt% V_2O_5 as the redox-active species and TiO_2 in the anatase phase as the support. Commercial V_2O_5/TiO_2 catalysts are promoted with around 3-10 wt% WO_3 for improved activity and stability [19].

Despite the “ V_2O_5 ” notation, vanadia is actually not present as a separate crystalline phase but as amorphous VO_x units due to its strong interaction with TiO_2 . This has profound structural implications because vanadia exists as octahedral VO_6 units in the bulk but as tetrahedral VO_4 units on the surface. Depending on the loading, VO_x can be present as monomeric, dimeric, and/or polymeric species [20]. Only when the monolayer coverage of 7-8 VO_x units per nm^2 [21] is reached, can V_2O_5 domains start to form. The formal oxidation state of supported vanadium oxide is either V^{5+} or V^{4+} , and the active phase cycles between both states during the reaction. VO_x sites can exhibit Lewis and Brønsted-Lowry acidity, and the ratio between the two acid sites can vary depending on the reaction conditions. For instance, the presence of water can increase the proportion of Brønsted-Lowry sites relative to Lewis sites [22].

TiO_2 proved to be the best suited support for vanadia-based SCR catalysts because of its advantageous chemical interaction with the active phase, resulting in a homogenous dispersion of vanadium oxide and high SCR activity [23]. Furthermore, TiO_2 plays a role in substrate adsorption as it interacts strongly with NH_3 . The anatase modification is used because it provides high surface area and thermodynamic stability up to 700°C. Above this temperature, anatase irreversibly transforms into rutile [24], which is undesirable as the latter has a significantly lower surface area. To delay the onset of rutilization, WO_3 is added as a promoter that induces high levels of TiO_2 lattice distortions, limiting sintering and particle growth [25]. Another important effect of WO_3 is the increase of surface acidity [26], which guarantees the NH_3 supply for the SCR reaction. Through the addition of WO_3 , the weak basic sites of TiO_2 disappear and the surface becomes much more acidic. The

presence of WO_x species also tends to crowd VO_x sites together, forming oligomeric VO_x units that have a higher turnover frequency than isolated species [27]. Additional promotional effects are poisoning resistance to alkali metal and arsenious oxides, and lower NH_3 and SO_2 oxidation at elevated reaction temperature [28-30].

Since the 1980's, the reaction mechanism on V-based catalysts has been actively investigated. The first popular proposal was an Eley-Rideal-type mechanism, where gaseous NO reacts with adsorbed NH_4^+ to form N_2 and H_2O [31]. The ammonium ion is thereby adsorbed on a V-OH Brønsted-Lowry acid site and an adjacent $\text{V}^{5+}=\text{O}$ species acts as the redox active site. The subsequent studies confirmed this reaction scheme with slight modifications and alterations [32, 33].

In the early 1990's, the "amide-nitrosamide" mechanism was proposed, which involves a Lewis acid site for the adsorption of NH_3 instead of a Brønsted acid site [22, 34, 35]. This mechanism was more detailed especially because of the introduction of the nitrosamide (NH_2NO) intermediate, which readily decomposes into N_2 and H_2O .

A combination of the adjacent V species and the "amide-nitrosamide" mechanisms were also proposed [36, 37]. In this combined mechanism, NH_3 adsorbs on a Brønsted-Lowry acid site and is activated by an adjacent $\text{V}^{5+}=\text{O}$ site acting as the redox center.

Recent time-resolved studies have advanced the understanding of the SCR reaction over $\text{V}_2\text{O}_5/\text{TiO}_2$ at the molecular level. Through transient infrared spectroscopy, Marberger et al. [38] showed that the active sites for SCR are Lewis acid sites, on which NH_3 binds and react instantaneously with NO. The introduced NH_3 adsorbed on Lewis and Brønsted-Lowry acid sites as NH_3 and NH_4^+ , respectively. Upon NO addition, the SCR reaction started and adsorbed NH_3 molecules were consumed preferentially over NH_4^+ species. The evolution of the water by-product of SCR also coincided with the consumption of Lewis-bound NH_3 . Only when the NH_3 supply from Lewis acid sites was almost fully depleted, did the NH_4^+ species from Brønsted-Lowry acid sites start to decrease. Parallel measurements using UV-visible spectroscopy revealed the reduction of the VO_x sites upon NO and NH_3 introduction, and its subsequent reoxidation once all of the adsorbed NH_3 was

consumed. In the same experiment, Marberger et al. [38] showed the formation of the NH_2NO intermediate, thereby confirming for the first time the SCR intermediate postulated almost three decades earlier. Although there are still open questions for the SCR mechanism over $\text{V}_2\text{O}_5/\text{TiO}_2$, some important reaction steps are generally accepted (Figure 1.1).

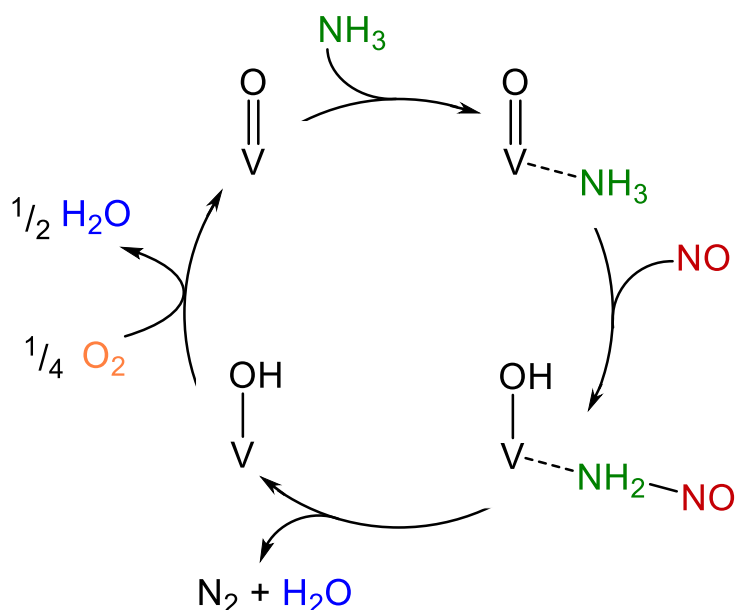


Figure 1.1. Proposed mechanism of SCR over $\text{V}_2\text{O}_5/\text{WO}_3\text{-TiO}_2$. Source: Marberger et al. [38].

In the first step, NH_3 coordinates with VO_x sites through an acid-base interaction. Adsorbed NH_3 then reacts with NO , most probably in the gas phase, to form nitrosamide (NH_2NO) as an intermediate. This step is also accompanied by the reduction of the V center from +5 to the +4 state. The nitrosamide intermediate is unstable and decomposes easily into N_2 and H_2O . In the last step, molecular O_2 oxidizes the V center back to the +5 state, releasing H_2O and closing the catalytic cycle.

The commercial success of $\text{V}_2\text{O}_5/\text{TiO}_2$ catalysts derives from their moderate cost and superior sulfur resistance. However, this catalyst type possesses two major drawbacks that limit their application in vehicles. First, they have a rather poor activity at low temperatures, which poses a problem during cold start-ups and short-distance driving, where the exhaust

gas does not reach the required temperature for sufficient NO_x conversion. Second, diesel particulate filters (DPF) – located upstream of SCR catalysts – need to be periodically regenerated at temperatures that are high enough to release volatile vanadium species and cause the undesirable transformation of TiO₂ from anatase to low-surface-area rutile. Nonetheless, they still find applications in stationary power plants, locomotives and ships, which require only a relatively narrow temperature window.

1.1.2. Copper-based SCR catalysts

Cu-based catalysts are known for a long time as catalysts for NO_x abatement. As early as the 1980's, researchers have found that Cu-exchanged zeolites can decompose NO into N₂ and O₂ directly [39]. Further research revealed that the NO_x conversion can be strongly improved when a selective reductant was introduced [40]. Since then, Cu-based catalysts have remained in the focus of SCR research.

The chemical nature of Cu-exchanged zeolites is well studied in the scientific literature. Cu can coordinate with negatively charged Al sites in the zeolite framework to form isolated Cu²⁺ or Cu-hydroxo (Cu⁺-OH) sites. CuO clusters typically do not form, unless all of the Al sites are already occupied. The Cu metal center serves as the active site of the catalyst, and possesses both redox and acidic functionalities. During the reaction cycle, Cu shuttles between two oxidation states: +1 in the presence of both NO and NH₃ and +2 after the reoxidation with O₂ or a stronger oxidizing agent such as NO₂ [41]. Likewise, Cu ions – as opposed to Cu metal – contain vacant *d* orbitals and can therefore function as Lewis acid sites, where reactant molecules can adsorb. The zeolite support is also involved in the catalytic process: aside from ensuring a high dispersion of the active site, its unique pore structure allows the permeation of reactants and provides spatial confinement for the reaction to occur. Furthermore, hydroxyl bridges act as Brønsted-Lowry acid sites that facilitate reactant adsorption.

For many years, the large-pore zeolites ZSM-5 and beta have been the standard carriers for Cu-based catalysts used in NH₃-SCR. While Cu-ZSM-5 was slightly more active than Cu-beta, the latter was more durable and enjoyed a wider acceptance in the industry. However,

neither possessed sufficient hydrothermal stability for long-term use. In one study, both catalyst samples lost more than 25% of their initial turnover rate after aging under 10 vol% H₂O at 800 °C [42]. The deactivation was reported to start already at 550 °C in some cases [43]. Several mechanisms were proposed for the observed activity loss, and there is a consensus that deactivation occurs when Al sites irreversibly detach from their original positions in the framework. Although this phenomenon – known as dealumination – is well documented for all zeolite materials working in the presence of steam, the situation is prohibitive for NH₃-SCR because large amounts of water are generated during combustion. Higher water contents favor the conditions for dealumination since water molecules can cooperate through proton shuttling to stabilize the transition state in the subsequent hydrolysis steps [44]. This process eventually leads to loss of Brønsted-Lowry acidity and collapse of the porous zeolite structure in favor of denser, more stable crystalline phases. Without the Al sites for anchoring, the high dispersion of Cu is lost, and SCR-inactive CuO phases are formed.

The most straightforward way to deal with this problem is to partially decrease the number of Al sites on the catalyst so that water has less sites to attack [45]. This can be achieved by controlled dealumination of the zeolite prior to the ion-exchange procedure. Although this strategy has been implemented in some applications, it comes with a serious drawback of obtaining a material with a sub-optimal Cu loading. Alternatively, a more thermostable carrier can be used, since the major constraint on catalyst stability is related to the support rather than the active phase. Recently, two support materials have been found to yield stable Cu-zeolites: SAPO-34 and SSZ-13. Both supports contain smaller pores than either ZSM-5 or beta. Indeed, the enhancement of the hydrothermal stability stems from the fact that the pores of these materials are so small (<4 Å) that the Al(OH)₃ dealumination product (~5 Å) cannot exit, thus preserving the integrity of the zeolite structure even under hydrothermal conditions [46, 47]. Consequently, both Cu-SAPO-34 and Cu-SSZ-13 have been commercialized and marketed as SCR catalysts.

SAPO-34 is a silicoaluminophosphate molecular sieve that shares its three-dimensional microporous framework with chabazite-type zeolites, to which SSZ-13 belongs. It has

excellent hydrothermal stability as evidenced by the fact that it is able to keep its structure intact at 600 °C under 20 vol% H₂O [48]. Interestingly, prolonged hydrothermal aging even improved the activity of Cu-SAPO-34 relative to the fresh state [49]. The rate enhancement was attributed to the migration of CuO_x clusters from the external surface of SAPO-34 to the Al exchange sites, where they could be stabilized as single Cu²⁺ sites. The demonstrated hydrothermal stability of Cu-SAPO-34 at high temperature is unprecedented, even surpassing that of Cu-SSZ-13 at 800 °C [50]. But surprisingly, Cu-SAPO-34 undergoes irreversible deactivation upon hydrothermal treatment at temperatures below 100 °C [51]. The deactivated samples still have the preserved zeolite framework and Brønsted-Lowry acidity, suggesting that the mechanism of activity loss is not due to dealumination but more likely due to the transformation of the Cu species. Recently, the molecular basis of the deactivation was revealed to originate from the reaction of Cu(OH)₂ with terminal Al species, forming SCR-inactive Cu-aluminate species [52]. Condensed water molecules facilitate this transformation, thus explaining the low-temperature nature of the deactivation. Even Cu-SAPO-34 samples stored under ambient conditions for a prolonged period are prone to this process, and exhibited transformation of the active Cu²⁺ sites into Cu-aluminates. Because of this unexpected but serious limitation, the industrial acceptance of Cu-SAPO-34 has started to decline.

Nowadays, Cu-SSZ-13 is the reference catalyst material for mobile SCR applications. It solves the pitfalls of vanadia-based and other Cu-exchanged zeolites, and offers both superior activity and hydrothermal stability. In particular, it has sufficient activity at temperatures below 200°C as well as stability at high temperatures when the DPF has to be regenerated. Due to its commercial success, it has been the subject of many spectroscopic and mechanistic studies. Atomically dispersed Cu²⁺ species are believed to be the active sites for NH₃-SCR. The molecular details of the reaction mechanism are still being debated, but there are some unifying features in all of the reports, which are summarized in Figure 1.2.

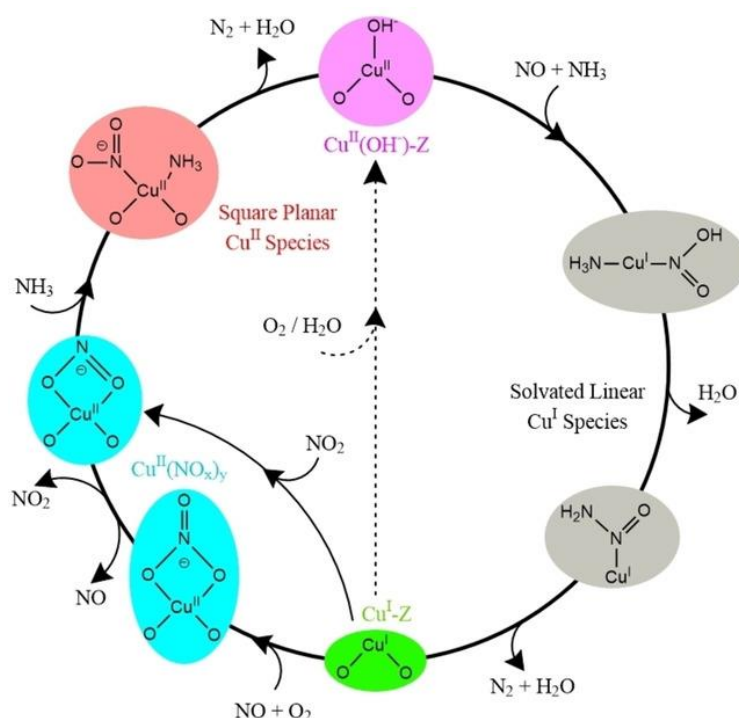


Figure 1.2. Proposed mechanism of SCR over Cu-SSZ-13. Source: Clark et al. [53].

Due to the basicity and polarity of NH_3 , it coordinates more strongly with the Cu^{2+} sites than NO does. Nonetheless, most reported mechanistic cycles indicate the co-adsorption of NH_3 and NO on the Cu^{2+} site to form a solvated linear Cu^+ complex as the first step [54, 55]. The Cu site only reduces in the presence of both NH_3 and NO. The formed intermediate is quite unstable, and decomposes readily into the SCR products, N_2 and H_2O . This generates a free Cu^+ species, which is the final product of the reducing half-cycle of the mechanism. The second half-cycle features the reoxidation of the Cu sites, which can be accomplished in two different ways. First, Cu^+ can be reoxidized directly to Cu^{2+} by the oxygen in the gas feed, closing the catalytic cycle immediately [53]. Alternatively, Cu^+ can form $\text{Cu}(\text{NO}_x)_y$ upon the adsorption of NO and oxygen. This is also accompanied by the change of oxidation state of Cu to +2. Then, NH_3 can coordinate with $\text{Cu}(\text{NO}_x)_y$ to yield a square planar Cu^{2+} complex that decomposes to produce N_2 and H_2O , regenerating the starting Cu^{2+} species. The rate-limiting step is thought to be the oxidation of Cu^+ back to Cu^{2+} , but recent data suggest that at high temperatures, when parasitic NH_3 oxidation becomes prevalent, it is the reduction of Cu^{2+} that determines the reaction rate [53, 55].

Cu-SSZ-13 is currently the best option for mobile SCR, providing unsurpassed low-temperature activity and high-temperature stability. However, it is not without drawback. Besides its much higher costs compared to vanadium-based systems, it is susceptible to N_2O formation, especially at high temperatures due to unselective NH_3 oxidation [56], and it deactivates in the presence of sulfur. Although Cu-SSZ-13 remains stable above 400 °C, its overall NO_x reduction tends to decrease at high temperatures.

1.1.3. Iron-based SCR catalysts

Fe-exchanged zeolites can serve as an alternative to Cu-based materials mostly for high-temperature applications. Although Fe catalysts suffer from low activity below 350 °C, they already surpass Cu-SSZ-13 in terms of NO_x conversion above 450 °C, and even vanadia-based catalysts above 550 °C. Moreover, thanks to the capability of Fe in catalyzing N_2O decomposition and reduction, negligible N_2O emissions are generally detected at elevated temperatures [57].

Analogous with Cu-exchanged zeolites, the Fe ions in the zeolite framework act as Lewis acid sites where NH_3 is activated to react with NO. The zeolite framework also provides Brønsted-Lowry acidity in the form of protonated Al-O-Si bonds, where NH_3 can also adsorb. The active Fe center changes from the +3 (oxidized) to the +2 state (reduced) and vice versa during the catalytic cycle. Fe-exchanged zeolites generally have a lower NH_3 storage capacity than their Cu counterpart, which may be explained by the inability of Fe to form a strong complex with NH_3 [58].

While Cu usually maintains a high degree of dispersion across the zeolite framework, Fe is more prone to form clusters or even particles. Fe-based catalysts can have (1) monomeric Fe sites with different coordination and framework environments; (2) oligomeric $\text{Fe}_x\text{O}_y(\text{OH})_z$ species possessing various degree of agglomeration; and (3) bulk Fe_xO_y particles of varying sizes and crystallinity. The ratio between these species primarily depends on the Fe loading, the synthesis procedure, and the zeolite structure [59, 60]. Moreover, these species may convert from one form to another under SCR conditions [61].

This diverse and dynamic speciation makes the molecular understanding of the SCR process over Fe-based materials particularly arduous.

Brandenberger et al. [60] proposed a direct relationship between the reaction temperature and the activity of Fe species of varying nuclearity. They suggested that at temperatures below 300 °C, monomeric Fe sites are the only species that determine the SCR activity. As the reaction temperature increases, the dimeric, oligomeric, and large Fe_xO_y sites also start to become active in the reverse order of their degree of nuclearity (i.e., the large Fe_xO_y clusters are the last to become active at higher temperatures). SCR selectivity is also influenced by the degree of agglomeration, with oligomeric and bulk Fe_xO_y species being widely recognized as the main contributors to the undesired NH_3 oxidation reaction. Hence, a high dispersion of Fe species is preferred. These findings were corroborated by Høj et al. [62], who reported a direct correlation between the NO_x conversion and degree of isolated Fe sites in the catalyst. They additionally proposed that not all monomeric sites have equal activity, thus suggesting that the zeolite environment has an impact on the activity as well.

The earliest Fe-exchanged zeolites studied had not only limited activity at low temperatures but also poor stability under hydrothermal conditions. Upon aging at high temperature in the presence of steam, Fe species detach from the exchange sites and agglomerate, which has a negative impact on selectivity [63]. Fe-based catalysts are also prone to poisoning by SO_2 and the formation of coke [64].

To improve the low-temperature activity of Fe-based catalysts, researchers adopted a synergistic approach where Fe is coupled with another material. It is well-established that Fe is more active at high temperatures whereas Cu at low temperatures. Hence, it is intuitive to combine both materials in one system to have a catalyst that can operate in a wider temperature range. This strategy was exploited to prepare Fe/Cu-exchanged zeolite catalysts [65], sequential dual-catalytic beds [66], and dual-layer Fe/Cu catalyst [67]. More recently, Liu et al. [68] prepared core-shell MoFe/Beta@CeO₂ materials, which improved the low-temperature activity by partially oxidizing NO to NO₂, thereby allowing the fast SCR reaction to proceed at low temperature.

Large pore BEA and medium pore ZSM-5 zeolites have been the most investigated supports for Fe-based SCR catalysts. Although satisfactory NO_x reduction activities are generally achieved, they deactivate quite readily at high temperatures in the presence of steam [69]. Because of this, small-pore chabazite-type zeolites such as SSZ-13 have received growing attention.

Gao et al. [70] synthesized a Fe-SSZ-13 catalyst with a remarkable low-temperature activity that can be retained up to 550 °C in the fresh state. Upon aging, the catalyst exhibited lower activity but still achieved 80% NO conversion at 450 °C. The hydrocarbon tolerance can be improved by careful selection of the zeolite framework.

Ma et al. [64] studied the effect of propene poisoning on the activity of Fe-BEA, Fe-ZSM-5, and Fe-MOR. While Fe-BEA and Fe-ZSM-5 deactivated significantly, Fe-MOR retained high NO_x conversion even after propene coking at 350 °C. The exceptional stability of Fe-MOR could be traced back to the one-dimensional pore structure of the zeolite framework, which could limit hydrocarbon diffusion in the first place. Furthermore, hydrocarbon activation is hindered in MOR because it is not as acidic as BEA and ZSM-5.

As with the two previously discussed catalysts, the mechanism of SCR over Fe-exchanged zeolites is still under debate. Nonetheless, the general features of the reaction cycle can be described without ambiguity (Figure 1.3).

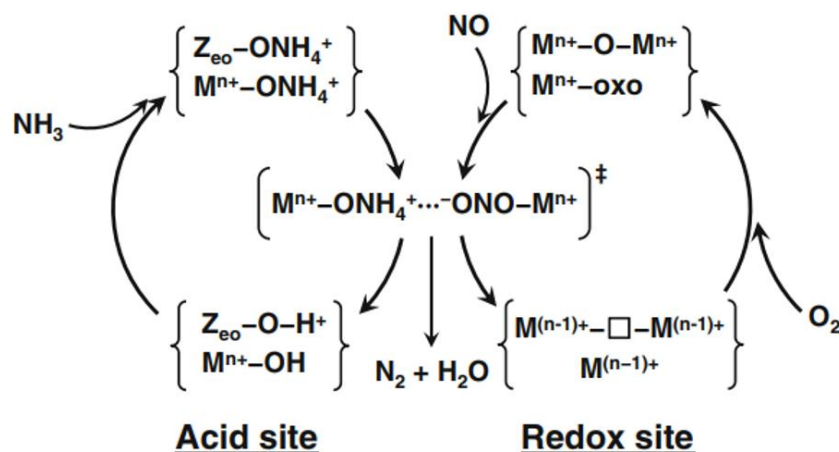


Figure 1.3. Proposed mechanism of SCR over Fe-exchanged zeolites. M^{n+} corresponds to Fe^{3+} while $\text{M}^{(n-1)+}$ corresponds to Fe^{2+} . Source: Nova and Tronconi [18].

Under reaction conditions, NH_3 populates the catalyst surface by adsorbing on both Brønsted-Lowry (protonated Al-O-Si groups) and Lewis acid sites (Fe centers). The first step of the reaction is the so-called NO oxidative activation, in which NO from the gas phase or weakly adsorbed state oxidizes on Fe^{3+} sites. This step is coupled with the reduction of the transition metal center to Fe^{2+} . While the occurrence of this step is widely accepted, the nature of the oxidized intermediate is still a matter of debate. Historically, NO_2 and its derivative N_2O_3 were proposed as intermediates [63], but recent evidence pointed toward other species such as HONO or nitrites [71]. Nonetheless, HONO and nitrites are ultimately produced by either NO_2 dimerization and disproportionation or N_2O_3 disproportionation. The successive reaction between HONO or nitrites species and adsorbed NH_3 possibly lead to the formation of the intermediate ammonium nitrite that decomposes into N_2 and H_2O . This step automatically regenerates the Brønsted-Lowry and Lewis acid sites, which are once again ready to adsorb NH_3 molecules. On the other hand, the reduced Fe^{2+} is oxidized back to Fe^{3+} by the action of molecular oxygen. While this step is considered rate-limiting by Ruggeri et al [71], Metkar et al. [72] suggested NO oxidation to surface-bound NO_2 as the rate determining step.

1.1.4. Comparison of the SCR catalysts

The advantages, disadvantages, and typical applications of the three major types of SCR catalysts are listed in Table 1.1.

Table 1.1. Comparison between the three most industrially relevant SCR catalysts

Type of catalyst	V-based catalysts	Cu-based catalysts	Fe-based catalysts
Main advantages	<ul style="list-style-type: none"> • High resistance to SO₂ poisoning • Moderate cost 	<ul style="list-style-type: none"> • Unparalleled activity at low temperature • High thermal stability (SSZ-13) 	<ul style="list-style-type: none"> • High SCR activity at high temperatures • Able to decompose N₂O readily
Main disadvantages	<ul style="list-style-type: none"> • Potential release of carcinogenic vanadium oxides • Poor thermal stability due to rutilization 	<ul style="list-style-type: none"> • Release of N₂O • Decrease in NO_x activity at high temperature 	<ul style="list-style-type: none"> • Prone to form clusters which lower the activity • Poor resistance against coking and steam (BEA and ZSM-5)
Typical applications	Stationary and marine systems	Mobile systems	

1.2. Transient experimentation and modulated excitation spectroscopy

Spectroscopy has contributed greatly to shedding light on the “black box” enclosing the mechanism of catalytic processes, including SCR. Through our knowledge of light-matter interaction, we have gained access to the molecular events occurring on the catalyst surface that were not possible some decades ago. As a result, the rational design of catalytic materials is starting to become more realistic than ever. Despite its great successes, however, modern spectroscopy still faces a number of limitations when applied to heterogeneous catalysis research due to the inherent complexity of solid catalytic systems. The prevailing difficulties stem from the following:

1. Catalysis results from simultaneous and often superimposed chemical phenomena [73]. These include reactant adsorption, surface reaction, and product desorption. As a consequence, the arising spectral signal will be a convolution of all of these processes. In some cases, one of the processes (and its spectral features), will predominate over the others in a steady-state process. Furthermore, the spectral features of different chemical species may have similar energy values and in practice appear as overlapping signals. For instance, Lewis-bound NH_3 , water, and nitrate species possess vibrational signature in the infrared spectrum at around 1620 cm^{-1} . The observed peak is then the result of the overlap of the signals of these three species, with no straightforward way of deconvolution [74].
2. In commercial catalyst formulations, the active phase is present in a much lower concentration in comparison with the other catalyst components (e.g., support, promoter, and binder) in order to maximize the atom efficiency of the active phase, which is usually more expensive and not earth-abundant. Conventional spectral features are therefore dominated by the signal originating from species coordinated to the support while the active phase, which is the catalytically relevant component, can only contribute weakly because of its low concentration. In addition, the active phase itself can be further divided into catalytically relevant and spectator/unresponsive species. Normally, the spectator species prevail in number,

and it remains a challenge to extract the signal contribution from the real species responsible for the activity [75].

3. Reactive intermediates are short-lived species, owing to their thermodynamic instability. In rare instances, intermediate species are sufficiently stable that they can be isolated and characterized extensively. This is especially true for some organic reactions [76, 77], but it is not the norm for inorganic reactions and those that occur via a radical mechanism. The transient presence of intermediates in the reaction is further complicated by the fact that compared to the reactants and products, only a very small fraction of the intermediate is present at any given time and thus will most likely be obscured by the signal contributed by the other species.

Difference spectroscopy may partially solve the problem of separating the signal of the active phase from that of the support [78], but it fails to address the other issues. A short example is described in Figure S-1.1. Chemometric methods can be employed to resolve complex envelopes of superimposed signals and are increasingly gaining popularity, but this normally requires large datasets and computing power. Alternatively, a different experimental approach may be implemented. First described in a seminal paper more than two decades ago [79], modulated excitation (ME) spectroscopy holds the potential of addressing all of the aforementioned difficulties.

ME is a type of a transient-response technique that consists of subjecting the reaction system with periodic perturbations of an external parameter. The stimulus is chosen in such a way that the species of interest (e.g., catalytically active sites) would respond selectively, if not exclusively, to the perturbation. In principle, there is no restriction on the type of stimulus that can be applied, and many examples exist in the literature. Controlled variations in reactant concentration [80, 81], temperature [82, 83], electric field [84], light flux [85], and X-ray energy [86] can all potentially elicit a signal change. By far, concentration modulation is the most commonly used technique in heterogeneous catalysis because it is fairly straightforward. As catalysis is a surface phenomenon, the active sites will have to interact with the reactants before a chemical transformation occurs. Hence,

changes in the reactant concentration will ultimately trigger modifications in the chemical state of the catalytically relevant sites, allowing them to be selectively detected.

The general principles of ME spectroscopy are illustrated in Figure 1.4. For the sake of this example, the stimulus (**S**; Figure 1.4a) can be taken as the reactant concentration, which is continuously changed throughout the experiment while the signal of the active species (**A**; Figure 1.4a) is being recorded. For simplicity, only one such signal is described here, but it should be noted that a single species could give rise to a host of different signals (e.g., a chemical intermediate with different IR-active functional groups). At the start of such periodic perturbations, there is typically an initial period when the chemical system acclimatizes to the pulses (equilibration; Figure 1.4a) before it eventually reaches a stably oscillating period (quasi steady-state; Figure 1.4a), at which point the mean value of the signal response is constant.

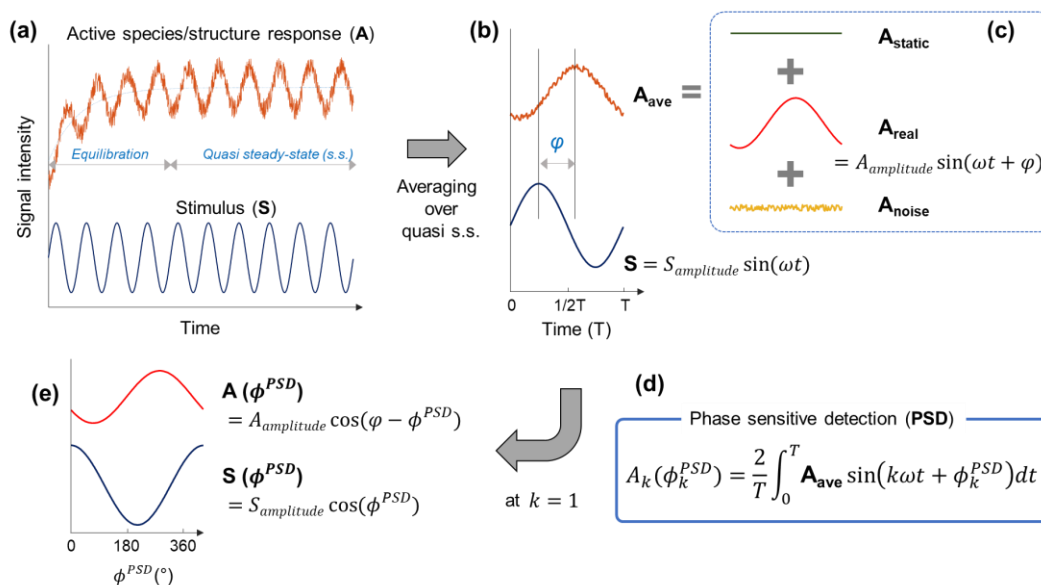


Figure 1.4. (a) Sinusoidal stimulus of an external parameter and a representative response of active species or structures affected by the stimulus; (b) the average response obtained after reaching quasi steady-state; (c) the three signal elements consisting of the actual response (A_{ave}), namely static signal (A_{static}), actual signal of interest (A_{real}) and noise (A_{noise}); (d) the mathematical engine of ME spectroscopy, phase-sensitive detection (PSD); and (e) the phase-domain response after PSD at the fundamental stimulus frequency demodulation ($k = 1$).

The first data processing is simple averaging of the signal over the cycles into one period after reaching a so-called quasi steady-state after the initial equilibration period (Figure 1.4b), with the dataset during the equilibration phase being excluded from further analysis. This reduces the data size and improves sensitivity as well as the signal-to-noise ratio by about \sqrt{N} according to Poisson statistics (where N is the number of averaged cycles). Actively responding species mainly respond at the same frequency as that of the stimulus, and the signal intensity oscillates in a sinusoidal manner but with some delay (ϕ ; Figure 1.4b). The magnitude of the delay is dependent on the kinetics of the underlying physicochemical processes (e.g. sorption, reaction, convection, diffusion). Furthermore, the frequency of stimulus affects the magnitude of the delay, and kinetic studies can be performed by varying the stimulus frequency (ω ; Figure 1.4b).

Even without further mathematical treatment, the averaged response and its delay already contain some information that can be used to understand the processes under investigation. However, the relative intensity of the signal actively changing in response to the stimulus is often extremely small and can be even at the level of noise. As a solution, the signal-to-noise ratio can be improved by increasing the number of cycles (N), but this increases the burden in the experiments and data processing. Hence, further analysis is usually performed.

In principle, the averaged signal (A_{ave}) comprises three elements (Figure 1.4c), namely static signal (A_{static}), the actual signal of interest (A_{real}), and noise (A_{noise}). A_{static} may arise from the support material, solvent (i.e., in case of liquid-phase measurements), or inactive spectator species. Although they are important for the proper functioning of the system, their dominant signal intensity should be reduced or eliminated completely so that A_{real} can be extracted and investigated. A_{noise} is always present in any measurement and typically contains high-frequency elements with respect to the stimulus frequency. Since A_{noise} becomes more significant when the time resolution of measurements is increased, the speed of data acquisition should be optimized. In the end, the goal is to extract A_{real} out of A_{ave} , and this is accomplished through a mathematical technique known as phase-sensitive detection (PSD; Equation 1.4) [79].

$$A_k(\varphi_k^{PSD}) = \frac{2}{T} \int_0^T A_{ave} \sin(k\omega t + \varphi_k^{PSD}) dt \quad (\text{Equation 1.4})$$

where $A_k(\varphi_k^{PSD})$ is the signal in the phase domain, T is the modulation period, A_{ave} is the averaged signal in the time domain, k is the demodulation index ($k = 1$ in most studies), ω is the stimulation frequency, and φ_k^{PSD} is the phase angle.

PSD, also colloquially called demodulation, is analogous to a Fourier transformation or a digital lock-in amplifier (Figure 1d). In a nutshell, the averaged signal (A_{ave}) is multiplied by another sine function at the frequency of $k\omega$. The sine function contains also a new variable φ_k^{PSD} , which is called phase angle. Generally, the multiplied sine function has the fundamental frequency of the stimulus (ω), meaning that $k = 1$. Then, the obtained response is integrated over the period (T) and then normalized by $\frac{2}{T}$ (Figure 1.4d).

After PSD treatment, the stimulus ($\mathcal{S}(\varphi_k^{PSD})$; Figure 1.4e) and the active species signal ($\mathcal{A}(\varphi_k^{PSD})$) are no longer a function of time, but rather of phase. More importantly, the A_{static} and the high-frequency A_{noise} terms are completely eliminated, and only the A_{ave} term is embedded in $\mathcal{A}(\varphi_k^{PSD})$. Therefore, ME and PSD can impart selectivity to the measurement and boost its detection sensitivity by removing the static signals and reducing the noise while retaining the key information of interest. This drastic improvement in the sensitivity is extremely useful to study weak and transiently present signals in catalytic reactions.

In a catalytic system involving more than one reactant species, the question arises on which type of perturbation should be applied. After all, modulation of one reactant or the other can produce different or no additional information, depending on the selected perturbation [87]. The decision of which reactant concentration to modulate can be decided based on the specific technique to be applied, in relation to the molecular information that is sought. For instance, IR spectroscopy can reveal the presence of adsorbed reactants and intermediates. Under SCR conditions, NH_3 populates the surface of the catalyst, with NO and O_2 both reacting from the gas phase. Furthermore, NH_3 can form two types of surface species, depending on which site it coordinates to: NH_4^+ on Brønsted-Lowry sites and NH_3 on Lewis acid sites. In order to determine which of the two species is active, a modulation

experiment concerning NO can be applied under constant NH_3 and O_2 . During the “SCR on” half-period, NO will selectively titrate either NH_3 or NH_4^+ while during the “SCR off” half-period, the sites from which NH_3 has been consumed, will have a chance to be replenished from the NH_3 in the gas phase. The constant presence of O_2 is also needed during this “SCR off” part because it ensures that most of the vanadyl species are in the V^{5+} state, which is where NH_3 is activated. Hence, NO modulation is a useful tool to combine with IR spectroscopy to study the active sites of SCR. In contrast, NH_3 modulation will probably not reveal the same depth of information. Since NO can interact only weakly with the catalyst, whatever NO adsorbs on the catalyst will just be displaced by NH_3 during the reactant pulse.

The reverse approach is true for a complementary experiment using Raman spectroscopy, which in the case of vanadia-based SCR probes the catalyst structure rather than the adsorbed species. Vanadyl species with different degrees of coordination provide slightly different Raman signals. In particular, the presence of adsorbed species red-shifts the main vanadyl peak because of the decreased $\text{V}=\text{O}$ bond strength. Under SCR conditions, the vanadyl species exhibit varying degrees of coordination, resulting in a broad Raman peak for $\nu(\text{V}=\text{O})$. If NO is pulsed in the NH_3 flow, all of the observable vanadyl species will remain in the NH_3 -coordinated state. As soon as they react with NO, they will be populated again with NH_3 due to the strong acid-base interaction. This will not reveal additional information beyond what is delivered by the steady-state approach. For this reason, NH_3 pulsing is the intuitive choice to observe changes in the distribution of vanadyl species and potentially reveal which is then responsible for the SCR activity.

Another applicable technique is UV-visible spectroscopy, which delivers information about the oxidation state of the active metal centers. For a modulation experiment of this type, O_2 concentration would be the preferred stimulation while keeping NH_3 and NO in constant supply. Without oxygen, the vanadyl sites are reduced under the joint presence of NH_3 and NO. The second half of the catalytic cycle is initiated only when O_2 is pulsed, reoxidizing the vanadyl sites to restart the cycle. While NH_3 or NO modulation could also

cause oxidation state changes, only O₂ pulsing can do so with the largest fraction of vanadyl species.

1.3. Scope of the thesis

The inherent complexity of the SCR reaction makes it an interesting case study for transient response experimentation and ME spectroscopy. PSD can amplify the signal of responsive species, resolve overlapping peaks, and enable the detection of intermediate species. This increased level of sensitivity can provide molecular information that transcends the boundaries of conventional spectroscopy under static conditions. Hence, the primary goal of this thesis is to further the mechanistic understanding of SCR through the application of complementary techniques under dynamic, non-steady-state conditions.

To implement such an experimental design, we have built a cell that acts not just as a sample holder for spectroscopic measurements, but also as a catalytic reactor (Chapter 2). The ME technique was then applied to Raman spectroscopy (Chapter 3) and IR spectroscopy (Chapter 4) to reveal mechanistic insights that can be observed only under transient conditions and PSD treatment.

Raw exhaust gases may contain notable levels of formaldehyde that can negatively impact the efficiency of SCR and result in the production of hydrogen cyanide. The molecular mechanism of this detrimental side reaction was studied through a series of catalytic tests (Chapter 5) and operando IR spectroscopy (Chapter 6) so that process adjustments can be put forward.

Cu-SSZ-13 has emerged recently as a viable material for mobile SCR. Transient XAS experiments were performed to capture the low-temperature inhibitory effect of NH₃ on the process so that adjustments can be made to improve the SCR activity while saving up on reductant consumption (Chapter 7).

The contents of this thesis are based on already published and soon-to-be published scientific manuscripts and book chapters, as declared on pp. 215-217.

Chapter 2 – Design of a Reactor Cell for Transient Response and Modulated Excitation Studies

2.1. Introduction

The scientific literature abounds with spectroscopic investigations of SCR catalysts, and debated reaction mechanisms have been proposed based on these studies [22, 36]. However, many of these experiments were carried out under static conditions, which may not be sufficient to extract in-depth mechanistic and kinetic details about the system. Furthermore, real-life automotive catalysts do not operate in a steady-state manner, but rather under dynamic conditions of temperature, pressure, and reactant composition that are dictated by the driving conditions. Therefore, transient-response experimentation such as modulated excitation (ME) are more suitable to investigate SCR catalysts.

Beside spectrometers with a high temporal resolution and the use of switching valves with sub-second response time, a suitable reactor cell with a low void volume is needed for ME experiments – a requirement that most commercial spectroscopic cells lack. Indeed, although commercial cells are suitable for routine in situ studies, they cannot exchange gases fast enough for transient response experiments. Special sample holders must be custom-built for this purpose, and various examples exist in the literature [88-94].

Here we describe in detail the design and performance characteristics of a custom-built spectroscopic cell with a reduced void volume, which makes it amenable to ME experimentation. Coupled to a suitable set-up, this cell can be used to reproduce the same type of experiment using complementary spectroscopic methods such as Raman, UV-visible, and infrared spectroscopy.

2.2. Materials and methods

2.2.1. Cell design and experimental set-up

The cell is presented in Figure 2.1 and was constructed according to the specifications given in Figure S-2.1 to Figure S-2.5. An actual image of the cell is presented in Figure S-2.6. It is based on the design of a Harrick spectroscopic cell and is used with a Praying MantisTM accessory for diffuse reflection. The cell can be used with automatic stages for mapping experiments similar to the commercial cell. Two major innovations contribute to reducing the void volume significantly. First, the design of the cell body (A; Figure 2.1) was revamped to remove the inner void volume present in the commercial cell. This was achieved by positioning the heat cartridge vertically and exploiting it to pre-heat the gas feed to the sample. The body confining the heating cartridge (B) also contains the sample cup (C). The gas feed runs within an annular void space of approximately 4 mL between A and B before meeting the sample in a very similar geometry to the commercial cell. In the current design, the thermocouple used to control the sample temperature (D) is inserted approximately 1 mm below the sample cup in the same body, while a second thermocouple (E) is placed parallel to this one and is used to record the temperature. For improved temperature control and monitoring, another thermocouple may be inserted perpendicular to the sample cup. Second, the cell cover consists of just one flat window (F) instead of two windows arranged in a dome-like configuration, as it is the case in the commercial cell.

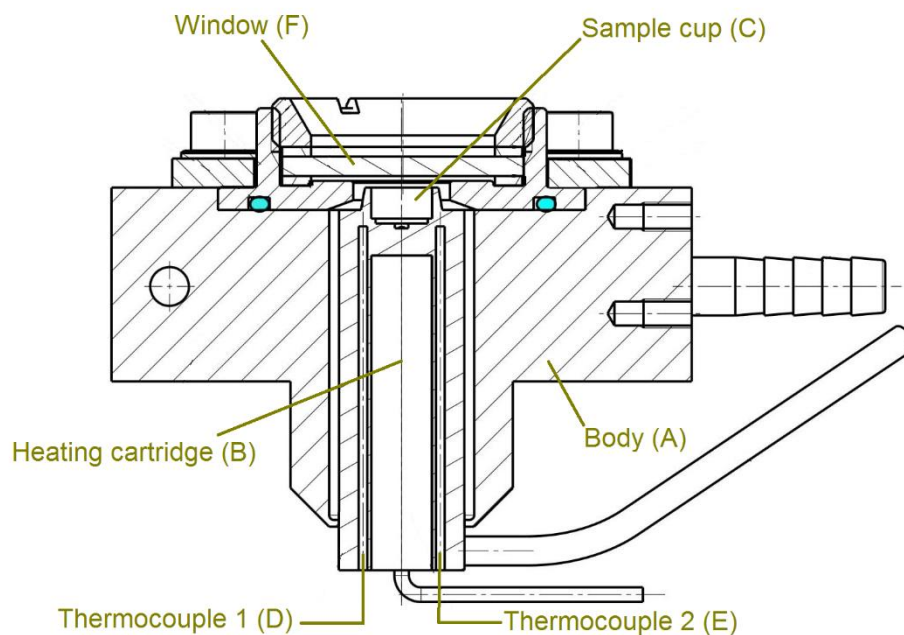


Figure 2.1. Design of the custom-built spectroscopic cell.

Although this geometry is not optimum for diffuse reflectance because of the specular component, the cell can be lifted up until the signals of the sample (not necessarily the amplitude of the IR signal) are maximized. This is shown in Figure 2.2 for a zeolite sample. The IR signals from the zeolite framework are clearly discernible in the single beam spectrum from 2000 to 1000 cm^{-1} . We have also exploited this geometry successfully in a different cell design [91]. The moveable clamps used to secure the window on top of the spectroscopic cell follow the design of the commercial cell.

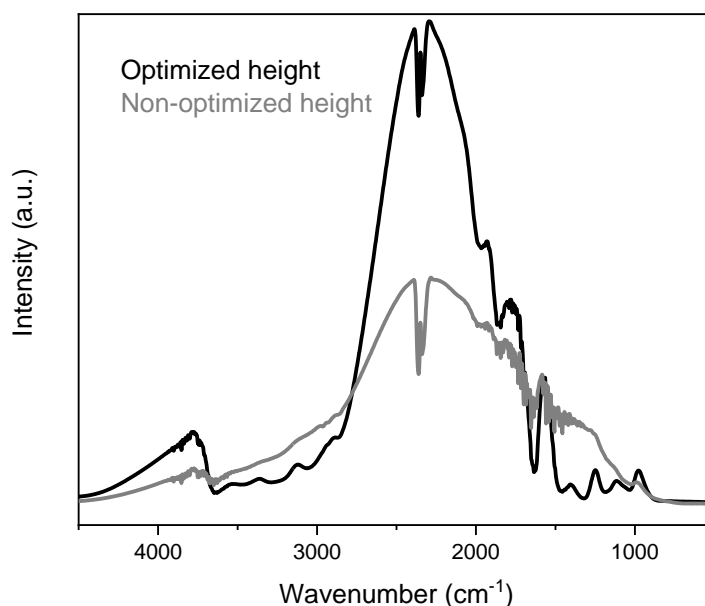


Figure 2.2. Single beam spectra of the sample position (optimized height) and of the window position (non-optimized height) as a function of the cell position in the z-axis.

We have demonstrated earlier that the cell can be used as a reactor for SCR studies [38, 95]. The cell is the heart of a setup enabling mixing gases and consisting of a main gas feed line and four auxiliary lines. The gas through the four auxiliary lines can be mixed with the one flowing through the main line using four independent Series 9 solenoid valves (Parker) controlled by the Rapid Scan TRS mode of the OPUS spectroscopy software (Bruker). The exit of the cell can be interfaced with an IR spectrometer or a mass spectrometer. All lines are stainless steel. Water is generated *in situ* from precise flows of H₂ and O₂ through a Pt/Al₂O₃ catalyst. This allows for a pulsation-free feeding of water.

The same cell and the same setup have been used for all spectroscopic experiments described in the following chapters.

2.2.2. Residence time distribution properties

The residence time distribution (RTD) analysis was performed using a pulse input experiment [89, 96]. NO (2 μ L) was introduced in an Ar-only gas feed (100 mL \cdot min⁻¹)

through the cell using a four-way valve. The concentration decay of the tracer was monitored using an OmniStar GSD 320 mass spectrometer (MS; Pfeiffer) that was connected downstream of the cell. The experiment was also repeated in a stainless steel gas line bypassing the reactor cell and flowing directly to the MS.

The RTD function $E(t)$ was calculated according to Equation 2.1.

$$E(t) = \frac{C(t)}{\int_0^\infty C(t) dt} \quad (\text{Equation 2.1})$$

where v is the volumetric flow rate, $C(t)$ is the concentration of the tracer leaving the reactor at time t . Since NO concentration is directly proportional to the mass-to-charge ratio of 30 ($m/z = 30$), it was used in the calculations. Integrating $E(t)$ over a time gives the fraction of the gas that has resided in the reactor for that specific period, thus:

$$\int_0^\infty E(t) dt = 1 \quad (\text{Equation 2.2})$$

Experimentally, this relationship is confirmed since the MS signal at $m/z = 30$ eventually returns to the baseline value after each tracer injection.

An important parameter that can be derived from the RTD analysis is the mean residence time t_m (Equation 2.3).

$$t_m = \int_0^\infty tE(t) dt \quad (\text{Equation 2.3})$$

This is the average time that a molecule spends within the reactor. For transient response studies, a spectroscopic cell with a low t_m is desired.

2.2.3. Materials synthesis

The catalysts used in this study were 2 wt% V_2O_5/TiO_2 , 2.6 wt% Fe-ZSM-5, and 1.6 wt% Cu-SSZ-13.

V_2O_5/TiO_2 was prepared by wet impregnation. A sufficient amount of ammonium metavanadate (Fluka, >99.0%) was dissolved in water at 60 °C, and was mixed for 1 h with

TiO₂ (DT-51, Cristal) calcined at 550 °C. After removal of water under reduced pressure, the sample was calcined in a muffle furnace at 600 °C for 5 h.

Fe-ZSM-5 was prepared by ion exchange. ZSM-5 (Si/Al=13; SM-27 P, Süd-Chemie) was mixed with a solution of 0.1 M FeSO₄·7H₂O (Sigma-Aldrich, >99.0%) at room temperature for 6 h. The sample was filtered, washed thrice with distilled water, and dried at 120 °C overnight. Then, it was calcined at 600 °C for 6 h.

Cu-SSZ-13 was prepared by hydrothermal synthesis and ion exchange, as described in detail elsewhere [55]. Briefly, the synthesized SSZ-13 was ion-exchanged with a solution of 0.1 M CuSO₄·5H₂O (Sigma-Aldrich, >98%) at 80 °C for 4 h, filtered, washed thrice with distilled water, and dried at 120 °C overnight. The sample was then calcined at 600 °C for 4 h.

Approximately 50 mg of each catalyst powder (100-150 μm) were loaded into the spectroscopic cell. Prior to each experiment, the sample was dehydrated in 5 vol% O₂/Ar (100 mL·min⁻¹) at 450 °C for 1 h.

2.2.4. Raman spectroscopy

Raman spectra were collected using a RamanRXN-1™ analyzer (Kaiser) equipped with a fiber optics probe and a 785-nm laser. Spectra were collected from 1500 cm⁻¹ to 100 cm⁻¹ at a resolution of 2 cm⁻¹ with a laser power of 100 mW and exposure time of 0.5 s.

The cell was equipped with a 2-mm thick sapphire window (Crystran) and attached to a Praying Mantis™ accessory. The fiber optics probe was mounted perpendicular to the cell.

ME was performed by pulsing 500 ppm of NO every 30 s in a gas feed of 500 ppm NH₃, 2 vol% H₂O, 5 vol% O₂ balanced in Ar (100 mL·min⁻¹). Each period consists of 30 consecutive spectra, which were collected every 2 s. At least 20 periods were averaged to generate the phase-resolved spectra.

2.2.5. Diffuse reflectance visible spectroscopy

Diffuse reflectance visible (DR-Vis) spectra were recorded using a Cary 4000 UV-Vis spectrometer (Agilent). Spectra were collected from 350 nm to 800 nm at a resolution of 1.1 nm and scan rate of $16.7 \text{ nm}\cdot\text{s}^{-1}$. Acquisition in the UV region was not performed because the time resolution would be compromised by changing the light source during the measurement.

The cell was equipped with a 2-mm thick CaF_2 window (Crystran) and attached to a Praying MantisTM Diffuse Reflection Accessory in the compartment of the UV-Vis spectrometer.

ME was performed by pulsing 1000 ppm NO every 120 s in a gas feed of 1000 ppm NH_3 , 5 vol% O_2 balanced in Ar ($100 \text{ mL}\cdot\text{min}^{-1}$). Each period consists of 10 consecutive spectra, which were collected every 24 s. At least 10 periods were averaged to generate the phase-resolved spectra.

2.2.6. Diffuse reflectance infrared Fourier transform spectroscopy

Diffuse reflectance infrared Fourier transform (DRIFT) spectra were collected using a Vertex70 spectrometer (Bruker) equipped with a HgCdTe detector. Spectra were recorded in the range of 4000 to 800 cm^{-1} at a resolution of 4 cm^{-1} and scanner velocity of 80 kHz . The sample and background spectrum resulted from 10 and 50 scans, respectively.

The cell was equipped with a 2-mm thick CaF_2 window (Crystran) and attached to a Praying MantisTM accessory in the compartment of the IR spectrometer.

ME was performed by pulsing 1000 ppm NO every 60 s in a gas feed of 1000 ppm NH_3 , 5 vol% O_2 balanced in Ar ($100 \text{ mL}\cdot\text{min}^{-1}$). Each period consists of 120 consecutive spectra, which were collected every 1 s. At least 20 periods were averaged to generate the phase-resolved spectra.

2.2.7. Phase-sensitive detection

The time-resolved spectra were converted into phase-resolved spectra using Equation 1.4 [79]. A MATLAB script was used for the data analysis.

2.3. Results and discussion

2.3.1. RTD analysis and mean residence time

Residence time distribution (RTD) analysis was performed to check the efficiency of gas exchange inside the reactor. The RTD profile of the NO pulse through the spectroscopic cell was calculated according to Equation 2.1, and the results are shown in Figure 2.3 and Table 2.1. At a flow rate of $100 \text{ mL} \cdot \text{min}^{-1}$, the RTD behaviors of the NO pulse through the cell and bypass show very similar shapes. The decay profile of the NO pulse that passed through the cell exhibited tailing, but the effect was offset by the high flow rate.

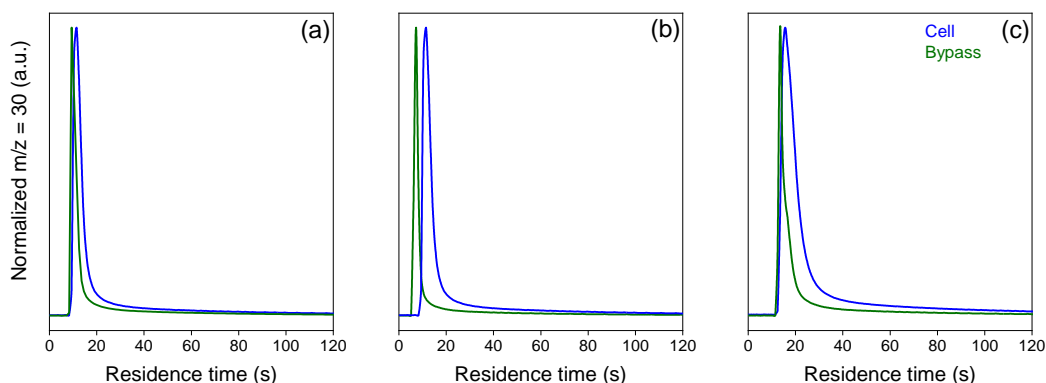


Figure 2.3. Normalized residence time distribution profiles of $2 \mu\text{L}$ NO pulsed in a gas feed of Ar through the spectroscopic cell and bypass at room temperature and atmospheric pressure in dependence of the total flow: (a) $100 \text{ mL} \cdot \text{min}^{-1}$, (b) $50 \text{ mL} \cdot \text{min}^{-1}$, and (c) $25 \text{ mL} \cdot \text{min}^{-1}$.

Decreasing the flow rate broadened the concentration decay curves considerably because of a more pronounced effect of the extra cell volume. The NO concentration reached its maximum value with a considerable time delay – a feature that was not observed at $100 \text{ mL} \cdot \text{min}^{-1}$. At a flow rate of $25 \text{ mL} \cdot \text{min}^{-1}$, the time at which the MS signal decayed to 90% of its initial value (t_{90}) was doubled when NO was injected through the cell instead of the bypass.

Table 2.1. Residence time distribution characteristics of the spectroscopic cell

	Flow rate					
	100 mL·min ⁻¹		50 mL·min ⁻¹		25 mL·min ⁻¹	
	Bypass	Cell	Bypass	Cell	Bypass	Cell
t_m (s)	21.6	22.9	23.8	26.2	28.4	31.2
t_{90} (s)	7.2	13.7	4.8	6.9	2.8	3.8
t_{95} (s)	11.7	24.5	8.0	12.2	5.0	6.5
t_{99} (s)	65.3	113.4	51.0	79.6	36.6	47.3

Legend: t_m = mean residence time; t_{90} = time for the MS signal to drop by 90% of the maximum value; t_{95} = time for the MS signal to drop by 95% of the maximum value; t_{99} = time for the MS signal to drop by 99% of the maximum value.

In all of the decay profiles presented in Figure 2.3, the tailing observed as the MS signal returned to the baseline value slowly after the pulse is most probably due to stagnant regions or residual void zones in the cell where the gas exchange might be less efficient. Such profile is characteristic of a non-ideal continuous-stirred tank reactor (CSTR) [96]. Indeed, the commercial cell which served as the basis of the current cell design was reported to be a CSTR according to recently published studies [89, 90]. It is also worth noting that the bypass line also showed a CSTR profile, which is contributed mainly by the MS detection chamber [90].

In ME experiments, the system will eventually reach a quasi-equilibrium state no matter how large the void volume of the reactor is. However, it is preferred that the concentration of the reactants in the gas phase is changed as much as possible in each half period because this will induce a more prominent change in the corresponding phase-resolved spectra. It is for this reason that the void volume of the spectroscopic cell must be as low as possible. For instance, when 1000 ppm NO is pulsed in a feed containing NH₃ (i.e., SCR on/off conditions), a reactor with appropriate gas exchange capabilities will allow the NO

concentration to drop as close to 0 ppm as possible when the supply is off. On the other hand, a spectroscopic cell with a high void volume might always have various levels of residual NO in the gas phase even though the supply is off. As a result, SCR would always be on and there would be weaker spectral changes to observe after phase-sensitive detection (PSD).

In the following ME experiments, the total gas flow was fixed at $100 \text{ mL}\cdot\text{min}^{-1}$. The calculated t_m under these conditions is approximately 22.9 s (Table 2.1). As a result, we ensured that the half-period of any ME experiment performed with the cell was well above this value (i.e., 30 s for Raman spectroscopy, 60 s for DRIFT spectroscopy, and 120 s for DR-Vis spectroscopy).

2.3.2. ME-Raman spectroscopy of $\text{V}_2\text{O}_5/\text{TiO}_2$

Figure 2.4a,b shows the time-resolved Raman spectra and the corresponding phase-resolved spectra of $\text{V}_2\text{O}_5/\text{TiO}_2$ obtained under repeated NO pulses. The strong bands at 395, 516, and 636 cm^{-1} are characteristic of crystalline TiO_2 in the anatase phase and correspond to B_{1g} , $\text{A}_{2g}+\text{B}_{1g}$, and E_g modes, respectively [97, 98]. The B_{1g} mode has a second overtone at around 800 cm^{-1} , which is visible as a weak band in the spectrum. The peak at around 1018 cm^{-1} is readily assigned to the $\nu(\text{V}=\text{O})$ stretch mode, which is centered at 1031 cm^{-1} under dry, oxidizing conditions [99]. The absence of the bulk V_2O_5 peak at 995 cm^{-1} indicates that the VO_x species are well-dispersed in agreement with the submonolayer coverage of the catalyst ($2 \text{ VO}_x\cdot\text{nm}^{-2}$) [100].

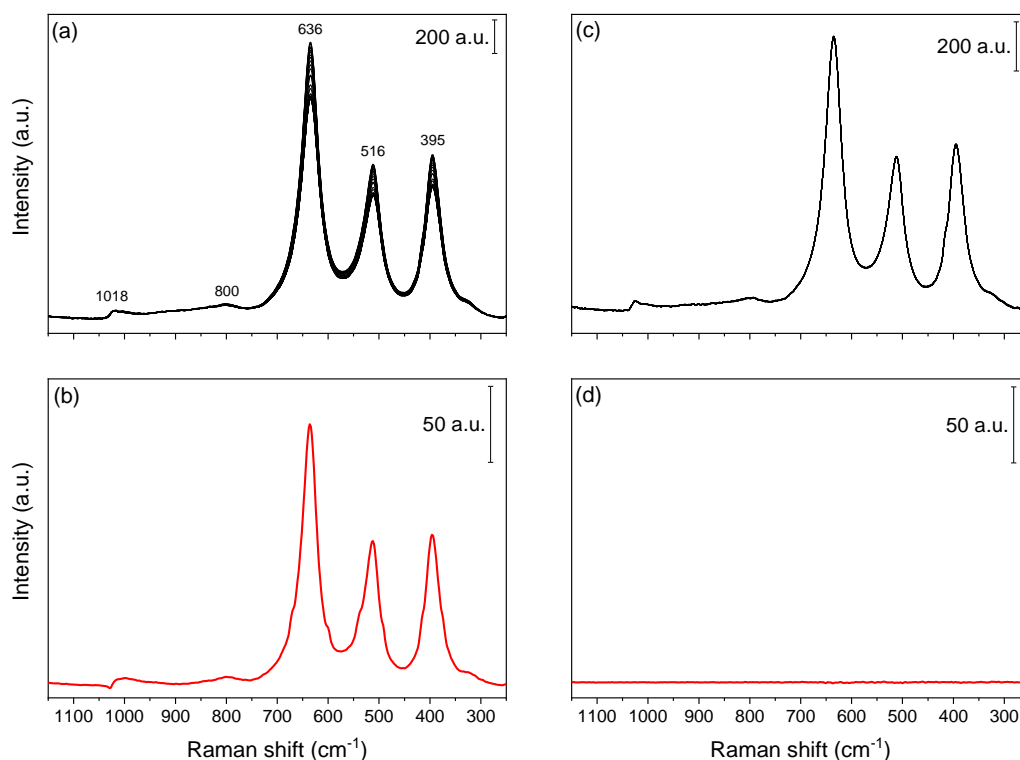


Figure 2.4. (a) Time-resolved Raman spectra and (b) the corresponding in-phase spectrum of V_2O_5/TiO_2 at 250 °C during 30-s pulses of 500 ppm NO in a gas feed of 500 ppm NH_3 , 2 vol% H_2O and 5 vol% O_2 balanced in Ar. (c) Time-resolved Raman spectra and (d) a selected phase-resolved spectrum of 2 wt% V_2O_5/TiO_2 at 250 °C during 30-s pulses of Ar in a gas feed of 2 vol% H_2O and 5 vol% O_2 balanced in Ar.

Spectral changes were already evident in the time-resolved spectra but were further amplified after PSD. All the three characteristic peaks of TiO_2 were strongly perturbed by the periodic NO pulses and thus appeared in the in-phase spectrum shown in Figure 2.4b. All other phase-resolved spectra showed the same features but with decreasing intensity. On the other hand, the Raman signal of VO_x was barely discernable even in the phase-resolved spectra. Hence, it appears that TiO_2 underwent the most prominent spectral changes during the concentration modulation.

The main role of the support material is to provide a high-surface-area environment that can disperse the active phase. In some instances, however, supports may have a non-innocent role in the catalytic process. In the case of NH_3 -SCR, TiO_2 provides vacant Ti^{4+} sites, where NH_3 can adsorb through a Lewis acid-base interaction. Hence, TiO_2 serves as a reservoir of adsorbed NH_3 molecules which can be delivered to the active sites to react if

NO is present. In our experiment, NH_3 was always present in the gas feed ensuring that the VO_x sites can be supplied with NH_3 molecules directly from the gas phase. However, the fact that TiO_2 peaks are present in the phase-resolved spectra suggests that the delivery of substrate molecules from TiO_2 to VO_x is still at work. Mechanistically, this is intuitively correct since bound NH_3 molecules are closer in proximity and easier to access than those that originate from the gas phase. In fact, some studies postulate that NH_3 adsorption occurs initially at TiO_2 before VO_x sites [101]. This molecular behavior is consistent with the results of our ME experiments.

Most of the VO_x species were coordinated with NH_3 and water present in the feed. This is the reason for the position of the $\nu(\text{V}=\text{O})$ mode in the time-resolved spectra at 1018 cm^{-1} instead of 1031 cm^{-1} [102]. The faint signal of VO_x in the phase-resolved spectra results from the constant presence of NH_3 molecules in the gas phase. The reaction between NO and adsorbed NH_3 should result ultimately in the production of coordinatively unsaturated VO_x sites. However, this process is so fast that the signal of “free” VO_x is not observed in the phase-resolved spectra under the time scale employed in the experiment. On the other hand, the transfer of NH_3 from neighboring TiO_2 to the active sites is probably slower, which explains why the characteristic peaks of TiO_2 are present in the phase-resolved spectra.

To confirm that the observed effect is in fact due to the SCR reaction, a control experiment was performed in the absence of SCR activity (Figure 2.4c,d). This was achieved by pulsing Ar in a gas feed containing 2 vol% H_2O and 5 vol% O_2 balanced in Ar. Although the time-resolved spectra showed all of the expected signals of VO_x and TiO_2 , the phase-resolved spectra did not present any signal. This means that neither VO_x nor TiO_2 was perturbed by the inert gas pulsing.

2.3.3. ME-DR-Vis Spectroscopy of Cu-SSZ-13

The active Cu site in the catalyst changes reversibly between two oxidation states (i.e., +2 and +1) during the course of the SCR reaction [54]. Cu(II) exhibits a *d-d* transition band in the region of 500-1100 nm and when it is supported on a zeolite, it has an additional band

at 220-380 nm due to ligand-to-metal charge transfer (LMCT) [41]. In contrast, Cu(I) does not possess a *d-d* transition band because of its fully filled 3d shell. Hence, the reversible Cu(II)↔Cu(I) redox changes in Cu-SSZ-13 can be monitored by following the appearance/disappearance of the characteristic bands of Cu(II).

The time-resolved and phase-resolved DR-Vis spectra as a result of repeated NO pulsing are presented in Figure 2.5a,b. The time-resolved spectra show very shallow bands in the region of 350-800 nm, but no obvious changes were observed. The difference spectra between Cu-SSZ-13 under NH₃ and NH₃/NO gas feeds could potentially reveal the characteristic Cu(II) bands, but the signal-to-noise-ratio is low (Figure S-2.7). Hence, the application of PSD is justified to accentuate the spectral changes. The in-phase spectrum in Figure 2.4b is very similar to the difference spectrum and exhibits a broad band above 500 nm that may be associated with the *d-d* transition band of Cu(II). The band extending below 430 nm originates from LMCT (in particular, O²⁻→Cu²⁺) and is not complete in the UV region because the acquisition was stopped at 350 nm to meet the required time resolution. These two bands vary in-phase (i.e., they increase and decrease simultaneously) because they both originate from the same chemical entity. All other phase-resolved spectra show only intensity variations of these two features.

Without SCR activity (i.e., in the absence of NO), most of the Cu species would be in the +2 oxidation state. The presence of both NH₃ and NO is needed to drive the reduction of Cu(II) to Cu(I), which is coordinated to both reactants and from which the nitrosamide intermediate forms. Although NH₃ alone can reduce Cu(II) in some Cu-based catalysts [103], temperatures higher than 250 °C are required. It is therefore the NO pulsing that induces the redox process in the experiment presented in Figure 2.5.

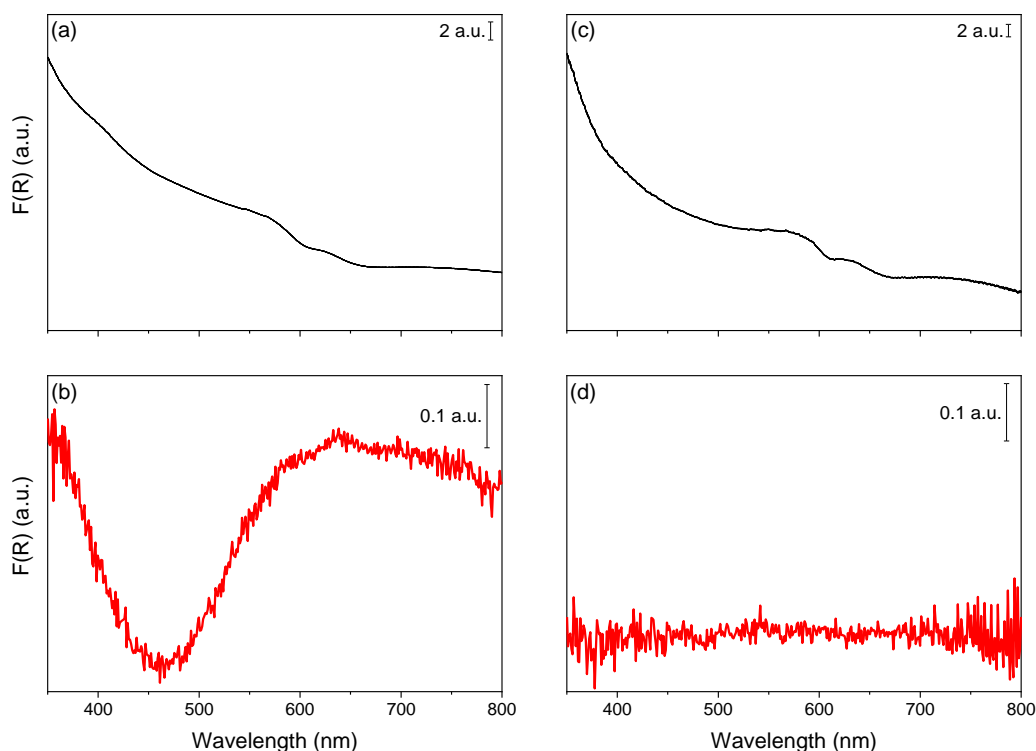


Figure 2.5. (a) Time-resolved DR-Vis spectra and (b) the corresponding in-phase spectrum of 1.6 wt% Cu-SSZ-13 at 250 °C during 120-s pulses of 1000 ppm NO in a gas feed of 1000 ppm NH₃, 2 vol% H₂O and 5 vol% O₂ balanced in Ar. (c) Time-resolved DR-Vis spectra and (d) a selected phase-resolved spectrum of 1.6 wt% Cu-SSZ-13 at 250 °C during 120-s pulses of Ar in a gas feed of 2 vol% H₂O and 5 vol% O₂ balanced in Ar.

Also in this case, a control experiment was performed in the absence of SCR activity by repeated Ar pulses (Figure 2.5c,d). No signal was observed in the phase-resolved spectrum, which confirms that the bands observed in Figure 2.5b clearly originate from the redox process of the Cu sites during SCR activity.

2.3.4. ME-DRIFT Spectroscopy of Fe-ZSM-5

Figure 2.6a,b shows the time-resolved and phase-resolved DRIFT spectra as a result of NO pulses in NH₃ while Figure 2.6c,d shows the equivalent set of spectra as a result of Ar pulses in NH₃. The time-resolved spectra of both experiments are practically identical – they are both dominated by the signal contribution from adsorbed water and NH₃. This is equally evident in the stretching region in 3500-2500 cm⁻¹ and the bending region in 1750-1250 cm⁻¹ as well. As a result, it is hard to rationalize the presence of other adsorbates and

intermediates on the catalyst surface. NO, for instance, is also expected to adsorb on the catalyst under these experimental conditions [104]. Some studies also hinted at the formation of NO-derived species such as nitrates, especially at lower temperatures [105]. However, the weak signal of adsorbed NO and its potential derivatives compared to water and NH₃ precludes their unequivocal identification in the time-resolved spectra.

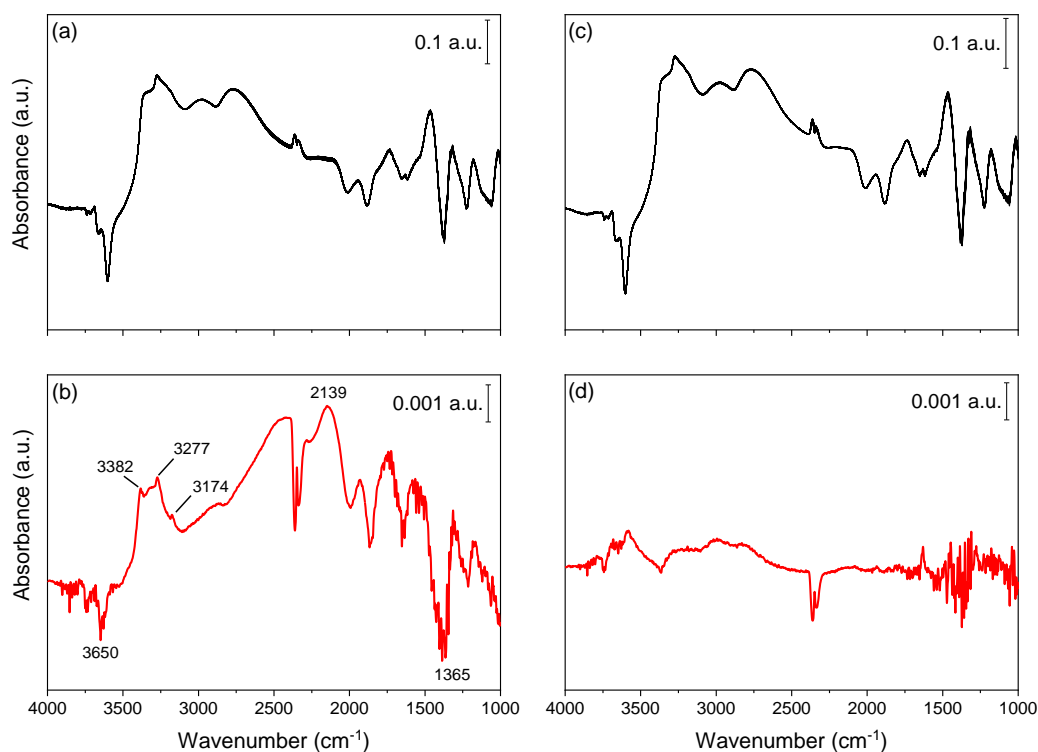


Figure 2.6. (a) Time-resolved DRIFT spectra and (b) the corresponding in-phase spectrum of 2.6 wt% Fe-ZSM-5 at 250 °C during 60-s pulses of NO in a gas feed of 1000 ppm NH₃, 2 vol% H₂O and 5 vol% O₂ balanced in Ar. (c) Time-resolved DRIFT spectra and (d) a selected phase-resolved spectrum of 1 wt% Fe-ZSM-5 at 250 °C during 60-s pulses of Ar in a gas feed of 1000 ppm NH₃, 2 vol% H₂O and 5 vol% O₂ balanced in Ar. The peaks at 2360 and 2330 cm⁻¹ originate from fluctuations in CO₂ concentration in the environment of the sample compartment and not from any adsorbed species.

On the contrary, the phase-resolved spectra uncovered substantial differences between the two experiments. When NO was pulsed, several signals were perturbed and appeared in the phase-resolved spectra. For example, hydroxyl groups (–OH; 3650 cm⁻¹), residual sulfate (–SO₄; 1365 cm⁻¹) from the ion-exchange procedure, adsorbed NH₃ (3382, 3277, and 3174 cm⁻¹) and nitrosyl species (NO⁺; 2139 cm⁻¹) were perturbed. The –OH and –SO₄ groups varied out-of-phase (i.e., exhibited opposite signal variation) with NH₃ and NO⁺ because

they are being titrated upon adsorption. When only Ar was pulsed (Figure 2.6c,d), the apparent signals in the selected phase-resolved spectrum are negligible compared with the experiment under SCR conditions. Furthermore, the presence of the phase-resolved signal of NH_3 in Figure 2.6b suggests that they are being consumed during the NO pulsing, proving the occurrence of the SCR reaction.

The peaks at 3382 and 3277 cm^{-1} correspond to NH_3 adsorbed on Brønsted–Lowry sites while the one at 3174 cm^{-1} originates from NH_3 bound to Lewis acid sites. The former are present in the zeolite framework due to the charge imbalance of Al–O–Si bonds while the latter can be attributed predominantly to the coordinatively unsaturated Fe sites. In the time-resolved spectra, it is hard to differentiate between the two adsorption sites because adsorbed water also provides a broad overlapping signal in this region of the spectrum. However, the three characteristic N–H bending peaks were revealed after PSD treatment. Hence, it appears from the phase-resolved spectra that both the active Fe sites and the support (Brønsted–Lowry sites) coordinate with NH_3 molecules. Steady-state catalytic tests have revealed that the metal-free ZSM-5 support did not exhibit any appreciable SCR activity at 250 °C (and even up to 450 °C). This means that it is the Fe active site that is solely responsible for the SCR activity, which rationalizes the perturbation of Lewis-bound NH_3 due to NO pulses. However, NH_3 bound to Brønsted–Lowry sites were also perturbed by NO, indicating that during the pulse duration, they might be transferred to Fe sites to react as well.

2.4. Conclusions

We have presented a reactor cell with a low void volume that can be used for ME spectroscopic studies such as (1) Raman spectroscopy of $\text{V}_2\text{O}_5/\text{TiO}_2$; (2) DR-Vis spectroscopy of Cu-SSZ-13; and (3) DRIFT spectroscopy of Fe-ZSM-5. Due to the low void volume of the cell, the gases were exchanged very efficiently in every pulse sequence, which induced large spectroscopic response after PSD treatment. The results presented here are obviously not sufficient to draw full mechanistic conclusions; rather, they are case studies targeted to prove the suitability of the cell for transient response and ME

experimentation. The demonstrated versatility of the cell with regard to various spectroscopic techniques paves the way for implementing time-resolved structural studies that are truly complementary with one another.

Chapter 3 – Modulated Excitation Raman Spectroscopy of V₂O₅/TiO₂: Mechanistic Insights into the Selective Catalytic Reduction of NO by NH₃

3.1. Introduction

Whereas adsorbates are best probed by IR spectroscopy, changes within the metal oxide structure are preferentially monitored using Raman spectroscopy. Due to their highly polarizable bonds with predominantly covalent character, transition metal oxides such as V₂O₅ and TiO₂ give rise to intense Raman-active vibrational modes [21].

Steady-state Raman experiments have undoubtedly revealed important structural information and redox features of the V₂O₅/TiO₂ system that cannot be obtained by other operando techniques [99, 102, 106]. However, isolation of the structure of responsive species within the large contribution of stationary species still remains a challenge. In addition, TiO₂ is acknowledged to play a role in NH₃ adsorption during SCR, but it has received only cursory attention in mechanistic studies because the changes to its signals are subtle [101].

The aforementioned issues call for a new strategy for Raman studies because the conventional approach based on steady-state experimentation cannot advance our understanding of the reaction mechanism any further. In an effort to extend the current capabilities of Raman spectroscopy, we performed experiments under transient conditions by applying the modulated excitation (ME) technique. Hence, signals from unresponsive or static species are effectively eliminated, and signals from the active sites and perturbed species are enhanced.

In this chapter, we demonstrate the increased level of mechanistic details that can be derived from this approach compared to steady-state experiments in the Raman spectroscopy of V_2O_5/TiO_2 .

3.2. Materials and methods

3.2.1. Materials synthesis

V_2O_5/TiO_2 (2 wt%) was prepared by wet impregnation. A sufficient amount of ammonium metavanadate (Fluka, >99.0%) was dissolved in water at 60 °C, and was mixed for 1 h with TiO_2 (DT-51-D, Cristal) that was pre-calcined at 550°C. After removal of water under reduced pressure, the sample was calcined at 600 °C for 5 h in a muffle furnace. The catalyst powder was then sieved to 150-200 μm .

The catalyst loading was kept at 2 wt% because it provides an active and stable catalyst and is close to the formulation of real-life industrial catalysts.

3.2.2. Catalyst characterization

X-ray diffraction (XRD) patterns were collected using a D8 ADVANCE diffractometer (Bruker) with Cu $K\alpha 1$ radiation ($\lambda = 1.5406 \text{ \AA}$). Data were recorded from 20° to 85° 2 θ using a step size of 0.02°·s⁻¹ acquisition time. The phases were identified with the X'Pert HighScore Plus software.

The Brunauer–Emmett–Teller (BET) surface area was measured by N_2 adsorption at -196 °C on a Autosorb I instrument (Quantachrome). Prior to the measurement, the samples were degassed at 350 °C for 4 h.

The VO_x surface coverage (S_{VOx}) of the catalyst sample was calculated according to Equation 3.1.

$$S_{VOx} = \frac{2 \times \%V \times N_A}{M_u \times SA \times 10^{20}} \quad (\text{Equation 3.1})$$

where $\%V$ is the V_2O_5 content of the sample, N_A is Avogadro's constant, M_u is the molar mass of V_2O_5 , and SA is the BET surface area (72 m²·g⁻¹ in this case).

3.2.3. Activity evaluation and kinetic studies

The catalytic activity was assessed in the spectroscopic cell containing approximately 30 mg of the sample under 500 ppm NH₃, 500 ppm NO, 2 vol% H₂O, and 5 vol% O₂ balanced in Ar (100 mL·min⁻¹) between 100 and 350 °C.

The concentration of the gas at the outlet was monitored using an OmniStar GSD 320 mass spectrometer (Pfeiffer). The *NO conversion* was calculated according to Equation 3.2.

$$NO\ conversion = \frac{NO_{in} - NO_{out}}{NO_{in}} \times 100\% \quad (\text{Equation 3.2})$$

where NO_{in} is the concentration of NO in the gas feed and NO_{out} is the concentration of NO in the outlet.

The rate constant (k) was calculated according to Equation 3.3.

$$k = V \times \frac{X_{NO}}{1 - X_{NO}} \quad (\text{Equation 3.3})$$

where V is the total gas flow rate (1.67 mL·s⁻¹ in this study) and X_{NO} is the fractional NO conversion

3.2.4. Raman spectroscopy

Raman spectra were recorded at 100 mW laser power and 0.5 s exposure time using a RamanRXN-1 analyzer (Kaiser) equipped with a fiber optics probe and a 785-nm laser. The Raman probe was mounted above the custom-built spectroscopic cell containing approximately 30 mg of the catalyst sample and heated at 250 °C. The cell was equipped with a 2-mm thick sapphire window (Crystran). Prior to every experiment, the sample was dehydrated at 350 °C for 1 h. All time-resolved Raman spectra were subjected to 1st order baseline correction. During the entire experiment, no laser damage was induced on the sample (Figure S-3.1).

For the purpose of the ME experiments, the SCR reaction was switched on and off by pulsing 500 ppm NH_3 every 30 s in a gas feed ($100 \text{ mL} \cdot \text{min}^{-1}$) containing 500 ppm NO, 2 vol% H_2O , and 5 vol% O_2 balanced in Ar.

3.2.5. Infrared spectroscopy

Infrared spectra were recorded using a Vertex 70 spectrometer (Bruker) with a Praying MantisTM diffuse reflection accessory (Harrick). The spectroscopic cell used in the Raman experiments was also used in the IR experiments, but the window was replaced with CaF_2 (Crystan). The spectra were collected from 4000 to 800 cm^{-1} at a resolution of 4 cm^{-1} by accumulating 50 (background) and 10 interferograms (sample) at a scanner velocity of 80 kHz.

3.2.6. Phase-sensitive detection

The time-resolved Raman spectra were converted into phase-resolved spectra using Equation 1.4 [79]. A MATLAB script was used to process the spectra. For each experiment, a minimum of 40 periods was used to generate the phase-resolved spectra.

3.3. Results and discussion

The time-resolved Raman spectra of the 2 wt% $\text{V}_2\text{O}_5/\text{TiO}_2$ catalyst (Figure 3.1a) are dominated by the contribution from the anatase phase of TiO_2 [97]. The intense peaks at 395 and 636 cm^{-1} correspond to the B_{1g} and E_g modes, respectively, and the peak at 516 cm^{-1} is a convolution of the two Raman-active modes B_{1g} and A_{2g} [98]. The weak band at around 800 cm^{-1} is the second overtone of the B_{1g} mode. The most prominent feature of the VO_x species is the weak peak in the region of $1010\text{--}1040 \text{ cm}^{-1}$ that is readily assigned to the $\nu(\text{V}=\text{O})$ stretch mode [99, 102, 106].

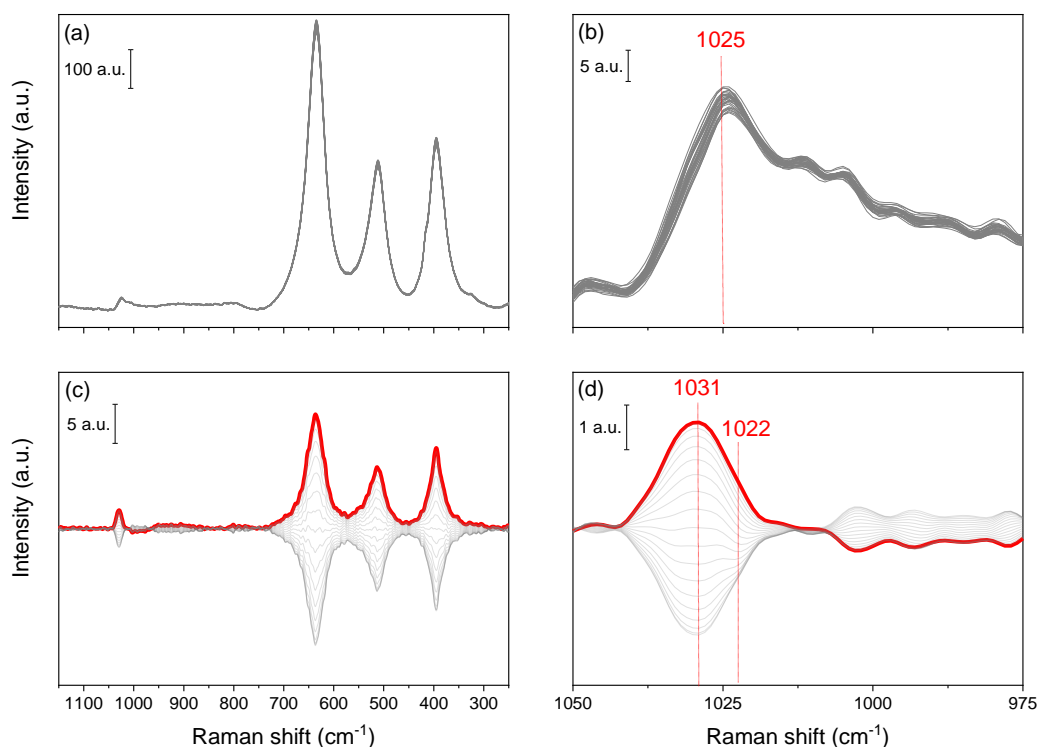


Figure 3.1. (a and b) Time-resolved Raman spectra and (c and d) the corresponding phase-resolved spectra of 2 wt% $\text{V}_2\text{O}_5/\text{TiO}_2$ at 250 °C during 30-s pulses of 500 ppm NH_3 in a gas feed of 500 ppm NO , 2 vol% H_2O , and 5 vol% O_2 balanced in Ar .

The submonolayer coverage of $2 \text{ VO}_x \cdot \text{nm}^{-2}$ was confirmed by the absence of the bulk V_2O_5 peak at 995 cm^{-1} and by the X-ray diffraction data (Figure S-3.2). Therefore, all the vanadyl species occurred exclusively as amorphous VO_x on the surface of TiO_2 .

For the purpose of the ME experiments, the SCR reaction was repeatedly switched on and off by pulsing NH_3 in a gas feed containing NO (Figure 3.2). The experiment was performed at 250 °C where the NO conversion was 26% (Figure S-3.3). Under these conditions, the surface of the catalyst was populated by adsorbed water and NH_3 (Figure S-3.4).

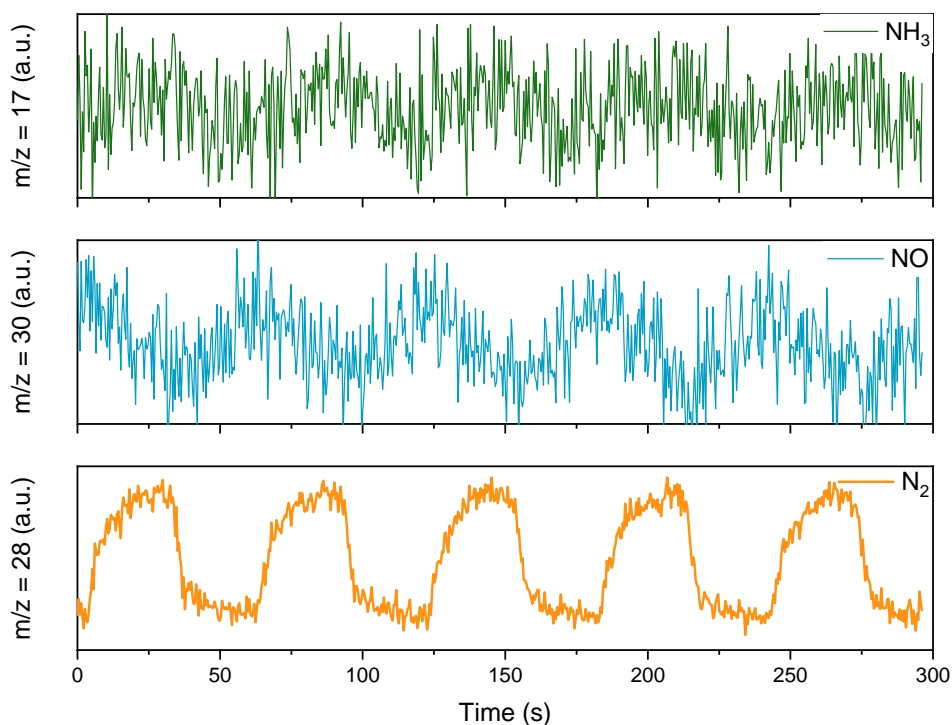


Figure 3.2. Concentration profiles of NH_3 ($m/z = 17$), NO ($m/z = 30$), and N_2 ($m/z = 28$) obtained from mass spectrometry during 30-s pulses of 500 ppm NH_3 in a gas feed containing 500 ppm NO .

No spectral changes are immediately noticeable in the time-resolved Raman spectra (Figure 3.1a), but it is clear after phase-sensitive detection (PSD) that the signals of both VO_x and TiO_2 responded to the changes in the gas phase composition (Figure 3.1c). Control ME experiments in the absence of SCR activity performed by (1) replacing the SCR reactants with Ar pulses on $\text{V}_2\text{O}_5/\text{TiO}_2$ at 250 °C, (2) applying NH_3 pulses in NO on $\text{V}_2\text{O}_5/\text{TiO}_2$ at room temperature, and (3) applying NH_3 pulses in NO on TiO_2 at 250 °C provided negligible phase-resolved signal (Figure S-3.5). Hence, the first information from the ME Raman data shown in Figure 3.1 is that both the VO_x active phase and the TiO_2 support are involved in the SCR process to some extent.

It is apparent in Figure 3.1b that the $\nu(\text{V}=\text{O})$ mode is very broad in the time-resolved spectra, but it is present as a narrower and well-defined peak in the phase-resolved spectra (Figure 3.1d). This suggests that while some of the VO_x species were perturbed by the NH_3 pulses and thus provided the phase-resolved signal, most of the VO_x population remained

largely unresponsive. Therefore, only a defined portion of VO_x species participate in the SCR reaction.

To interpret Figure 3.1 further, we determined the influence of each individual gas component on the Raman spectra. Changes in the shape, intensity, and energy of Raman bands reflect structural transformations within the catalyst. A simplified model such as the ball-and-spring model can help to rationalize these phenomena as they relate to molecular vibrations [107, 108]. In the context of the present experiment, a change in force constant (κ) occurs when the bond order increases/decreases while a change in reduced mass (μ) takes place when substrate molecules adsorb/desorb. Figure 3.3 displays the evolution of the $\nu(\text{V}=\text{O})$ mode upon exposure of $\text{V}_2\text{O}_5/\text{TiO}_2$ to SCR-relevant gases.

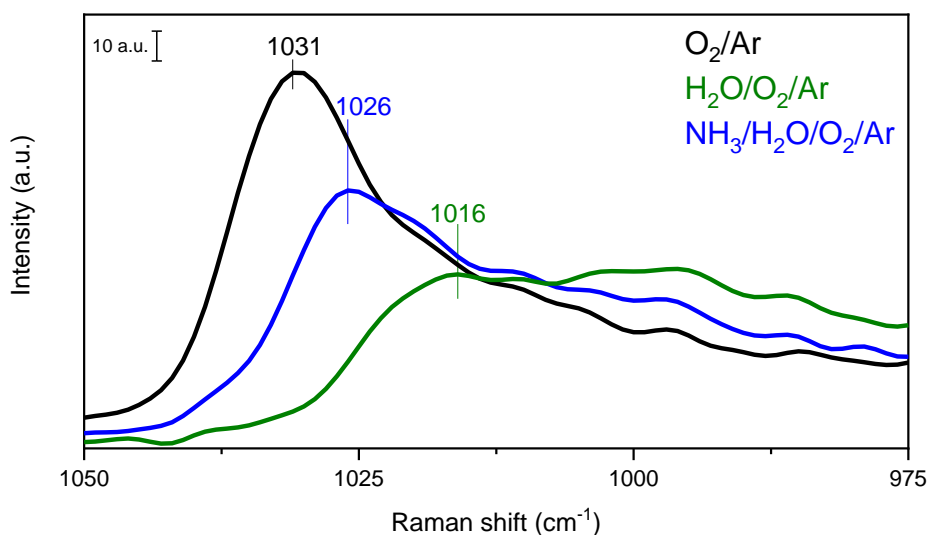


Figure 3.3. Raman spectra of 2 wt% $\text{V}_2\text{O}_5/\text{TiO}_2$ at 250 °C showing the changes of the $\text{V}=\text{O}$ peak under different gas environments: 5 vol% O_2 balanced in Ar (black); 2 vol% H_2O and 5 vol% O_2 balanced in Ar (blue); 500 ppm NH_3 , 2 vol% H_2O , and 5 vol% O_2 balanced in Ar (green).

Under O_2 , the peak appeared relatively narrow and centered at 1031 cm^{-1} . The species responsible for this signal correspond to vanadyl Lewis acid sites. Upon water introduction, the peak broadened considerably and redshifted to 1026 cm^{-1} . Water can act as a Lewis base and adsorb on the VO_x sites or form a network of hydrogen bonds with the oxidic structure of the catalyst surface [99, 102]. In both cases, μ increases which translates into a redshift. It is also able to hydroxylate some of the $\text{V}=\text{O}$ bonds, transforming them from

Lewis to Brønsted-Lowry acid sites. NH_3 , a much stronger base, produced an even more pronounced effect. The initial $\text{V}=\text{O}$ peak was barely discernable and shifted even further to 1016 cm^{-1} . NH_3 may interact with the catalyst in at least two ways. Firstly, it can adsorb on vacant Brønsted-Lowry and Lewis sites of VO_x , and on the Lewis Ti^{4+} sites of the support (Figure 3.4a) [38, 109]. These molecular events change μ due to the additional mass of strongly bound NH_3 . Secondly, NH_3 can reduce the vanadyl center and change the bonding of V with the O atoms, thus affecting κ .

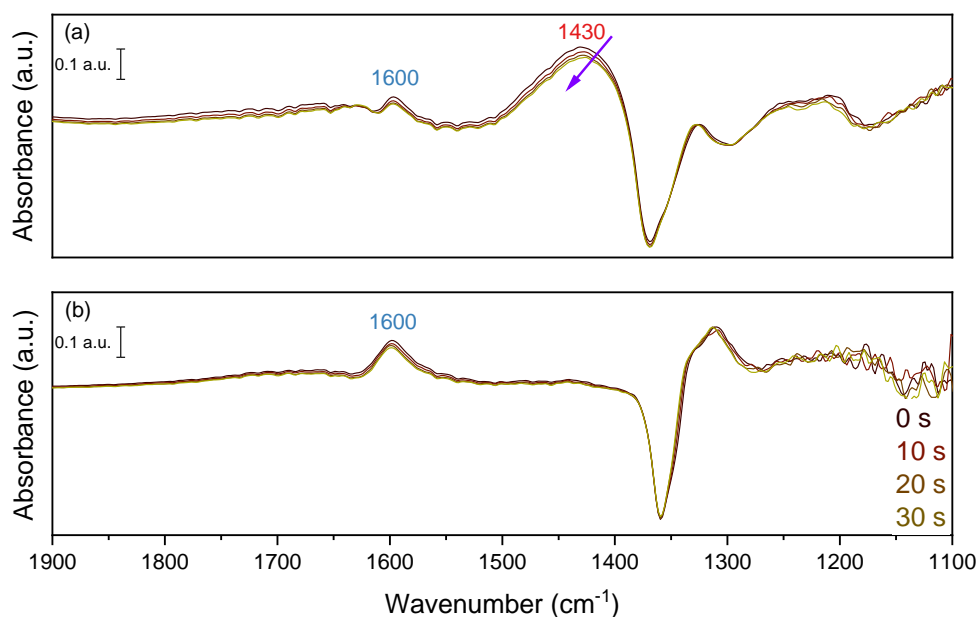


Figure 3.4. IR spectra of (a) 2 wt% $\text{V}_2\text{O}_5/\text{TiO}_2$ and (b) TiO_2 at 250 °C in a gas feed of 2 vol% H_2O , 5 vol% O_2 balanced in Ar after NH_3 cut-off. Adsorbed NH_3 on Brønsted-Lowry sites (1430 cm^{-1}) present in 2 wt% $\text{V}_2\text{O}_5/\text{TiO}_2$ were more susceptible to desorption than those adsorbed on Lewis sites (1600 cm^{-1}). Spectra are shown up to 30 s because this corresponds to the length of the NH_3 pulse in the ME experiments. In practice, adsorbed NH_3 on Lewis V^{5+} and Ti^{4+} sites appear as a single peak.

The peak shifts indicate that NH_3 interacts more strongly with VO_x than water, which is in agreement with previous reports [109, 110] and the corresponding IR spectra under these conditions (Figure S-3.6).

TiO_2 responded to the changes in the gas environment as well (Figure S-3.7). The intensity of the characteristic TiO_2 peaks decreased slightly upon exposure to water and NH_3 , but they retained their energy positions. This suggests that there is a marked difference between

the scattering power of “free” TiO_2 and adsorbate-bound TiO_2 . This behavior may also originate from, among other things, the changes in the catalyst color during the redox cycling. The subtle response of TiO_2 is a direct consequence of its role as the catalyst support. While VO_x is well-dispersed and occurs exclusively on the surface, TiO_2 also exhibits bulk domains. In contrast to the surface species that can accommodate adsorbates, the great majority of Ti-O bonds providing the Raman signal is in the bulk and cannot interact with the molecules in the gas phase. Hence, the overall change of the Raman intensity is not large because only a small fraction of TiO_2 (i.e., the surface atoms) is probed by the changes in the gas feed.

We now expand our discussion of the ME Raman data in light of the steady-state experiments. Figure 3.1b,d shows that the $\nu(\text{V}=\text{O})$ mode does not coincide in the time-resolved and phase-resolved domains. In the former, it is centered at $1016\text{--}1026\text{ cm}^{-1}$ which is expected due to the presence of water and NH_3 (Figure 3.3). In the phase-resolved spectra, however, the maximum occurs at 1031 cm^{-1} , which is reminiscent of the VO_x species observed in the absence of adsorbates. Therefore, the responsive VO_x species are most likely coordinatively unsaturated. From a mechanistic perspective, this is intuitive since the active site cannot be coordinated to another molecule in order to accommodate the reactant with which it will perform the catalysis. While the majority of the VO_x population is engaged with adsorbed/coordinated molecules of water and NH_3 as indicated by the time-resolved data (Figure 3.1b), the portion of VO_x that becomes coordinatively unsaturated during the pulse sequence, is able to perform the redox cycle of the SCR reaction. The practical relevance of this molecular level information is demonstrated by the finding that the presence of hydroxylation-resistant species positively correlated with the increased NO reduction rates of activated catalysts [24].

A weak peak was also observed at 1022 cm^{-1} in the phase-resolved spectra that appears to vary asynchronously with the main $\nu(\text{V}=\text{O})$ mode (Figure 3.1d). Our steady-state experiments shown in Figure 3.3 suggests that this peak is not associated with a coordinatively unsaturated species because it is significantly redshifted from the dehydrated VO_x peak at 1031 cm^{-1} ; rather, this VO_x species appears to be bound to a ligand,

particularly NH_3 that induces the VO_x peak maximum to shift. In light of these observations, we tentatively assign this peak to the VO_x species that were previously bound to NH_3 . As soon as the products are desorbed from the catalyst surface, the coordinatively unsaturated VO_x species are formed again. The transition from the NH_3 -coordinated (1022 cm^{-1}) to the coordinatively unsaturated state (1031 cm^{-1}) as soon as the reaction occurs can explain the phase lag between the two peaks.

To isolate the effect of reaction from adsorption/desorption, we performed NH_3 pulsing experiments in the absence of NO (Figure 3.5). As in the previous case, changes around the $\nu(\text{V}=\text{O})$ mode during NH_3 pulses without NO became very noticeable only in the phase-resolved spectra. In contrast to the behavior under SCR conditions, the response of TiO_2 to NH_3 adsorption-desorption was very limited. Instead, it was the signal of VO_x that exhibited the greatest intensity variation.

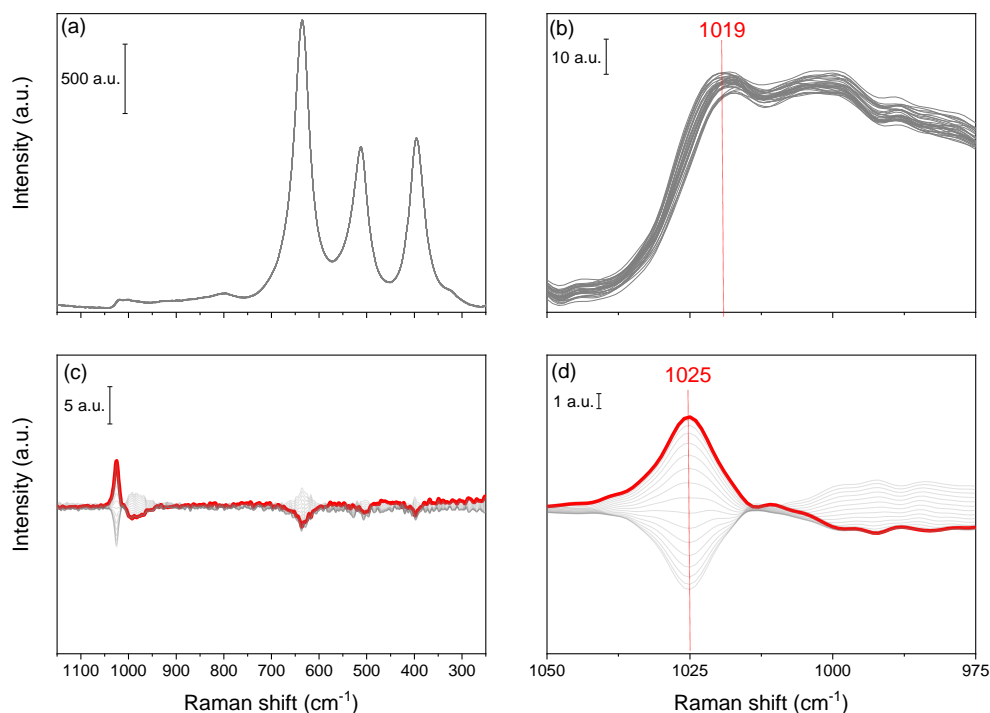


Figure 3.5. (a and b) Time-resolved Raman spectra and (c and d) the corresponding phase-resolved spectra of 2 wt% $\text{V}_2\text{O}_5/\text{TiO}_2$ at $250\text{ }^\circ\text{C}$ during 30-s pulses of 500 ppm NH_3 in a gas feed of 2 vol% H_2O and 5 vol% O_2 balanced in Ar.

Molecular NH_3 can adsorb on either the V^{5+} sites of VO_x or the Ti^{4+} sites of TiO_2 . Previous studies have demonstrated that NH_3 is more strongly (and will be preferentially) adsorbed on the Ti^{4+} sites especially at low V loading [102]. The ME results are consistent with this behavior since the signal from TiO_2 is practically absent in the phase-resolved spectra. During the first few pulses of NH_3 , all of the TiO_2 sites on the surface might have already been saturated with NH_3 molecules which are so strongly bound that they do not desorb significantly even in the presence of water at 250 °C. This stable interaction renders TiO_2 only weakly responsive to the perturbations in the gas environment, as supported by the IR spectra (Figure 3.4b). In contrast, the interaction of NH_3 with VO_x sites is much weaker. At 250 °C, some adsorbed NH_3 species – particularly those at Brønsted-Lowry sites – may desorb due to poor thermal stability (Figure 3.4a) [111]. When NH_3 is present in the feed, it can adsorb on the VO_x sites; once the NH_3 supply is interrupted, NH_3 can desorb from those sites where the adsorption is rather weak. The liberated sites can then be occupied by new NH_3 molecules when the supply is turned on again. This dynamic behavior explains the significant presence of the $\text{V}=\text{O}$ peak in the phase-resolved spectra.

Under steady-state conditions, the presence of NH_3 caused the $\text{V}=\text{O}$ peak to shift from 1031 to 1016 cm^{-1} (Figure 3.3). In the NH_3 adsorption ME experiment, the maximum of the $\text{V}=\text{O}$ signal in the phase-resolved spectra was centered at 1025 cm^{-1} (Figure 3.5d), which corresponds to the observed redshift when water is present in the steady state spectra. Hence, it seems that the responsive VO_x species during NH_3 adsorption/desorption are coordinatively saturated and bound to ligands. This process is different from the one discussed in Figure 3.1.

The same ME experiment was repeated by pulsing NO , the other key reactant in standard SCR (Figure S-3.8). The phase-resolved spectra did not deliver any discernable signal, indicating that neither VO_x nor TiO_2 was perturbed significantly by the NO pulses. This result is consistent with the generally accepted view that NO is not strongly adsorbed on the $\text{V}_2\text{O}_5/\text{TiO}_2$ surface [110]. Unlike NH_3 , NO is not basic and cannot interact with the acidic sites of the catalyst.

It is remarkable to note that TiO_2 peaks are present in the PSD data when NH_3 was pulsed in a gas feed containing NO (Figure 3.1) whereas they are almost nonexistent if NO was absent (Figure 3.5). This confirms that TiO_2 plays a dynamic role in the SCR process; it also discards the possibility that the phase-resolved signals observed in Figure 3.1 and Figure 3.5 were provoked solely by color changes due to the redox VO_x species, which could also result in intensity changes. Furthermore, when TiO_2 alone was subjected to the same pulsing sequences, no significant spectral changes were observed (Figure S-3.5e). When there was no SCR reaction, most of the adsorbed NH_3 molecules remained bound to TiO_2 even in the presence of water at 250 °C, which was confirmed by equivalent IR experiments (Figure 3.4b). However, when the feed returned to SCR conditions, TiO_2 -bound NH_3 molecules were mobilized to the VO_x active sites to react with NO. Although TiO_2 is not directly involved in the actual SCR reaction at this temperature, this NH_3 storage and release mechanism rationalizes the presence of the characteristic Raman peaks of TiO_2 in the phase-resolved spectra. We therefore provide evidence using ME Raman spectroscopy that TiO_2 acts as a dynamic pool of adsorbed NH_3 .

The role of TiO_2 is further exemplified by the differences in the behavior of the responsive species in the phase-resolved spectra. In Figure 3.1c, both VO_x and TiO_2 vary in-phase because under SCR conditions, the delivery of NH_3 from TiO_2 to VO_x is frequent. In contrast, VO_x and TiO_2 vary out-of-phase in Figure 3.5c because NH_3 adsorption/desorption require no delivery of NH_3 to the active sites.

We then consider the relationship between phase angle and time domain [112]. Figure 3.6 shows the evolution of the normalized signal intensity of TiO_2 and VO_x appearing in Figure 3.1c as a function of phase angle. The phase angle dependence of the characteristic peaks of TiO_2 at 395 and 515 cm^{-1} was identical. This is justified by the fact that while these two peaks originate from different symmetry representations, they both stem from the same molecular species. On the contrary, the peak at 1031 cm^{-1} , which corresponds to VO_x groups, was shifted by approximately 9° with respect to the TiO_2 peaks. The phase delay between VO_x and TiO_2 suggests that the two species followed non-identical behaviors during the NH_3 pulse, and that coordinatively unsaturated VO_x species appeared prior to

the liberation of adsorbed NH_3 from TiO_2 . Given the high level of noise in the time-resolved spectra, such type of kinetic information can be obtained solely from the phase-resolved spectra.

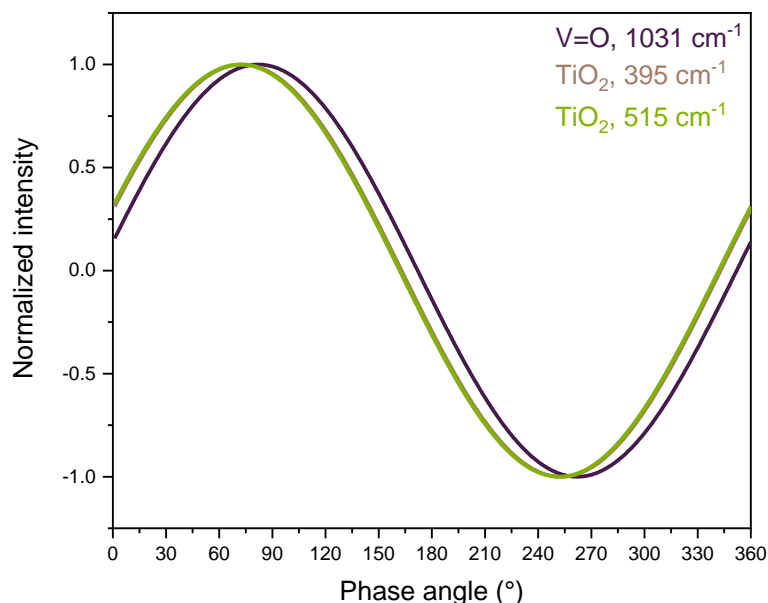


Figure 3.6. Phase angle dependence of the Raman signal intensity of V=O and TiO_2 during SCR on/off experiments.

The maximum intensity variation of the VO_x signal in the phase-resolved spectra correlated with the SCR activity (Figure 3.7). As NO conversion decreased with decreasing temperature, the peak intensities of VO_x and TiO_2 decreased as well. In the phase domain, the signal intensity depends on the fraction of dynamic species perturbed by the repeated gas pulses. The interaction strength between the molecular adsorbates and the metal oxides increases with decreasing temperature, and hampers molecular motion and desorption. Furthermore, fewer NH_3 molecules are activated at the VO_x sites at lower temperature and correspondingly, less NH_3 molecules need to be transferred from TiO_2 . The decrease in the SCR activity reduced the fraction of dynamic species involved, which in turn resulted in less intense signals in the phase-resolved spectra.

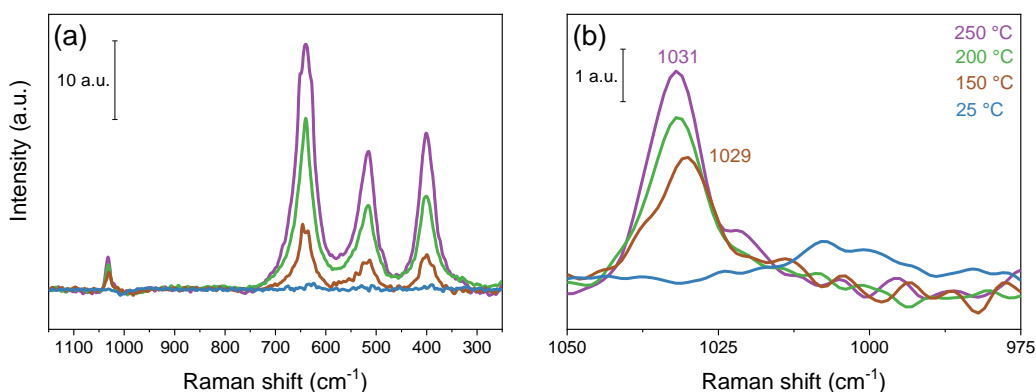


Figure 3.7. Effect of temperature on the (a) in-phase phase-resolved spectra and (b) their VO_x region. Conversion values: 25°C, 0%; 150°C, 4%; 200°C, 10%; 250°C, 26%.

The activity decrease was accompanied by the redshift of the VO_x peak maximum from 1031 to 1029 cm^{-1} , which may be associated to the increase in the population of hydrated VO_x species. As the temperature decreased, water desorption from the catalyst was increasingly less favorable. The relatively narrow shape of the VO_x peak was retained, but the peak area decreased with decreasing temperature. This suggests that even a smaller fraction of the VO_x species were active for SCR at low temperatures, which is supported by the activity measurements (Figure S-3.3). Even at a conversion level of 4%, changes were observed in the phase-resolved spectra. In contrast, the time-resolved spectra at 26% conversion (Figure 3.1a) did not provide any discernable change. This demonstrates the sensitivity enhancement that PSD offers to Raman spectroscopy.

Arrhenius-type relationships confirmed the involvement in SCR of the coordinatively unsaturated species giving rise to the phase-resolved signal at 1031 cm^{-1} . Figure 3.8 shows that the maximum peak intensity of these species in the phase-resolved data correlates with the rate constant (k) under steady-state. An apparent activation energy of approximately 40 $\text{kJ}\cdot\text{mol}^{-1}$ is comparable to those obtained for $\text{V}_2\text{O}_5/\text{TiO}_2$ catalysts [113].

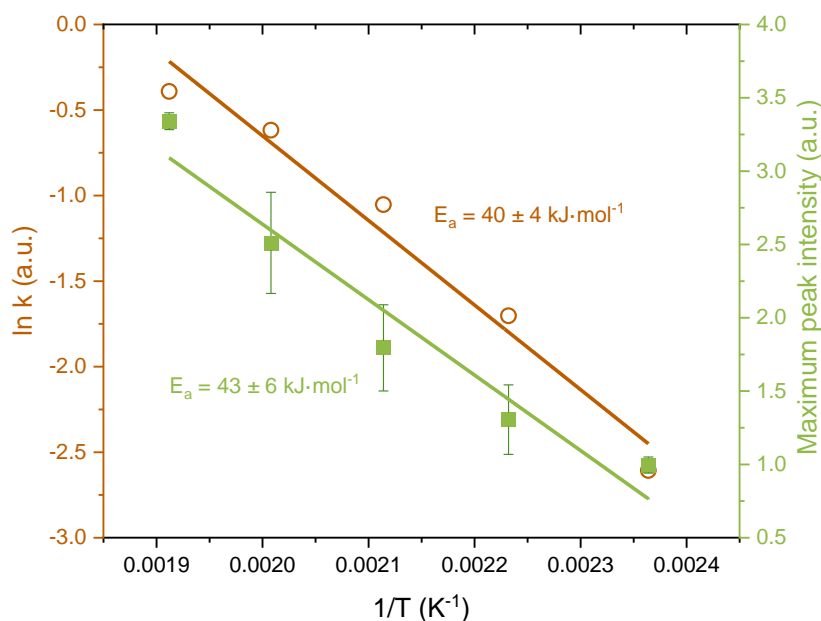


Figure 3.8. Arrhenius plots constructed from kinetic data and VO_x Raman peak intensity.

3.4. Conclusions

In summary, the application of ME and PSD revealed important mechanistic information about SCR that are not apparent in steady-state Raman experiments. We have provided mechanistic evidence using the ME approach that (1) both the VO_x active phase and the TiO₂ support are involved in the SCR process; (2) only a defined portion of the VO_x species are active in the SCR reaction, and they are coordinatively unsaturated; and (3) TiO₂ acts as a reservoir of NH₃ molecules which can be delivered to the VO_x sites to react if NO is present. These novel mechanistic insights could be extracted from the Raman spectra only due to the increased sensitivity offered by ME experimentation and PSD.

Further ME Raman studies on V₂O₅-based catalysts should focus on the effect of promoters and of gas phase components such as NO₂ and SO₂, which co-exist with the standard SCR reactants in the exhaust gas. The presence of NO₂ shifts the catalytic system towards the fast SCR reaction, whose mechanism can also be investigated using our approach.

To achieve the required time resolution, we have used an IR laser source for our experiments. UV laser sources are expected to deliver even more structural information

due to resonance scattering effects [114], but they are currently limited by their long acquisition times. Hence, future improvements in UV Raman spectroscopy will certainly benefit the ME approach.

In this study, we have demonstrated the utility of ME Raman spectroscopy in the specific case of SCR, but the technique can be easily adapted to study the mechanism of other industrially relevant reactions, especially those that are catalyzed by metal oxides. Therefore, ME Raman spectroscopy opens up new possibilities in deciphering structure-reactivity relationships of metal oxide catalyst systems.

Chapter 4 – Interconversion between Lewis and Brønsted-Lowry Acid Sites on Vanadia-Based Materials

4.1. Introduction

Vanadia-based materials rank among the most ubiquitous and versatile systems in heterogeneous catalysis. Originally investigated for various oxidation reactions [115, 116], industrial interest in vanadia catalysts underwent a resurgence in the 1970's when their potential for the ammonia-mediated selective catalytic reduction (NH₃-SCR) was first realized [7]. Both Lewis acid sites (LAS) and Brønsted-Lowry acid sites (BAS) are thought to be involved in the SCR process to varying extents, particularly in the initial step of NH₃ adsorption, and their ratio influences the catalytic activity. Previous studies have already dealt with probing these acid sites using infrared (IR) spectroscopy under reduced pressure – a technique that can reveal the total amount of Lewis and Brønsted-Lowry functionality [22, 111]. Despite being highly quantitative, this approach employs conditions that are far away from real-life situations and may not represent the effective number of acid sites that can function during the actual reaction.

In this study, we probed the LAS and BAS of various V₂O₅/WO₃-TiO₂ catalysts using IR spectroscopy as a function of temperature, water content, and WO₃ loading. Furthermore, we implemented in situ water pulses to follow the kinetics of the transient interconversion between the two sites in more detail.

4.2. Materials and methods

4.2.1. Materials synthesis

V₂O₅/WO₃-TiO₂ catalysts (Table 4.1) were prepared by wet impregnation. A sufficient amount of ammonium metavanadate (Fluka, >99.0%) and ammonium metatungstate hydrate (Sigma-Aldrich, >99.0%) was dissolved in water at 60 °C, and was mixed for 1 h

with TiO₂ (DT-51D, Cristal) that was pre-calcined at 550°C. After removal of water under reduced pressure, the samples were calcined at 600 °C for 5 h in a muffle furnace. The catalyst powders were then sieved to obtain a particle size of 150-200 µm.

Table 4.1. Composition of the V₂O₅/WO₃-TiO₂ catalysts

Designation	V ₂ O ₅ loading (wt%)	WO ₃ loading (wt%)
2V5WT	2	5
2V10WT	2	10
2V20WT	2	20

4.2.2. Activity evaluation

The catalytic activity was measured by loading approximately 40 mg of the sieved catalyst powder in the spectroscopic cell, whose outlet was connected to an OmniStar GSD 320 mass spectrometer (Pfeiffer). The feed comprised 1000 ppm NO, 1000 ppm NH₃, and 5 vol% O₂ balanced in Ar with a total flow of 100 mL·min⁻¹.

4.2.3. X-Ray diffraction

X-ray diffractograms (XRD) were collected using a D8 ADVANCE diffractometer (Bruker) with Cu Kα1 radiation ($\lambda = 1.5406 \text{ \AA}$). Data were recorded from 20° to 85° 2 θ at a step size of 0.02°·s⁻¹. The phases were identified with the X'Pert HighScore Plus software.

4.2.4. Raman spectroscopy

Raman spectra were recorded at 100 mW laser power and 0.5 s exposure time using a RamanRXN-1 analyzer (Kaiser) equipped with a fiber optics probe and a 785-nm laser. All time-resolved Raman spectra were subjected to 1st order baseline correction. The Raman

probe was mounted above the custom-built spectroscopic cell containing the catalyst sample. The cell was equipped with a 2-mm thick sapphire window (Crystran).

4.2.5. Transmission Fourier transform infrared spectroscopy

Transmission infrared spectra were collected using a iS50 spectrometer (Thermo Scientific) equipped with a deuterated triglycine sulfate detector. A custom-built quartz cell and a furnace for high temperature treatment were used to enclose the pelletized samples (approximately 30 mg). The spectra were collected at a resolution of 4 cm^{-1} by accumulating 128 interferograms.

Prior to the experiments, the samples were dried in situ at 400 °C for 1 h under 5 vol% O_2 balanced in Ar. After the activation, 1000 ppm NH_3 and 5 vol% O_2 balanced in Ar were admitted to the cell. Where required, 2 vol% H_2O was added to the feed from the reaction of H_2 and O_2 through a monolithic Pt/ Al_2O_3 catalyst. The total flow for all experiments was fixed at 100 $\text{mL}\cdot\text{min}^{-1}$.

4.2.6. Diffuse reflectance infrared Fourier transform spectroscopy

Diffuse reflectance infrared Fourier transform (DRIFT) spectra were recorded using a Vertex 70 spectrometer (Bruker) with a Praying MantisTM diffuse reflection accessory (Harrick). The spectra were collected at a resolution of 4 cm^{-1} by accumulating 50 (background) and 10 (sample) interferograms using a scanner velocity of 80 kHz. The spectroscopic cell used in the Raman experiments was also used in the IR experiments, but the window was replaced with CaF_2 (Crystan).

Prior to the experiments, the sample was dried in situ at 400 °C for 1 h under 5 vol% O_2 balanced in Ar. After the activation, 1000 ppm NH_3 , 2 vol% H_2O , and 5 vol% O_2 balanced in Ar were admitted to the cell. Modulated excitation (ME) was performed by repeatedly introducing and cutting off 2 vol% H_2O in the gas feed every 60 s. The total flow for all experiments was fixed at 100 $\text{mL}\cdot\text{min}^{-1}$.

4.2.7. Phase-sensitive detection

The time-resolved DRIFT spectra from at least five equilibrated modulation periods were converted into phase-resolved spectra using Equation 1.4 [79].

4.3. Results and discussion

The main material used in the study is 2 wt% V_2O_5 /10 wt% WO_3 /TiO₂ (2V10WT), which represents the typical composition of commercial SCR catalysts [117]. The vanadyl and tungstenyl species are present as amorphous units, as evidenced by the absence of reflections except for those of anatase in the X-ray diffractogram (Figure S-4.1). This is further supported by the Raman spectra, which revealed the presence of neither bulk V_2O_5 nor bulk WO_3 (Figure S-4.2). In contrast, the presence of surface VO_x and WO_x species were confirmed by virtue of the fundamental vibrations of the respective M=O stretches at 1031 and 1013 cm^{-1} [24].

The transmission infrared spectrum of the catalyst after NH_3 adsorption does not differ significantly from those previously published in the literature (Figure S-4.3) [38, 118]. The negative band at 3634 cm^{-1} stems from the $\nu(O-H)$ modes of the surface hydroxyl groups while the peaks at 2051 and 2004 cm^{-1} are overtones of the fundamental $\nu(V=O)$ and $\nu(W=O)$ modes [24], respectively, which were also detected by Raman spectroscopy. The spectrum is also characterized by $\nu(N-H)$ bands at 3365, 3255, and 3163 cm^{-1} as well as $\delta(N-H)$ bands at 1600, 1422, and 1233 cm^{-1} . Of particular importance are the peaks centered at 1422 and 1233 cm^{-1} , which are assigned to NH_3 bound to BAS and to LAS, respectively [109, 119]. To quantify the acid sites, the area encompassed by these curves were integrated.

Figure 4.1 shows the areas of NH_3 bound to BAS and LAS of the catalyst as a function of temperature. Both bands decreased with temperature, but the decline was more pronounced for BAS. Indeed, the BAS area was larger than that of LAS at 150 °C, but this trend was reversed at 400 °C. Assuming that the points lie on a straight line since the correlation coefficients for both approach unity (i.e., $|r| > 0.99$), we can calculate that the slope of BAS

is up to 25% steeper than that of LAS (Figure S-4.4). Hence, this suggests that NH_3 molecules interact less strongly with BAS than LAS because they are more likely to desorb from BAS at higher temperatures. While the superior thermostability of LAS-bound NH_3 was already reported previously [22, 111], such conclusions were derived from IR studies conducted in vacuum – under which conditions, the BAS sites may be transformed into LAS due to the artificial reduction of vanadyl sites, as already pointed out by other studies [109, 120].

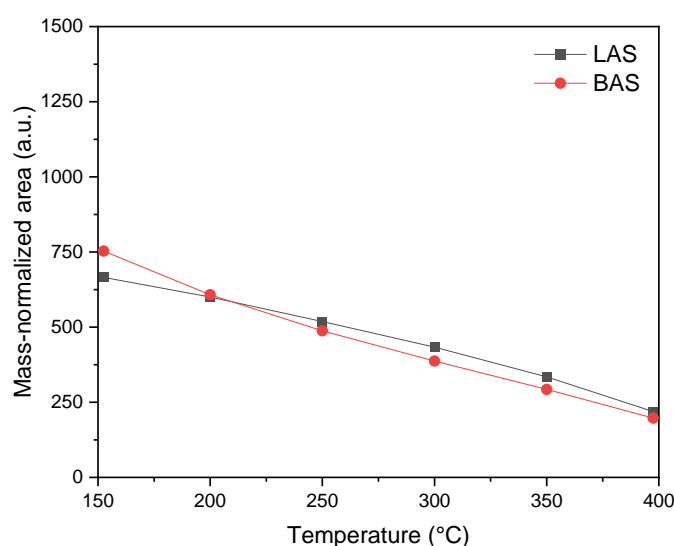


Figure 4.1. Integrated mass-normalized LAS and BAS areas of 2V10WT under 1000 ppm NH_3 and 5 vol% O_2 in Ar from 150 to 400 °C.

Water influences the distribution of the acid sites on the catalyst. In particular, it can undergo dissociative adsorption on the surface to generate hydroxyl groups, which can serve as BAS, often at the expense of pre-existing LAS. Figure 4.2 shows the peak areas corresponding to LAS- and BAS-bound NH_3 in the presence of 2 vol% water. The influence of moisture is evident as the BAS area dominated that of the LAS across the entire temperature range. As an illustration, the ratio of BAS to LAS at 150 °C increased by more than two-fold from 1.1 without water to 2.5 with water. This effect persisted at higher temperatures, but the difference between the areas corresponding to the two acid sites decreased, suggesting that water had a less prominent effect in this regime. Furthermore,

Figure 4.2 shows that BAS are less thermally stable than LAS even in the presence of water since their area decreased much more steeply, which is the same trend observed in the water-free experiment.

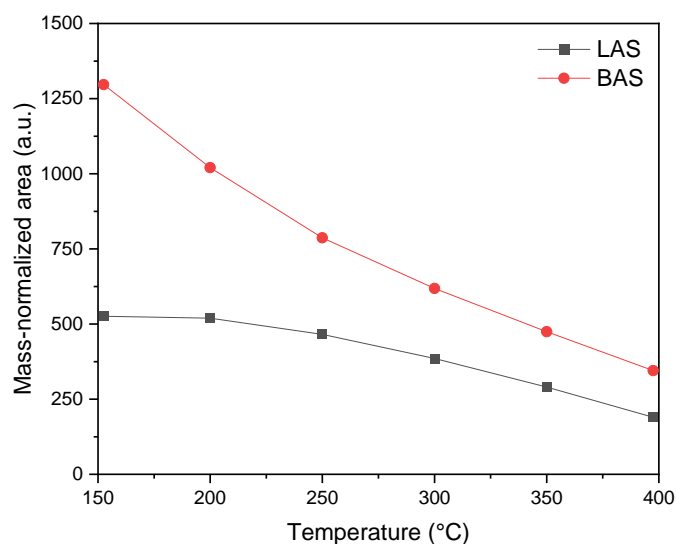


Figure 4.2. Integrated mass-normalized LAS and BAS areas of 2V10WT under 1000 ppm NH_3 and 5 vol% O_2 , and 5 vol% H_2O in Ar from 150 to 400 °C.

WO_3 incorporation provides more BAS that can improve catalytic performance [121]. Indeed, 2V5WT showed 3 to 4.5 times less BAS than 2V10WT (Figure 4.3), translating to about 10 to 17% lower NO conversion (Figure S-4.5). However, adding WO_3 beyond 10 wt% did not increase the BAS as 2V20WT showed approximately the same amount of such sites as 2V10WT (Figure 4.3). Correspondingly, the difference in catalytic activity between 2V10WT and 2V20WT was not significant (Figure S-4.5). Further analysis revealed that 2V20WT already showed formation of microcrystalline WO_3 (Figure S-4.1 and Figure S-4.2), which do not contribute to surface acidity. Hence, the WO_3 loading should be limited to the monolayer coverage (i.e., $4.5 \text{ WO}_x \cdot \text{nm}^{-2}$) [122, 123].

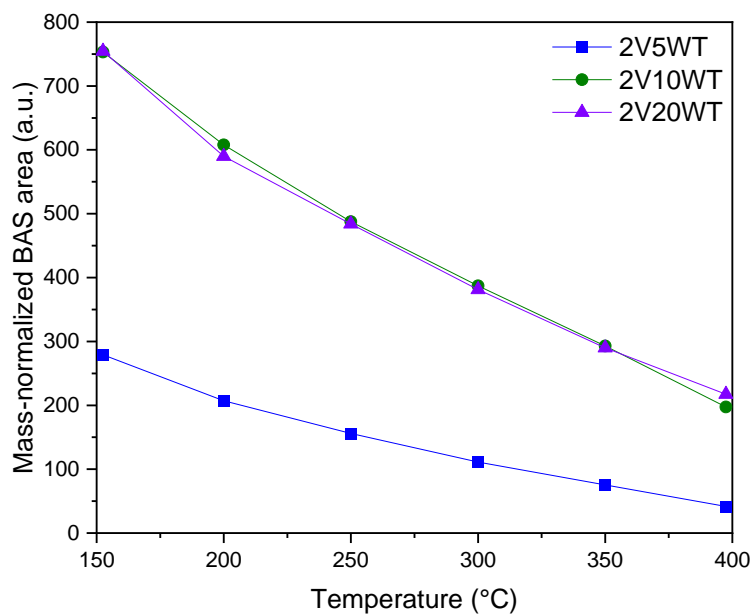


Figure 4.3. Integrated mass-normalized BAS areas of 2V5WT, 2V10WT, and 2V20WT under dry conditions.

To investigate the transient LAS-to-BAS interconversion, we performed ME by pulsing 2 vol% H₂O in a feed containing a constant flow of 1000 ppm NH₃ while collecting DRIFT spectra. The time-resolved and phase-resolved spectra of the catalyst at 400 °C are shown in Figure 4.4.

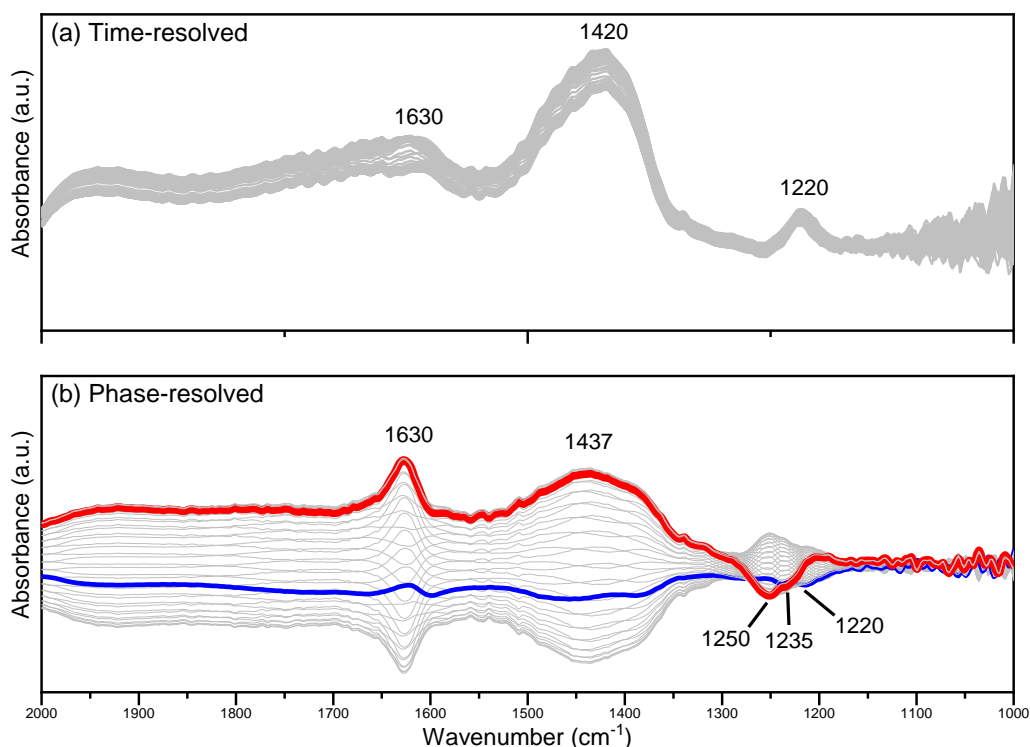


Figure 4.4. (a) Time-resolved and (b) phase-resolved spectra of 2V10WT at 400 °C resulting from 60-s pulses of 2 vol% H₂O in a gas feed containing 1000 ppm NH₃.

The phase-resolved spectra contain only the signals of the species that responded to the repeated gas pulses, irrespective of how weakly or strongly they are represented in the time-resolved spectra [79, 124]. This signal amplification can be exemplified by the peak at 1630 cm⁻¹, which can be assigned to the $\delta(\text{O-H})$ mode of physisorbed water. In the time-resolved spectra, this signal appeared less pronounced compared with that of the NH₃ adsorbed on BAS or LAS. This is expected due to the weaker basicity of water and hence the correspondingly weaker interaction with the acidic surface of the catalyst. On the other hand, it appeared as a sharp and pronounced peak in the phase-resolved spectra. The high temperature ensured that water could only be retained on the surface if it were continuously supplied from the gas phase. As soon as water was cut off, desorption occurred, diminishing the signal of physisorbed water. Overall, this indicates that while water was not as strongly adsorbed as NH₃, its presence was strongly affected by the concentration pulses.

Figure 4.4b also shows a broad signal centered at 1437 cm⁻¹, which is assigned to NH₃ bound to BAS. Interestingly, the peak maximum in the phase-resolved spectra was blue-

shifted from that of the time-resolved spectra. It is clear that the signals at 1630 and 1437 cm^{-1} varied in phase, reaching their maximum and negative values at approximately the same phase angles. This reinforces the observation that water increases the proportion of BAS, as concluded from the steady-state experiments. Closer inspection of the respective phase angles reveals that there is only a 5° delay between the two signals, with the BAS-bound NH_3 reaching the maximum absorbance at a higher phase angle than water (Figure 4.5). Considering the relationship between the phase angle and the time domain [112], we can therefore surmise that the BAS-bound NH_3 appeared before physisorbed water. From a mechanistic point of view, this means that water molecules are first preferentially consumed to produce BAS, most probably by surface hydroxylation. Only once this process has occurred, could water molecules adsorb and accumulate on the catalyst. It should be pointed out that this detailed kinetic information could be revealed only due to the sensitivity enhancement offered by phase-sensitive detection (PSD).

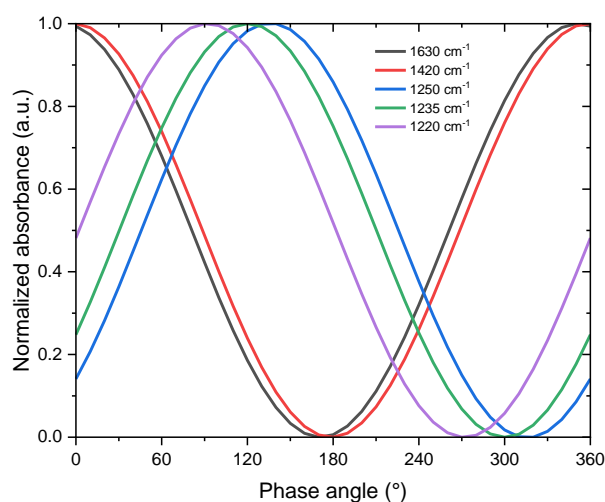


Figure 4.5. Phase angle dependence of the IR signal of physisorbed water (1630 cm^{-1}), NH_3 bound to Brønsted-Lowry acid sites (1420 cm^{-1}), and Lewis acid sites (1250 , 1235 , and 1220 cm^{-1}).

While physisorbed water and BAS-bound NH_3 followed similar phase behaviors, the LAS-bound NH_3 did not. In fact, Figure 4.4b shows that it evolved out-of-phase with respect to either water or BAS-bound NH_3 . As a corollary, LAS-bound NH_3 decreased when water

and BAS-bound NH_3 increased. Logically, this further corroborates the LAS-to-BAS transformation in the presence of water.

At first glance, the time-resolved spectra in Figure 4.4a seem to suggest that there is only one type of LAS in the catalyst, as the single peak centered at 1220 cm^{-1} appeared reasonably Gaussian with a hint of neither skewness nor multimodality. However, the phase-resolved spectra suggest otherwise as the PSD treatment revealed at least three different types of peaks across the region assigned to LAS-bound NH_3 . The peaks at 1250 and 1235 cm^{-1} changed opposite to that of water, but there was still a phase delay of around 15° between them. A reasonable conclusion is that these are two different types of LAS that have different stabilities when exposed to moisture. In particular, the LAS associated with 1250 cm^{-1} was the most susceptible to BAS conversion as it not only gave the highest absorbance in the phase-resolved spectra in Figure 4.4b, but also recorded the highest phase angle at which its value reaches maximum among the three LAS (Figure 4.5).

In comparison, the third LAS (1220 cm^{-1}) was rather less affected by the water pulses as confirmed by a phase angle delay of approximately 90° between it and the external stimulation. Figure 4.4b also conveys that this peak reached its minimum value when that of water was only starting to increase and when that of the NH_3 bound to BAS was still negative. This indicates that this particular LAS type did not convert into BAS under the experimental conditions. Such sites were experimentally observed in vanadia-based materials that were hydrothermally aged in a controlled manner [24]. These hydroxylation-resistant species were found to be more active for SCR and can maintain the NO_x conversion in the presence of water.

Giraud et al. [125] also reported two types of LAS, with the one appearing at higher frequency being more susceptible to hydration. However, these two peaks merge into one for vanadia-containing materials [126, 127]. These results are therefore in line with our findings, which showed that the LAS peaks at 1250 and 1235 cm^{-1} were less stable toward water exposure than the one at 1220 cm^{-1} . Due to the sample composition, the heterogeneity of LAS is not unexpected. Isolated VO_x , polymeric VO_x , and exposed TiO_2 sites can all

serve as LAS [128], but NH_3 molecules bound to these sites typically appear as a single peak in the spectra, as can be seen in Figure 4.4a. However, there can be subtle differences between the absorption characteristics and energy assignments between these sites, which could only be revealed by employing more sensitive techniques such as ME and PSD. While further experiments and theoretical calculations are still needed to assign the three different LAS peaks conclusively, our report already highlights the advantages that ME and PSD can offer in operando spectroscopy.

To study the effect of temperature further, another water modulation experiment was conducted at 200 °C – a temperature at which water and NH_3 are adsorbed much more strongly on the catalyst surface. The results are shown in Figure 4.6. It must be mentioned that the rotational and vibrational IR bands of gas-phase water are more pronounced at this low temperature.

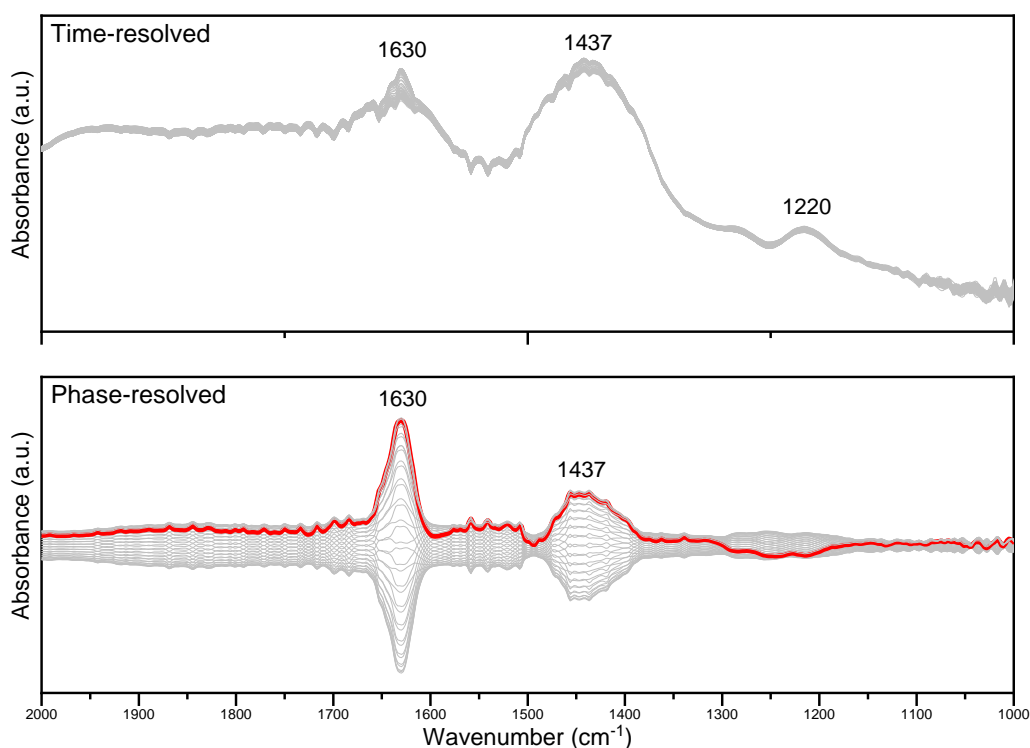


Figure 4.6. (a) Time-resolved and (b) phase-resolved spectra of 2V10WT at 200 °C as a result of 60-s pulses of 2 vol% H_2O in a gas feed containing 1000 ppm NH_3 .

The most intense peak in the phase-resolved spectra (Figure 4.6b) is from the physisorbed water molecules, as is the case in Figure 4.4b. Similarly, the signal from NH_3 bound to BAS is in phase with that of water, proving that water drives the formation of these sites regardless of the temperature. However, there are two important differences between the experiments conducted at 400 and 200 °C. First, the signal from the NH_3 adsorbed onto LAS is almost non-existent in the phase-resolved spectra at 200 °C, which can only mean that their concentration remained (almost) constant. Second, the ratio between the peaks at 1630 and at 1437 cm^{-1} is close to unity at 400 °C, but comparatively smaller at 200 °C, implying that the concentration of BAS did not vary much at 200 °C, regardless of whether water was present or not. As mentioned previously, water can hydroxylate the VO_x sites in the catalyst to convert them from LAS into BAS. This process is more pronounced at low temperature since water would have a stronger retention at the surface, as already exemplified by the high BAS-to-LAS ratio at low temperatures in Figure 4.2. Hence, physisorbed water could continuously persist on the surface even if the gas phase supply is removed. During the equilibration stage (i.e., prior to the modulation experiment), all of the interconvertible LAS were already transformed into BAS, and they remained as such even if the water supply was cut off because of the stability of adsorbed water at low temperature. This explains the absence of the LAS peak in Figure 4.6b.

While the number of LAS remained fairly constant at 200 °C, the number of BAS varied with the water concentration. Observing that the IR sensitivities of the $\delta(\text{N-H})$ modes associated with LAS and BAS are considered sufficiently similar (i.e., 0.7 to 1.0) [109, 129], we can assume that the formed BAS must not have come from the LAS. Therefore, BAS can be produced not just by converting LAS into such sites, but also possibly by generating them spontaneously on the surface, with both processes being driven by water. This may rationalize the non-proportional increase of BAS over the decrease of LAS in the presence of water, as shown in Figure 4.2.

4.4. Conclusions

Several factors influence the interconversion between Lewis and Brønsted-Lowry acid sites in vanadia-based catalysts. Low temperature, addition of water, and high WO_3 loading generally increase BAS, often at the expense of LAS. The combination of ME and PSD revealed the presence of at least three LAS that have different stabilities and interaction strengths with water. Finally, water increases BAS by two plausible routes: (1) conversion of pre-existing LAS and (2) spontaneous generation of new sites.

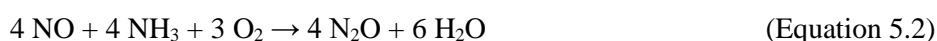
Chapter 5 – Hydrogen Cyanide Production from Formaldehyde over Vanadia-, Copper-, and Iron-Based Catalysts under Selective Catalytic Reduction Conditions

5.1. Introduction

Although modern catalyst formulations and process design considerations have greatly hampered the occurrence of side reactions during SCR, some of them can still occur in parallel. This is because of the inherent complexity of the exhaust gas composition and gas-catalyst interactions. The most commonly encountered side reaction is the direct oxidation of NH_3 with O_2 (Equation 5.1) [130, 131].



Although the major product of this parasitic reaction is nitrogen, NO can also form at high temperature, thereby negating the beneficial effect of NH_3 addition in the first place. Another undesirable side reaction is the formation of nitrous oxide (N_2O), a very potent greenhouse gas (Equation 5.2) [132-134].



The extent of N_2O formation is catalyst-dependent, with Cu- and Fe-based SCR catalysts being more susceptible than V-based ones especially below 350 °C [56, 135].

The production of hydrogen cyanide (HCN), a gas considered immediately dangerous to life, is another highly undesirable SCR side reaction. It was first observed over Cu-ZSM-5 when hydrocarbons were used as the reductant instead of NH_3 [136]. The extent of HCN formation followed a volcano-shaped profile with temperature, and the activity depended on the type of hydrocarbon used. With ethene and propene, the HCN concentration reached a maximum value at 325 and 225 °C, respectively. The presence of water in the feed

generally increased the amount of HCN produced [9]. It became evident that HCN formation did not solely apply to Cu-ZSM-5, but also to other catalysts operating under hydrocarbon-SCR [137-139].

HCN was also observed during NH₃-SCR when ammonium formate decomposition was exploited to generate NH₃ instead of urea (Equation 5.3) [140].



As this is an endothermic reaction ($\Delta_r H^\circ = 85 \text{ kJ} \cdot \text{mol}^{-1}$), the equilibrium shifts in favor of ammonium formate at low temperature. This can give rise to another decomposition pathway wherein it undergoes subsequent dehydration steps to form formamide (Equation 5.4) and eventually HCN (Equation 5.5).



Both formamide and HCN were observed below 250 °C under SCR-relevant conditions, and the decrease in HCN production correlated well with the increase of SCR activity. As more NH₃ was consumed to satisfy the increased NO_x reduction at higher temperatures, more ammonium formate was decomposed according to Equation 5.3, thereby rendering Equation 5.4 and Equation 5.5 less probable. Nonetheless, this reaction path showed very low HCN yield. A very recent study proposed that a similar route was responsible for HCN production under NH₃-SCR conditions in the presence of formaldehyde (HCHO) [141]. Formed due to the incomplete oxidation of hydrocarbons, formaldehyde is a noxious compound that is nominally present as a trace constituent in the exhaust of internal combustion engines [142-145]. This is particularly problematic for stationary natural gas engines, which usually do not operate an oxidation catalyst upstream of the SCR catalyst. The unwanted side reaction between formaldehyde and NH₃ can potentially lower NO_x conversion by consuming NH₃ that is otherwise reserved for SCR. While the decrease in SCR activity is certainly detrimental, the major problem really stems from the high toxicity

of the produced HCN. The European Commission set the maximum occupational exposure limit of HCN at only 0.9 ppm. Hence, the release of even minute quantities of HCN to the environment can have grave consequences for air quality and human health [146, 147]. It is therefore imperative to investigate this side reaction in detail to develop potential measures for mitigation.

In this study, we show that formaldehyde reacts with NH_3 to form HCN with high yields under SCR conditions, and that the mechanism does not require the formation of ammonium formate.

5.2. Materials and methods

5.2.1. Materials synthesis

The catalyst in this study comprised of $\text{V}_2\text{O}_5/\text{WO}_3\text{-TiO}_2$ (2 wt %) that was prepared by wet impregnation. A sufficient amount of ammonium metavanadate (Fluka, >99.0%) was dissolved in water at 60 °C, and was mixed with 10 wt% WO_3/TiO_2 (DT-52, Cristal) for 1 h. After removal of water under reduced pressure, the sample was calcined in a muffle furnace at 550 °C for 10 h. The surface area of the calcined catalyst is $\sim 90 \text{ m}^2 \cdot \text{g}^{-1}$, which does not vary significantly from that of the starting 10 wt% WO_3/TiO_2 material [19]. At this relatively low loading and calcination temperature, V_2O_5 and WO_3 are well-dispersed and only reflections from anatase could be detected by X-ray diffraction [19, 24]. For comparative purposes, TiO_2 (DT-51, Cristal; $\sim 100 \text{ m}^2 \cdot \text{g}^{-1}$) was also used without additional modification. Cordierite honeycomb monoliths (Corning, 400 cpsi, 17 mm x 12 mm x 50 mm) were repeatedly immersed in an aqueous slurry of $\text{V}_2\text{O}_5/\text{WO}_3\text{-TiO}_2$ or TiO_2 and then dried in air to achieve a loading of $130 \text{ g} \cdot \text{L}^{-1}$ of material. The washcoated monoliths were dried and then calcined in a muffle furnace at 500 °C for 5 h.

Fe-ZSM-5 and Cu-BEA (400 cpsi cordierite monoliths) were obtained from industrial partners and were used as received. Cu-SSZ-13 in monolith form was prepared by repeatedly immersing the monolith in a suspension containing the powder form (2.2 wt% Cu) to achieve a loading of $118 \text{ g} \cdot \text{L}^{-1}$.

5.2.2. Catalytic measurements

The measurements were carried out in a custom-built model gas test bench (Figure 5.1). Mass flow controllers (MFCs) were used to regulate the flows of air, N₂, H₂, O₂, NO, and NH₃. Water was generated in situ from the reaction of H₂ and O₂ through a Pt-based catalyst (H₂O generator), which is preferred over conventional water vaporization as it allows for a pulsation-free water feed.

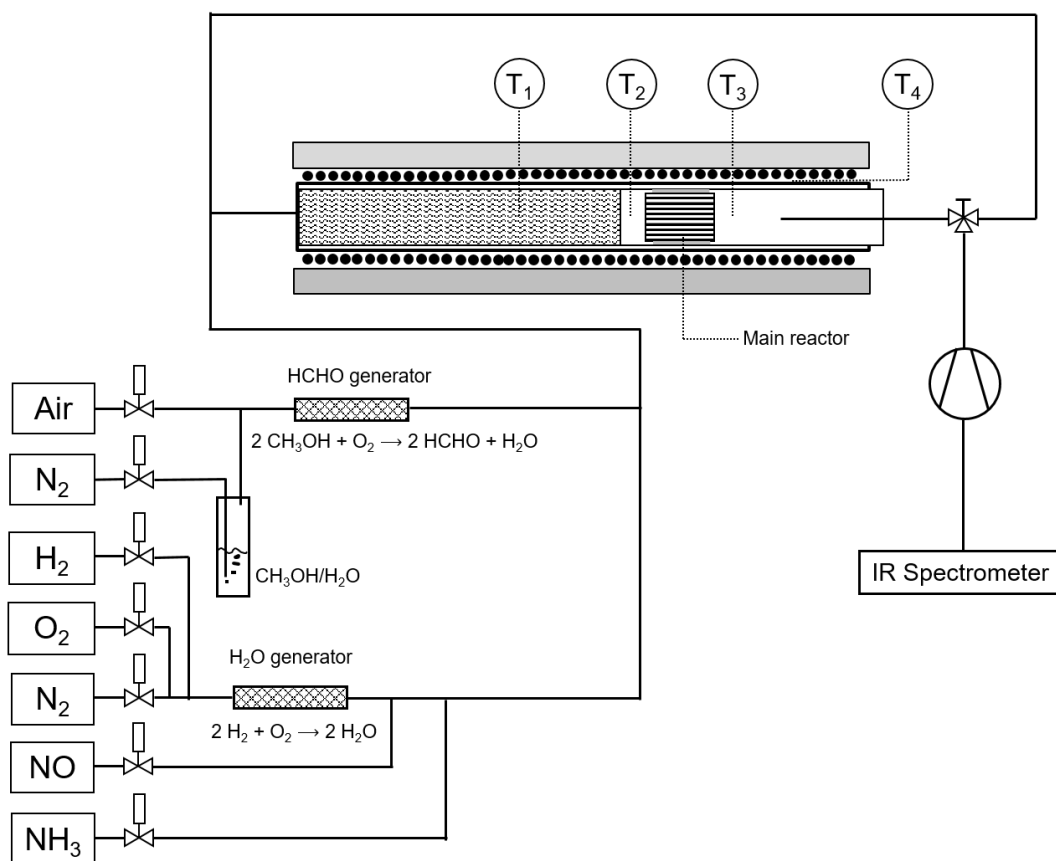


Figure 5.1. Experimental set-up with the mass flow controllers, H₂O generator, HCHO generator, main reactor, heating system, and IR spectrometer for gas analysis.

Formaldehyde was generated in situ through the partial oxidation of methanol over V₂O₅/WO₃-TiO₂ (200-500 μm) in a separate stainless steel reactor (HCHO generator). For this purpose, N₂ was bubbled through a 50 vol% aqueous solution of methanol at ambient temperature before mixing with air and flowing through the catalyst bed heated at 250 °C to produce 150 ppm formaldehyde. Under these conditions, methanol oxidation was not

complete, and the feed to the main reactor contained also 10-15 ppm methanol as well as 1 ppm formic acid, 350 ppm CO, and 0.1-0.2 vol% H₂O. All gas lines were heated to 150 °C to prevent condensation of components with low vapor pressure.

The model gas (GHSV = 50000 h⁻¹) consisted of 10 vol% H₂O and 10 vol% O₂ balanced in N₂ with variable amounts of formaldehyde, NO, and NH₃ as indicated in Table 5.1.

Table 5.1. Feed conditions employed in the study.

Feed label and composition	Formaldehyde (ppm)	NO (ppm)	NH ₃ (ppm)
SCR feed (NH ₃ /NO/H ₂ O/O ₂ /N ₂)	0	300	Required concentration to achieve ~10 ppm NH ₃ slip
HCHO feed (HCHO/H ₂ O/O ₂ /N ₂)	150	0	0
HCHO + SCR feed (HCHO/NH ₃ /NO/H ₂ O/O ₂ /N ₂)	150	300	Same concentration as in “SCR feed”
HCHO + adj. SCR feed (HCHO/adj. NH ₃ /NO/H ₂ O/O ₂ /N ₂)	150	300	Required concentration to achieve ~10 ppm NH ₃ slip

In most SCR catalytic studies, NH₃ and NO_x are dosed at the same concentration across the temperature range under study. This technique is often sufficient to compare catalysts with different activities. However, for practice-relevant measurements, it is more useful to determine the NO_x conversion by varying the NH₃ dosage until a defined NH₃ slip occurs (usually 10 ppm) [148]. For this purpose, the catalyst in this study was exposed to a constant feed of NO_x and increasing dosages of NH₃ at a given temperature until the outlet

concentration is ~10 ppm. All of the NH_3 dosages as well as outlet concentrations of NO and NH_3 are reported in Table S-5.1.

The effects of O_2 and water on HCN formation were also investigated. The O_2 content was varied from 2.5 to 15 vol% in a gas feed containing 10 vol% H_2O , 150 ppm formaldehyde, and 300 ppm NH_3 . In a similar way, the water content was changed from 0 to 12.5 vol% in a gas feed containing 10 vol% O_2 , 150 ppm formaldehyde, and 300 ppm NH_3 .

For comparison, formic acid was also dosed in the reactor instead of formaldehyde by bubbling N_2 through a 30 vol% solution of formic acid in water at ambient temperature. The HCHO generator was bypassed in order to prevent any subsequent oxidation of formic acid prior to meeting the catalyst in the main reactor. This resulted in 150 ppm formic acid in the feed.

The main reactor (quartz glass tube; $d_{\text{int}} = 28$ mm) had three heating zones, including the preheating zone (T1), which was filled with ceramic beads to avoid radial temperature gradients of the model gas feed. Thermocouples inserted in the center of the quartz tube before (T2) and after the catalyst module (T3) ensured uniform temperature control of the catalyst bed. The temperature of the reactor outlet was measured and controlled via the thermocouple (T4) installed on the outer wall of the reactor. After being wrapped in ceramic fiber paper, the washcoated monolith piece was inserted in the rectangular opening of a cylindrical stainless steel holder that was itself wrapped with ceramic fiber paper for sealing against the reactor wall.

The outlet of the main reactor and the bypass line were connected to a gas feed pump (KNF) that was heated at 170 °C. A manual three-way valve allowed the gas from either the reactor or the bypass line to pass through a 2-m gas cell mounted in the sample compartment of a Nexus Fourier transform infrared spectrometer (Thermo-Nicolet) and heated at 180 °C. The gas components were quantified using the Omnic/Quantpad software. The acquisition time was 8 s per measurement point, whereby 4 spectra were recorded and averaged per measurement point. To obtain the lowest possible detection limit (DL), a total of 10

measurement points were averaged. Typical DL values ranged from 0.2 to 1 ppm (Table S-5.2).

The degree of NO_x conversion was calculated according to Equation 5.6.

$$NO_x \text{ conversion} = \frac{[NO]_{in} - [NO_x]_{out}}{[NO]_{in}} \cdot 100\% \quad (\text{Equation 5.6})$$

where $[NO]_{in}$ and $[NO_x]_{out}$ are the concentration of NO in the gas feed, and the concentration sum of NO and NO_2 after the reactor, respectively.

As mentioned previously, the oxidation of methanol in the HCHO generator was not complete and left 10-15 ppm methanol in the feed to the main reactor. This unreacted fraction could potentially be oxidized once it passes through the catalyst sample. Hence, the formaldehyde conversion was calculated according to Equation 5.7 to account for the unreacted methanol.

$$HCHO \text{ conversion} = \left(1 - \frac{[HCHO]_{out}}{[HCHO]_{in} + [CH_3OH]_{in}}\right) \cdot 100\% \quad (\text{Equation 5.7})$$

where $[HCHO]_{out}$, $[HCHO]_{in}$, and $[CH_3OH]_{in}$ are the concentrations of formaldehyde after the reactor, formaldehyde in the gas feed, and methanol in the gas feed, respectively.

The HCN yield from formaldehyde was calculated according to Equation 5.8.

$$HCN \text{ yield} = \frac{[HCN]_{out}}{[HCHO]_{in} + [CH_3OH]_{in}} \quad (\text{Equation 5.8})$$

where $[HCN]_{out}$, $[HCHO]_{in}$, and $[CH_3OH]_{in}$ are the concentrations of HCN after the reactor, formaldehyde in the gas feed, and methanol in the gas feed, respectively.

Aside from HCN, other products can also form from formaldehyde, with CO and CO_2 (CO_x) being the most notable. Hence, the selectivity of formaldehyde consumption toward the formation of HCN and CO_x is given by Equation 5.9 and Equation 5.10, respectively.

$$HCN \text{ selectivity} = \frac{[HCN]_{out}}{[HCN]_{out} + [CO_x]_{out}} \quad (\text{Equation 5.9})$$

$$CO_x \text{ selectivity} = \frac{[CO_x]_{out}}{[HCN]_{out} + [CO_x]_{out}} \quad (\text{Equation 5.10})$$

where $[HCN]_{out}$ and $[CO_x]_{out}$ are the concentration of HCN after the reactor and the concentration sum of CO and CO₂ after the reactor, respectively.

5.3. Results and discussion

5.3.1. Influence of formaldehyde on the SCR reaction over V₂O₅/WO₃-TiO₂

Figure 5.2 shows the NO_x conversion obtained at 10 ppm NH₃ slip over V₂O₅/WO₃-TiO₂ and the actual amount of NH₃ dosed. The performance of V₂O₅/WO₃-TiO₂ in the absence of formaldehyde (Figure 5.2; SCR feed) was comparable with those reported in the literature for the same V loading and GHSV [19, 24]. Regardless of the conditions applied, the trends followed a similar profile. The NO_x conversion increased between 200 and 300 °C, and passed through a maximum value between 350 and 400 °C. Two factors can contribute to the decrease in the NO_x conversion above 450 °C: the direct oxidation of NH₃ that becomes increasingly favorable at high temperature and the decreased amount of adsorbed NH₃.

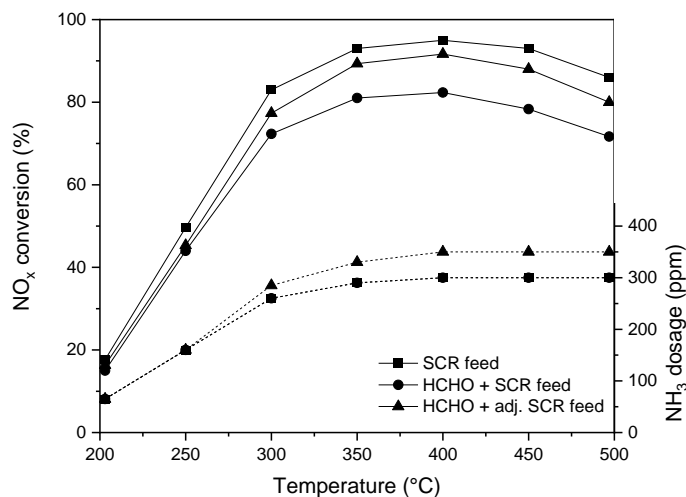


Figure 5.2. NO conversion over V₂O₅/WO₃-TiO₂ at 10 ppm NH₃ slip in the presence and absence of formaldehyde and the corresponding NH₃ dosage (experimental conditions listed in Table 5.1 and Table S-5.1). The NH₃ dosages for SCR feed and HCHO + SCR feed are the same and therefore the respective curves perfectly overlap.

The presence of formaldehyde had a negative effect on the NO_x conversion at the same NH_3 dosage (Figure 5.2; $\text{HCHO} + \text{SCR}$ feed). As an illustration, nearly 95% of the NO_x in the gas feed could be abated with 300 ppm NH_3 at 400 °C in the absence of formaldehyde, but this value dropped to 82% with formaldehyde. The decrease in the catalytic performance could be attributed to the depletion of the available NH_3 for SCR as it is consumed in the presence of formaldehyde.

At low temperatures, a lower NH_3 dosage was necessary to achieve 10 ppm of NH_3 slip because the catalytic activity was rather limited. Correspondingly, the NO_x conversion was not affected significantly by the presence of formaldehyde, with less than 5% of catalytic performance being lost at 250 °C. Although NH_3 could react with formaldehyde, it was still preferentially consumed by SCR. Hence, formaldehyde competed with NO_x for reaction with NH_3 only when the temperature was sufficiently high (i.e., above 300 °C). These results imply that the activation energy for the side reaction is much higher than that of the SCR reaction.

To further investigate the effect of formaldehyde on the SCR reaction, the NH_3 dosage was readjusted to meet 10 ppm NH_3 slip (i.e., compensation for the amount of NH_3 lost in the side reaction). As more NH_3 became available for SCR, the NO_x conversion increased, but did not return to the original value obtained in the absence of formaldehyde (Figure 5.2; $\text{HCHO} + \text{adj. SCR}$). When the NH_3 dosage was adjusted from 300 to 350 ppm at 400 °C, the NO_x conversion increased from 82% to 92%, but not to the initial 95% obtained in the absence of formaldehyde. This behavior implies that the side reaction consuming formaldehyde could take place at the same catalytic sites responsible for SCR.

5.3.2. Formaldehyde conversion over $\text{V}_2\text{O}_5/\text{WO}_3\text{-TiO}_2$

Figure 5.3 shows the formaldehyde conversion over the same catalyst. Under a purely oxidative atmosphere (Figure 5.3; HCHO feed), formaldehyde conversion increased from 9% to 89% as the temperature was varied from 200 to 500 °C. CO was the major product observed, which reflects the oxidation activity of $\text{V}_2\text{O}_5/\text{WO}_3\text{-TiO}_2$ catalysts. At 200 °C, traces of formic acid were also detected in the gas phase. This suggests that formic acid is

the first reaction step of formaldehyde oxidation. Indeed, previous infrared spectroscopic studies have shown that surface formate species were formed almost instantaneously upon introduction of formaldehyde, and that they prevailed over surface formaldehyde species [149, 150]. Nonetheless, formates do not desorb as formic acid significantly, suggesting that the formed surface species are reaction intermediates. Above 450 °C, traces of CO₂ were also observed in the gas phase.

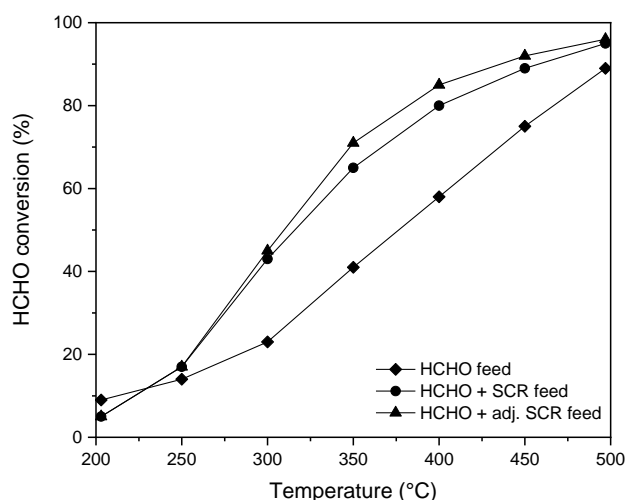


Figure 5.3. Formaldehyde conversion over V₂O₅/WO₃-TiO₂ in the presence and absence of SCR (experimental conditions listed in Table 5.1 and Table S-5.1).

Formaldehyde conversion generally increased under SCR conditions (Figure 5.3; HCHO + SCR feed). The only exception was at 200 °C where it was slightly lower (5% vs. 9%), indicating that NH₃ probably inhibits the oxidation of formaldehyde at low temperature. As the temperature increased, more formaldehyde was consumed in presence of the SCR feed. The maximum difference of 24% in formaldehyde conversion between the two feed conditions was recorded at 350 °C. This behavior suggests that formaldehyde started to react with NH₃. At 500 °C, the two formaldehyde conversion levels were again very close. It is important to note that addition of 300 ppm NO in the absence of NH₃ (Table S-5.3) did not cause any change in formaldehyde conversion, demonstrating that NO is not involved in side reactions with formaldehyde.

When the NH_3 feed was adjusted to meet 10 ppm NH_3 slip (Figure 5.3; HCHO + adj. SCR feed), the formaldehyde conversion improved particularly in the temperature regime between 300 and 500 °C, indicating that the side reaction was further promoted by the increased NH_3 dosage. Hence, an increase in NH_3 concentration increases NO_x conversion but promotes simultaneously the side reaction of NH_3 , effectively subtracting it from the main SCR reaction pathway.

Under similar conditions, TiO_2 was also able to oxidize formaldehyde to some degree, reaching 15% and 25% conversion at 500 °C in the absence and presence of NH_3 , respectively (Figure S-5.1). Formaldehyde conversion was low likely because TiO_2 did not have appreciable redox activity in the temperature range studied.

5.3.3. Formation of HCN over $\text{V}_2\text{O}_5/\text{WO}_3\text{-TiO}_2$

Figure 5.4 shows the concentration of HCN formed as a function of temperature in the same experiment presented in Figure 5.2 and Figure 5.3. In the absence of either formaldehyde or NH_3 , no HCN was observed (Figure 5.3; SCR feed and HCHO feed).

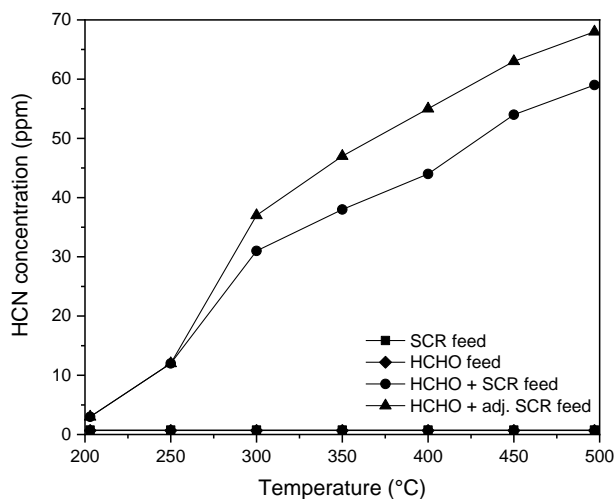


Figure 5.4. HCN formation at 10 ppm NH_3 slip over $\text{V}_2\text{O}_5/\text{WO}_3\text{-TiO}_2$ (experimental conditions listed in Table 5.1 and Table S-5.1). The HCN concentrations for SCR feed and HCHO feed are the same and therefore the respective curves perfectly overlap.

When formaldehyde and NH_3 were fed simultaneously, the HCN concentration increased from 3 to 59 ppm as the temperature was raised from 200 to 500 °C (Figure 5.4; HCHO + SCR feed). The steepest rise occurred between 250 and 300 °C, where the HCN concentration more than tripled.

When the NH_3 dosage was adjusted to meet the 10 ppm slip, even more HCN was produced (Figure 5.4; HCHO + adj. SCR feed). For example, HCN increased from 44 to 55 ppm when the NH_3 supply was changed from 300 to 350 ppm. This explains why the NO_x conversion reported in Figure 5.2 did not reach the same levels in the absence of formaldehyde, even if additional NH_3 was supplied. HCN production is therefore confirmed to be in direct competition with SCR, especially at high temperatures.

Even a non-reducible material such as TiO_2 showed mild HCN formation under similar conditions, with the HCN concentration varying from 2 ppm at 350 °C to 11 ppm at 500 °C (Figure S-5.2). While the presence of redox-active sites such as VO_x increases HCN production significantly, the metal oxide support already provides a non-negligible baseline activity.

HCN formation over $\text{V}_2\text{O}_5/\text{WO}_3\text{-TiO}_2$ was strongly temperature-dependent, but it remained constant when the O_2 content was varied from 2.5 to 15.0 vol% (Figure S-5.3). This suggests that excess O_2 does not cause the side reaction to stop in favor of the direct oxidation of formaldehyde. In fact, formaldehyde conversion and CO_x formation were also found to be independent of O_2 content.

In contrast, water had a significant impact on HCN production. Formaldehyde conversion decreased from 99% to 89% as the water concentration increased from 0 to 12.5 vol% (Figure 5.5). This might be due to the co-adsorption of water on the catalyst, which is also known to inhibit the SCR reaction by decreasing the adsorption sites for NH_3 , among other effects [128].

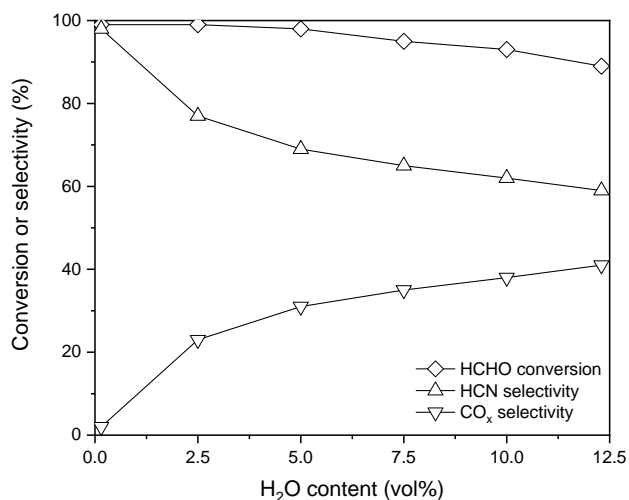


Figure 5.5. Effect of water content on the formaldehyde conversion, HCN selectivity, and CO_x selectivity over V₂O₅/WO₃-TiO₂ at 350 °C.

HCN selectivity also decreased similar to formaldehyde conversion, which suggests that formaldehyde requires close proximity with the active sites for HCN production. However, CO_x selectivity followed an opposite trend. Without water, CO_x formation was negligible, but CO_x selectivity increased to 41% at the highest water level investigated in the study. Water could transform formaldehyde into adsorbed formate species [149, 150], which were already proposed to be intermediates for CO_x formation in the previous sections. The positive effect of water on CO_x formation further confirms this pathway. The same strong effect of water was observed on TiO₂. In the absence of H₂O, 111 ppm HCN were produced from reaction of formaldehyde and NH₃ at 500 °C with practically full conversion of formaldehyde, while only 11 ppm HCN and 25% formaldehyde conversion were observed with 10 vol% H₂O (Figure S-5.4).

The increase in water concentration and the subsequent formation of formate species appeared to be detrimental for HCN formation, suggesting that it follows a different mechanism than CO_x formation. To confirm that formate species were not relevant for HCN formation, formic acid was dosed together with NH₃ over V₂O₅/WO₃-TiO₂ (Figure 5.6). Similar to the case of formaldehyde, HCN formation from formic acid was also negatively affected by the presence of water. Under 10 vol% H₂O – which is the usual

water content in exhaust gas and the same condition applied in the measurements presented in Figure 5.4 – HCN did not form in significant amounts; all of the measurements fell below the detection limit of 1 ppm. Even when the water content was decreased to 5 vol%, no HCN was observed. In fact, it is only in the absence of water that formic acid formed HCN, but in rather limited amount compared to formaldehyde. This proves that HCN formation from formaldehyde cannot proceed through the formate route; instead, HCN more likely originates from the direct reaction of formaldehyde with NH_3 .

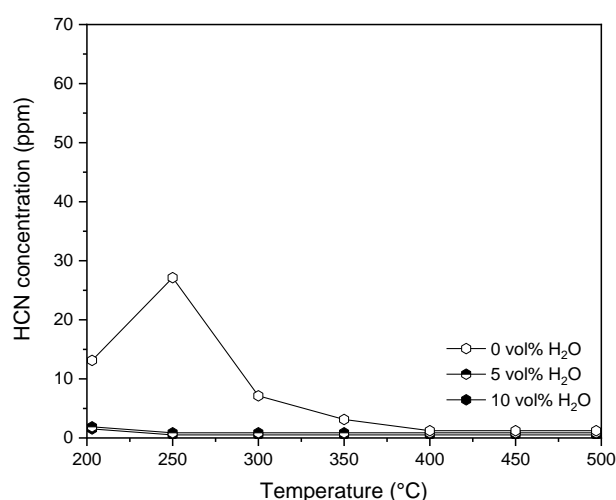


Figure 5.6. HCN formation from formic acid over $\text{V}_2\text{O}_5/\text{WO}_3\text{-TiO}_2$.

Finally, it is important to note that HCN formation from formaldehyde and formic acid followed different behaviors with temperature. Whereas HCN formation increased continuously with temperature when formaldehyde was the reactant (Figure 5.4), it experienced a maximum at 250 °C and then decreased rapidly when formic acid was used instead (Figure 5.6). This is the same behavior observed in a previous study where ammonium formate was used as a reducing agent for SCR [140]. Hence, this confirms that two different mechanisms are responsible for HCN formation depending on the carbonyl precursor: a high-yielding route with formaldehyde that is active above 300 °C and a moderate one with formic acid that operates only below 300 °C.

5.3.4. Comparison with Fe-ZSM-5, Cu-BEA, and Cu-SSZ-13

Figure 5.7 shows the HCN production over different catalysts during the SCR reaction in presence of formaldehyde. As reported in the previous sections, V_2O_5/WO_3-TiO_2 exhibited a continuous HCN formation with increasing temperature from 20 ppm at 200°C to 70 ppm at 500°C. Over Fe-ZSM-5, HCN formation was comparable between 200 and 300°C, and dropped from approximately 40 ppm at 300°C to around 20 ppm at 500°C. On both catalysts, formaldehyde had a rather moderately negative influence on the SCR reaction.

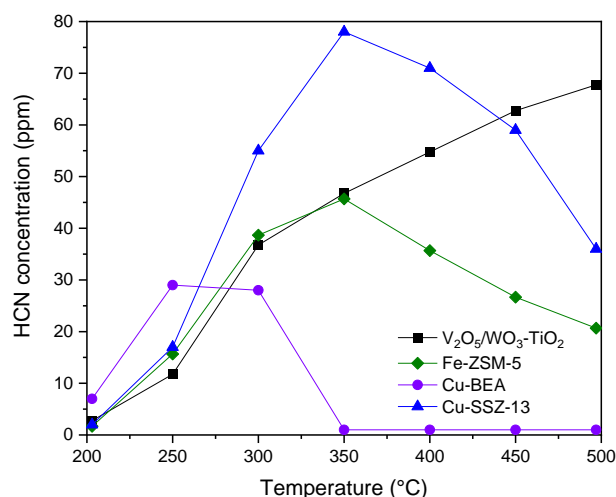


Figure 5.7. HCN formation at 10 ppm NH_3 slip ($HCHO$ + adj. SCR feed) over V_2O_5/WO_3-TiO_2 , Fe-ZSM-5, Cu-BEA, and Cu-SSZ-13.

Within the two Cu-exchanged zeolites, the behavior strongly depended on framework type. Over Cu-BEA, a maximum value of 40 ppm HCN was found only at 200-300°C, while no HCN formation was observed above 300°C. Formaldehyde exerted a very strong inhibition of SCR reaction between 200 and 250°C. In contrast, HCN formation reached 60-70 ppm on Cu-SSZ-13 at 350°C together with a strong negative influence on the SCR reaction, especially at low temperature. Thus, practically complete NO conversion was achieved at 250°C without formaldehyde, and only 50% with formaldehyde.

For V_2O_5/WO_3-TiO_2 , Fe-ZSM-5, and Cu-SSZ-13, the other major product from the side reaction is CO and only a small amount of CO_2 is observed. However, this is not the case

for Cu-BEA, which formed CO₂ in significant amounts at high temperatures. Hence, this strong oxidizing capability explains why no HCN was produced over Cu-BEA above 300 °C.

5.3.5. Practical Relevance

HCN forms under SCR conditions in the temperature range of 250-500 °C. This side reaction is highly undesired because of two reasons. First, HCN is a poisonous gas that harms human health and the environment. Second, the side reaction leading to HCN formation not only consumes NH₃ parasitically, but also retards SCR activity by up to 20% (Figure S-5.5). This means that a larger catalyst bed or monolith brick would be needed to achieve the same reactivity in the absence of formaldehyde.

Formaldehyde and other potential carbonyl species in the gas feed result from the partial oxidation of hydrocarbons. Hence, these species must be fully oxidized to avoid potential side reactions before passing through the SCR catalyst compartment. For mobile systems, this is not really an issue because oxidation catalysts and NH₃ slip catalysts are typically installed before and after SCR catalysts, respectively. These materials are usually based on Pt and possess high activity for formaldehyde oxidation [151, 152]. Even if some formaldehyde escaped oxidation and eventually formed HCN, the NH₃ slip catalyst could oxidize it prior to release to the environment. We have shown that Pd- and Pt-based catalysts abate HCN effectively above 300 °C [153], which is the temperature region where maximum levels of HCN were detected. Nonetheless, both formaldehyde and HCN can resist oxidation at lower temperatures, and therefore still represent a potential issue.

While mobile exhaust treatment systems are in principle already well designed to prevent HCN formation or emission, not all stationary systems are. Many stationary SCR installations function as standalone units directly downstream of the engine. Where operation conditions of the engine allow formation of formaldehyde in the exhaust gas, a catalytic oxidation system must be installed upstream of the SCR unit to avoid HCN formation.

Currently, HCN is not monitored in the exhaust of vehicles and stationary plants. However, legislations are constantly evolving [154], and it is recommendable to include HCN in the lists of regulated emissions due to its hazardous effects.

5.4. Conclusions

HCN can form in significant amounts during the SCR treatment of formaldehyde-containing exhaust gases over V_2O_5/WO_3-TiO_2 . This undesired reaction not only lowers the SCR activity and consumes NH_3 parasitically, but also results in the production of a highly poisonous substance. While the detailed mechanism is not yet conclusive, we provide evidence that HCN production occurs from the direct reaction of formaldehyde and NH_3 , and not through the formation of formic acid or ammonium formate. These results should serve as a basis for system designs and/or environmental legislation to prevent HCN emissions.

Chapter 6 – Operando Detection of Cyanide Intermediate Species during the Reaction of Formaldehyde with Ammonia over V₂O₅/WO₃-TiO₂

6.1. Introduction

Hydrogen cyanide (HCN) is a highly poisonous gas that can form through the reaction between formaldehyde and ammonia (NH₃) in the exhaust of lean burn gas engines as shown in the previous chapter. While this detrimental side reaction has been the subject of recent catalytic studies under selective catalytic reduction (SCR) conditions [141, 155], the molecular mechanism leading to the release of HCN remains far from elucidated.

In the formation of HCN during hydrocarbon SCR, adsorbed NO_x molecules were proposed to react with the hydrocarbon from the gas phase to form an organic nitro compound, which then transforms into HCN, cyanogen (C₂N₂), or isocyanic acid (HNCO) before eventually being reduced into nitrogen gas (N₂) [156]. Addition of water increased the level of HCN production and SCR activity in general up to 275 °C, which was attributed to the ability of water to suppress the formation of carbonaceous residues. Above this temperature, the presence of water limited HCN production in conjunction with enhanced N₂ formation. This apparent promotion of NO_x conversion was attributed to HCN hydrolysis to ammonia (NH₃), which is a more powerful reducing agent than hydrocarbons [137].

In the case of NH₃-SCR, Zengel et al. [141] proposed that HCN formation over Fe-ZSM-5, Fe-BEA, Cu-SSZ-13 and V₂O₅/WO₃-TiO₂ passes through a formate route, which is similar to the previously proposed ammonium formate pathway. In their reported mechanism, formaldehyde initially undergoes surface oxidation to formic acid and reacts with NH₃ to form formamide, which then dehydrates to yield HCN. This was supported by the detection of adsorbed formate species and formamide on Fe-ZSM-5 by infrared spectroscopy. In another study, Ngo et al. [155] showed that the formamide intermediate

decomposes between 250 and 400 °C by dehydration to form HCN, but can also undergo decarbonylation to a smaller extent to yield carbon monoxide (CO) and NH₃. Above 400 °C, the formed HCN decomposes to carbon dioxide (CO₂), nitric oxide (NO), and water.

In this study, we report the detection of the cyanide intermediate species by operando diffuse reflectance infrared spectroscopy (DRIFTS), thereby providing unambiguous evidence that the HCN-forming reaction occurs on the catalyst surface. These mechanistic insights should serve as a basis for understanding the chemistry responsible for the side reaction so that mitigation measures can be put forward.

6.2. Materials and methods

6.2.1. Materials synthesis

V₂O₅/WO₃-TiO₂ (2 wt%) was prepared by wet impregnation. A sufficient amount of ammonium metavanadate (Fluka, >99.0%) was dissolved in water at 60 °C, and was mixed with 10 wt% WO₃/TiO₂ (DT-52, Cristal) for 1 h. After removal of water under reduced pressure, the sample was calcined at 550 °C for 10 h in a muffle furnace.

TiO₂ (DT-51-D, Cristal) was calcined at 550 °C for 10 h in a muffle furnace without additional modification.

Both powders were sieved to obtain a particle size between 150 and 200 µm prior to use.

6.2.2. Diffuse reflectance infrared Fourier transform spectroscopy

Diffuse reflectance infrared Fourier transform (DRIFT) spectra were collected using a Vertex70 spectrometer (Bruker) equipped with a HgCdTe detector. Spectra were recorded from 4000 to 1000 cm⁻¹ at a resolution of 4 cm⁻¹ and scanner velocity of 80 kHz. The sample and background spectra resulted from averaging 10 and 50 scans, respectively.

Approximately 50 mg of each sample were loaded in the custom-built spectroscopic cell, which was equipped with a 2-mm-thick calcium fluoride window (Crystran) and was

attached to a Praying Mantis diffuse reflection accessory (Harrick). Prior to every experiment, the sample was dehydrated under 5 vol% O₂/Ar at 400 °C for 1 h.

For the operando experiments, various mixtures of 150 ppm formaldehyde or formic acid, 1000 ppm NH₃ and 5 vol% O₂ balanced in Ar were admitted to the cell. Where required, 2 vol% H₂O was added to the feed to study the effect of high water content. An OmniStar GSD 320 mass spectrometer (Pfeiffer) was connected at the outlet of the cell to monitor $m/z = 17$ (NH₃), 18 (H₂O), 27 (HCN), 29 (formaldehyde), and 32 (O₂ or methanol).

Formaldehyde was generated in situ from the reaction of methanol and O₂ in a pre-oxidation reactor containing the same V₂O₅/WO₃-TiO₂ catalyst (200-500 μm). For this purpose, Ar was bubbled through a 50 vol% aqueous solution of methanol at ambient temperature before mixing with air and flowing through the catalyst bed heated at 250 °C to produce 150 ppm formaldehyde. Under these conditions, methanol oxidation was not complete and the feed to the cell contained 10-15 ppm methanol as well as 1 ppm formic acid, 350 ppm carbon monoxide (CO) and 2000 ppm water.

Formic acid was dosed in the reactor by bubbling Ar through a 30 vol% aqueous solution of formic acid at ambient temperature and by-passing the pre-oxidation reactor. This resulted in 150 ppm formic acid in the feed.

In the experiments with water feed, water was generated in situ from the reaction of H₂ and O₂ through a monolithic Pt/Al₂O₃ catalyst. The total flow for all experiments was fixed at 100 mL·min⁻¹.

After background collection at 300 °C, the catalyst was equilibrated with formaldehyde (or formic acid)/O₂ flow for 30 min followed by addition of NH₃ for 30 min. An identical experiment was performed by pre-equilibrating the catalyst with NH₃/O₂ for 30 min followed by addition of formaldehyde for 30 min. Cut-off experiments were conducted to establish the stability of the observed species and consisted of the sequential removal of formaldehyde and then NH₃ from a formaldehyde/NH₃/O₂ feed each time after equilibration for 30 min.

Modulated excitation (ME) experiments were conducted by exposing the sample to alternate pulses (60 s) of NH_3 and formaldehyde/ NH_3 at 300 °C after drying, background acquisition, and equilibration in formaldehyde/ NH_3 / O_2 feed for 30 min. Each pulse consisted of 47 spectra that were collected by acquiring 10 scans at 4 cm^{-1} time resolution and 80 kHz scanner velocity (1.3 s/spectrum). The time-resolved DRIFT spectra obtained along at least ten modulation periods were converted into phase-resolved spectra using Equation 1.4 [79, 124].

6.3. Results and discussion

6.3.1. Adsorption of formaldehyde and NH_3

Figure 6.1 shows the DRIFT spectra obtained during the adsorption of formaldehyde on $\text{V}_2\text{O}_5/\text{WO}_3\text{-TiO}_2$ at 300 °C. Additionally, Table 6.1 lists the important infrared (IR) signals that will be discussed in the succeeding subsections. Under oxidative conditions, formaldehyde converts into CO and, to a lesser extent, CO_2 but neither was observed in the spectra.

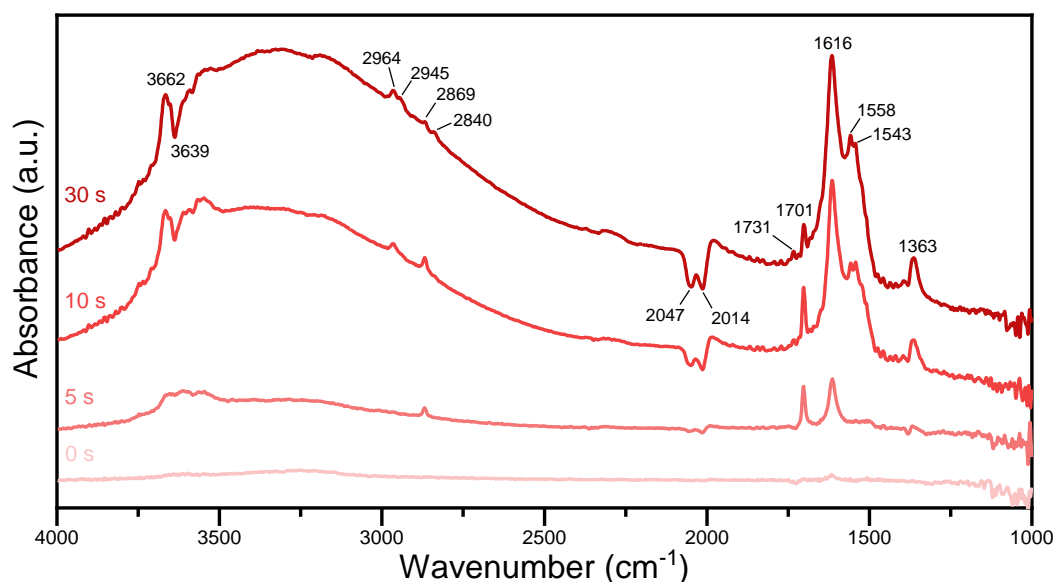


Figure 6.1. DRIFT spectra of $\text{V}_2\text{O}_5/\text{WO}_3\text{-TiO}_2$ during formaldehyde adsorption at 300 °C. Experimental conditions: 150 ppm HCHO and 5 vol% O_2 in Ar.

Table 6.1. List of important infrared signals.

Wavenumber (cm ⁻¹)	Assignment	Reference(s)
3686	$\nu(\text{O-H})$	Ti-OH
3639	$\nu(\text{O-H})$	V-OH [24, 38]
2964	$\nu_{\text{as}}(\text{O-C-O})+\delta(\text{C-H})$	bidentate formate [157]
2945	$\nu_{\text{as}}(\text{O-C-O})+\delta(\text{C-H})$	bridged formate [157]
2893	$\nu(\text{CH}_2)$	hydrogen-bonded formaldehyde
2869	$\nu(\text{C-H})$	Lewis-adsorbed formaldehyde
2869	$\nu(\text{C-H})$	bidentate formate
2840	$\nu(\text{C-H})$	bridged formate
2215, 2196	$\nu(\text{C}\equiv\text{N})$	[158-160]
2047	$2\nu(\text{V=O})$	[24, 38]
2014	$2\nu(\text{W=O})$	[38]
1731	$\nu(\text{C=O})$	hydrogen-bonded formaldehyde [161]

1701	$\nu(\text{C=O})$	Lewis-adsorbed formaldehyde	[162]
1720	$\nu(\text{C=O})$	formic acid	[163, 164]
1686	$\nu(\text{C=O})$	amide	[155]
1672	$\nu(\text{C=O})$	monodentate formate	[165, 166]
1616	$\delta(\text{O-H})$	water	[38]
1602	$\delta_{\text{as}}(\text{N-H})$	Lewis-adsorbed NH_3	[24, 38]
1578	$\nu_{\text{as}}(\text{O-C-O})$	bridged formate	[157]
1558	$\nu_{\text{as}}(\text{O-C-O})$	bidentate formate	[149, 150]
1436	$\delta(\text{N-H})$	Brønsted-Lowry-bound NH_3	[24, 38]
1363	$\nu_{\text{s}}(\text{O-C-O})$	bidentate formate	[149, 150]
1332	$\nu_{\text{s}}(\text{O-C-O})$	bridged formate	[157]
1237	$\delta_{\text{s}}(\text{N-H})$	Lewis-adsorbed NH_3	[24, 38]

Two peaks at 2869 and 1701 cm^{-1} appeared as soon as formaldehyde entered the cell and correspond to the $\nu(\text{C-H})$ and $\nu(\text{C=O})$ modes of molecularly adsorbed formaldehyde, respectively [149, 162]. The red-shift of $\nu(\text{C=O})$ from the gas phase value of 1741 cm^{-1} suggests that formaldehyde coordinated specifically to Lewis acid sites [157]. Water, which was produced as a by-product of methanol oxidation, was also observed by virtue of the $\delta(\text{O-H})$ mode at 1616 cm^{-1} . Although residual methanol was detected at the outlet of the pre-oxidation reactor, no signal that could be assigned to adsorbed methoxy groups was

observed, suggesting that the small amount of methanol that escaped oxidation before the DRIFT cell was oxidized upon contact with the catalyst at 300 °C.

Formaldehyde underwent chemical transformations rapidly, as the IR spectrum changed significantly between 5 and 10 s on stream. The peaks appearing at 1558 and 1363 cm^{-1} are associated with the asymmetric and symmetric $\nu(\text{O}-\text{C}-\text{O})$ modes of bidentate formate species, respectively [149, 150]. These bands are accompanied by the corresponding $\nu_{\text{as}}(\text{O}-\text{C}-\text{O})+\delta(\text{C}-\text{H})$ and $\nu(\text{C}-\text{H})$ modes at 2964 and 2869 cm^{-1} , respectively.[157] Therefore, formaldehyde was oxidized under these conditions into surface formate species, which is in agreement with previous reports on TiO_2 -based catalysts [167, 168]. The negative peaks at 2047 and 2014 cm^{-1} correspond to the first overtones of $\nu(\text{V}=\text{O})$ and $\nu(\text{W}=\text{O})$ modes of the surface termination in vanadyl and tungstenyl oxido-groups, respectively, reflecting the interaction of these sites with the adsorbates [38]. The negative signal at 3639 cm^{-1} is assigned to the stretch mode of $\text{V}-\text{OH}$ groups, which were consumed by the interaction with formaldehyde and its products [169].

After 30 s, two new bands appeared at 2945 and 2840 cm^{-1} that we tentatively assign to the evolution of formate species with different geometry (i.e., bridged formates). The corresponding $\nu_{\text{as}}(\text{O}-\text{C}-\text{O})$ and $\nu_{\text{s}}(\text{O}-\text{C}-\text{O})$ modes of the bridged species likely overlap with the existing signals of the bidentate species.

The weak signal at 1731 cm^{-1} suggests the presence of formaldehyde molecules that interact more weakly with the catalyst surface compared to those adsorbed on Lewis acid sites [170, 171]. It is worth noting that the peaks corresponding to formaldehyde decreased in favor of the peaks belonging to formate species, suggesting the occurrence of the surface oxidation reaction. However, the persistence of the formaldehyde peaks at 1731 and 1701 cm^{-1} proves that the oxidation was only partial and that adsorbed formaldehyde is still available to react. Continuation of the experiment up to 30 min resulted in the equilibration of all signals.

Figure S-6.1 shows the spectrum obtained after NH_3 adsorption on the catalyst. Two types of adsorbed NH_3 can be detected: NH_3 adsorbed molecularly on Lewis acid sites and

characterized especially by the signals at 1602 and 1237 cm^{-1} , and ammonium ions coordinated to Brønsted-Lowry acid sites, which are represented by the peaks at 1670 and 1432 cm^{-1} [38]. There does not appear to be a difference in the kinetics of adsorption of these two species as both appeared and evolved synchronously. If we assume a similar extinction coefficient for the two signals at 1602 and 1432 cm^{-1} [109], the large area of the latter suggests that the majority of adsorbed NH_3 species is in the form of NH_4^+ . Indeed, the addition of WO_x to the catalyst is recognized to impart Brønsted-Lowry acidity [121] at the expense of terminal Ti^{4+} Lewis acid sites [24]. NH_3 adsorption produced the same negative signals at 2047 cm^{-1} ($2\nu(\text{V}=\text{O})$) and 2014 cm^{-1} ($2\nu(\text{W}=\text{O})$) observed upon reaction of formaldehyde, in addition to negative signals at 3686 and 3639 cm^{-1} due to coordination with $\text{Ti}-\text{OH}$ and $\text{V}-\text{OH}$ groups, respectively.

6.3.2. Reaction of formaldehyde and NH_3

Figure 6.2a shows the spectrum obtained after formaldehyde adsorption followed by NH_3 addition. For comparison, the spectra obtained after 30 min of formaldehyde (Figure 6.1) and NH_3 adsorption (Figure S-6.1) are also given in Figure 6.2c and Figure 6.2b, respectively. The simultaneous presence of formaldehyde and NH_3 on the catalyst surface produced chemical species that were reflected in a number of strong peaks at 1731, 1686, 1578, 1332 cm^{-1} , and other signals that remain to be assigned conclusively. An almost identical spectrum was obtained for the opposite sequence (i.e., NH_3 adsorption and then formaldehyde addition), suggesting that the result of the interaction on the catalyst surface was independent of the sequence of admittance of the two compounds (Figure S-6.2).

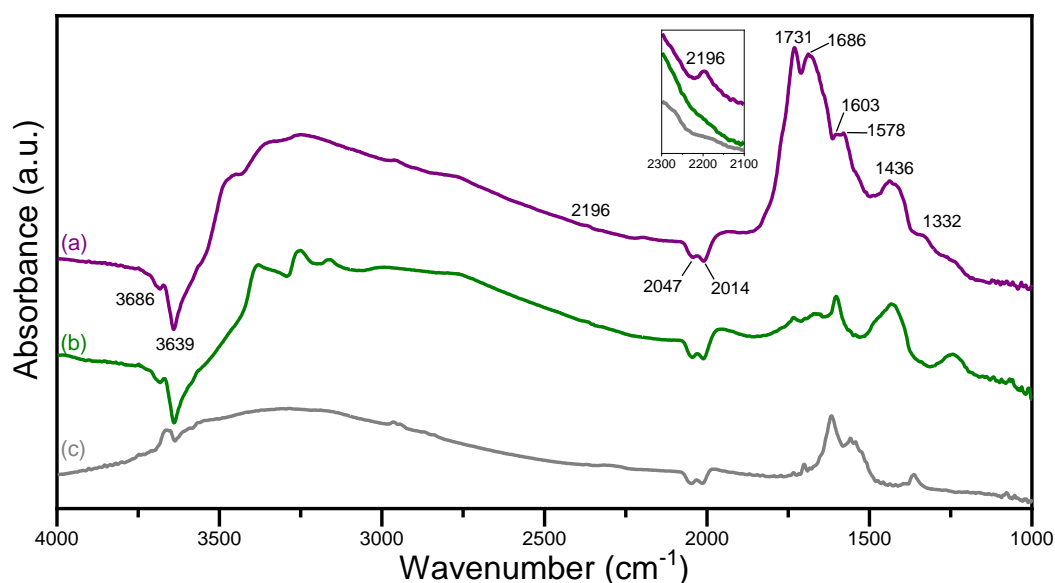


Figure 6.2. DRIFT spectra of $\text{V}_2\text{O}_5/\text{WO}_3\text{-TiO}_2$ after 30 min of (a) formaldehyde and NH_3 reaction; (b) NH_3 adsorption; and (c) formaldehyde adsorption at 300 °C. Experimental conditions: 150 ppm formaldehyde, 1000 ppm NH_3 and 5 vol% O_2 in Ar.

The sharp and strong signal at 1731 cm^{-1} corresponds to the hydrogen-bonded formaldehyde molecules that appeared already in the absence of NH_3 (Figure 6.1) [161, 170]. While we cannot discard the continued presence of species responding to the peak at 1701 cm^{-1} (i.e., Lewis-bound formaldehyde) under reaction conditions, the signal at 1731 cm^{-1} was remarkably more intense than it was in Figure 6.1. The abundance of these weakly bonded formaldehyde species can be rationalized by the presence of NH_3 , which can interact more strongly with the acidic surface of the catalyst, thereby preventing formaldehyde from adsorbing onto the acid sites and transforming directly into formate species. Furthermore, the layer formed by NH_3 upon adsorption provides donor sites, with which the electronegative O atom of formaldehyde can form hydrogen bonds. Yu et al [170] reported such signal in the overlays of formaldehyde on $\text{TiO}_2(110)$.

The strong signal at 1686 cm^{-1} could originate from formate species, but the assignment can be disregarded because the signals in the high frequency region typical of the C-H stretch and the $\nu_{\text{as}}(\text{O-C-O})+\delta(\text{C-H})$ combination mode were missing. The signals at 1691 and $1685/1676\text{ cm}^{-1}$ were assigned to formamide under similar conditions in the IR spectra of Fe-ZSM-5 [141] and $\text{V}_2\text{O}_5/\text{WO}_3\text{-TiO}_2$ [155], respectively. Similarly, adsorption of

formamide on other metal oxide surfaces provided a signal at 1690 cm^{-1} [172, 173]. In order to assign this peak conclusively, formaldehyde was cut-off from the feed after 30 min of reaction to evaluate the stability of the observed signals. Figure 6.3a shows that the intensity of the signals of the carbonyl products was significantly decreased in the spectrum recorded 30 min after cut-off. The rapid extinction of the band at 1731 cm^{-1} upon the removal of gas-phase formaldehyde supports assignment of this signal to formaldehyde. This implies that the adsorbed formaldehyde desorbed and/or reacted with NH_3 . Despite some intensity decrease, likely also caused by the simultaneous consumption of the signal at 1731 cm^{-1} , the species associated with the signal at 1686 cm^{-1} persisted on the catalyst surface even after cutting-off NH_3 from the gas feed. Physical inspection of the powder sample revealed that the original yellowish catalyst powder exhibited white spots after the experiment, hinting to the formation of a residue of polymeric nature. The continuous slow increase of the signals upon NH_3 addition to the feed observed above supports this assignment. Hence, the species producing the signal at 1686 cm^{-1} was most likely a polyamide-like residue.

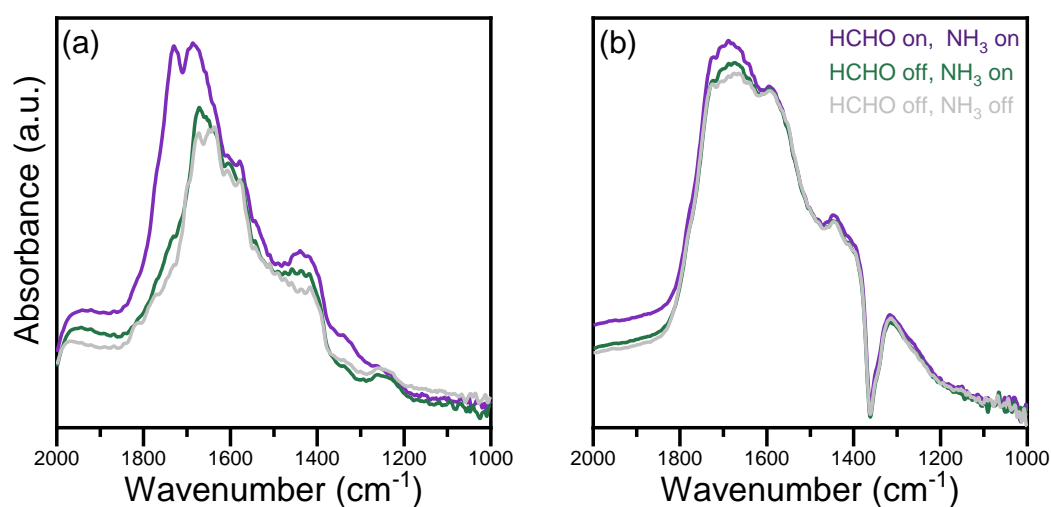


Figure 6.3. DRIFT spectra of (a) $\text{V}_2\text{O}_5/\text{WO}_3\text{-TiO}_2$ and (b) TiO_2 after 30 min of formaldehyde + NH_3 reaction, NH_3 exposure, and treatment under O_2 at 300°C . Experimental conditions: 150 ppm formaldehyde, 1000 ppm NH_3 and 5 vol% O_2 in Ar.

The experiment was repeated on TiO_2 under otherwise identical conditions (Figure 6.3b). The decrease in the intensity of the envelope centered at 1686 cm^{-1} was even smaller, and no other signal experienced the same significant attenuation as that of 1731 cm^{-1} in

V₂O₅/WO₃-TiO₂. This behavior supports the absence of reactive carbonyl species on bare TiO₂.

The peak at 2196 cm⁻¹, which can be seen more clearly in the inset of Figure 6.2, can be assigned to the C≡N stretch of adsorbed cyanide species [158-160], which manifested only when both formaldehyde and NH₃ were present. Figure 6.4 shows the temporal evolution of this IR signal together with the MS data for HCN and formaldehyde upon introduction of NH₃. Smoothed data are given in Figure S-6.3. Adsorbed cyanide species increased even before HCN was detected in the gas phase, concomitant with the decrease of gas-phase formaldehyde. This is the first time that the cyanide intermediate species was detected on the surface of the catalyst upon reaction of formaldehyde with NH₃. Furthermore, this is a direct evidence that the side reaction occurs on the catalyst surface.

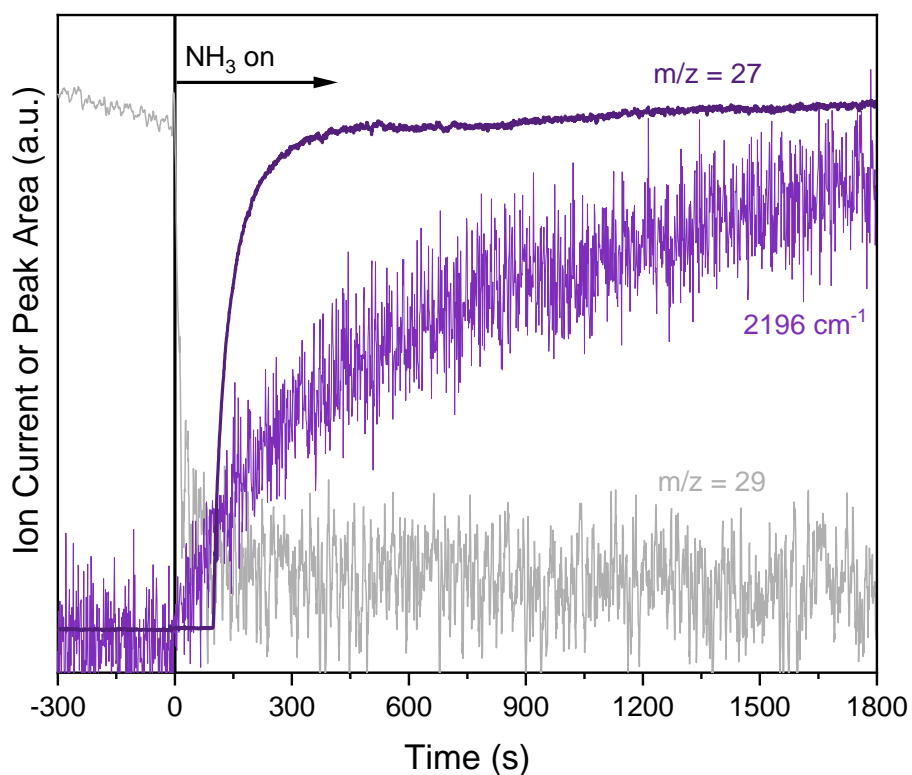


Figure 6.4. Temporal evolution of the area of the $\nu(\text{C}\equiv\text{N})$ mode as well as the MS signals of HCN ($m/z = 27$) and formaldehyde ($m/z = 29$) signals upon NH₃ addition. Experimental conditions: 150 ppm formaldehyde, 1000 ppm NH₃ and 5 vol% O₂ in Ar.

A modulated excitation experiment consisting of formaldehyde pulses in a gas feed containing NH_3 was performed in order to identify the source of the cyanide species as well as other species that can be catalytically relevant. In this approach, the time-resolved spectra exhibit all the characteristic signals of IR-active species on the catalyst surface. After phase-sensitive analysis, only the signals of the species responding to the pulses appear, while those of the spectator species are removed, thus enabling the disentanglement of complex spectral envelopes [112]. Figure 6.5a and Figure 6.5b show the time-resolved and phase-resolved spectra, respectively, for the formaldehyde pulsing experiment in a feed containing NH_3 . The time-resolved spectra are characterized by the negative signals at 3649, 2047, and 2014 cm^{-1} and by the positive signals at 2196, 1731, 1686, and 1578 cm^{-1} , which are already visible in the steady-state spectra presented in Figure 6.2a. Besides baseline variations between 3400 and 2000 cm^{-1} , likely as a result of the simultaneous addition of water together with formaldehyde, no other evident change is observed as a result of the pulses. On the contrary, the most prominent feature in the selected phase-resolved spectrum is the sharp $\nu(\text{C}\equiv\text{N})$ peak at 2196 cm^{-1} (Figure 6.5b). This reveals that although cyanide species could be a minor species because of their weak signal in the time-resolved spectra, their surface concentration was strongly affected by formaldehyde and its production was repeatedly switched on and off upon formaldehyde pulses. Moreover, this also confirms that most of the other signals appearing in the region are accumulation products because their response to the modulation was poor, in agreement with the previous discussion.

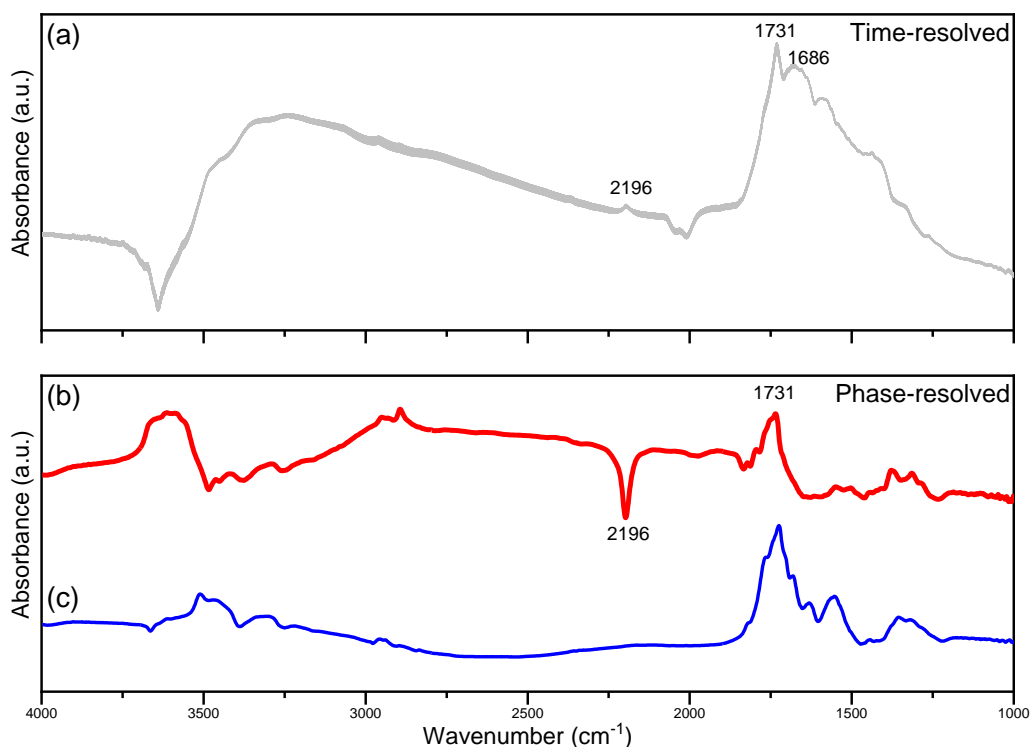


Figure 6.5. (a) Time-resolved DRIFT spectra and (b) a selected phase-resolved spectrum ($\varphi^{PSD} = 200^\circ$) as a result of 60-s pulses of 150 ppm formaldehyde in a gas feed containing 1000 ppm NH_3 and 5 vol% O_2 in Ar at 300 °C. (c) Selected phase-resolved DRIFT spectrum ($\varphi^{PSD} = 300^\circ$) of a similar experiment with 2 vol% H_2O . The full set of phase-resolved spectra of (b) and (c) are given in Figure S-6.4 and Figure S-6.5, respectively.

The carbonyl compounds exhibited different responses to the formaldehyde pulses. The peak assigned to the weakly bonded formaldehyde (1731 cm^{-1}) was clearly visible in the phase-resolved spectra and varied out of phase with the signal at 2196 cm^{-1} – a clear indication of the transformation of formaldehyde into cyanide species. In contrast, the signal from the amide product was not appreciably perturbed, indicating that its surface concentration was not sensitive to variations in the gas-phase concentration of formaldehyde on the time scale of the pulses (60 s).

The phase-resolved spectra also revealed the presence of weaker signals at 1998 and 1776 cm^{-1} , which are likely to be assigned to the perturbation of VO_x and WO_x groups, and of signals at 1832, 1813, 1784, 1549, 1503, 1461, 1378, 1315, 1287 and 1234 cm^{-1} that are not discernable in the time-resolved data. Aside from the peak at 1731 cm^{-1} , two other carbonyl signals appeared clearly in the phase-resolved data at 1765 and 1751 cm^{-1} , which

were asynchronous and delayed, suggesting a possible sequence of transformation of carbonyl groups. A clear signal appearing at 2893 cm^{-1} ($\nu(\text{C-H})$) varied synchronously to the envelope of signals around that at 1731 cm^{-1} , and probably belongs to hydrogen-bonded formaldehyde. The signals at 1501 and 1234 cm^{-1} could also belong to the same species [157]. The nature of some of the signals between 1900 and 1200 cm^{-1} leaves some room for discussion, but already suggests that the chemistry involved in the reaction of formaldehyde with NH_3 is complex and that it could follow several paths. We cannot exclude that some of the still unassigned signals can originate from the species present in the formaldehyde feed (e.g. methanol and formic acid) and only becomes visible because of the increased sensitivity after PSD. However, our time-resolved spectra are not significantly different from those reported by Ngo et al. [155].

Water was shown to inhibit HCN formation partly under SCR conditions (Figure 5.5). Since 2000 ppm of water was produced upon formaldehyde generation in the pre-reactor, its effect was intrinsically present in all the spectra presented thus far. When water was deliberately added to the gas feed to the catalyst to reach 2 vol\% , the $\nu(\text{C}\equiv\text{N})$ signal vanished almost completely in the corresponding modulation experiment (Figure 6.5c). A plausible explanation for the absence of signals of cyanide species in this experiment and for the decreased HCN production in presence of water is that water destabilizes $\text{C}\equiv\text{N}$ groups through competitive adsorption, and changes the product distribution to favor CO/CO_2 [155].

To probe deeper into the kinetics of reactant consumption and product formation, the temporal behavior of the selected species upon single reactant cut-off was analyzed. Figure 6.6 shows that the formation of cyanide species followed a two-stage process. As soon as formaldehyde was introduced, $\nu(\text{C}\equiv\text{N})$ increased abruptly and then levelled off after 20 s . In the subsequent formaldehyde cut-off, the signal dropped, indicating that the production of HCN stopped. However, the signal at 2196 cm^{-1} started to increase again after 80 s despite the absence of gas-phase formaldehyde in the feed. This implies that NH_3 could still react with the adsorbed carbonyl compounds, although the major reaction was with the gas-phase reactant.

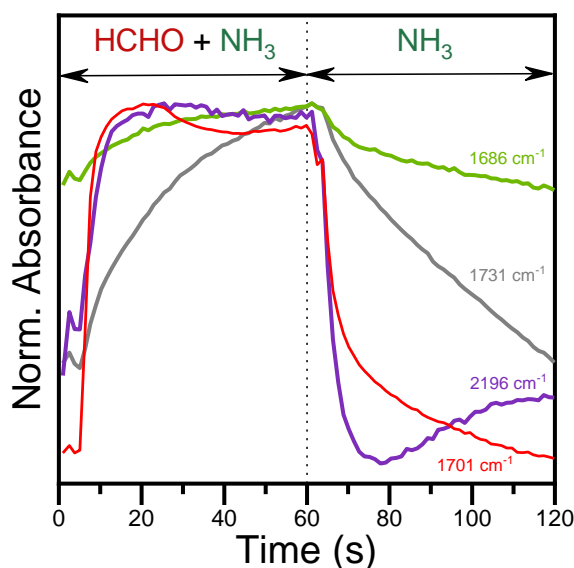


Figure 6.6. Temporal evolution of the signals of cyanide (2196 cm^{-1}), formaldehyde (1731 cm^{-1}), and amide (1686 cm^{-1}) species during alternate exposures to a gas feed containing formaldehyde/ NH_3 and NH_3 at $300\text{ }^\circ\text{C}$. The signal of formaldehyde in a NH_3 -free cut-off experiment is also presented in for comparison. Experimental conditions: 150 ppm formaldehyde, 1000 ppm NH_3 , and 5 vol% O_2 in Ar.

Formaldehyde and the amide product followed somewhat similar trends: both signals at 1731 and 1686 cm^{-1} increased in the presence of formaldehyde and decreased upon cut-off. The intensity of the signal assigned to the amide product varied less throughout the period, confirming the observation from the phase-resolved spectrum shown in Figure 6.5b. If this signal were modulated, it would still strongly overlap with the signals of other species that are more susceptible to the formaldehyde modulation, thus showing larger intensity variations.

Adsorbed formaldehyde, on the other hand, did not accumulate immediately when gas-phase formaldehyde was introduced. In an alternative experiment where NH_3 was absent, adsorbed formaldehyde reached a plateau almost immediately (Figure 6.6). This implies that HCN was preferentially formed in the presence of NH_3 before formaldehyde could accumulate significantly on the surface. Thus, formaldehyde most likely reacts from the gas phase.

The complementary experiment where NH_3 was cut-off instead of formaldehyde is shown in Figure 6.7. Since formaldehyde was always present in the feed, the signal at 1731 cm^{-1} remained constant throughout the period. In contrast, both the amide and the surface cyanide species decreased when NH_3 was removed, indicating that their formation required the presence of both formaldehyde and NH_3 .

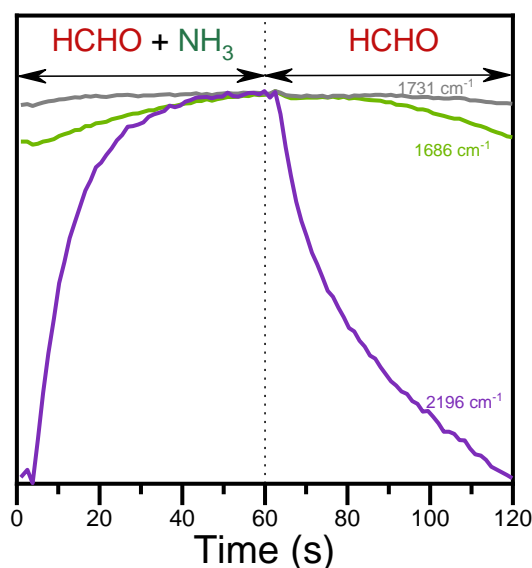


Figure 6.7. Temporal evolution of the signals of cyanide (2196 cm^{-1}), formaldehyde (1731 cm^{-1}), and amide (1686 cm^{-1}) species during alternate exposures to a gas feed containing formaldehyde/ NH_3 and formaldehyde at $300\text{ }^{\circ}\text{C}$. Experimental conditions: 150 ppm formaldehyde, 1000 ppm NH_3 , and 5 vol% O_2 in Ar.

The evolution of the $\nu(\text{C}\equiv\text{N})$ signal in Figure 6.6 and Figure 6.7 followed different kinetics. In the case of formaldehyde addition to the feed, the adsorbed cyanide species reached its maximum signal promptly, just after 10 s. On the other hand, it took more than 40 s for the signal to reach a plateau in the case of NH_3 addition to the feed. These data suggest that NH_3 adsorption preceded the formation of cyanide species, which is expected due to the strong acid-base interaction between the catalyst and NH_3 . The side reaction under investigation probably proceeds through an Eley-Rideal-type mechanism, where gas-phase formaldehyde reacts with pre-adsorbed NH_3 , which is analogous to the reaction of NO with adsorbed NH_3 in the case of the SCR reaction, and thus competes with SCR as indicated by the catalytic data [141, 155].

6.3.3. Reactivity of formate species

Figure 6.1 shows that formate species formed on the catalyst surface upon formaldehyde introduction. The relatively fast kinetics of this oxidative transformation limits the concentration of adsorbed molecular formaldehyde. Nonetheless, both formate species and adsorbed formaldehyde were present on the catalyst surface, and could potentially react with NH_3 to form HCN. The ammonium formate route was proposed as a possible pathway for HCN production at low temperature (150°C) [141, 155]. To determine whether formate species play a role in the side reaction at 300°C , formic acid was admitted to the cell instead of formaldehyde. The resulting spectrum is presented in Figure 6.8a. For comparison, the spectra for NH_3 -only and formic acid-only adsorption experiments are also shown in Figure 6.8b and Figure 6.8c, respectively.

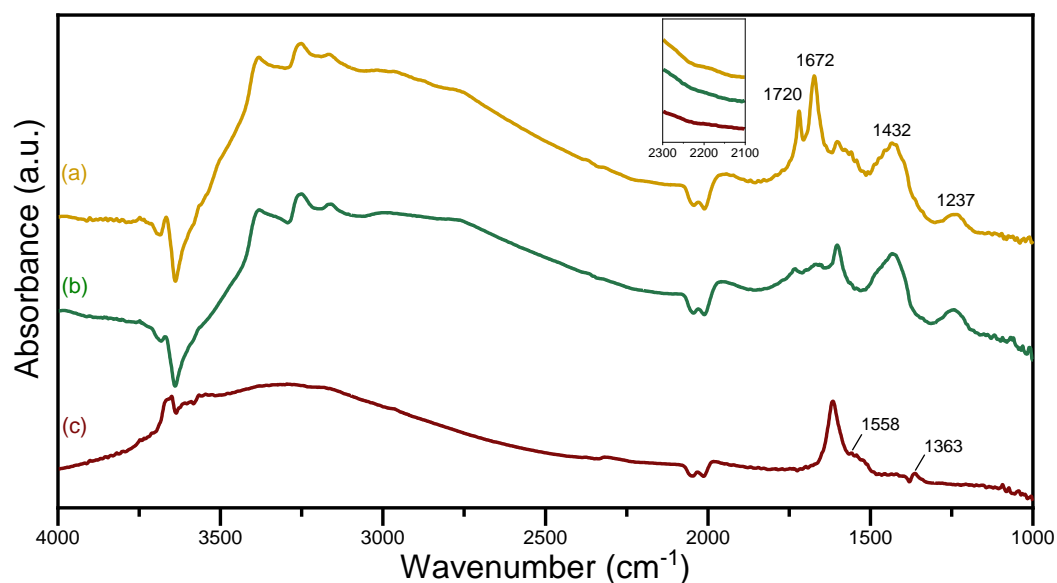


Figure 6.8. DRIFT spectra of $\text{V}_2\text{O}_5/\text{WO}_3\text{-TiO}_2$ after 30 min of (a) formic acid + NH_3 reaction; (b) NH_3 adsorption; and (c) formic acid adsorption at 300°C . Experimental conditions: 150 ppm formaldehyde, 1000 ppm NH_3 and 5 vol% O_2 in Ar.

Under these conditions, formate species were also observed (1558 and 1363 cm^{-1}), together with the signals of physisorbed water. While comparison of diffuse reflectance experiments is not straightforward, the much weaker intensity of the signal at 2961 cm^{-1} suggests that the overall less evident signals obtained with formic acid compared to the formaldehyde

experiment (Figure 6.1) are a result of the lower coverage of formate species obtained with formic acid.

The adsorbed formate species did interact with NH_3 , as evidenced by the appearance of new peaks at 1720 and 1672 cm^{-1} that can be assigned to carbonyl-containing species (Figure 6.8a). However, the frequencies of these peaks were significantly different from those obtained with formaldehyde (Figure 6.2a). These species are therefore of different nature. The peak at 1672 cm^{-1} could be assigned to the $\nu(\text{C}=\text{O})$ of monodentate formate species [163, 166], but it could also be attributed to an amide species because of the absence of formate signals above 2800 cm^{-1} compared to the spectrum obtained in the absence of NH_3 . A change of adsorption geometry from bidentate (without NH_3) to monodentate (with NH_3) is difficult to justify but could be explained with the strong adsorption of NH_3 on the acid sites, which likely limits the access to formate species and makes the monodentate geometry more favorable. However, the signal at 1672 cm^{-1} is very close to the signal at 1676 cm^{-1} that was assigned by Ngo et al to adsorbed formamide [155].

Furthermore, the peak at 1720 cm^{-1} could be assigned to the $\nu(\text{C}=\text{O})$ mode of formic acid [163, 164]. The same strong interaction of NH_3 with the catalyst could prevent the adsorption of formic acid. In this scenario, a layer of adsorbed NH_3 forms on the catalyst surface. With some of the active sites blocked, formic acid can then build up on top of the NH_3 layer. Formic acid appeared also less reactive than formaldehyde: the typical signals of adsorbed NH_3 above 3000 cm^{-1} were evident with formic acid but were absent in the spectrum obtained from formaldehyde and NH_3 (Figure 6.2a).

If we turn our attention towards the inset of Figure 6.8, it is clear that no signal was detected in the region between 2300 and 2100 cm^{-1} . This signal is very weak compared to the broad background induced by the presence of water and NH_3 , but the contour plots of the experiments with formaldehyde (Figure 6.9a; Figure S-6.6) and with formic acid (Figure 6.9b; Figure S-6.7) emphasize clearly the difference between the two experiments. The appearance of the peak at 2196 cm^{-1} with time on stream was visible only in the case of formaldehyde, suggesting that no cyanide intermediate was produced when formic acid

reacted with NH_3 . Therefore, no cyanide species was formed when the signal at 1672 cm^{-1} was present.

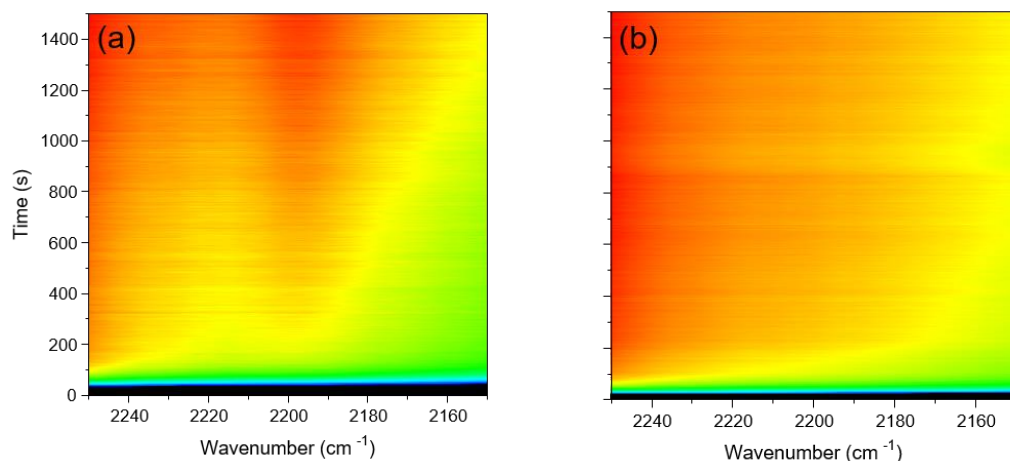


Figure 6.9. Contour plots of the $\nu(\text{C}\equiv\text{N})$ region upon NH_3 addition to $\text{V}_2\text{O}_5/\text{WO}_3\text{-TiO}_2$ pre-equilibrated with (a) formaldehyde and (b) formic acid feeds. Conditions: 150 ppm formaldehyde (or 150 ppm formic acid), 1000 ppm NH_3 and 5 vol% O_2 in Ar_2 .

While the amide products were formed in the presence of either formaldehyde or formic acid, the intense envelope of signals observed with formaldehyde in the region of $1900\text{--}1200\text{ cm}^{-1}$ (Figure 6.2) and the different position of the $\text{C}=\text{O}$ signal of the amide product suggest that the reaction of formaldehyde with NH_3 occurred via a more complex chemistry than oxidation of formaldehyde to formic acid followed by reaction with NH_3 , and that it involved possibly other species. The subsequent reaction to produce cyanides and then HCN may be affected by the source of the amide product. The absence of adsorbed cyanide species in the case of formic acid (Figure 6.8) confirms that formate species are not responsible for the HCN produced by the side reaction of formaldehyde and NH_3 at this temperature (300°C) over $\text{V}_2\text{O}_5/\text{WO}_3\text{-TiO}_2$. Adsorbed amide species can decompose to CO and NH_3 , but no gaseous CO signal was observed in the spectra [155].

6.3.4. Role of VO_x , WO_x , and TiO_2

In previous modulation experiments where SCR was repeatedly turned on and off by pulsing NO in a gas feed containing NH_3 , VO_x and WO_x species exhibited significant contribution to the phase-resolved spectra [38]. In that set of pulses, NH_3 bound to VO_x

was consumed intermittently by NO. WO_x cannot activate NH_3 to perform SCR under the experimental conditions but serves as a reservoir to transfer adsorbed NH_3 to the active sites. These roles of VO_x and WO_x species in SCR caused their signals to be present in the phase-resolved spectra. In contrast, Figure 6.5 shows that while the negative signals of VO_x and WO_x species were visible in the time-resolved spectra during formaldehyde pulsing, they provided only a very weak response in the corresponding phase-resolved spectra (1998 and 1976 cm^{-1}). This stands in contrast with the observation that the weak signal of cyanides in the time-resolved spectra was dominant in the phase-resolved spectra. Hence, the adsorbates accumulating on the catalyst justify the negative signals of VO_x and WO_x in the time-resolved spectra, but neither species is essential in the reaction of formaldehyde with NH_3 , which explains the weak signals in the phase-resolved spectra.

To obtain more insights into this behavior, TiO_2 was also investigated under the same experimental conditions. The resulting spectrum after the reaction on TiO_2 is shown in Figure 6.10a. For comparison, the spectrum obtained in the case of $\text{V}_2\text{O}_5/\text{WO}_3\text{-TiO}_2$ is presented in Figure 6.10b, which is identical to Figure 6.2a. As indicated in Figure 6.3b, similar adsorbed species were obtained on TiO_2 upon flowing formaldehyde and NH_3 at $300\text{ }^\circ\text{C}$. However, the removal of formaldehyde from the feed did not result in appreciable changes, hinting that the adsorbates are more stable on TiO_2 than on $\text{V}_2\text{O}_5/\text{WO}_3\text{-TiO}_2$. The major carbonyl product produced by TiO_2 was most probably an amide but as the corresponding peak was rather broad, the presence of other carbonyl compounds cannot be discarded. Other notable features present in Figure 6.10 include formate species and the negative peak at 1378 cm^{-1} , which originates from the interaction of sulfate groups present in the commercial TiO_2 material with NH_3 . At high frequency, the characteristic hydroxyl groups of TiO_2 at 3705 , 3668 and 3633 cm^{-1} were consumed by the presence of the adsorbates. A signal centered at 2215 cm^{-1} also appeared, which can be assigned to cyanide species.

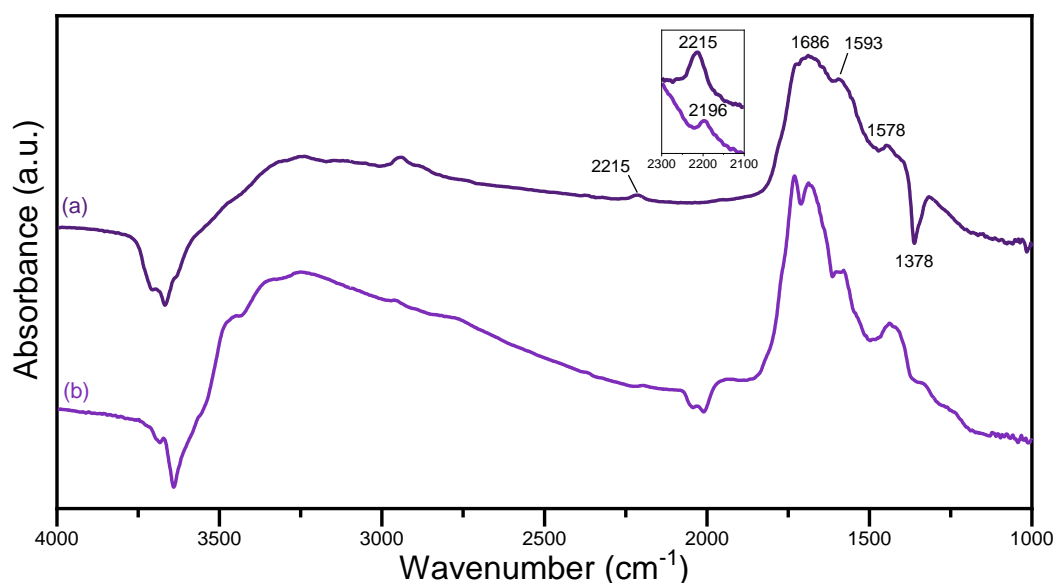


Figure 6.10. DRIFT spectra of (a) TiO_2 and (b) $\text{V}_2\text{O}_5/\text{WO}_3\text{-TiO}_2$ after formaldehyde + NH_3 reaction at 300 °C. Experimental conditions: 150 ppm formaldehyde, 1000 ppm NH_3 and 5 vol% O_2 in Ar,

Figure 6.11 displays the region that we attribute to cyanides in ME experiments with $\text{V}_2\text{O}_5/\text{WO}_3\text{-TiO}_2$ and TiO_2 . Figure 6.11b demonstrates no evident signal for cyanides at 2196 cm^{-1} on TiO_2 that is on the contrary the only detected signal in this region on $\text{V}_2\text{O}_5/\text{WO}_3\text{-TiO}_2$ (Figure 6.11a). The change of baseline giving rise to the evident change in color in the whole region is due to the presence of water entering the cell together with formaldehyde. On TiO_2 , the broad signal centered at 2215 cm^{-1} appeared in the presence of formaldehyde and blue-shifted during the formaldehyde pulse, while it red-shifted after removal of formaldehyde. Only phase-sensitive analysis helped to identify the same signal at 2196 cm^{-1} observed for $\text{V}_2\text{O}_5/\text{WO}_3\text{-TiO}_2$ as shown in Figure 6.11c. On the other hand, Figure 6.11d shows the phase-resolved spectrum ($\varphi^{\text{PSD}} = 130^\circ$) where the signal at 2196 cm^{-1} was maximum and a second one ($\varphi^{\text{PSD}} = 170^\circ$) characterized by a weaker signal at 2215 cm^{-1} and no corresponding signal at 2196 cm^{-1} . The difference in the phase angles suggests that the two signals followed different kinetics. The latter signal likely represents the fraction of species that contributes to the broad signal that shifts in the time-resolved spectra. Hence, the phase-resolved spectra reveal that cyanide species respond to the presence of formaldehyde on both catalysts but that on TiO_2 other species are additionally present aside from the one that contributes to HCN formation. We tentatively assign this

additional species and the signal at 2215 cm^{-1} to a pool of cyanides present on TiO_2 that is absent on $\text{V}_2\text{O}_5/\text{WO}_3\text{-TiO}_2$ because of VO_x and WO_x . At this point, we cannot conclude on the role they play in HCN formation, but VO_x and WO_x species may contribute either to clean the surface from this species or to convert them efficiently into the active cyanide species at 2196 cm^{-1} . The presence of this species on TiO_2 could also be related to the lower reactivity of the signals below 1800 cm^{-1} compared to $\text{V}_2\text{O}_5/\text{WO}_3\text{-TiO}_2$ as shown in Figure 6.3.

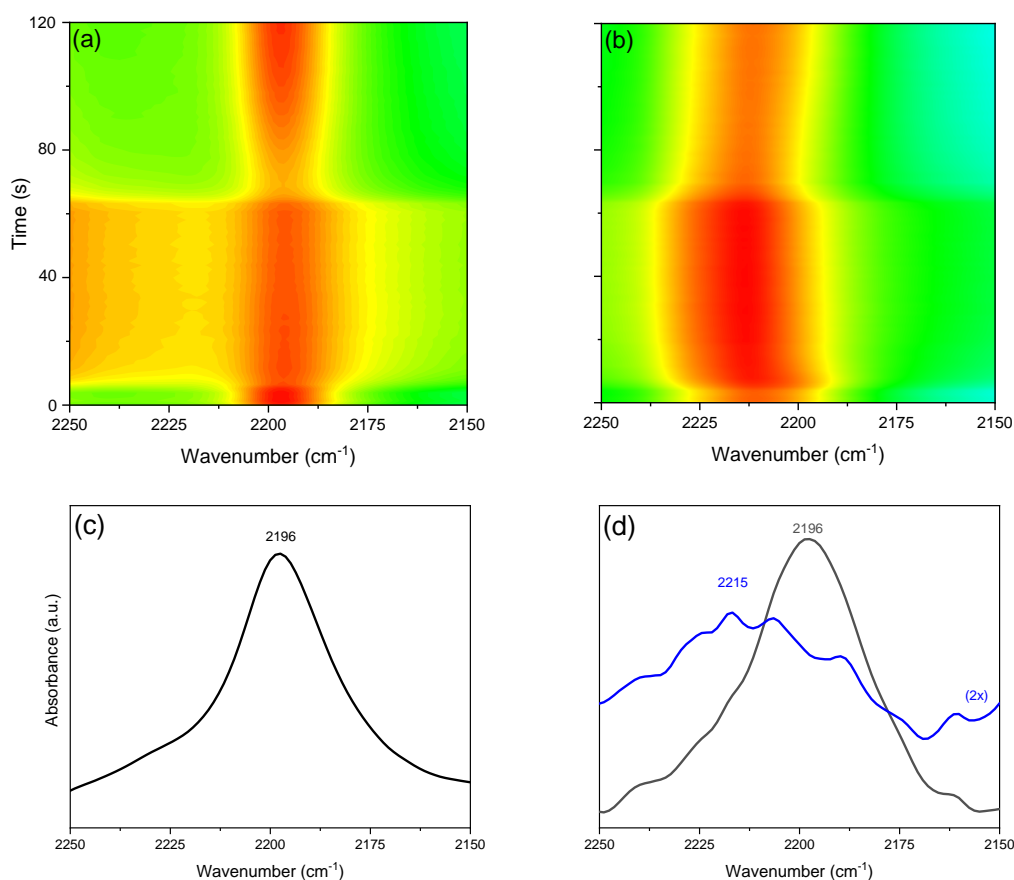


Figure 6.11. Time-resolved DRIFT spectra around the $\nu(\text{C}\equiv\text{N})$ signal during alternated pulses of 150 ppm formaldehyde in a gas feed containing 1000 ppm NH_3 and 5 vol% O_2 in Ar at $300\text{ }^\circ\text{C}$ on (a) $\text{V}_2\text{O}_5/\text{WO}_3\text{-TiO}_2$ and (b) TiO_2 . Selected phase-resolved spectra are shown for (c) $\text{V}_2\text{O}_5/\text{WO}_3\text{-TiO}_2$ ($\varphi^{PSD} = 200^\circ$) and (d) TiO_2 ($\varphi^{PSD} = 130$ and 170°).

The different behavior of TiO_2 with respect to adsorbed cyanides is also mirrored by the different response of the hydroxyl groups of the two materials that is visible in Figure 6.10. While the hydroxyl groups of TiO_2 were perturbed by the adsorbates, in $\text{V}_2\text{O}_5/\text{WO}_3\text{-TiO}_2$

the even larger negative signal of hydroxyl groups at 3639 cm^{-1} suggests the blockage of the TiO_2 surface by VO_x and WO_x groups, thus reducing the contribution of TiO_2 to the observed chemistry. VO_x and WO_x provide additional sites, which activate the adsorbates differently. Hence, while the presence of VO_x and WO_x was not needed to produce cyanides, they nonetheless functioned to prevent formation of stable amide and cyanide species in favor of intermediates that can be ultimately converted into HCN.

6.3.5. Proposed reaction pathway

Figure 6.12 shows the proposed reaction pathway of HCN formation over $\text{V}_2\text{O}_5/\text{WO}_3\text{-TiO}_2$. When formaldehyde adsorbs onto the catalyst, it can readily transform into formate species due to the oxidizing atmosphere of the gas feed, as verified by the IR experiments (Figure 6.1). It can then be oxidized further to CO and CO_2 , with the former being the major product of formaldehyde oxidation. However, not all formaldehyde is oxidized, and some of it can still react with other exhaust gas components, particularly NH_3 .

The carbonyl carbon of formaldehyde is susceptible to nucleophilic attack by NH_3 . This step yields methanolamine and is analogous to the reaction of aldehydes with water to form a geminal-diol or with an alcohol to form a hemiacetal [174-176]. Methanolamine was not detected probably due to its transient behavior under reaction conditions (i.e., it is produced and consumed very quickly) or the absence of unique IR signatures.

Methanolamine can undergo oxidative dehydration, which requires at least a mild oxidation catalyst. Because of the excess O_2 in the feed and the fact that VO_x supported on TiO_2 possesses oxidation activity, methanolamine can easily transform into formamide, which was detected by virtue of the carbonyl peak at 1686 cm^{-1} (Figure 6.2).

Finally, formamide dehydrates to form HCN in an endothermic reaction ($\Delta_r H^\circ = 140\text{ kJ}\cdot\text{mol}^{-1}$). This reaction pathway is in agreement with the high levels of HCN observed as the temperature was increased (Figure 5.4).

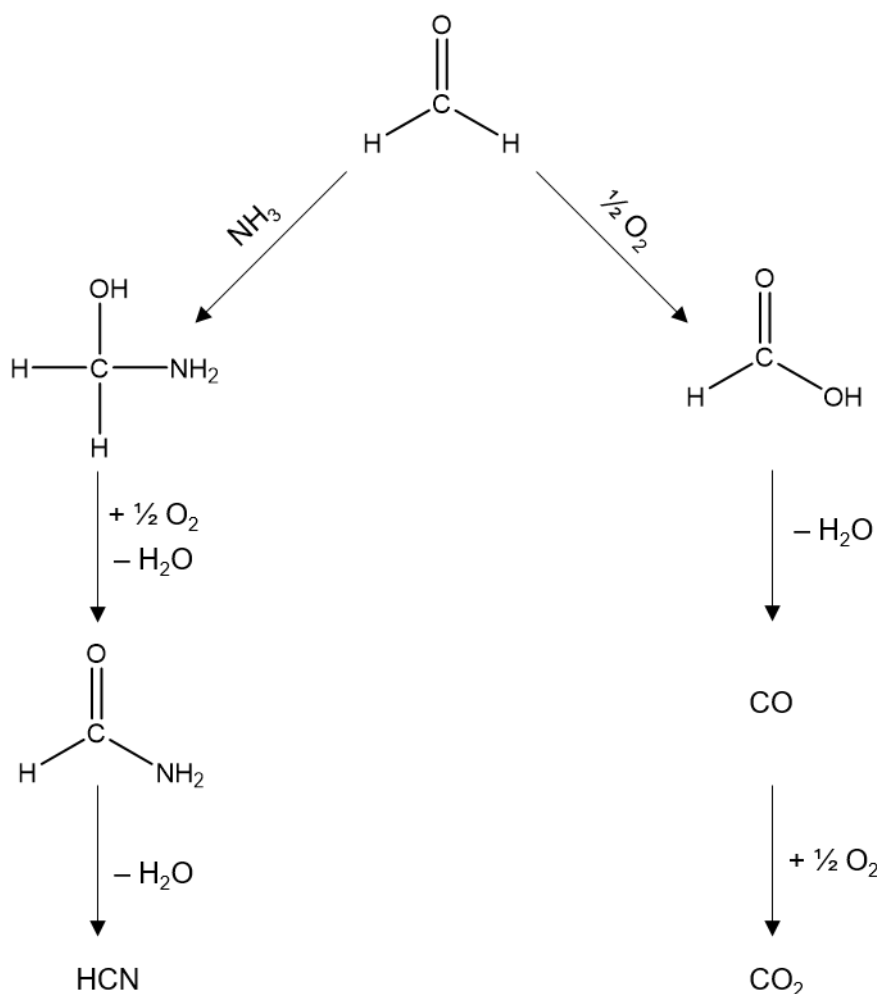


Figure 6.12. Proposed reaction pathway of HCN formation.

6.4. Conclusions

In this work, we used operando DRIFT spectroscopy to study the transformations that formaldehyde and NH_3 undergo on $\text{V}_2\text{O}_5/\text{WO}_3\text{-TiO}_2$ and TiO_2 and their contribution to the formation of HCN. Formaldehyde reacts from the gas phase with pre-adsorbed NH_3 to form amide species, and eventually HCN. For the first time, we reported the observation of adsorbed cyanide species that are related to the gas-phase product, and are strongly affected by the presence of the reactants. The adsorbed formate species are not responsible for the formation of the cyanide species under the investigated conditions. TiO_2 alone is already active for the side reaction, but VO_x and/or WO_x sites promote the reaction by preventing the formation of unreactive amides and cyanides.

Chapter 7 – NH₃-Mediated Inhibition of the SCR Reaction over Cu-SSZ-13 at Low Temperature

7.1. Introduction

While vanadia-based materials remain to be the preferred option for stationary SCR installations, Cu-based zeolites have become the catalyst of choice for mobile SCR applications in recent years. Cu-SSZ-13 in particular has emerged to be a commercial solution because of its unparalleled activity at low temperature and high thermal stability, making it well suited for the dynamic temperature changes encountered during vehicle operation. Isolated single-atom Cu sites have been identified as the active centers for the SCR reaction [177]. The presence of NH₃ solvates these species to form highly mobile complexes, which can travel to the neighboring cages in the framework [178, 179]. These amminated complexes are very stable at low temperature and could represent a bottleneck in the reaction cycle [53, 55]. In this operando study, the inhibitory effect of NH₃ was investigated in more detail by varying the reductant dosage as well as the temperature.

7.2. Materials and methods

7.2.1. Materials synthesis

Cu-SSZ-13 (1.6 wt% Cu; Si/Al = 14.4) was prepared by hydrothermal synthesis followed by ion exchange, according to a previously published procedure [55]. A gel with a molar composition of 10 parts trimethyladamantyl ammonium hydroxide (TMAda), 10 parts sodium hydroxide (NaOH), 4 parts alumina (Al₂O₃), 100 parts silica (SiO₂), and 2,200 parts water was prepared by mixing sufficient amounts of NaOH pellets (98%; Sigma-Aldrich), 80 mL of water, 20 mL of aqueous TMAda solution (25%; Sachem), and then adding the required amount of Al₂O₃ (Sigma-Aldrich) and fumed SiO₂ (Sigma-Aldrich). The gel was aged at room temperature for 2 h, transferred into a stirred autoclave, and treated hydrothermally at 160 °C for 120 h. After washing with acetone and water, the powder was

dried at 120 °C for 12 h and calcined at 575 °C for 8 h. The solid was then ion-exchanged three times with an excess of 1 M ammonium nitrate (98%; Sigma-Aldrich) solution and calcined at 500 °C for 2 h. Finally, the zeolite was ion-exchanged with 0.1 M copper sulfate (98%; Sigma-Aldrich) solution at 80 °C for 4 h, dried at 120 °C for 12 h, and calcined at 600 °C for 4 h.

7.2.2. Operando X-ray absorption spectroscopy (XAS)

Approximately 25 mg of Cu-SSZ-13 were loaded into a custom-built spectroscopic cell [91, 180], fixed between quartz wool plugs, and sealed with 20- μm graphite windows. This system ensures sufficient X-ray transmission in an airtight environment. Prior to the experiment, the sample was dried at 400 °C for 1 h under 5 vol% O_2 in Ar.

Cut-off experiments were performed by removing NH_3 from a gas feed containing 500-2000 ppm NH_3 , 1000 ppm NO , 0-2 vol% H_2O , and 5 vol% O_2 balanced in Ar. Water was generated in situ from the reaction of H_2 and O_2 through a monolithic $\text{Pt}/\text{Al}_2\text{O}_3$ catalyst. The total flow was fixed at 100 $\text{mL}\cdot\text{min}^{-1}$.

An OmniStar GSD 320 mass spectrometer (Pfeiffer) was connected at the outlet of the cell to monitor $m/z = 17$ (NH_3), 18 (H_2O), 28 (N_2), 30 (NO), 32 (O_2), and Ar (40).

Time-resolved XAS spectra were measured at 1 Hz at the Cu K-edge (8.9789 keV) in transmission mode using N_2 -filled ionization chambers at the SuperXAS beamline of the Swiss Light Source. A Cu reference foil was measured simultaneously for energy calibration.

The spectra were extracted, normalized, averaged, and post-processed using the ProQEXAFS software [181]. Linear combination fitting (LCF) was performed in the X-ray absorption near edge structure (XANES) region between the energy range of 8950.0 and 9050.0 eV using spectral components that were obtained from multivariate curve resolution (MCR). The analysis was performed under the constraints that the concentrations cannot be negative and that the sum of all the components should be equal to unity.

7.3. Results and discussion

Figure 7.1 shows the NO conversion at 200 °C and 300 °C at different NH_3 concentrations. At 200 °C and equimolar NH_3 :NO concentration, the conversion was 36%, which decreased to 32% upon cutting the NH_3 dosage by half. When the NH_3 :NO ratio was increased to 2:1, the NO conversion decreased significantly to 16% even if there were theoretically more reductant available to react. Hence, this highlights the inhibitory effect of NH_3 on the SCR reaction at 200 °C. At a higher temperature (300 °C), the NO conversion increased as the NH_3 concentration was increased, illustrating that more NH_3 was needed to sustain the improved SCR activity. At equimolar NH_3 :NO concentration, the NO conversion was 66%, which improved marginally to 70% upon doubling the NH_3 dosage. However, the conversion was notably low at 40% under suboptimum NH_3 concentration. Therefore, the NH_3 inhibition effect was less pronounced, if not non-existent, in the high temperature regime.

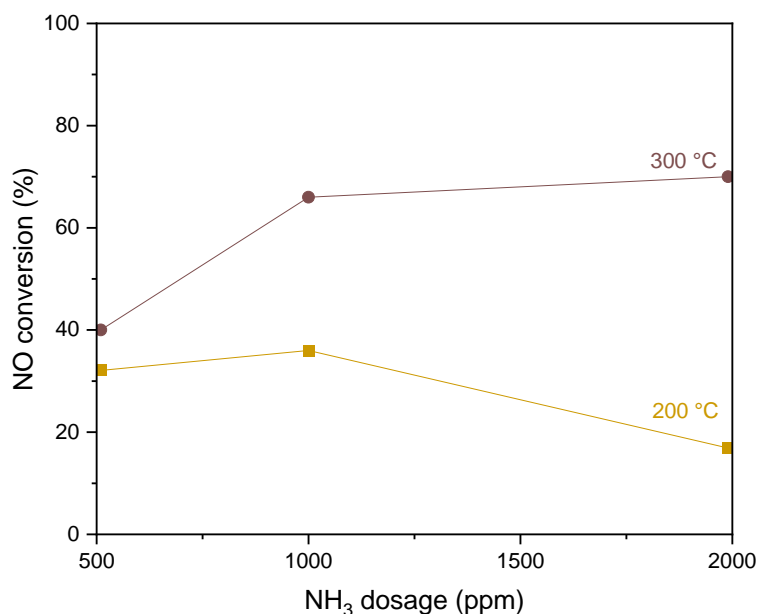


Figure 7.1. Steady-state NO conversion over Cu-SSZ-13 at 200 °C and 300 °C as a function of the NH_3 dosage. Experimental conditions: 500-2000 ppm NH_3 , 1000 ppm NO, and 5 vol% O_2 balanced in Ar.

To rationalize the effect of NH_3 on the inhibition at 200 °C, the Cu speciation of the catalyst was followed by time-resolved XAS. Figure 7.2 shows the spectra of the MCR-derived Cu components, which were used as standards in the LCF analysis. These five species represent the most probable coordination and oxidation states that the Cu species adopt under SCR conditions. $\text{Cu(II)(NO}_x)_y$ denotes oxidized Cu bound to either nitrate or nitrite species as the spectral difference between the two is negligible, particularly in the XANES region [55, 182]. $\text{Cu(I)(NH}_3)_2$ represents the linear, solvated form of the reduced Cu species, whose spectrum is marked by a strong pre-edge feature arising from the $1s \rightarrow 4p$ transition at 8982.8 eV [183-186]. Cu(II)-Z designates the coordinatively free, fully oxidized Cu species, which are characterized by a weak pre-edge peak at 8977.8 eV due to the $1s \rightarrow 3d$ transition in their spectra [187-189]. Cu(I)-Z denotes the reduced species interacting directly with the zeolite framework. Similar to that of $\text{Cu(I)(NH}_3)_2$, its spectrum contains a sharp pre-edge but was blue-shifted to 8983.3 eV since this feature is strongly dependent on the coordination environment [190, 191]. Finally, $\text{Cu(II)(NH}_3)_4$ represents the four-fold coordinated Cu(II) species in a square planar configuration [192].

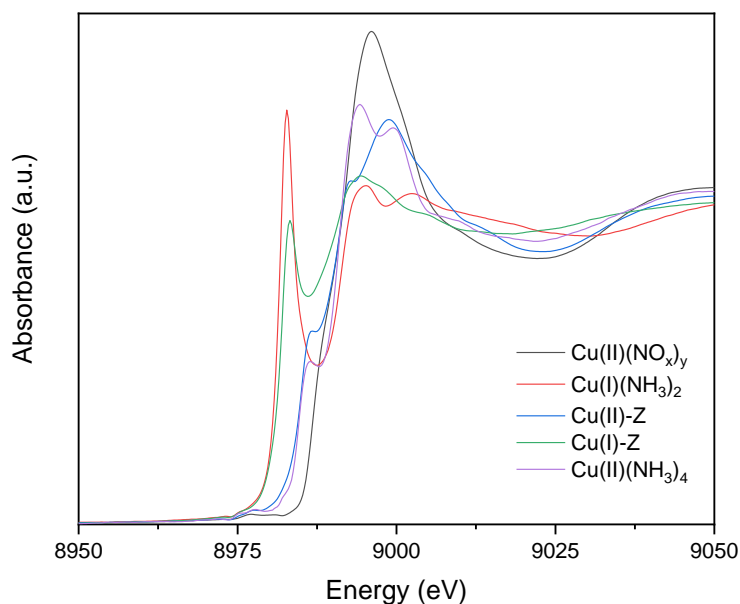


Figure 7.2. Reference spectra of different Cu species derived from MCR.

It is important to note that the solvated species $\text{Cu(I)(NH}_3)_2$ and $\text{Cu(II)(NH}_3)_4$ may not be limited to purely ammine complexes as the XANES spectra of species having mixed or different ligands (most notably nitrates) may not significantly differ [193, 194]. However, these labels would be used throughout the text for the sake of simplicity.

The XANES spectrum of Cu-SSZ-13 after activation under O_2 resembles that of Cu(II)-Z (Figure S-7.1), ensuring that the catalyst was fully oxidized prior to the start of the experiment. After equilibration of the catalyst at 200 °C under SCR with varying dosages on NH_3 , the XANES changed significantly (Figure 7.3), implying that the Cu species adopted different oxidation states and coordination environments (Figure 7.4).

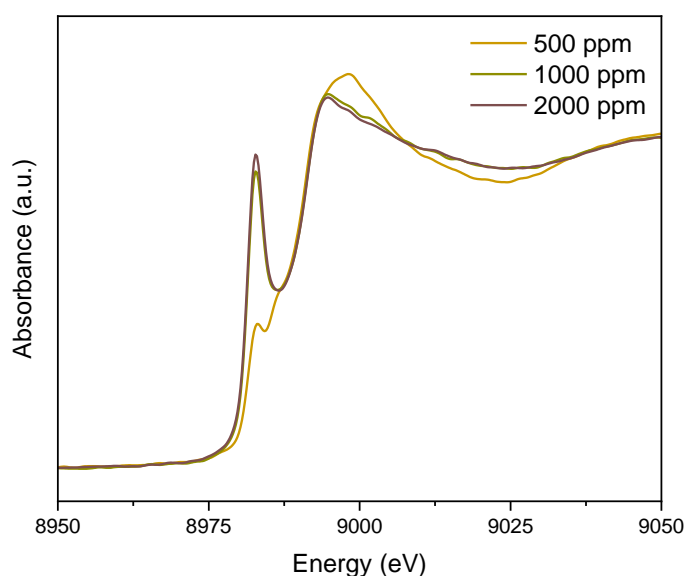


Figure 7.3. Steady-state XANES of Cu-SSZ-13 under SCR conditions at 200 °C. Experimental conditions: 500-2000 ppm NH_3 , 1000 ppm NO , and 5 vol% O_2 balanced in Ar.

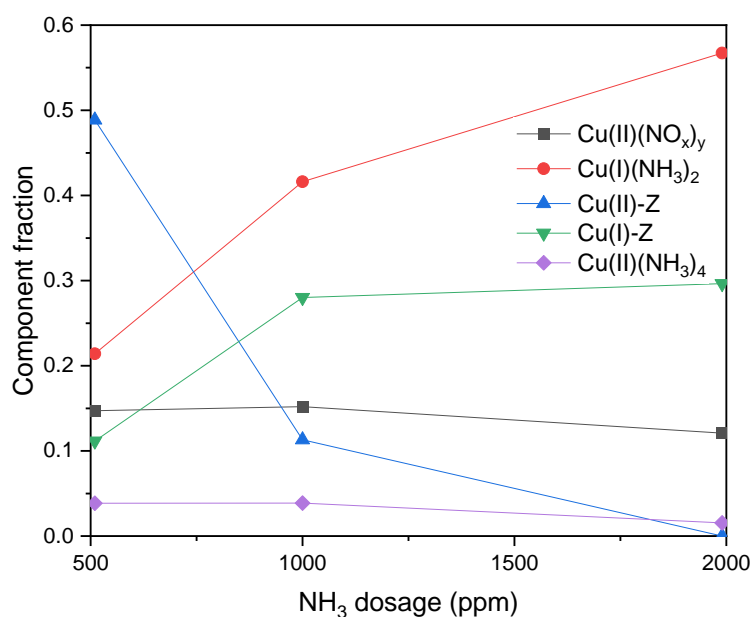


Figure 7.4. Steady-state Cu speciation of Cu-SSZ-13 under SCR conditions at 200 °C. The summed Cu(I) and Cu(II) fractions are given in Figure S-7.2. Experimental conditions: 500-2000 ppm NH₃, 1000 ppm NO, and 5 vol% O₂ balanced in Ar.

As the NH₃ dosage increased from 500 to 2000 ppm, the Cu(I)(NH₃)₂ fraction increased from 21 to 57%, demonstrating the reducing power of NH₃ and the relative ease by which it forms a complex with Cu sites. This is accompanied by the initial increase of Cu(I) sites, which levelled off and did not increase significantly between 1000 and 2000 ppm NH₃. Correspondingly, the Cu(II)-Z species decreased from 49 to almost 0% in the same concentration regime, indicating that the solvation of the Cu sites predominate at low temperature and that such complexes are stable. In contrast, Cu(II)(NO_x)_y and Cu(II)(NH₃)₄ were not as strongly affected by the NH₃ concentration as the other species. However, it is interesting to point out that the Cu(II)(NH₃)₄ fraction remained constant at 4% from 500 to 1000 ppm but decreased to 1% at 2000 ppm NH₃. While amminated species in general should be favored by the presence of gas-phase NH₃, the reducing atmosphere brought about by excess NH₃ and the concurrent SCR reaction likely converted the square planar Cu(II)(NH₃)₄ into linear Cu(I)(NH₃)₂ species.

The time-resolved XAS experiments give more detailed insights into the NH_3 inhibition effect. Figure 7.5 shows the changes in the Cu speciation and the corresponding MS data upon cutting off 2000 ppm NH_3 at 200 °C. The NO concentration promptly decreased upon removal of NH_3 , reaching as low as 480 ppm – a marked improvement from the steady-state value of 840 ppm (Figure 7.5b). This translates to more than a threefold improvement in the NO conversion. From the point of view of XAS, the NH_3 cut-off was accompanied by the rapid decrease of $\text{Cu(I)(NH}_3)_2$ species (Figure 7.5a), which is an unavoidable consequence of the loss of ligands that reacted with NO and could no longer be replenished from the gas phase. This species practically vanished after 600 s, and its disappearance was accompanied by the continuous increase of the NO concentration, suggesting the termination of the SCR reaction.

Simultaneous to the decrease of $\text{Cu(I)(NH}_3)_2$, the fraction of $\text{Cu(II)(NH}_3)_4$, increased, further proving that NH_3 inhibits the reaction by keeping the reaction stuck at the reductive half-cycle. The increase of $\text{Cu(II)(NH}_3)_4$ was just transient and stopped at 150 s (i.e., 90 s after NH_3 removal) before disappearing at 250 s. This is also the time when the NO conversion was starting to reach its maximum value. Hence, this confirms that the $\text{Cu(II)(NH}_3)_4$ species is a relevant intermediate for SCR.

Cu(II)-Z started to increase already upon NH_3 removal, but it levelled off between 200 and 280 s, at which point the $\text{Cu(II)(NH}_3)_4$ species underwent its decline. Then, the Cu(II)-Z species started to increase again and eventually reached 76% due to the net oxidizing effect of the gas feed (NO and O_2).

The aforementioned discussions can be explained in the context of the generally accepted SCR reaction cycle as shown in Figure 1.2. At the start of the experiment, the excess NH_3 in the gas phase forces most of the Cu species to be locked into the $\text{Cu(I)(NH}_3)_2$ state. The continued NO conversion as well as the presence of other Cu species along the SCR cycle prove that the SCR reaction was still taking place anyway, but that it was not optimum. As soon as NH_3 was removed, the Cu species under less reducing atmosphere became free to convert from $\text{Cu(I)(NH}_3)_2$ into Cu(II)-Z and $\text{Cu(II)(NH}_3)_4$ – both of which are oxidized

forms of Cu and populate the oxidation half of the reaction. The transient accumulation of $\text{Cu(II)(NH}_3)_4$ points out that it also served as the bottleneck of the reaction cycle for a short time, most probably due to its stability at low temperature.

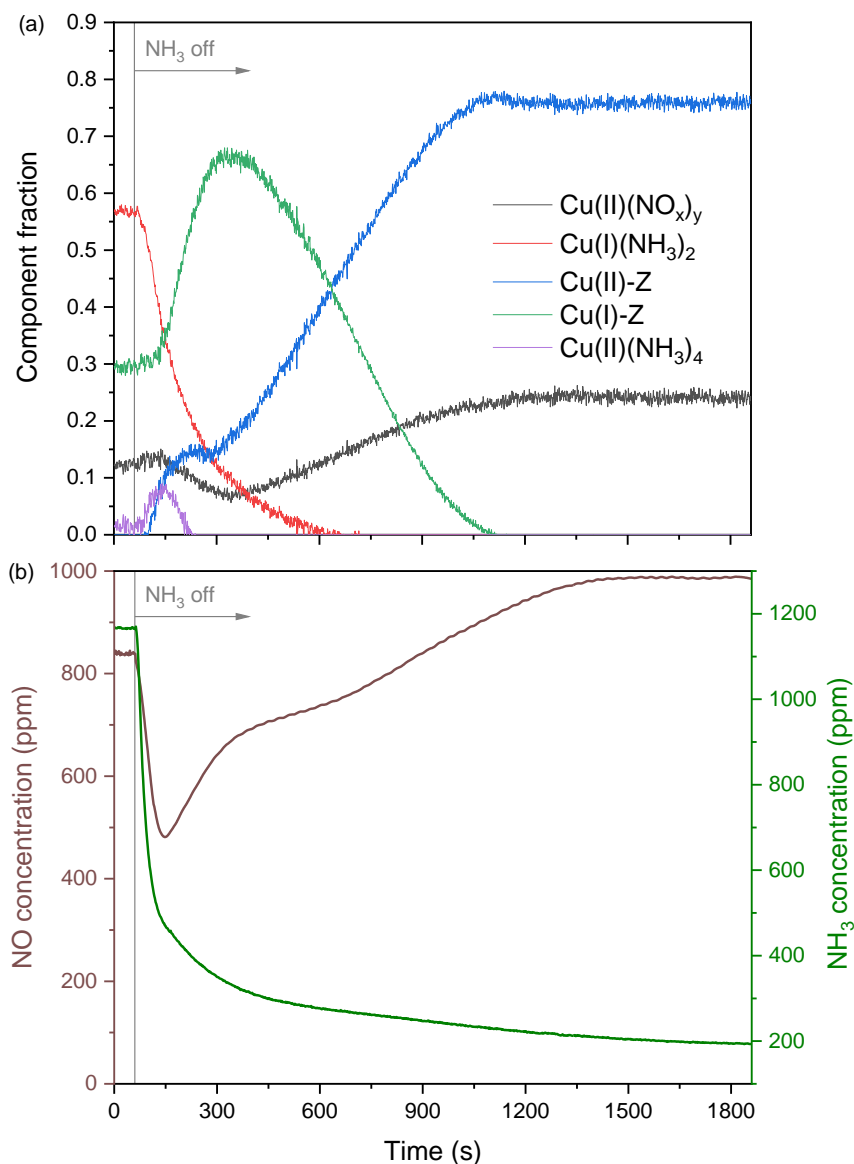


Figure 7.5. Time-resolved (a) Cu speciation of Cu-SSZ-13 and (b) NO and NH_3 concentrations under SCR conditions upon cut-off of 2000 ppm NH_3 at 200 °C. The summed Cu(I) and Cu(II) fractions are given in Figure S-7.3. Experimental conditions: 2000 ppm NH_3 , 1000 ppm NO, and 5 vol% O_2 balanced in Ar.

At around the time that $\text{Cu(II)(NH}_3)_4$ started to decrease at 150 s, the Cu(I)-Z fraction started to increase, eventually reaching a maximum value of 68% between 330 and 350 s. The reoxidation of Cu(I) is recognized as the rate-determining step of SCR [54]. Indeed, the ability of Cu-based catalysts to oxidize NO to NO_2 helps in this slow step because NO_2 is a stronger oxidant than the excess O_2 in the feed [195, 196]. Therefore, under optimum or sub-optimum NH_3 dosage, the Cu species are arrested in the Cu(I)-Z state as they have to be oxidized first before they can proceed through the SCR cycle. This explains the prominence of the Cu(I)-Z species more than 250 s after NH_3 cut-off. If there were no NH_3 inhibition, then the Cu(I)-Z species would have increased much sooner since there would be less species locked at the $\text{Cu(I)(NH}_3)_2$ state. After it reached its maximum, Cu(I)-Z declined slowly and then ceased to exist at around 1120 s, signaling the complete extinction of adsorbed NH_3 and the cessation of the SCR reaction, as also indicated by the MS data.

In contrast to the four other Cu species, $\text{Cu(II)(NO}_x)_y$ underwent only minor changes. It initially decreased in favor of Cu(II)-Z and Cu(I)-Z but eventually increased again due to the simultaneous presence of NO and O_2 .

Figure 7.6 shows the cut-off experiment at 200 °C for 1000 ppm NH_3 . The general behavior of the system stayed essentially the same, but it reached equilibrium much faster. There was also a transient increase in the NO conversion, but it was only 1.6 times that of the steady-state value prior to NH_3 cut-off.

In contrast, the sub-stoichiometric dosing of NH_3 changed the Cu speciation significantly (Figure 7.7). In particular, the transient increase of $\text{Cu(II)(NH}_3)_4$ was not observed, owing to the deficit of available NH_3 . Instead, Cu(I)-Z increased immediately upon NH_3 cut-off, suggesting that the system was not hindered at any of the solvated states. The NO conversion also increased, but only 1.3 times relative to the steady-state value and hence lower than in the two previous cases.

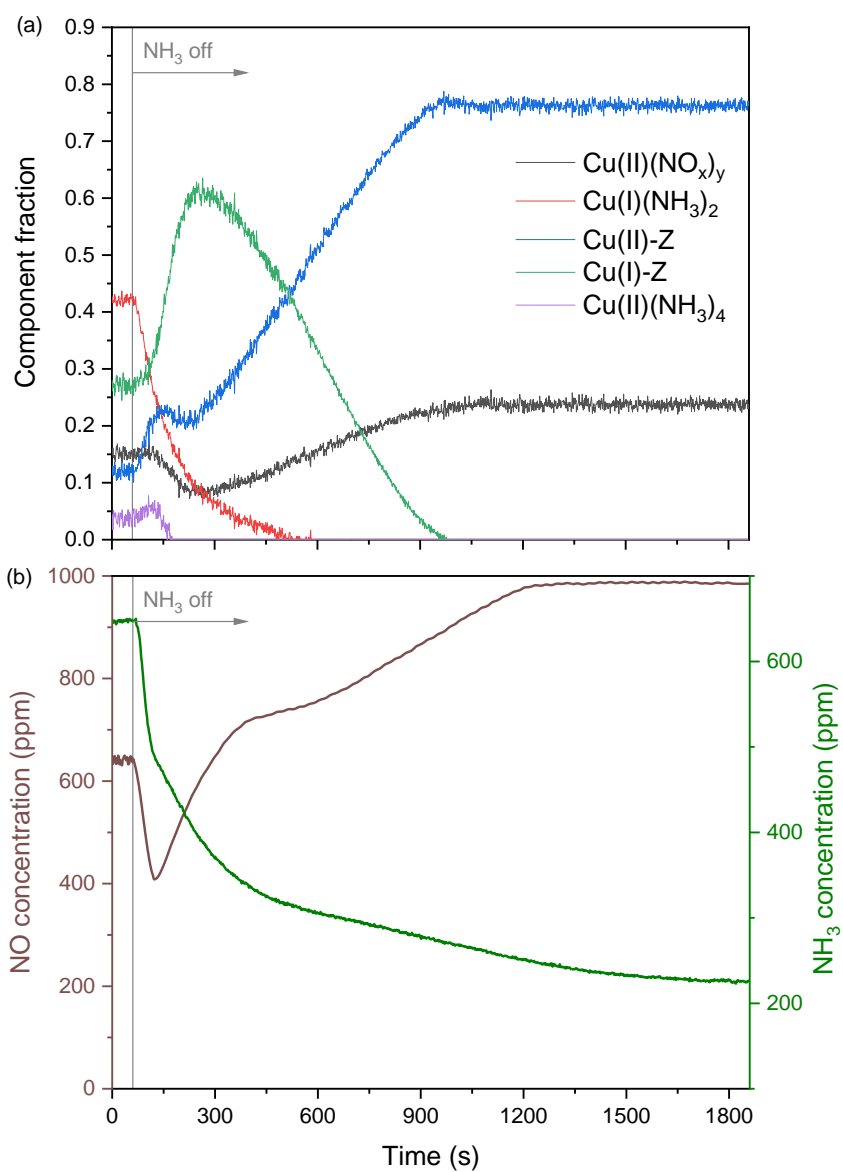


Figure 7.6. Time-resolved (a) Cu speciation of Cu-SSZ-13 and (b) NO and NH₃ concentrations under SCR conditions upon cut-off of 1000 ppm NH₃ at 200 °C. The summed Cu(I) and Cu(II) fractions are given in Figure S-7.4. Experimental conditions: 1000 ppm NH₃, 1000 ppm NO, and 5 vol% O₂ balanced in Ar.

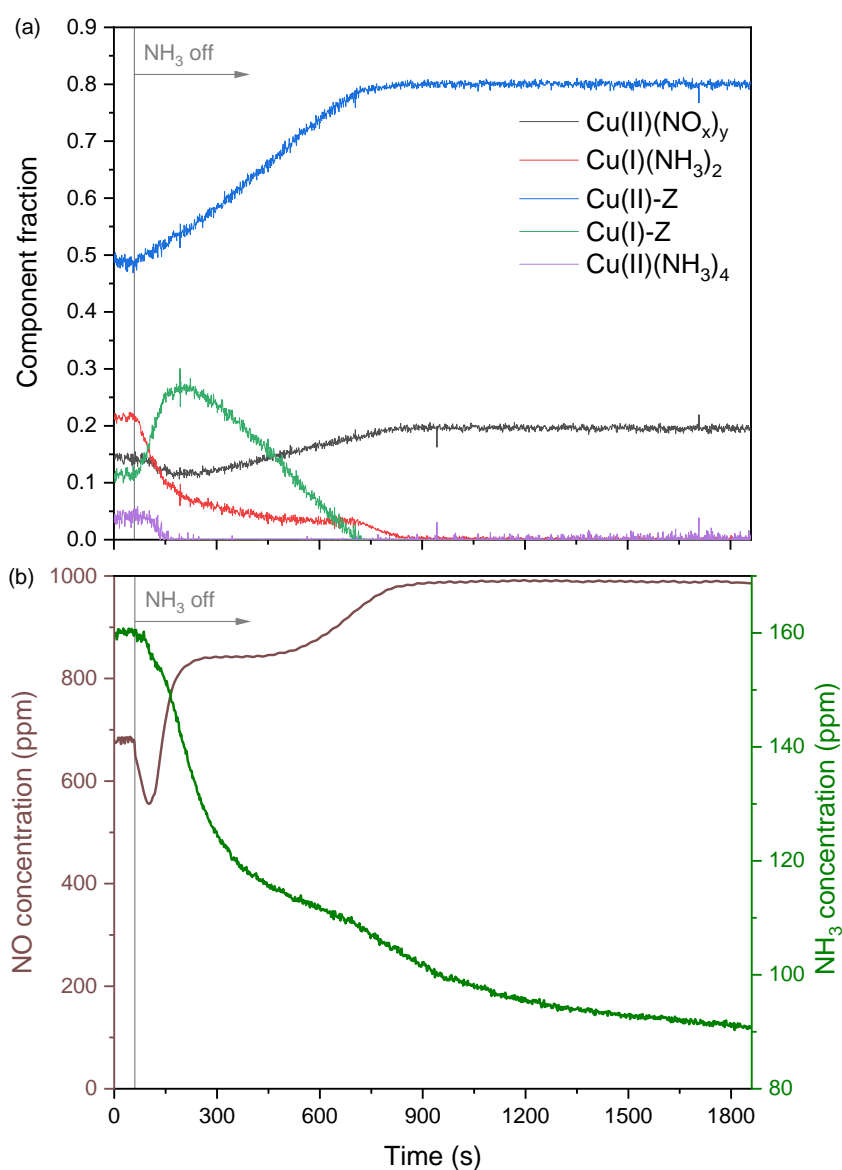


Figure 7.7. Time-resolved (a) Cu speciation of Cu-SSZ-13 and (b) NO and NH_3 concentrations under SCR conditions upon cut-off of 500 ppm NH_3 at 200 °C. The summed Cu(I) and Cu(II) fractions are given in Figure S-7.5. Experimental conditions: 500 ppm NH_3 , 1000 ppm NO, and 5 vol% O_2 balanced in Ar.

A detailed comparison of the Cu(I)-Z fractions is given in Figure S-7.6. The length of delay before the onset of Cu(I) increase and the maximum fraction it reached are both related to the degree of the inhibition and by extension the improvement in the SCR activity upon NH_3 removal. The evolution of the Cu(II)-Z species varied as well across the different

concentration regimes (Figure S-7.7). While the increase in Cu(II)-Z appeared to be a multi-step process under equimolar and excess NH_3 conditions, it was decisively a one-stage event in the case of sub-stoichiometric dosing. The transient pause of Cu(II)-Z increase at higher NH_3 concentration could be a consequence of the formation of $\text{Cu(II)(NH}_3)_4$, which was not observed considerably at 500 ppm NH_3 .

The same NH_3 cut-off experiments were performed at 300 °C, a temperature at which there should be considerably less NH_3 inhibition, if at all, as suggested by Figure 7.1. A summary of the steady-state speciation is presented in Figure 7.8. The most obvious difference is the small percentage of amminated species. As an illustration, the $\text{Cu(I)(NH}_3)_2$ species under 500 ppm NH_3 was represented by only 2% of the population at 300 °C whereas it accounted for 21% at 200 °C. This is already suggestive of less inhibition at elevated temperatures. Cu(I)-Z increased from 500 to 1000 ppm, but decreased significantly at 2000 ppm NH_3 , which might suggest its transformation into solvated species. The Cu(II)-Z, Cu(II)(NH_3)₄, and Cu(NO_x)_y fractions followed the same behavior as in the low-temperature region.

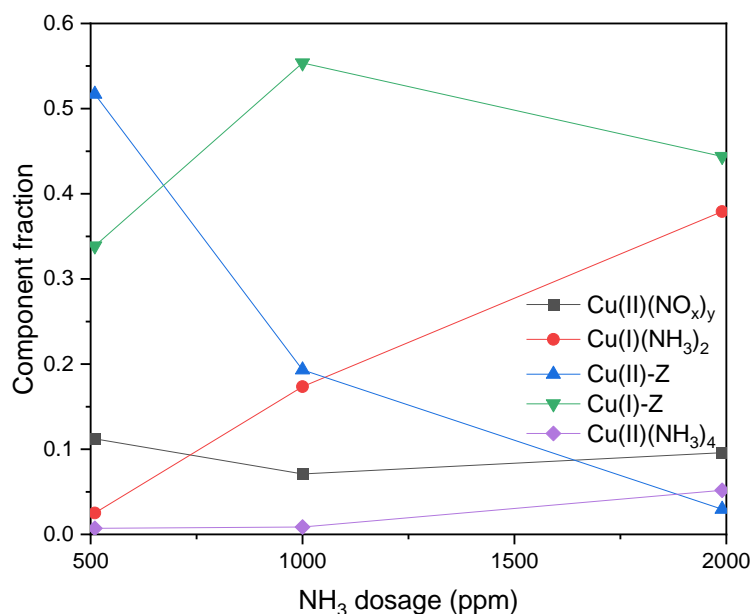


Figure 7.8. Steady-state Cu speciation of Cu-SSZ-13 under SCR conditions at 200 °C. The summed Cu(I) and Cu(II) fractions are given in Figure S-7.8. Experimental conditions: 500-2000 ppm NH_3 , 1000 ppm NO , and 5 vol% O_2 balanced in Ar.

The results of the 2000-ppm NH_3 cut-off experiment at 300 °C are presented in Figure 7.9. There was no transient increase in the NO conversion upon NH_3 removal; on the contrary, the NO level increased immediately. This further proves the absence of inhibition at higher temperatures.

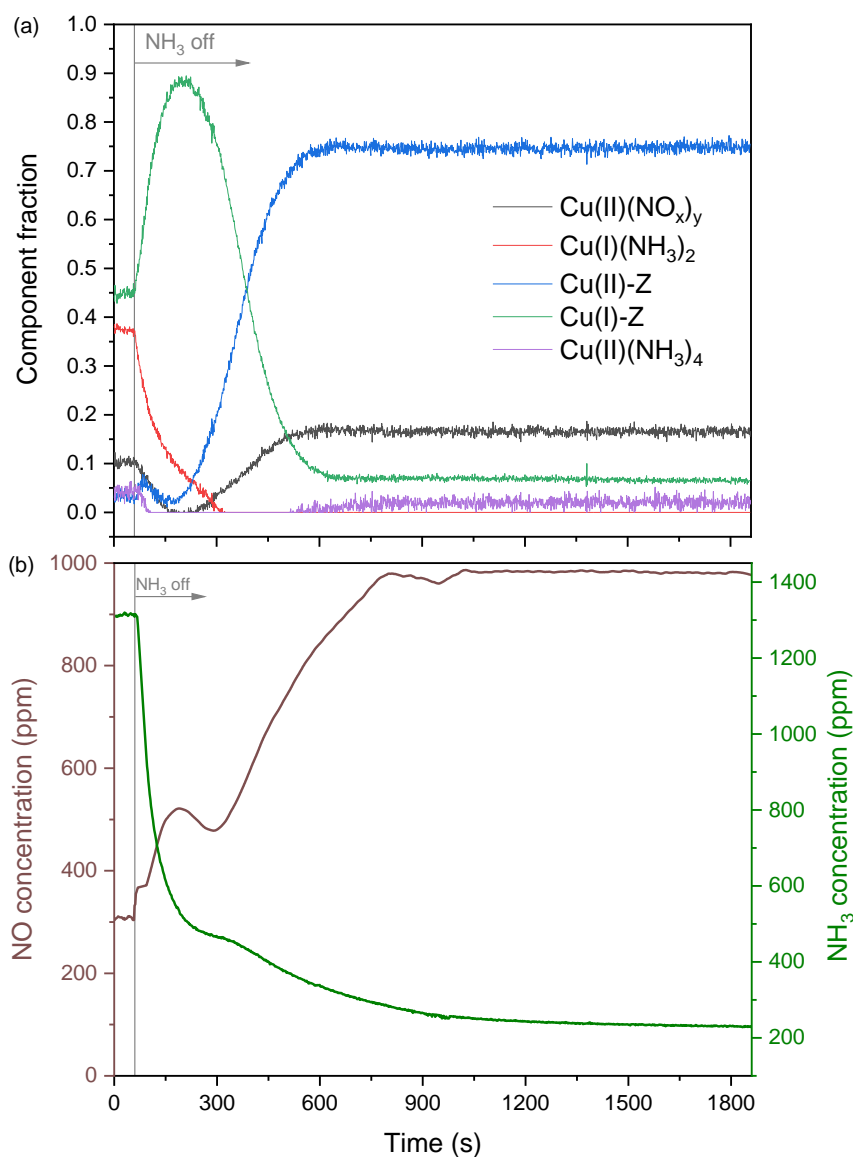


Figure 7.9. Time-resolved (a) Cu speciation of Cu-SSZ-13 and (b) NO and NH_3 concentrations under SCR conditions upon cut-off of 2000 ppm NH_3 at 300 °C. The summed Cu(I) and Cu(II) fractions are given in Figure S-7.9. Experimental conditions: 2000 ppm NH_3 , 1000 ppm NO, and 5 vol% O_2 balanced in Ar.

At around 250 s, there was a dip in the NO level, which we tentatively associate to the activation of zeolite-bound NH_3 . The stabilization of the MS signals correlated with that of the XAS.

The sharp decrease of the $\text{Cu(I)(NH}_3)_2$ species was accompanied by the instantaneous increase of Cu(I)-Z. Hence, while most species existed in the $\text{Cu(I)(NH}_3)_2$ state, they could be readily converted into the succeeding species along the reaction cycle, thereby effectively escaping inhibition. This is likely caused by the decreased stability of amminated species at elevated temperatures. Furthermore, the absence of the transient increase of $\text{Cu(II)(NH}_3)_4$ also points out the absence of inhibition under these conditions. Once the adsorbed NH_3 was consumed and the SCR reaction stopped, all the Cu species were in the Cu(II)-Z and $\text{Cu(NO}_x)_y$ states.

The results of these measurements are useful from a fundamental point of view as they permit the visualization of the specific steps in the SCR catalytic cycle by means of monitoring the fraction of the Cu species. In the temperature range studied (200-300 °C), the oxidation of Cu(I) into Cu(II) remains the rate-determining step of the reaction. However, when excess NH_3 is present, then the Cu species accumulate as $\text{Cu(I)(NH}_3)_2$, which is very stable at 200 °C that NH_3 inhibition occurs. In other words, the cycle is not just slowed down by the reoxidation of Cu(I)-Z but also by the conversion of $\text{Cu(I)(NH}_3)_2$ into Cu(I)-Z. The transient increase of $\text{Cu(II)(NH}_3)_4$ under stoichiometric or excess NH_3 conditions also corroborates the low-temperature stability of the complex. Fortunately, the loss of ligands is favored at higher temperatures so the SCR activity can be preserved. Even if the amminated complexes were formed significantly at 300 °C, they can be converted quite readily so the bottleneck would be solely the $\text{Cu(I)} \rightarrow \text{Cu(II)}$ transition.

The main advantage of Cu-based catalysts is their unsurpassed NO_x conversion at low temperature, which is of utmost importance in automobile applications (e.g., during cold start-up of vehicles when the exhaust is not yet sufficiently hot). Therefore, the optimum NH_3 dosage should be delivered from the very start to maximize the catalyst performance. This cannot be emphasized enough, as many studies in the literature gauge the catalytic

activity under equimolar concentration of NH_3 and NO [47, 52, 177, 197-199]. Although this practice is convenient, it can massively underestimate the low-temperature capability of the catalyst under investigation, especially if it has a high NH_3 storage capacity like zeolites and zeolite-like materials. A more practice-oriented protocol would be to measure the NO conversion at 10 ppm NH_3 slip [148].

While excess NH_3 is detrimental for low-temperature SCR, it is still nonetheless needed for the process to take place. Figure 7.6b and Figure 7.7b show that the transient increase in NO_x conversion upon NH_3 removal peaks at around 50 s; beyond which, the NH_3 coverage is no longer optimal and the over-all performance decreases. Therefore, it is intuitive that intermittent pulsing of NH_3 could increase the NO_x conversion above the steady-state value. Figure 7.10 shows an experiment where the NH_3 supply was cut off for 10 s every minute (i.e., 10 s of NH_3 off and 50 s of NH_3 on) in sub-stoichiometric conditions (750 ppm NH_3 and 1000 ppm NO). Under static conditions, the NO level was 641 ppm, which corresponds to 36% NO conversion. Intermittent pulsing of NH_3 lead to a marked increase in the catalytic performance with the NO conversion values fluctuating between 43 and 51%, resulting in an average conversion of 46%. This not only corresponds to a 1.3 times increase compared the steady-state conversion value, but also translates to around 17% savings in NH_3 consumption.

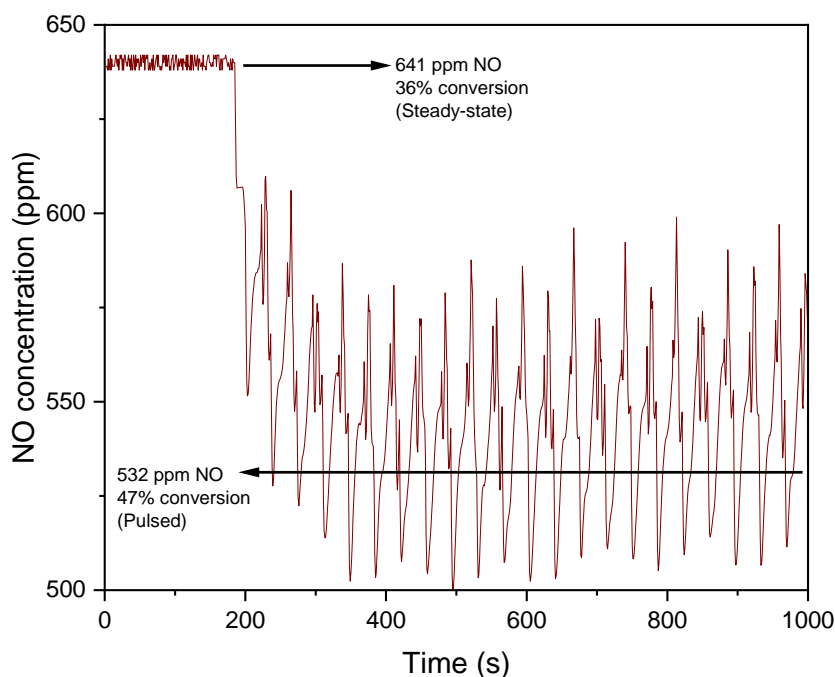


Figure 7.10. NO concentration during steady-state and pulsed operation (10 s NH_3 off and 50 s NH_3 on) at 200 °C. Experimental conditions: 750 ppm NH_3 , 1000 ppm NO, and 5 vol% O_2 balanced in Ar.

7.4. Conclusions

The rate-determining step of the SCR reaction over Cu-SSZ-13 between 200 and 300 °C is the reoxidation of Cu(I)-Z to Cu(II)-Z. However, NH_3 can additionally inhibit the reaction pathway at low temperature by halting the cycle at the linearly solvated $\text{Cu(I)(NH}_3)_2$ state, which is very stable at 200 °C as revealed by time-resolved XAS. Hence, the NO conversion increases transiently upon cutting off NH_3 as the $\text{Cu(I)(NH}_3)_2$ species could be converted further along the cycle. Taking advantage of this molecular information, we were able to increase the NO conversion by up to 30% through the intermittent introduction of NH_3 .

Chapter 8 – Conclusions and Outlook

The primary goal of the thesis is to use transient-response based methodologies and modulated excitation (ME) to investigate the mechanism of SCR. The application of these approaches revealed mechanistic insights that would otherwise not be obtained by steady-state experimentation.

The first requirement for such system is to have an appropriate cell that would serve as a reactor during the spectroscopic experiments. This was accomplished by fabricating a low-void-volume cell that can be utilized for a wide range of complementary methods such as infrared, Raman, and UV-visible spectroscopy.

The advantages of ME and phase-sensitive detection (PSD) are first exhibited in the case of Raman spectroscopy. Through this approach, the VO_x active phase and the TiO_2 support were shown to play a role in the SCR process. Furthermore, only the catalytic active centers were identified to be the coordinatively unsaturated portion of the VO_x species. TiO_2 might not be involved in the reaction, but it serves as a reservoir of NH_3 molecules that can be transferred to the active sites.

Using the same approach in IR spectroscopy revealed insights into the interconversion between Lewis and Brønsted-Lowry sites over vanadia-based materials. While the Lewis functionality appears as a single peak in the steady-state IR spectra, PSD revealed that it is actually composed of at least three different species with different degrees of resistance to hydroxylation.

The formation of HCN is detrimental from an engineering and environmental point of view. Hence, its formation was studied by catalytic tests and operando spectroscopy. It was found that formaldehyde and NH_3 react directly without passing through the formate route. This

information is important to design an efficient after-treatment system that would prevent the release of HCN to the environment.

Transient XAS experiments captured the mechanistic basis of the NH_3 inhibition effect observed on Cu-SSZ-13 at low temperature. Through the molecular-level information obtained, a proposed intermittent pulsing procedure was developed to improve the SCR activity while saving up valuable reductant supply.

Further studies should focus on the application of these techniques to other SCR catalytic systems, most notably iron-based catalysts and other copper-exchanged zeolites with different framework types. In addition, the ME-PSD approach can be easily extended to other catalytic reactions so that the structure-reactivity relationship of industrially relevant catalysts can also be established. Indeed, the mechanistic insights obtained from these studies go beyond mere scientific curiosity as these pieces of information can be exploited to design better catalysts and continually improve chemical processes in a rational manner.

Annex – Teaching Infrared Spectroscopy in the Context of SCR: A Learning Activity for In-Person and Virtual Laboratory Classes

A.1. Introduction

Spectroscopy has continuously remained at the forefront of scientific advancement since it was first formally described in the 17th century. A most versatile tool, it served as the impetus for many fundamental discoveries across all imaginable scales – from the extremely small such as in the determination of individual atomic masses [200], to the infinitely large such as in the observation of expanding galaxies [201]. Hence, it forms an integral part of virtually all science and engineering undergraduate curricula [202, 203]. Chemistry majors would typically encounter the foundational aspects of spectroscopy in as early as their general chemistry courses, and would then go on to learn its theoretical basis and practical applications in their upper-division undergraduate studies. Infrared (IR) spectroscopy has become one of the most taught spectroscopic techniques because of its simplicity and wide applicability [204-207]. In addition, the lectures can be easily supplemented with laboratory exercises since an IR spectrometer is relatively cheap to own and does not require complicated maintenance [208].

IR spectroscopy as taught in undergraduate programs almost exclusively exists in the realm of organic chemistry, where it is used to distinguish different functional groups and support the identification of unknown compounds. Furthermore, the application scope is usually limited to ex-situ investigation, which can only provide static snapshots of molecular properties at a particular moment. While this is obviously sufficient for organic compound characterization, it does not showcase the full breadth of IR spectroscopy. In fact, the real power of this technique lies in its utility in mechanistic investigations, where it can be used

(under in situ or operando conditions) to monitor the transformation of molecules in real time. A quintessential example is the study of catalytic processes [209, 210].

Given its vast industrial significance, catalysis is also ingrained in the chemistry curriculum [211, 212], but its concept is usually not introduced in conjunction with IR spectroscopy except in specialized electives or graduate-level courses. Notwithstanding, IR spectroscopy remains to be one of the most widely used characterization techniques in catalysis research.

Here we present a laboratory experiment where IR spectroscopy is used to investigate the mechanism of selective catalytic reduction (SCR), which is the most efficient method of curbing NO_x emissions.

NO_x not only contributes to photochemical smog and acid rain, but also gives rise to a myriad of respiratory diseases. Hence, NO_x reduction technologies such as SCR have become an indispensable part of modern pollution control strategies worldwide. By selecting a chemical process of great environmental and economic relevance as the topic of this laboratory activity, we wish to reiterate the importance of fundamental-level research in real-life applications.

The experiment has been successfully implemented in two higher education institutions in Switzerland since 2018. Although it was originally intended for master and/or first-year PhD students, some bachelor students also managed to participate without problem so we deem it suitable for upper-undergraduate curricula as well. Due to the restrictions during the COVID-19 pandemic, we were not able to offer this course in-person during the last three semesters. Instead, we adapted the course to an online format where every individual step was discussed in detail through the use of photos and other visual aids.

A.2. Learning outcomes

At the end of this learning exercise, the students will:

1. Learn how to operate a Fourier-transform infrared spectrometer and a typical set-up used to investigate catalysts under in situ conditions;

2. Summarize, plot, and analyze the spectroscopic data using a scientific graphing software;
3. Integrate their knowledge of spectroscopy and catalysis to answer the discussion questions; and
4. Practice and improve their scientific writing skills.

A.3. Experimental overview

The schematic diagram of the set-up is shown in Figure A.1. In brief, it comprises three parts:

1. A set of mass flow controllers that dose ammonia (NH_3), nitric oxide (NO), oxygen (O_2), hydrogen (H_2), and argon (Ar) in conjunction with a platinum-based catalyst to generate water from H_2 and O_2 ;
2. A spectroscopic cell where the catalyst powder (2 wt% V_2O_5 /10 wt% WO_3/TiO_2) is placed; and
3. An IR spectrometer (Bruker Vertex70) equipped with a diffuse reflectance accessory (Harrick Praying Mantis™)

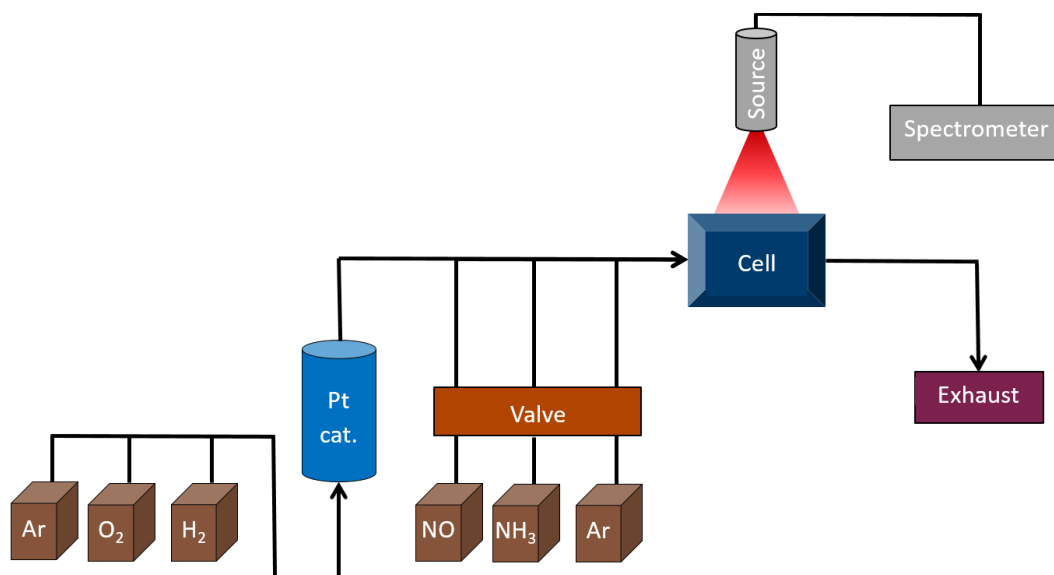


Figure A.1. Schematic diagram of the experimental setup.

The students were divided into groups of 3 or 5 depending on their majors (chemistry, chemical engineering, and environmental sciences). Each group is guided by a teaching assistant during the entire experiment. When the course was offered online, the experiment was explained in the form of a detailed presentation to three groups simultaneously.

The full experimental procedure is given in the Appendix. The catalyst was first loaded into the spectroscopic cell, which was then mounted into the sample stage of the spectrometer and heated to 400 °C for 30 minutes under 5 vol% O₂. After that, the temperature was decreased to 250 °C. Prior to any actual measurement, the detector was cooled with liquid nitrogen and the IR signal was optimized. Then, a background spectrum of the catalyst was collected. For the succeeding steps, sample spectra were recorded every 5 s, which is a sufficient time resolution to follow the chemical processes in real time. To study its interaction with the catalyst, NH₃ (1000 ppm) was introduced and cut off for 10 minutes each time. The corresponding addition-removal sequence was also performed with the other major SCR reactant, NO (1000 ppm). Water (2 vol%) was then introduced to investigate its influence in the process, as it is always present in real-life exhaust. Finally, NH₃ (1000 ppm) was also introduced to study its competitive adsorption with water.

After the actual experiment, the course participants were asked to analyze the spectroscopic data and answer the discussion questions. The students who participated virtually were given the data from the previous cohort. Consultation sessions were held, as needed. The students were required to submit a laboratory report in the format of a scientific publication.

Deviations from the original procedure can be done, if needed. The catalyst composition may be changed for as long as it is primarily vanadia supported on titania (V₂O₅/TiO₂). The set-up may be also modified and adapted to the pre-existing infrastructure of the laboratory. For instance, a water bubbler may be used in lieu of the in situ water generation system described here. Measurements via transmission instead of diffuse reflectance are also possible as long as an appropriate cell is available. Lastly, this in situ experiment can be converted into an operando experiment if the outlet of the cell would be connected to a gas analyzer (e.g., mass spectrometer).

A.4. Safety hazards

Gas cylinders must be equipped with the appropriate regulators. All gas lines must be checked for leaks prior to the start of the experiment. H₂ and nitrogen dioxide (NO₂) detectors must be available at all times. H₂ is flammable so it must be used under the supervision of someone with compressed gas training. Whenever possible, pre-diluted stock gases of NO and NH₃ should be used as the necessary working concentrations of these gases are just 1000 ppm anyway.

The detector of the IR spectrometer requires liquid nitrogen (-196 °C), which should be handled only by someone wearing complete personal protective equipment (i.e., laboratory coat, safety goggles, thermal gloves, and closed shoes).

A.5. Results and discussion

As of this writing, a total of 126 students have already taken this course over the course of six academic semesters. Of which, 65 students participated in-person (Fall 2018, Spring 2019, and Fall 2019) and 61 participated online during the COVID-19 pandemic (Spring 2020, Fall 2020, and Spring 2021).

Since the course was designed for master students, most participants have had already some experience with infrared spectroscopy. However, these are often limited to ex situ characterization of organic compounds and the interpretation of their spectra. Except for a few PhD students, none of the participants had performed an in situ spectroscopic experiment yet. The majority of the students used Origin to analyze and plot their data, but a few preferred Microsoft Excel or Python.

The students were asked a total of 9 questions, of which the first 8 have designated correct answers. An answer is judged to be a “satisfactory response” if it provides the necessary data and appropriate explanations with little to no errors. The performance of the students are presented in Table A.1.

Table A.1. Performance of students in the laboratory exercise.

Question no.	Section	% of satisfactory responses		
		In-person	Virtual	Total
		(N = 65)	(N = 61)	(N = 126)
1	Catalyst pre-treatment	91	100	96
2	Adsorption of NH ₃	94	89	91
3	Adsorption of NH ₃	100	90	94
4	Desorption of NH ₃	94	80	86
5	Reaction of pre-adsorbed NH ₃ with NO	68	61	64
6	Desorption of NO	87	92	90
7	Adsorption of water	100	92	95
8	Adsorption of water and NH ₃	87	93	91
Total		90	87	88

The students performed quite well in the exercise, answering most questions satisfactorily. It is important to note that there is only a small difference between the performance of the students who participated in-person (90% satisfactory responses) and virtually (87% satisfactory responses). While there is no perfect substitute to an in-person laboratory exercise, these results show that a virtual offering of the course could be a viable option in

case of extraordinary circumstances. The answer key as well as the performance of the students in each individual item will be discussed in the succeeding subsections.

Catalyst pre-treatment

Prior to the experiment, the catalyst underwent pre-treatment at 400 °C under an oxidizing atmosphere. The students were asked about the purpose of this step. The correct responses are (1) to remove any residual moisture or adsorbates that may be present on the catalyst surface and (2) to fully oxidize the catalytic centers to V^{5+} . Most of the students (96%) gave satisfactory responses, but some only answered with the first one. If the goal of the initial treatment were just to remove the pre-adsorbed species, then heating up under Ar would have been just as effective. However, the presence of O_2 was also needed to activate the catalyst since its vanadyl sites need to be fully oxidized to interact appropriately with NH_3 . Were the catalyst noble metal-based instead, then a high-temperature treatment under reducing atmosphere would have been more appropriate.

Adsorption of NH_3

The first part of the experiment involves admitting NH_3 to the cell and monitoring its interaction with the catalyst. The participants were asked to plot the corresponding spectrum and to perform a short literature review to properly assign the associated peaks. Table A.2 and Figure A.2 summarize the expected answers from the students.

Table A.2. Assignment of major bands in the of IR spectrum of 2 wt% V_2O_5 /10 wt% WO_3 /TiO₂ under 1000 ppm NH_3 . [22, 111]

Wavenumber / cm^{-1}	Assignment
3642	O–H stretch
3389, 3252, 3162	N–H stretch
2043	V=O stretch (overtone)

2006	W=O stretch (overtone)
1670, 1432	N–H bend of NH_4^+ (Brønsted-Lowry acid sites)
1601, 1235	N–H bend of NH_3 (Lewis acid sites)

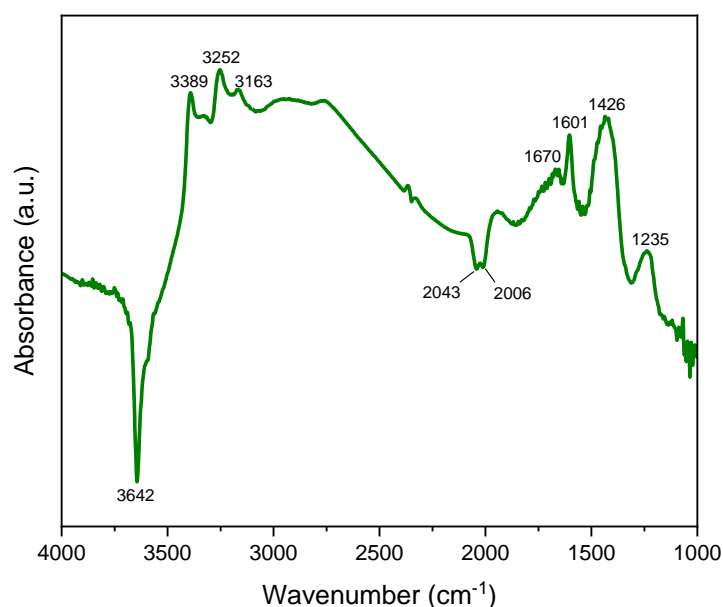


Figure A.2. IR spectrum of 2 wt% V_2O_5 /10 wt% WO_3/TiO_2 under 1000 ppm NH_3 at 250 °C.

VO_x can function as either Lewis or Brønsted-Lowry acid sites. WO_x provides additional Brønsted-Lowry acid sites whereas TiO_2 has only Lewis functionality.

Around 90% of the participants managed to answer this question satisfactorily with only a few minor mistakes. Some notable errors include labelling the y-axis of the graph as “intensity” instead of “absorbance” and the x-axis as “wavelength” instead of “wavenumber.” In some reports, the vanadyl and tungstenyl $\text{M}=\text{O}$ overtones were incorrectly labeled as “ $\nu(\text{M}=\text{O})$ ” as opposed to “ $2\nu(\text{M}=\text{O})$ ” since they are not fundamental vibrational modes. Furthermore, the O–H stretch at 3642 was sometimes attributed to water, whereas they should have been assigned to the surface hydroxyl groups.

The participants were also asked to explain why some peaks appeared positive and negative in the spectrum, and 94% answered correctly. The reason is purely mathematical as the clean catalyst surface was taken as the background. Hence, the positive peaks correspond to those species that were not present during the background acquisition but are now adsorbed on the catalyst surface (e.g., NH_3). On the other hand, the negative peaks represent the sites that were titrated or occupied (e.g., V=O , W=O , O-H).

Desorption of NH_3

To study the adsorption strength of NH_3 , the students plotted the signal of the two major adsorbed NH_3 species as a function of time upon NH_3 cut-off. Compared to the previous items, this task requires a rather extensive procedure as the peaks have to be first accurately identified, integrated, normalized, and then plotted. A sample correct solution is presented in Figure A.3.

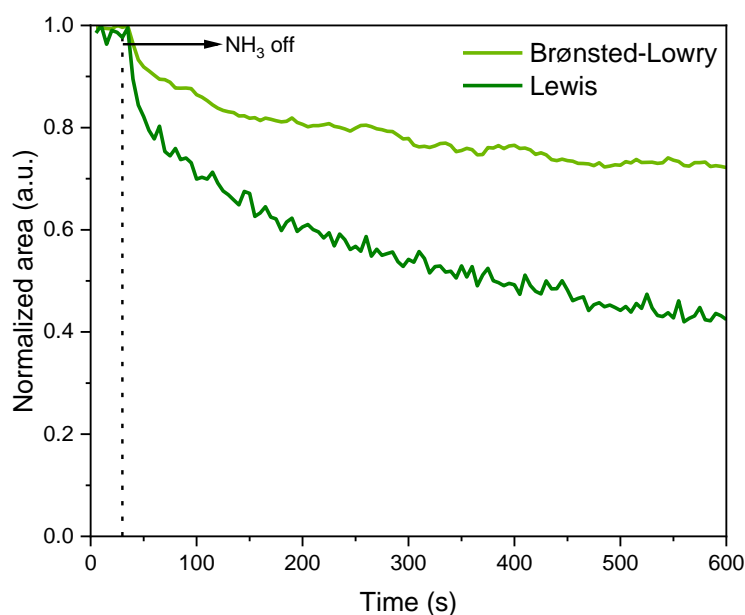


Figure A.3. Evolution of the normalized areas of NH_4^+ adsorbed on Brønsted-Lowry acid sites (1310 to 1543 cm^{-1}) and NH_3 adsorbed on Lewis acid sites (1179 to 1310 cm^{-1}) upon cut-off of 1000 ppm NH_3 at 250 °C .

Even after 10 minutes of desorption at 250 °C, both NH_4^+ and NH_3 persisted on the surface, suggesting that they were strongly adsorbed. This is due to their favorable interaction with the acidic sites of the catalyst. Overall, 86% of the students managed to provide correct responses. Some common errors include failure to normalize the peak areas and plotting the peak height instead of the peak areas as instructed.

Reaction of pre-adsorbed NH_3 with NO

The remaining NH_3 molecules on the surface were then reacted away with 1000 ppm NO, and the participants were tasked to plot the signal evolution. A sample graph is shown in Figure A.4.

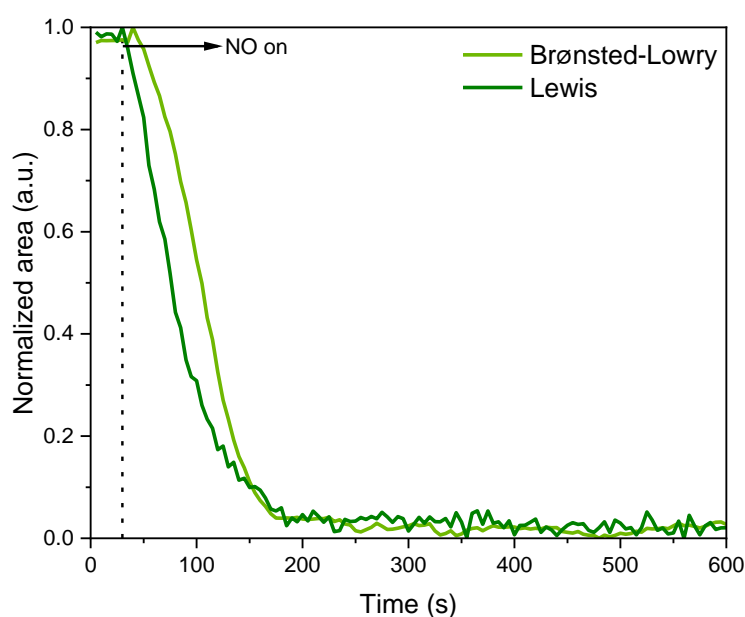


Figure A.4. Evolution of the normalized areas of NH_4^+ adsorbed on Brønsted-Lowry acid sites (1310 to 1543 cm^{-1}) and NH_3 adsorbed on Lewis acid sites (1179 to 1310 cm^{-1}) upon introduction of 1000 ppm NO at 250 °C.

As soon as NO was introduced, both NH_4^+ and NH_3 decreased, signaling the onset of the SCR reaction. However, the two adsorbed species did not follow similar kinetics. In particular, NH_3 molecules adsorbed on Lewis acid sites were consumed preferentially over NH_4^+ adsorbed on Brønsted-Lowry acid sites, as observed in previous studies [38, 109,

118]. The higher reactivity of Lewis acid sites can be construed to mean that they are the active sites for the SCR reaction.

Remarkably, only 64% of the students succeeded in providing the correct graph and the corresponding interpretation. As mentioned in the previous subsection, some students did not normalize the areas or plotted the wrong parameter. Another complication arises from the choice of which peaks to integrate. For Brønsted-Lowry acid sites, the decision is relatively straightforward as the peak centered at 1432 cm^{-1} is considerably more prominent than the one at 1670 cm^{-1} . As a result, all students chose to work with this peak. However, this is not the case for Lewis acid sites as either peak at 1601 and 1235 cm^{-1} can be potentially used. Coincidentally, water is one of the products of SCR, and after the reaction, it can remain adsorbed on the catalyst surface at $250\text{ }^{\circ}\text{C}$ and give rise to an IR signal at 1630 cm^{-1} . As NH_3 is being consumed and the peak at 1601 cm^{-1} decreases, water is concurrently being produced and the peak at 1630 cm^{-1} increases. Hence, those who chose to integrate the peak at 1601 cm^{-1} encountered problems as they falsely integrated the peak of the water product toward the end of the experiment. As a result, the area did not approach zero. This explains the relatively low percentage of correct answers in this subsection. Interestingly, some groups initially chose to integrate the peak 1601 cm^{-1} , but then realized this complication so they chose to work with 1235 cm^{-1} instead.

Desorption of NO

After the SCR reaction, two major peaks appeared: one at 1630 cm^{-1} , which is related to physisorbed water as previously discussed; and the other at 2183 cm^{-1} , which corresponds to nitrosyl (NO^+) groups (Figure A.5) [38]. To determine the strength of NO adsorption on the catalyst, a desorption experiment was performed. Just after a few seconds of NO removal, the peak at 2183 cm^{-1} was gone completely, as opposed to NH_3 , which persisted on the surface even after 10 minutes of desorption. This corroborates that NO is only weakly adsorbed on the catalyst, as correctly concluded by 90% of the participants. Many even went as far as to mention that the weak interaction is due to the fact that NO is not basic and can therefore not interact strongly with the acidic sites of the catalyst as NH_3 .

Indeed, the molecular interaction between NO and the catalyst is restricted to that of a purely dipole-dipole type, and even then, NO is not very polar.

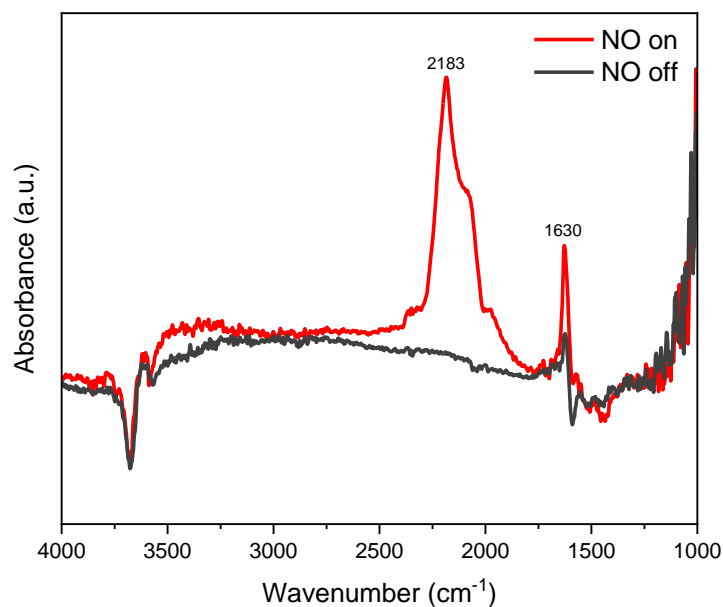


Figure A.5. IR spectrum of 2 wt% V_2O_5 /10 wt% WO_3 / TiO_2 under 1000 ppm NO at 250 °C.

Adsorption of water

As one of the major products of combustion, water is omnipresent in exhaust gas and may affect the subsequent after-treatment processes. To probe its interaction with the SCR catalyst, water was also introduced to the system. Table A.3 and Figure A.6 summarize the major bands associated with adsorbed water. Since this is a straightforward task, 95% of the participants gave the correct response.

Table A.3. Assignment of major bands in the of IR spectrum of 2 wt% V_2O_5 /10 wt% WO_3 /TiO₂ under 2 vol% H₂O.

Wavenumber / cm ⁻¹	Assignment
3800-2400	O-H stretch of hydrogen-bonded water
3642	O-H stretch of the catalyst
2043	V=O stretch (overtone)
2006	W=O stretch (overtone)
1616	O-H bend of physisorbed water

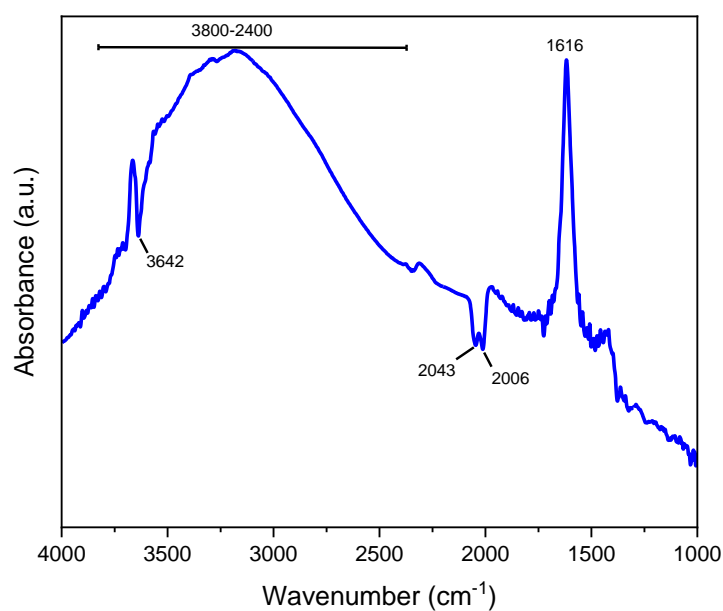


Figure A.6. IR spectrum of 2 wt% V_2O_5 /10 wt% WO_3 /TiO₂ under 2 vol% H₂O at 250 °C.

Adsorption of water and NH₃

Because water can also adsorb significantly on the catalyst, it may compete for adsorption sites with NH₃, potentially impairing the SCR activity. The last part of the experiment is

thus dedicated to estimating the extent of the co-adsorption between these species from the perspective of IR spectroscopy. The students were asked to plot the spectrum collected in the presence of both 2 vol% H₂O and 1000 ppm NH₃ (Figure A.7), and decide which species most likely predominates on the surface.

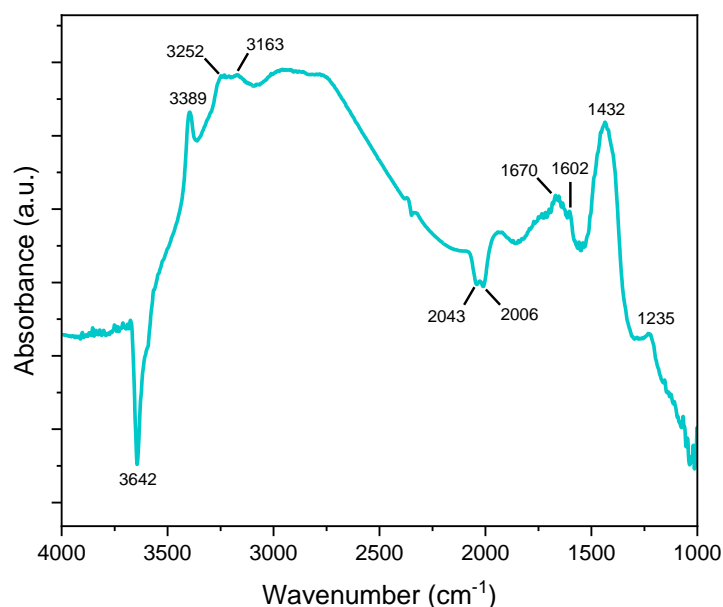


Figure A.7. IR spectrum of 2 wt% V₂O₅/10 wt% WO₃/TiO₂ under 2 vol% H₂O and 1000 ppm NH₃ at 250 °C.

As most of the students (91%) correctly answered, NH₃ easily displaces water from the SCR catalyst. This can be readily seen visually as the spectrum in the presence of both species resembles more the spectrum in the presence of just NH₃ (Figure A.2) than that of just water (Figure A.6). Indeed, the signal of physisorbed water (1616 cm⁻¹) was replaced with that of NH₄⁺ (1670 cm⁻¹) and NH₃ (1602 cm⁻¹). Many students answered further that the adsorption strength is strongly correlated with the basicity of the adsorbates: since NH₃ is more basic than water, it can correspondingly interact with the acidic surface of the catalyst much stronger. This is actually beneficial for NO_x removal since it means that the SCR process can proceed even in the presence of water. A few students answered that water was more strongly adsorbed on the basis that the wide hydroxyl band between 3800 and

2400 cm⁻¹ persisted. However, this only proves that some water molecules still interact with the catalyst, but they are no longer the dominant species on the surface as can be observed in the bending region of the spectrum.

Assessment of learning outcomes

The students performed the entire experiment with only minimal supervision from the teaching assistant, who was only there to explain the set-up in detail and ensure that safety protocols were followed. The students took turns performing the experiment – from loading the catalyst in the cell, through calculating the required mass flow controller openings, to operating the software of the IR spectrometer. This gave them familiarity not just with the setup, but also with how typical in situ experiments are conducted. Hence, LO 1 was achieved. Since the virtual students were not able to do the experiments themselves, LO 1 cannot be assessed accurately in their case. However, careful consideration was taken to provide them with as much detail as possible on how to do the experiment during the presentation.

While they had some problems with the sixth question (which was understandably tricky), the students managed to produce the required graphs and explanations satisfactorily as shown in Table A.1. The small discrepancy between the performance of in-person and virtual participants also proves the effectiveness of the online offering. In this regard, LO 2 and LO 3 were achieved.

The students were requested to hand in their laboratory reports in the format of a scientific publication so they had the opportunity to train their writing skills. Aside from scientific corrections, they also received feedback and suggestions pertaining to their writing style (e.g., diction, text structure, clarity). LO 4 could thus be judged to be achieved.

A.6. Conclusions

In situ IR spectroscopy and catalysis were successfully introduced in the context of SCR. The consistently high percentage of satisfactory responses proved that the virtual offering of this course could be just as effective as the in-person version. Furthermore, the students

had the opportunity to practice their literature review, data analysis, and technical writing skills – all of which would be beneficial for whichever career they choose to pursue in the future. Already in use since 2018, this laboratory exercise will be continually administered and improved in the succeeding semesters.

Appendix

Supporting Information for Chapter 1

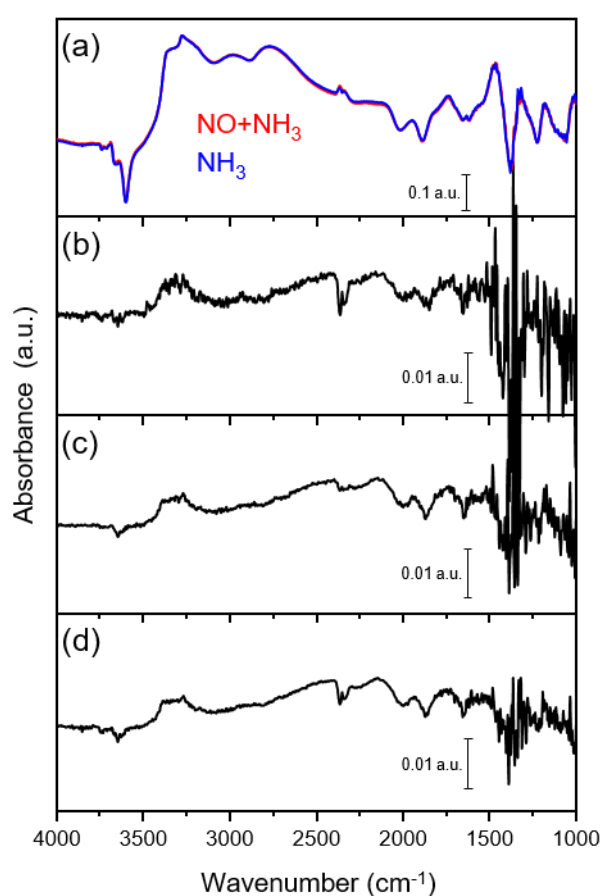


Figure S-1.1. (a) Selected diffuse reflectance IR spectra of 2.6 wt% Fe-ZSM-5 at 250 °C obtained in a modulation experiment consisting of alternate pulses of 1000 ppm NO, 1000 ppm NH₃, 2 vol% H₂O, 5 vol% O₂ balanced in Ar and of 1000 ppm NH₃, 2 vol% H₂O, 5 vol% O₂ balanced in Ar as indicated. (b-d) Difference spectra under NO+NH₃ and NH₃ obtained for one cycle, five cycles, and ten cycles. The signal-to-noise ratio decreases as the number of cycle increases.

Supporting Information for Chapter 2

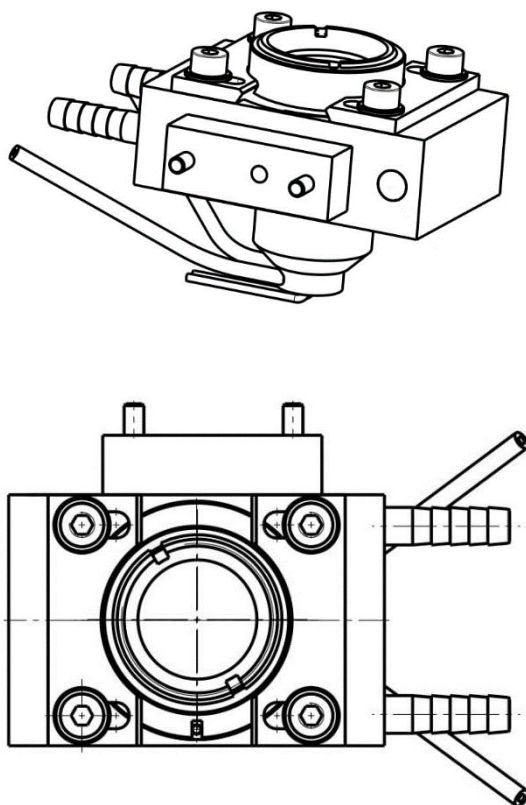
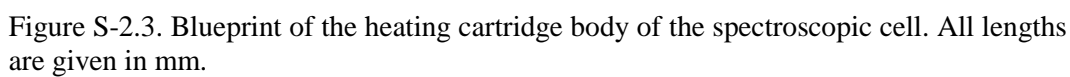


Figure S-2.1. Profile view and top view of the spectroscopic cell.





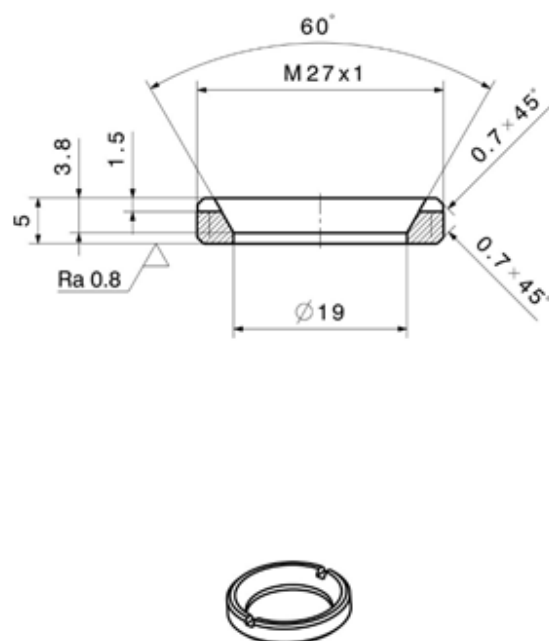


Figure S-2.4. Blueprint of the annular thread of the spectroscopic cell. All lengths are given in mm.

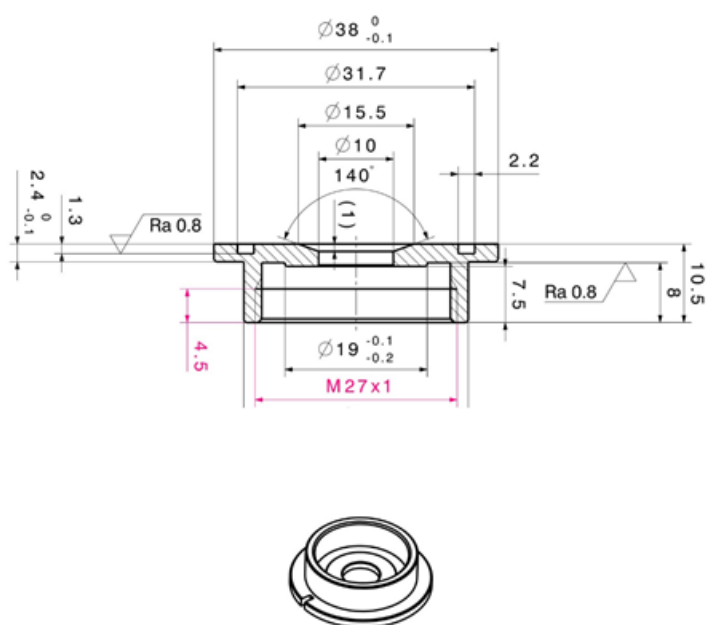


Figure S-2.5. Blueprint of the window holder of the spectroscopic cell. All lengths are given in mm.

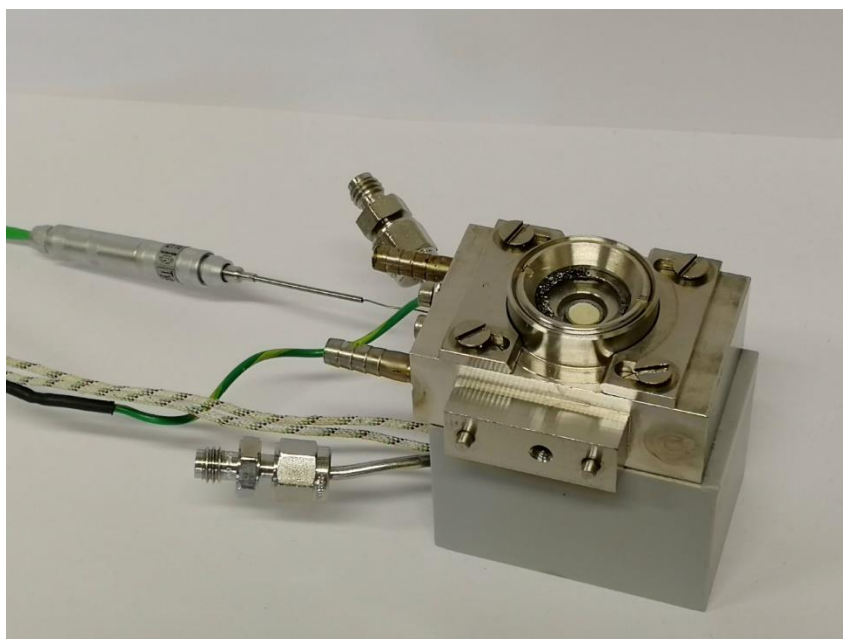


Figure S-2.6. Profile view of the spectroscopic cell. The cell can be attached to the right side of the the Praying Mantis™ diffuse reflectance accessory (Harrick Scientific). A graphite O-ring is used to secure the annular thread to the window.

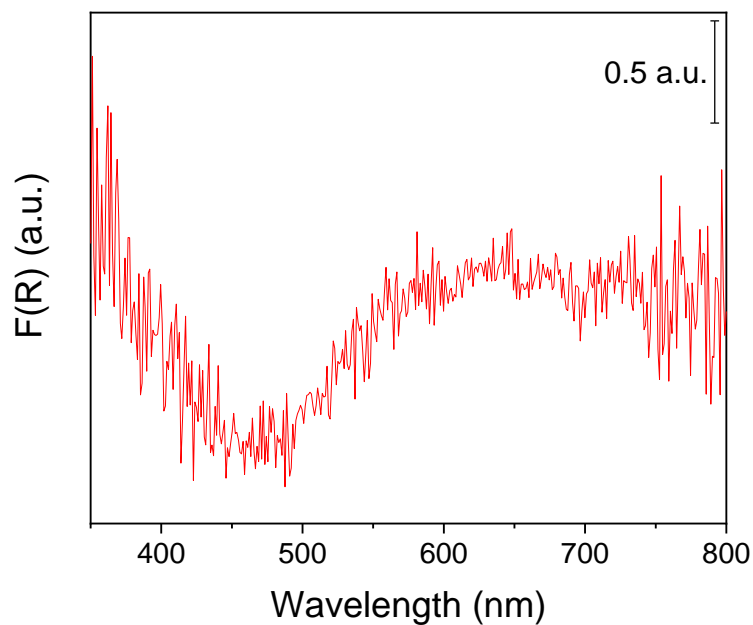


Figure S-2.7. Difference DR-Vis spectrum of Cu/SSZ-13 exposed to NH_3/NO and NH_3 alone (data from Fig. 5a).

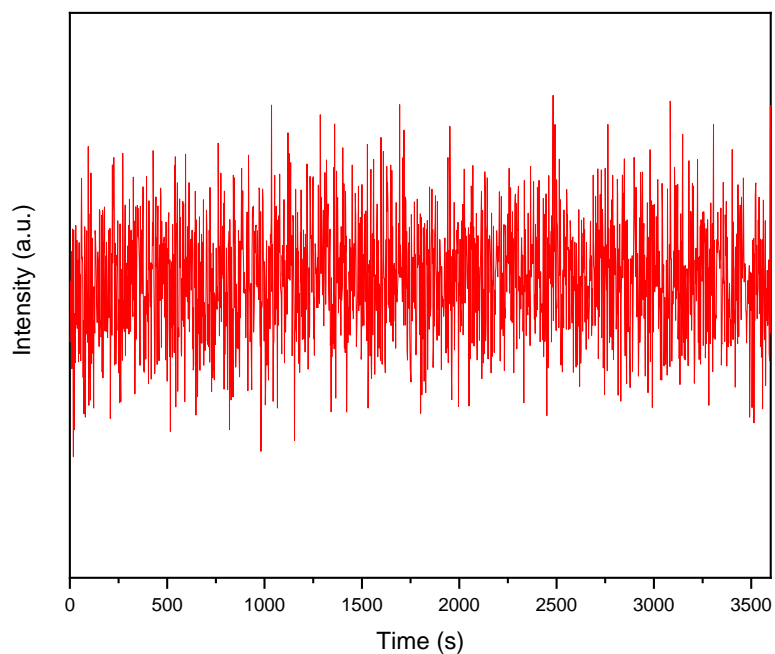
Supporting Information for Chapter 3

Figure S-3.1. Laser damage test. Intensity of the VO_x peak at 1031 cm⁻¹ during continuous exposure to a 785-nm laser with a power of 100 mW and exposure time of 0.5 s. No decrease in signal was observed after 1 h of experiment. Furthermore, no sample discoloration was observed. Hence, it was concluded that no laser damage was induced on the sample.

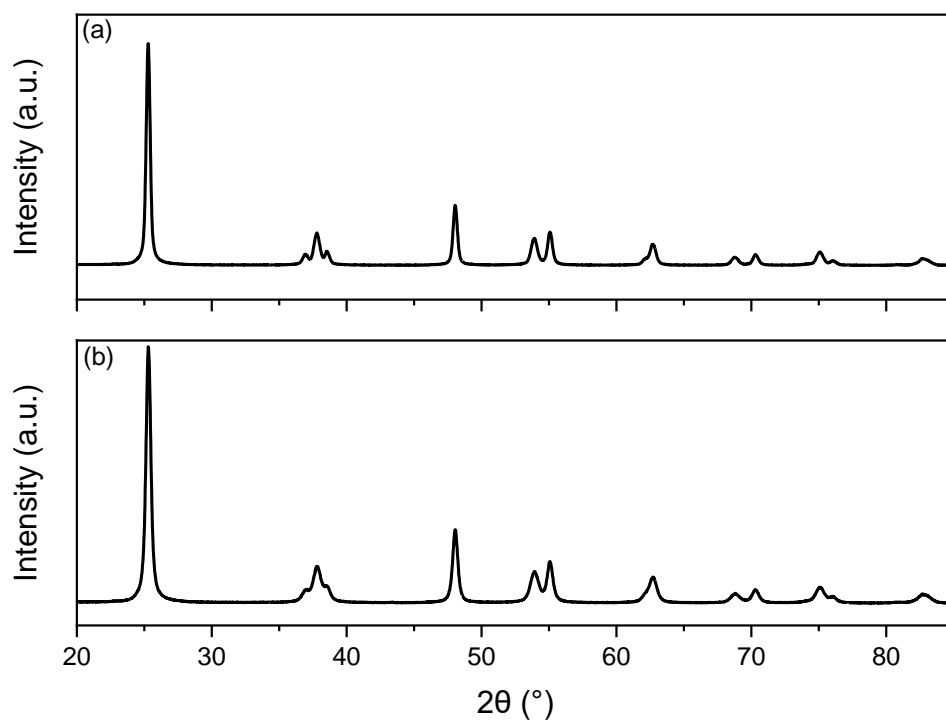


Figure S-3.2. X-ray diffractograms of (a) 2 wt% $\text{V}_2\text{O}_5/\text{TiO}_2$ and (b) TiO_2 . Only anatase reflections were observed in the x-ray diffractogram of 2 wt% $\text{V}_2\text{O}_5/\text{TiO}_2$. Hence, there were no microcrystalline/bulk V_2O_5 domains in the catalyst.

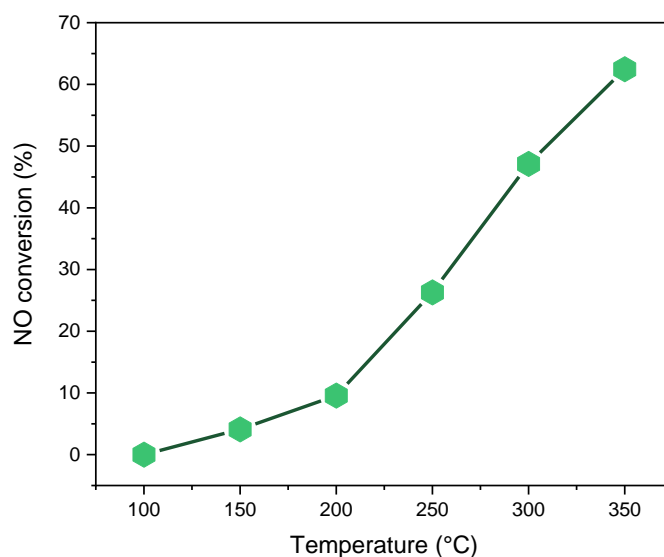


Figure S-3.3. Catalytic activity of 2 wt% $\text{V}_2\text{O}_5/\text{TiO}_2$ inside the spectroscopic cell in a gas feed of 500 ppm NO, 500 ppm NH_3 , 2 vol% H_2O , 5 vol% O_2 balanced in Ar (total flow: $100 \text{ mL} \cdot \text{min}^{-1}$).

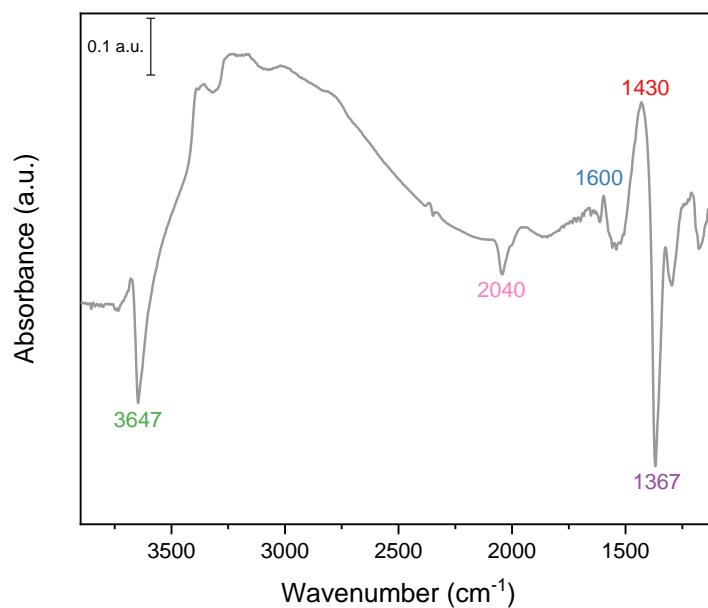


Figure S-3.4. IR spectrum of 2 wt% $\text{V}_2\text{O}_5/\text{TiO}_2$ after equilibration in a gas feed of 500 ppm NO, 500 ppm NH_3 , 2 vol% H_2O , 5 vol% O_2 balanced in Ar (prior to the modulated excitation experiment). The peaks at around 1430 and 1600 cm^{-1} correspond to NH_3 molecules adsorbed on Brønsted-Lowry sites and Lewis sites, respectively. Furthermore, the peaks at 3650, 2040, and 1367 cm^{-1} are assigned to $-\text{OH}$ groups, $2\nu(\text{V}=\text{O})$ mode, and $-\text{SO}_4$ groups, respectively. These peaks are negative because the sites were covered by NH_3 and water during the experiment. No signal from adsorbed NO was observed.

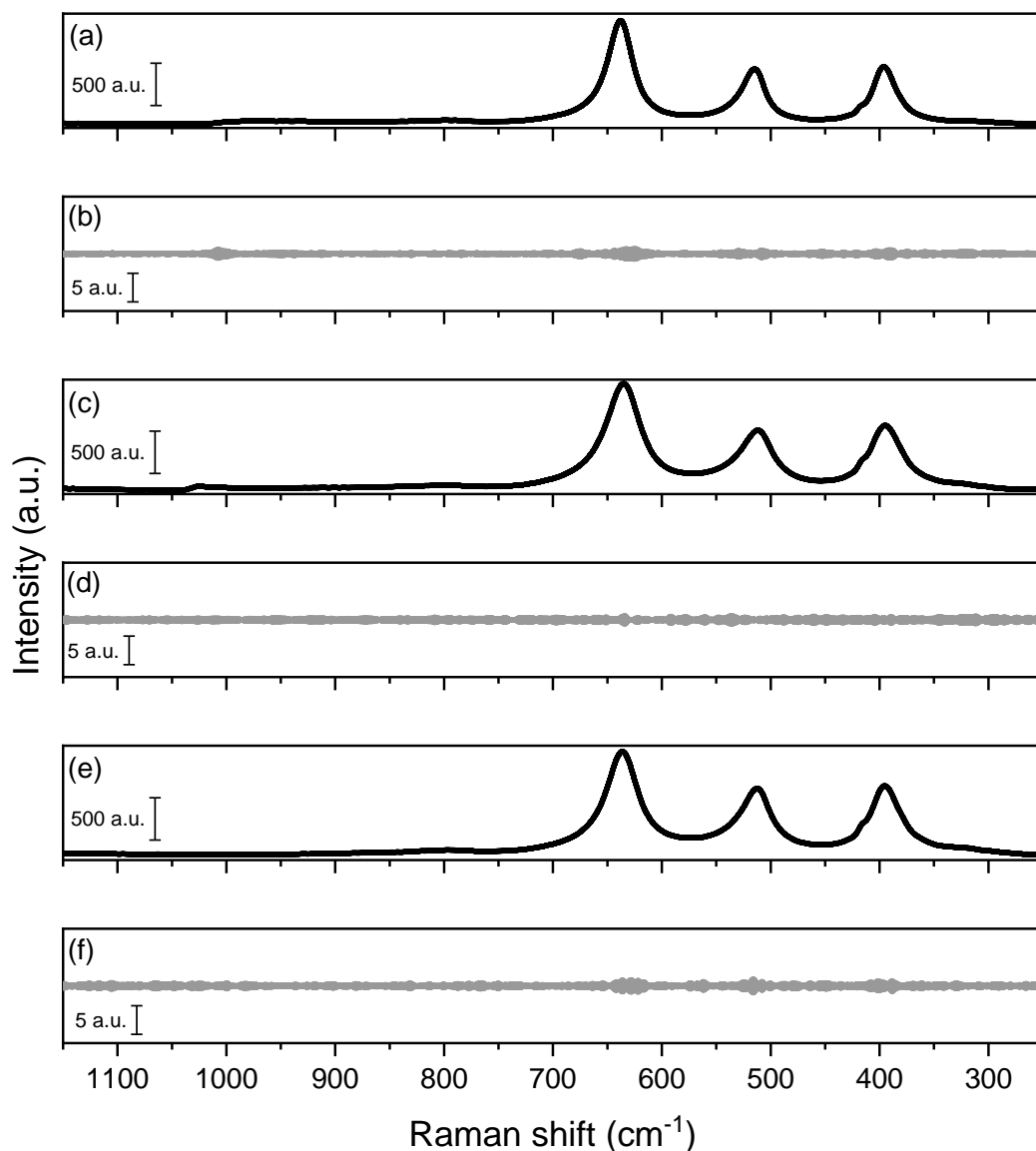


Figure S-3.5. (a) Time-resolved Raman spectra and (b) the corresponding phase-resolved spectra of 2 wt% $\text{V}_2\text{O}_5/\text{TiO}_2$ at room temperature during 30-s pulses of 500 ppm NH_3 in a gas feed of 500 ppm NO , 2 vol% H_2O and 5 vol% O_2 balanced in Ar ; (c) Time-resolved Raman spectra and (d) the corresponding phase-resolved spectra of 2 wt% $\text{V}_2\text{O}_5/\text{TiO}_2$ at 250 °C during 30-s pulses of Ar in a gas feed of 500 ppm NO , 2 vol% H_2O and 5 vol% O_2 balanced in Ar ; (e) Time-resolved Raman spectra and (f) the corresponding phase-resolved spectra of TiO_2 at 250 °C during 30-s pulses of 500 ppm NH_3 in a gas feed of 500 ppm NO , 2 vol% H_2O and 5 vol% O_2 balanced in Ar .

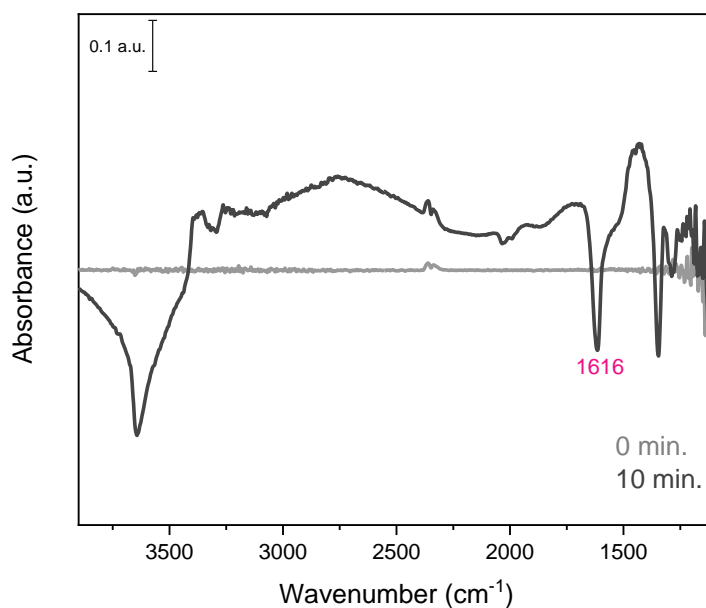


Figure S-3.6. IR spectra of 2 wt% $\text{V}_2\text{O}_5/\text{TiO}_2$ after exposure to NH_3 at 250 °C. The background was taken under 2 vol% H_2O , 5 vol% O_2 balanced in Ar. The negative peak at 1616 cm^{-1} corresponds to previously bound water that was displaced by NH_3 .

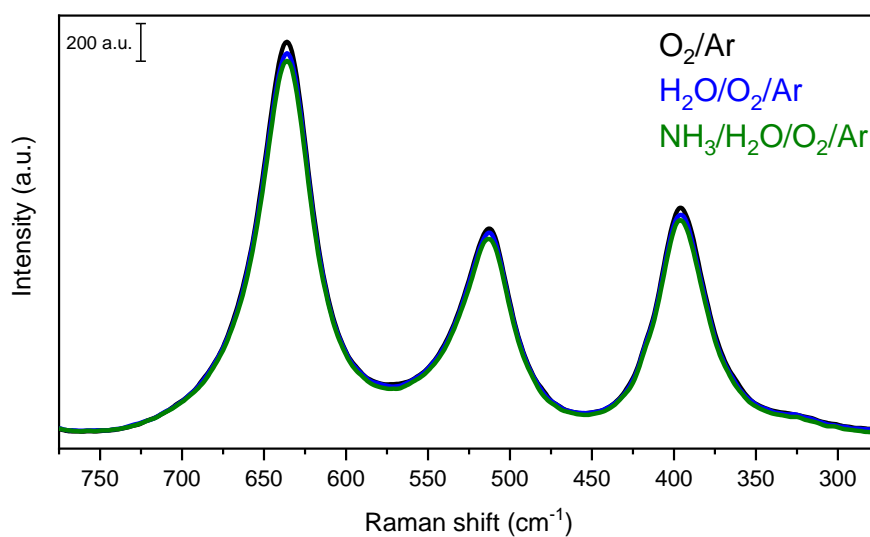


Figure S-3.7. Raman spectra of TiO_2 at 250 °C in different gas feeds: 5 vol% O_2 balanced in Ar (black); 2 vol% H_2O and 5 vol% O_2 balanced in Ar (blue); 500 ppm NH_3 , 2 vol% H_2O , and 5 vol% O_2 balanced in Ar (green).

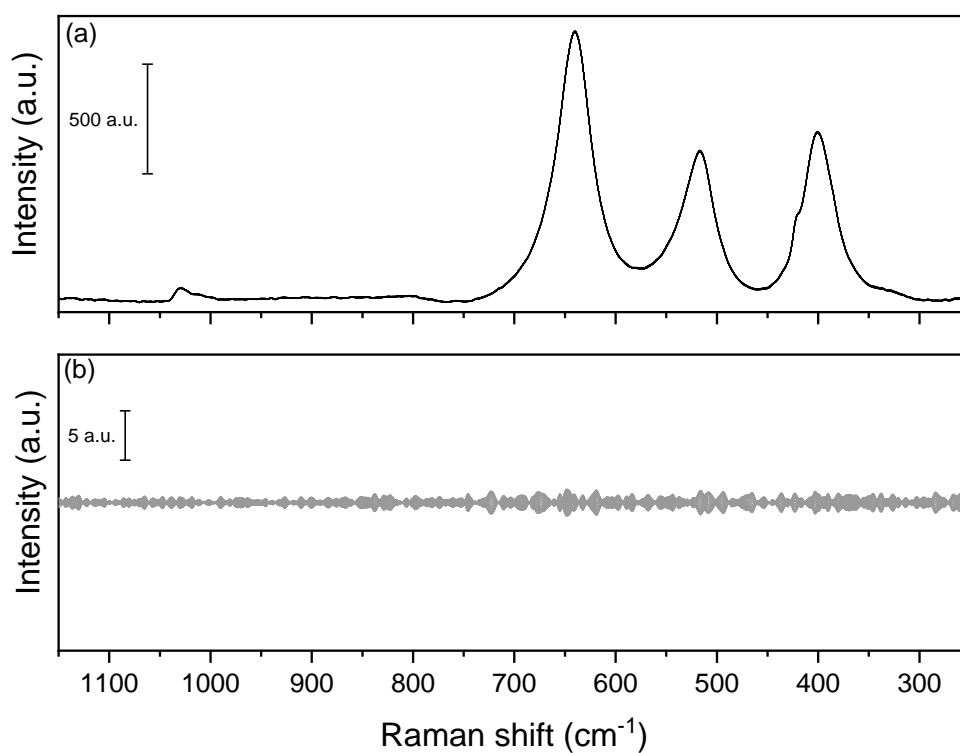


Figure S-3.8. (a) Time-resolved Raman spectra and (b) the corresponding phase-resolved spectra of 2 wt% $\text{V}_2\text{O}_5/\text{TiO}_2$ at 250 °C during 30-s pulses of 500 ppm NO in a gas feed of 2 vol% H_2O and 5 vol% O_2 balanced in Ar.

Supporting Information for Chapter 4

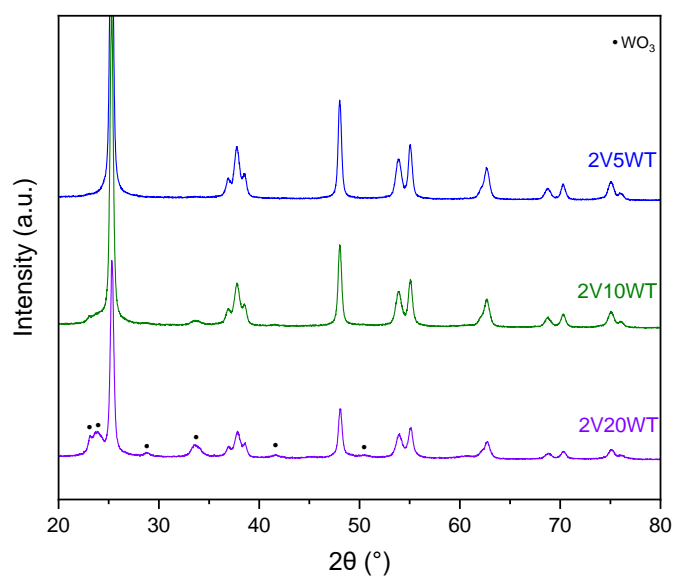


Figure S-4.1. Powder XRD of 2V5WT, 2V10WT, and 2V20WT.

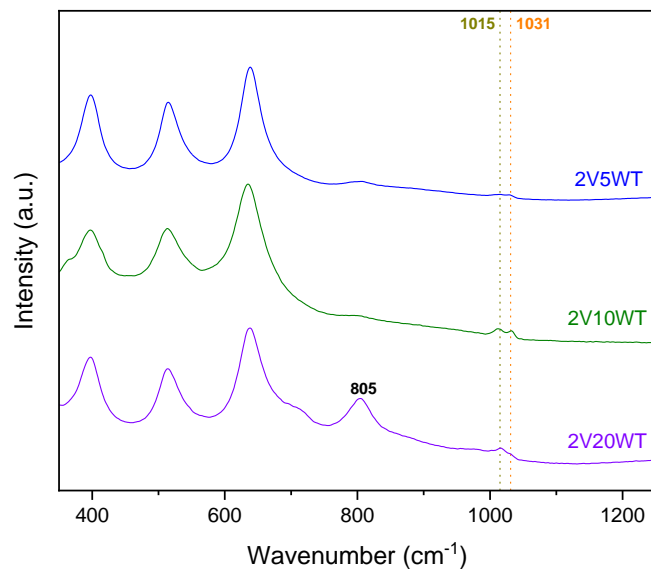


Figure S-4.2. Raman spectra of 2V5WT, 2V10WT, and 2V20WT under 5 vol% O₂ balanced in Ar at 250 °C. The vibrations at 1031 and 1015 cm⁻¹ are the stretching modes of V=O and W=O groups, respectively, while the vibration at 806 cm⁻¹ belongs to bulk WO₃.

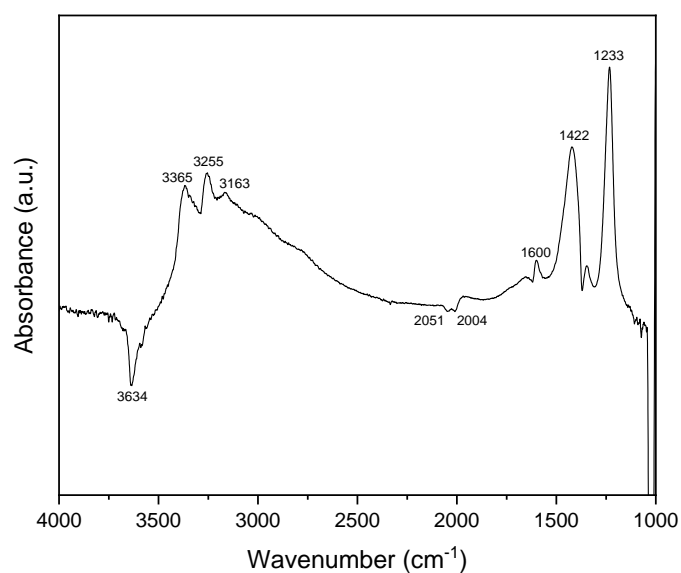


Figure S-4.3. Transmission IR spectrum of 2V10WT under 1000 ppm NH₃ and 5 vol% O₂ balanced in Ar at 400 °C.

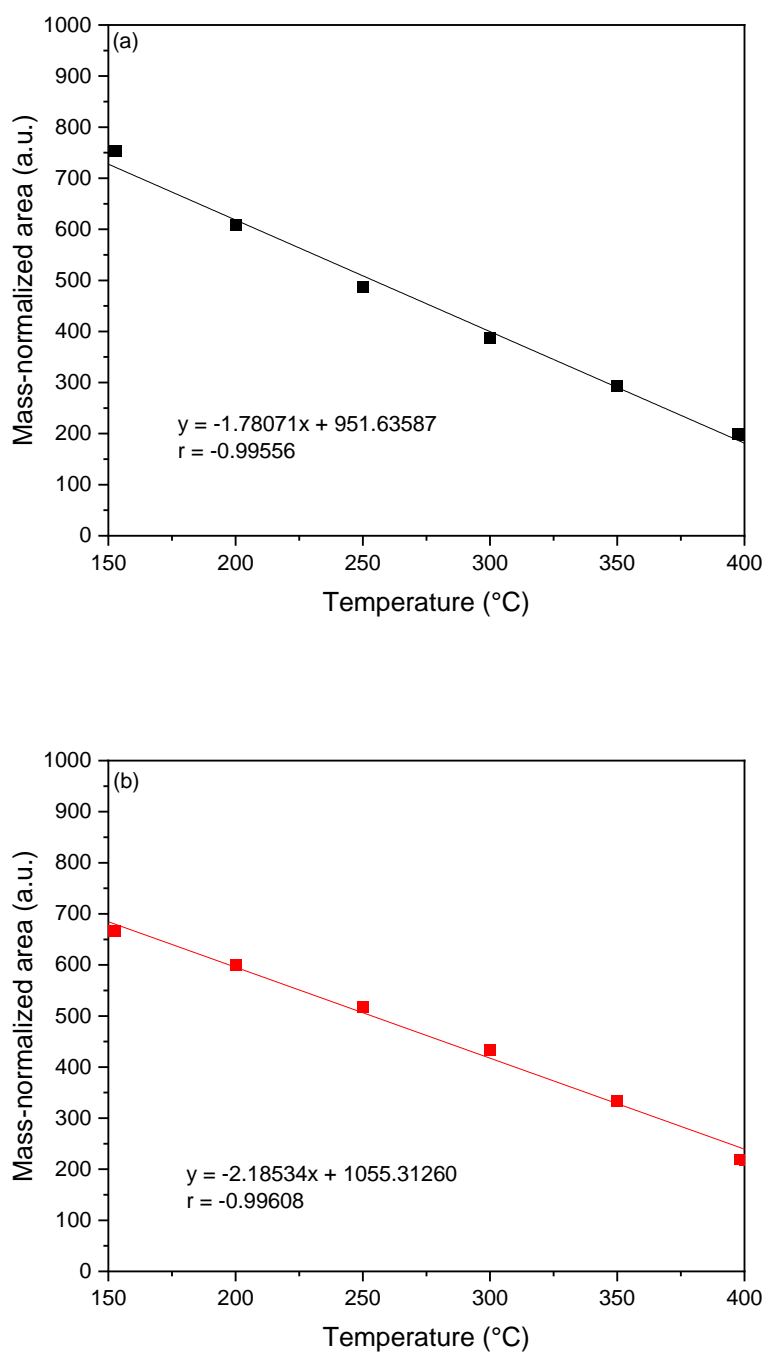


Figure S-4.4. Linear fitting of the mass-normalized areas of (a) Lewis and (b) Brønsted-Lowry acid sites as a function of the temperature.

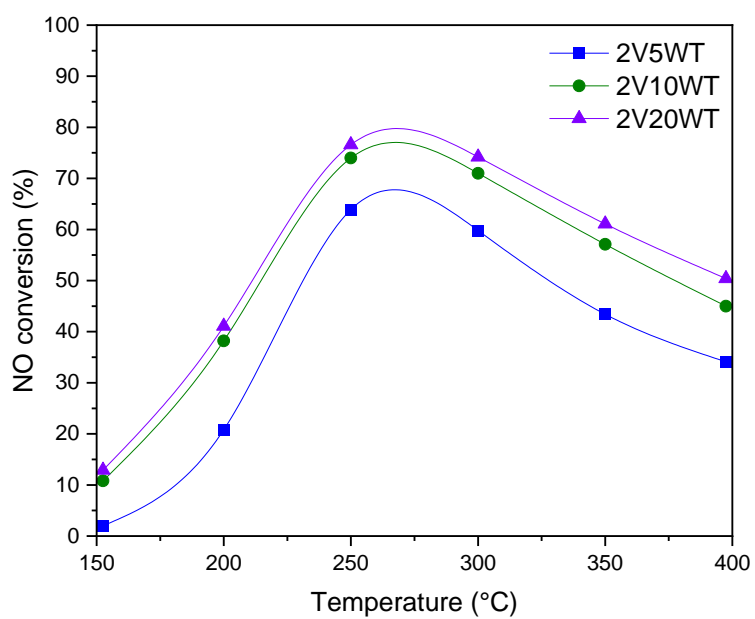


Figure S-4.5. NO conversion of 2V5WT, 2V10WT, and 2V20WT in the spectroscopic cell. Experimental conditions: 1000 ppm NO, 1000 ppm NH₃, 5 vol% O₂ balanced in Ar.

Supporting Information for Chapter 5
Table S-5.1. NH₃ dosage, NO_x concentration at the outlet, and NH₃ slip

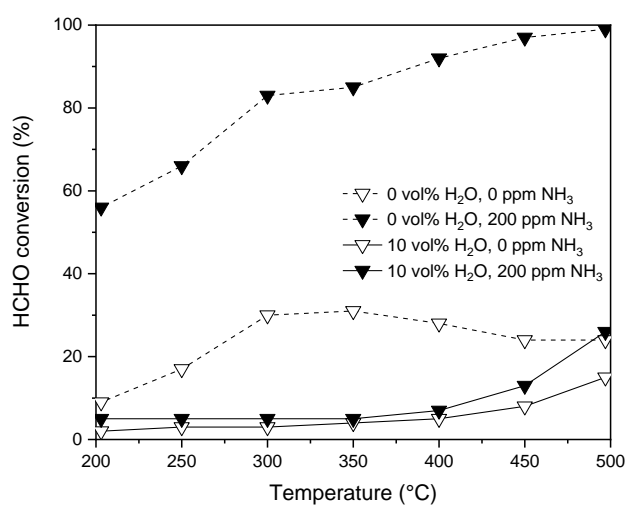
Temperature (°C)	NH ₃ /NO/ H ₂ O/O ₂ /N ₂			HCHO/NH ₃ /NO/ H ₂ O/O ₂ /N ₂			HCHO/adj. NH ₃ /NO/ H ₂ O/O ₂ /N ₂		
	[NH ₃] _i	[NO _x] _o	[NH ₃] _o	[NH ₃] _i	[NO _x] _o	[NH ₃] _o	[NH ₃] _i	[NO _x] _o	[NH ₃] _o
	ppm	ppm	ppm	ppm	ppm	ppm	ppm	ppm	ppm
500	300	42	12	300	85	7	350	60	12
450	300	21	15	300	65	7	350	36	14
400	300	15	13	300	53	6	350	25	14
350	290	21	10	290	57	5	330	32	10
300	260	51	11	260	83	7	285	68	11
250	160	151	10	160	164	11	160	164	11
200	65	247	11	65	251	13	65	251	13

Table S-5.2. Detection limits for the calibrated components

Component	Detection limit / ppm
Carbon dioxide (CO ₂)	1
Carbon monoxide (CO)	0.5
Formaldehyde (HCHO)	0.2
Formic acid (HCOOH)	0.5
Methanol (CH ₃ OH)	1
Hydrogen cyanide (HCN)	0.5
Methyl formate (HCOOCH ₃)	2
Isocyanic acid (HCNO)	0.2
Formamide (HCONH ₂)	1
Hexamethylenetetramine (C ₆ H ₁₂ N ₄)	1

Table S-5.3. Formaldehyde conversion in the absence and presence of 300 ppm NO.

Temperature (°C)	HCHO feed (%)	HCHO feed + NO (%)
500	89	89
450	75	76
400	58	59
350	41	41
300	23	23
250	14	14
200	9	8

Figure S-5.1. Formaldehyde conversion over TiO₂ under the indicated feed conditions.

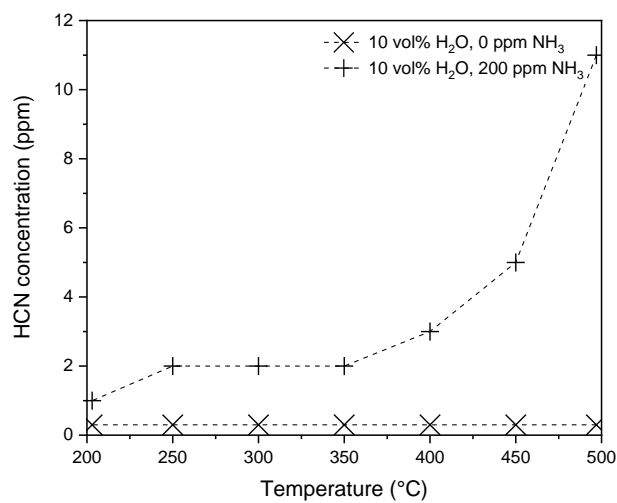


Figure S-5.2. HCN concentration over TiO₂ under the indicated feed conditions.

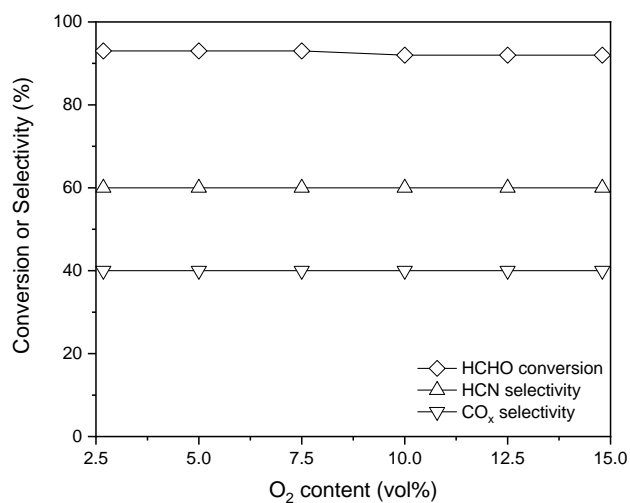


Figure S-5.3. Effect of O₂ content on the formaldehyde conversion, HCN selectivity, and CO_x selectivity over V₂O₅/WO₃-TiO₂ at 350 °C.

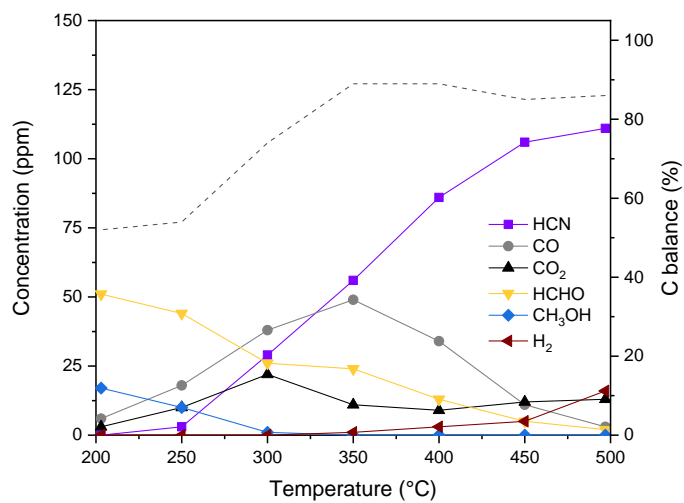


Figure S-5.4. Product distribution of formaldehyde conversion over TiO_2 without water but with 200 ppm NH_3 .

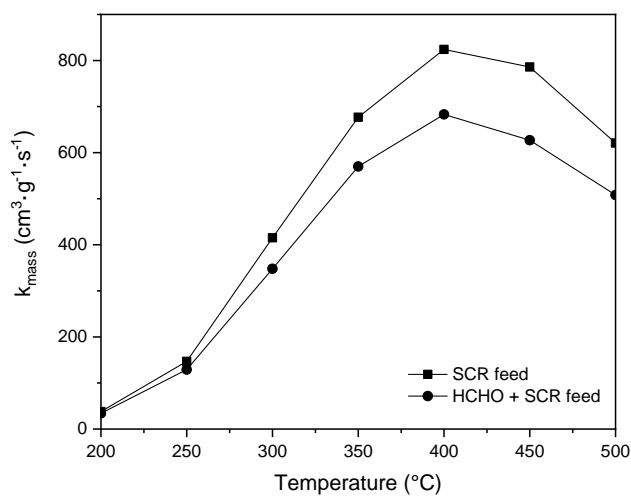


Figure S-5.5. k_{mass} of the SCR reaction at 10 ppm NH_3 slip over $\text{V}_2\text{O}_5/\text{WO}_3\text{-TiO}_2$ under different feed conditions.

Supporting Information for Chapter 6

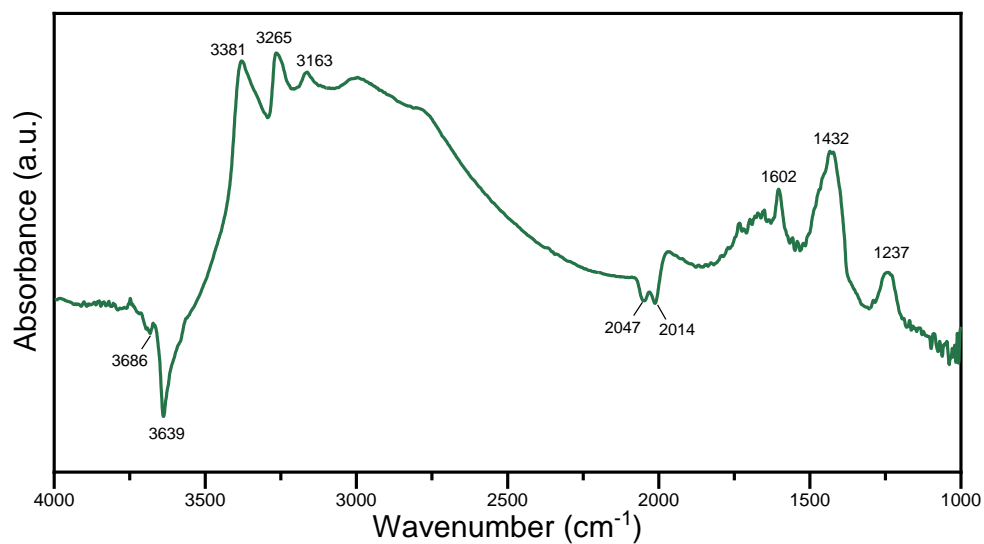


Figure S-6.1. DRIFT spectra of V₂O₅/WO₃-TiO₂ after NH₃ adsorption for 30 s at 300 °C. Experimental conditions: 1000 ppm NH₃ and 5 vol% O₂ in Ar.

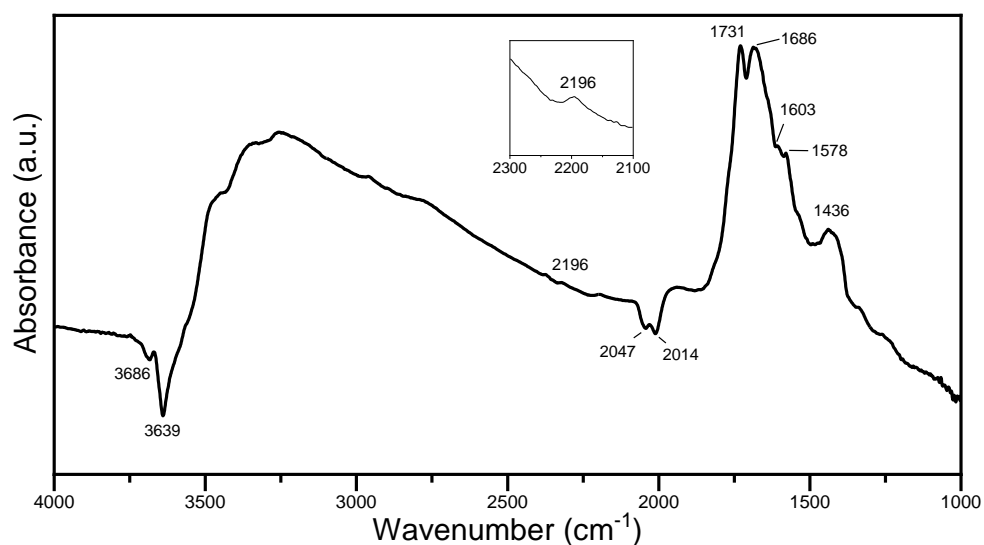


Figure S-6.2. DRIFT spectra of $\text{V}_2\text{O}_5/\text{WO}_3\text{-TiO}_2$ after 30 min of NH_3 adsorption followed by formaldehyde introduction. Experimental conditions: 150 ppm formaldehyde, 1000 ppm NH_3 and 5 vol% O_2 in Ar.

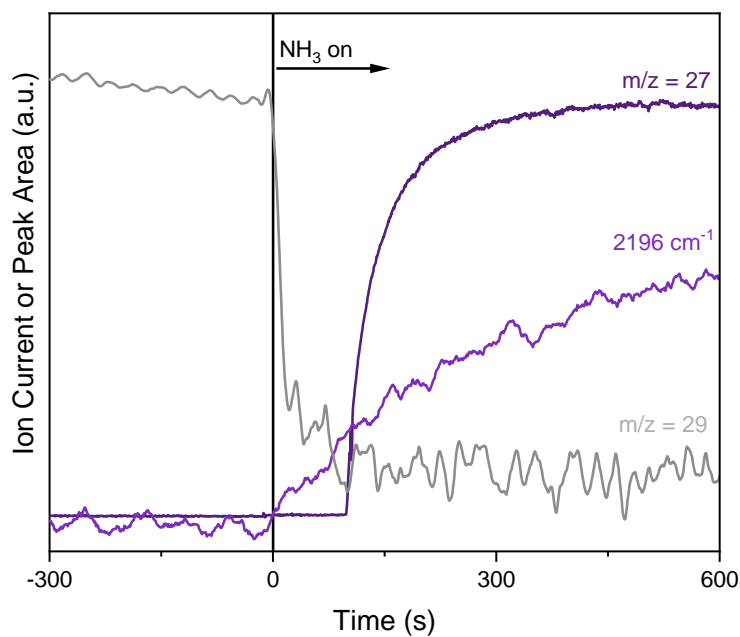


Figure S-6.3. Smoothed and truncated version of Figure S-5.3, which shows the temporal evolution of the area of the $\nu(\text{C}\equiv\text{N})$ mode as well as the signals of HCN ($m/z = 27$) and formaldehyde ($m/z = 29$) signals upon NH_3 addition. Experimental conditions: 150 ppm formaldehyde, 1000 ppm NH_3 and 5 vol% O_2 in Ar.

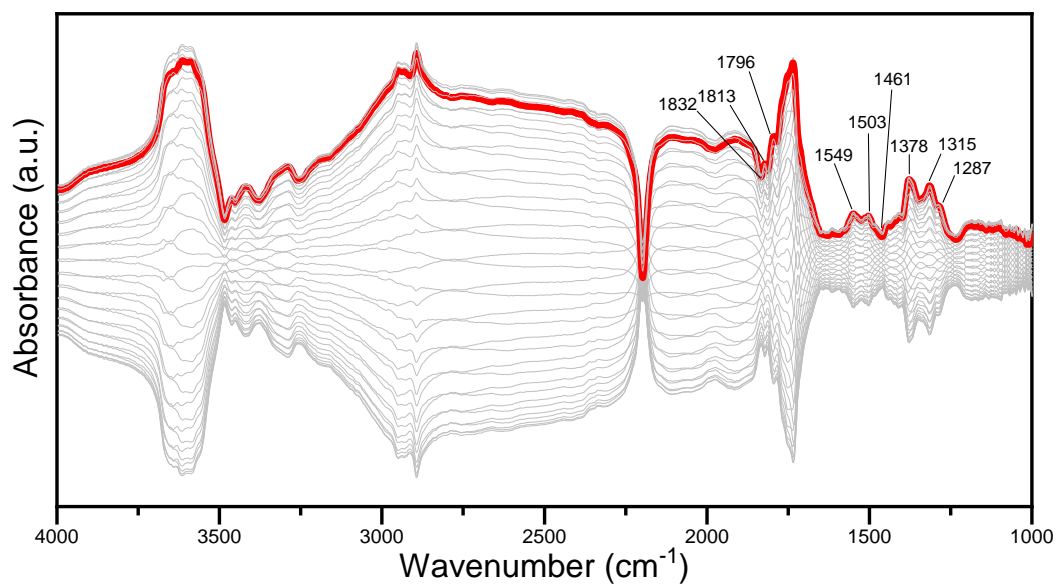


Figure S-6.4. Phase-resolved spectra as a result of 60-s pulses of 150 ppm formaldehyde in a gas feed containing 1000 ppm NH_3 and 5 vol% O_2 in Ar at 300 °C.

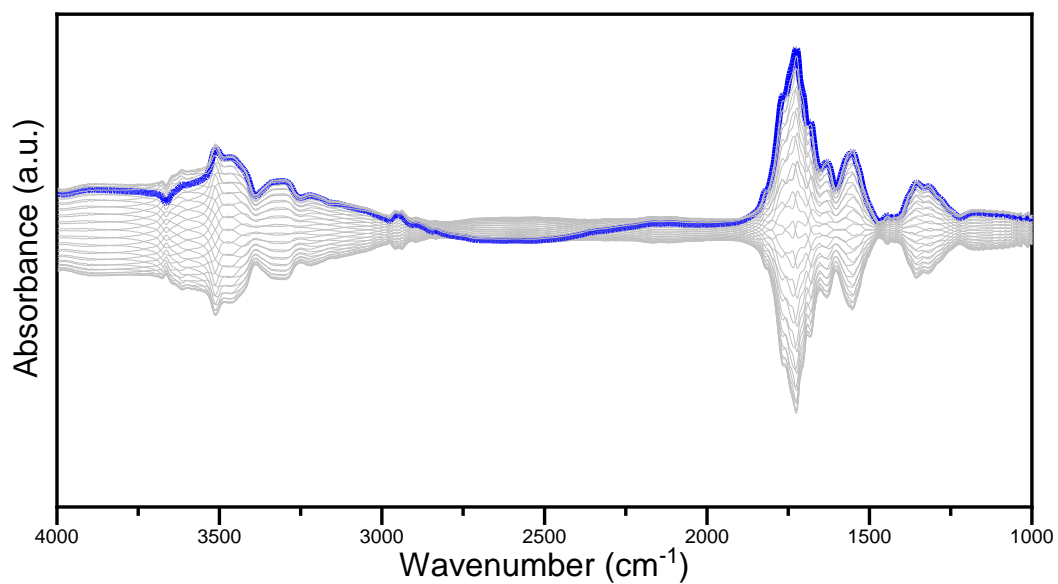


Figure S-6.5. Phase-resolved spectra as a result of 60-s pulses of 150 ppm formaldehyde in a gas feed containing 1000 ppm NH_3 , 2 vol% H_2O , and 5 vol% O_2 in Ar at 300 °C.

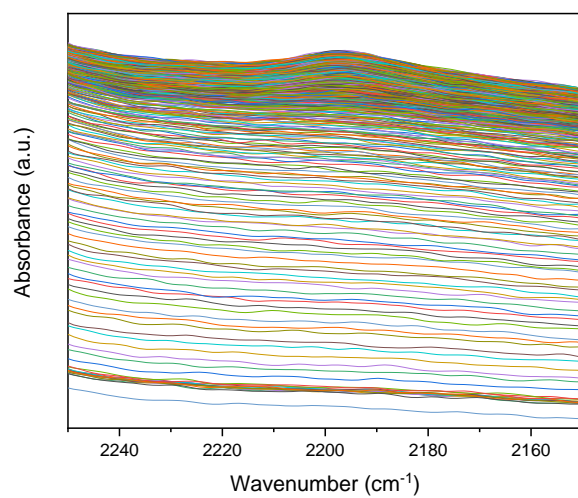


Figure S-6.6. Time-resolved spectra of the C≡N stretch region upon NH₃ addition to a formaldehyde-containing gas feed.

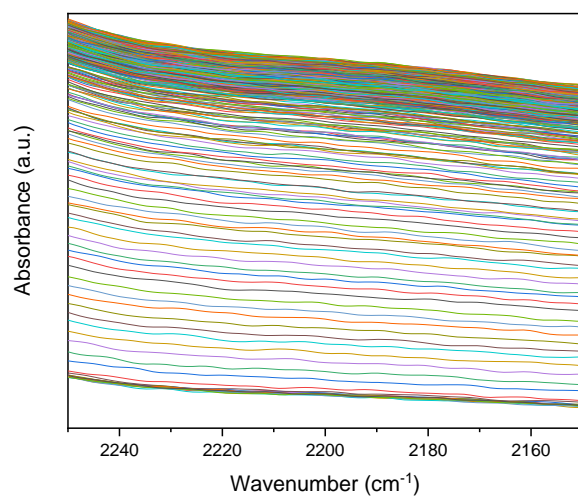


Figure S-6.7. Time-resolved spectra of the C≡N stretch region upon NH₃ addition to a formic acid-containing gas feed.

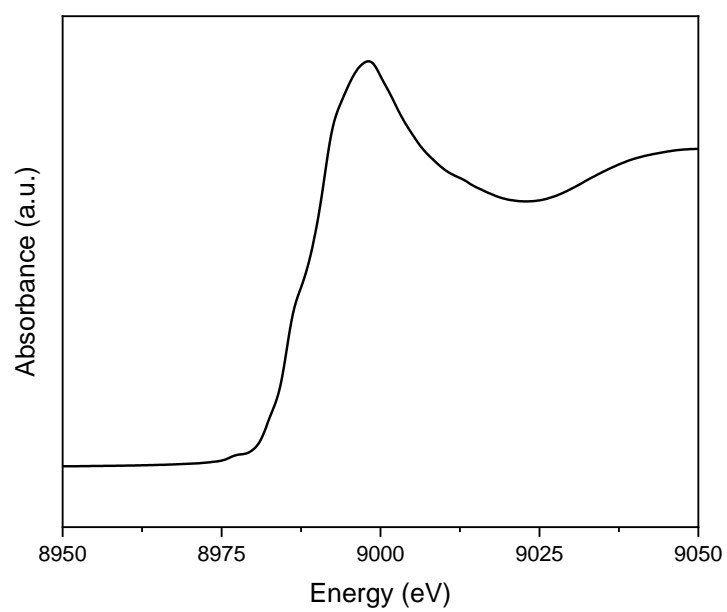
Supporting Information for Chapter 7

Figure S-7.1. XANES spectrum of Cu-SSZ-13 after activation under 5 vol% O₂ in Ar at 400 °C.

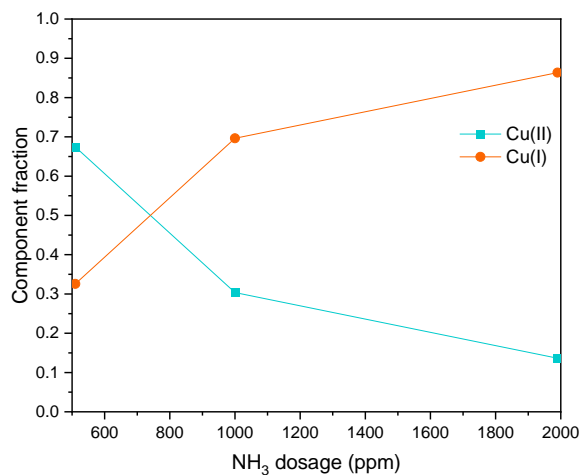


Figure S-7.2. Steady-state Cu(I) and Cu(II) speciation of Cu-SSZ-13 under SCR conditions at 200 °C. Experimental conditions: 500-2000 ppm NH₃, 1000 ppm NO, and 5 vol% O₂ balanced in Ar.

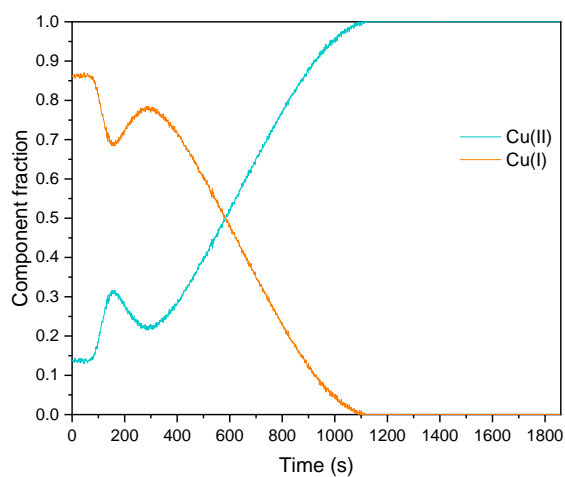


Figure S-7.3. Time-resolved Cu(I) and Cu(II) speciation of Cu-SSZ-13 upon cut-off of 2000 ppm NH₃ at 200 °C. Experimental conditions: 2000 ppm NH₃, 1000 ppm NO, and 5 vol% O₂ balanced in Ar.

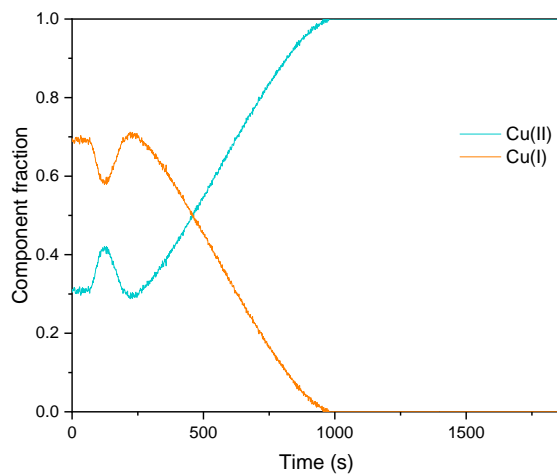


Figure S-7.4. Time-resolved Cu(I) and Cu(II) speciation of Cu-SSZ-13 upon cut-off of 1000 ppm NH_3 at 200 °C. Experimental conditions: 1000 ppm NH_3 , 1000 ppm NO, and 5 vol% O_2 balanced in Ar.

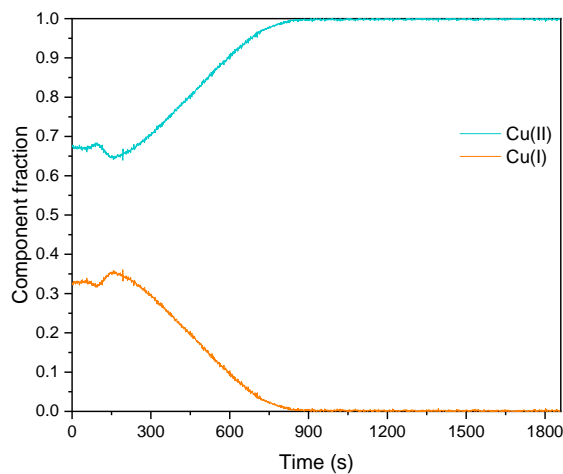


Figure S-7.5. Time-resolved Cu(I) and Cu(II) speciation of Cu-SSZ-13 upon cut-off of 500 ppm NH_3 at 200 °C. Experimental conditions: 500 ppm NH_3 , 1000 ppm NO, and 5 vol% O_2 balanced in Ar.

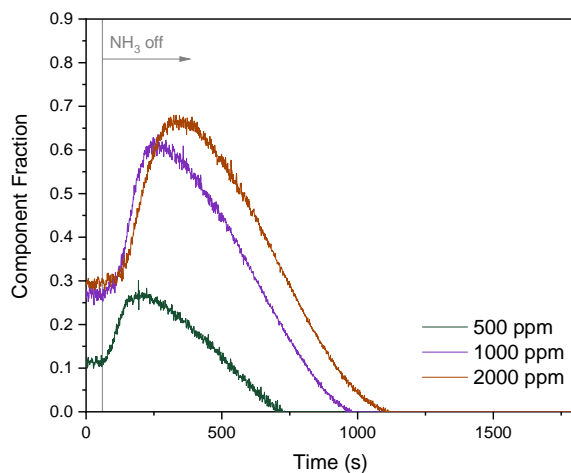


Figure S-7.6. Time-resolved evolution of the Cu(I)-Z fraction of Cu-SSZ-13 upon cut-off of NH_3 at 200 °C. Experimental conditions: 500-2000 ppm NH_3 , 1000 ppm NO, and 5 vol% O_2 balanced in Ar.

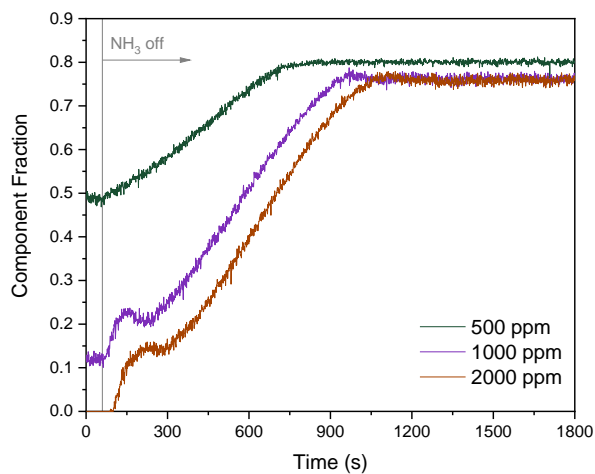


Figure S-7.7. Time-resolved evolution of the Cu(II)-Z fraction of Cu-SSZ-13 upon cut-off of NH_3 at 200 °C. Experimental conditions: 500-2000 ppm NH_3 , 1000 ppm NO, and 5 vol% O_2 balanced in Ar.

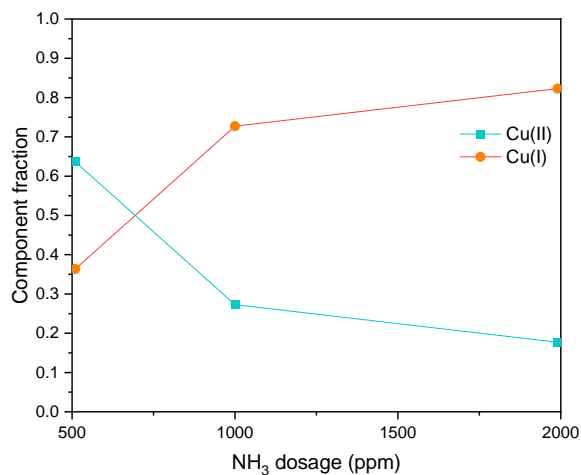


Figure S-7.8. Steady-state Cu(I) and Cu(II) speciation of Cu-SSZ-13 under SCR conditions at 300 °C. Experimental conditions: 500-2000 ppm NH₃, 1000 ppm NO, and 5 vol% O₂ balanced in Ar.

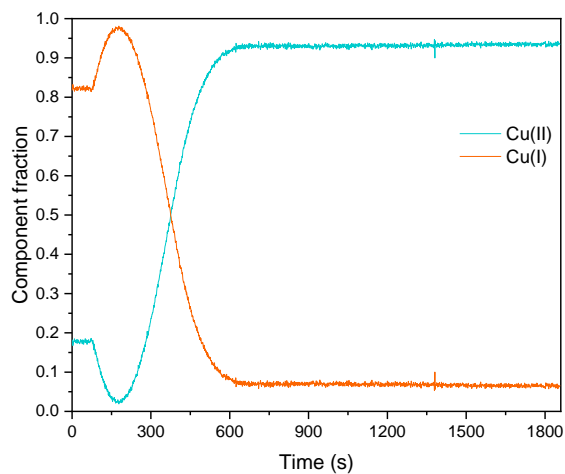


Figure S-7.9. Time-resolved Cu(I) and Cu(II) speciation of Cu-SSZ-13 upon cut-off of 2000 ppm NH₃ at 200 °C. Experimental conditions: 2000 ppm NH₃, 1000 ppm NO, and 5 vol% O₂ balanced in Ar.

Supporting Information for the Annex

The procedure for the laboratory experiment described in the Annex is given in the next pages.

In Situ Infrared Spectroscopy of NO_x Reduction Catalysts

Course Instructor: Rob Jeremiah G. Nuguid (rob.nuguid@psi.ch)

Objectives

- To familiarize with a typical experimental set-up used to investigate catalysts under in situ conditions
- To learn how to operate a modern Fourier-transform infrared spectrometer and analyze the corresponding spectroscopic data
- To practice writing technical and scientific publications

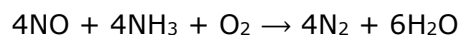
Introduction

When catalysis was first established two centuries ago, it emerged as an overwhelmingly empirical science whose progress relied heavily on chemical intuition and pure serendipity. The traditional view of a catalytic reactor was that of a “black box” which on the one hand managed to produce valuable chemical products, but on the other hand provided no real insight as to which molecular events are involved in the actual transformation. As such, trial and error constituted the bulk of catalyst discovery methods up until the early 20th century. A classic example is the development of the Haber-Bosch process: it was said that Haber and his co-workers at BASF had to test some 20,000 candidate materials before arriving at the optimum Fe-based catalyst formulation that set the standard for NH₃ synthesis today. As you can imagine, this process is not only resource-intensive but also time-consuming. During the last 100 years, however, catalysis science has undergone a renaissance. Modern spectroscopic techniques, coupled with theoretical and computational methods, have paved the way for a more systematic study of catalytic materials. Now we are equipped with tools that give us access to the molecular events happening in a chemical transformation. Knowing the reaction mechanism goes beyond mere scientific curiosity; rather, we can take advantage of this information to design improved and more durable catalytic materials in a rational manner.

Infrared (IR) spectroscopy was one of the first operando techniques to be applied in catalysis research. Although the IR region in its entirety spans a much wider range, the mid-IR region between 200 and 4,000 cm⁻¹ is the most relevant to us since it is where molecular vibrations are excited. For a particular vibration to be IR-active, the dipole moment of a molecule must change as a result of stretching or bending events after excitation. Consequently, diatomic molecules such as O₂ and N₂ cannot give rise to an IR

signal because they do not have a dipole moment while molecules possessing polar bonds with high ionic character (e.g., O-H and N-H) have IR-active modes. Many reactant molecules and adsorbates fall into the latter category, thus making IR spectroscopy a convenient method of catalyst characterization.

In this experiment, we will investigate a reaction that lies at the heart of worldwide pollution control strategies – the selective catalytic reduction of NO_x:



Left untreated, NO_x emissions not only contribute to photochemical smog formation and acid rain, but also give rise to a myriad of respiratory diseases. Hence, SCR is both industrially and environmentally important.

We will use IR spectroscopy to investigate the processes happening on the surface of a V₂O₅-WO₃/TiO₂ catalyst such as the adsorption of the reactants and their consumption under reaction conditions.

Experimental Setup

The set-up consists of three major parts (Figure 1):

- A set of mass flow controllers that dose Ar, O₂, H₂, NO, and NH₃ in conjunction with a platinum (Pt)-based catalyst to generate water from H₂ and O₂;
- A spectroscopic cell where the catalyst powder is placed; and
- An IR spectrometer (Bruker Vertex70) equipped with a diffuse reflectance accessory (Harrick Praying Mantis™).

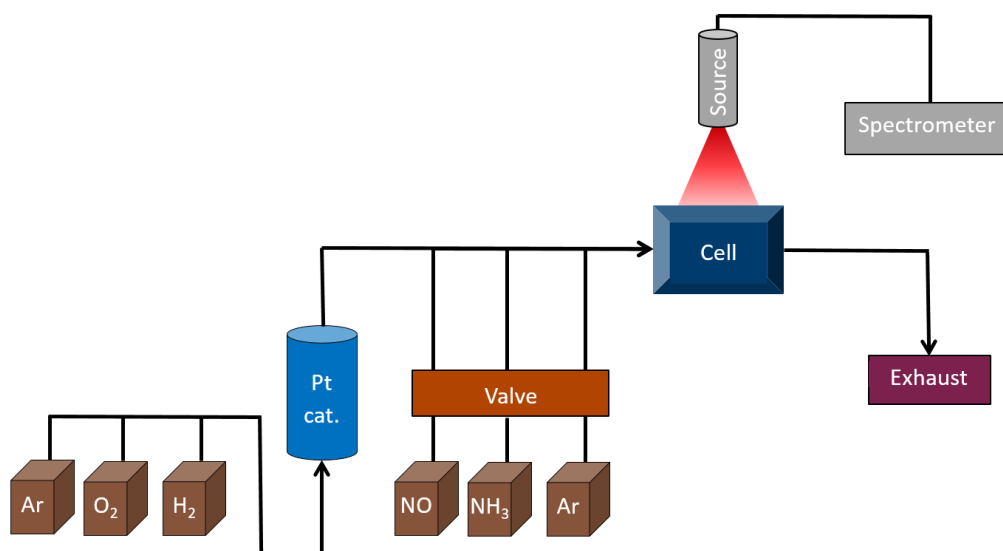


Figure 1. Schematic diagram of the experimental set-up.

Procedure

1. Load approximately 40 mg of the catalyst powder (2 wt% V_2O_5 /10 wt% WO_3/TiO_2) into the sample holder of the spectroscopic cell. Flatten the sample using a spatula. Cover the cell with a 2-mm CaF_2 window.
2. Mount the cell into the sample stage, and connect it with the gas inlet and outlet tubes.
3. Set the gas flow to $100 \text{ mL} \cdot \text{min}^{-1}$ with a composition of 5 vol% O_2/Ar . Heat the cell to $400 \text{ }^\circ\text{C}$ at a rate of $20 \text{ }^\circ\text{C} \cdot \text{min}^{-1}$. Maintain the temperature at this setting for 30 min.
4. Cool down the cell to $250 \text{ }^\circ\text{C}$ at a rate of $20 \text{ }^\circ\text{C} \cdot \text{min}^{-1}$.
5. Add liquid nitrogen into the compartment for the detector of the IR spectrometer. Fill it to the brim. **IMPORTANT:** Wear a laboratory coat, goggles, and gloves when handling liquid nitrogen.
6. Optimize the signal by adjusting the height of the cell. The cell should be as close to the mirrors as possible without having any specular reflection from the window.
7. Record a background spectrum (100 scans, 80 kHz). Save the file as **IR-BKG-O2-Ar-250C**. Use this background spectrum for all the succeeding measurements.
8. *Ammonia adsorption*. Record IR spectra every 5 seconds for 10 min (10 scans, 80 kHz). After 30 s of measurement, introduce NH_3 by changing the gas composition to 1000 ppm NH_3 /5 vol% O_2/Ar . Save the file as **IR-NH3-ads-O2-Ar-250C**.
9. *Ammonia desorption*. Record IR spectra every 5 seconds for 10 min (10 scans, 80 kHz). After 30 s of measurement, remove NH_3 by changing the gas composition to 5 vol% O_2/Ar . Save the file as **IR-NH3-des-O2-Ar-250C**.
10. *Reaction with nitric oxide*. Record IR spectra every 5 seconds for 10 min (10 scans, 80 kHz). After 30 s of measurement, introduce NO by changing the gas composition to 1000 ppm NO /5 vol% O_2/Ar . Save the file as **IR-NO-rxn-O2-Ar-250C**.
11. *Nitric oxide desorption*. Record IR spectra every 5 seconds for 10 min (10 scans, 80 kHz). After 30 s of measurement, remove NO by changing the gas composition to 5 vol% O_2/Ar . Save the file as **IR-NO-des-O2-Ar-250C**.
12. *Water adsorption*. Record IR spectra every 5 seconds for 30 min (10 scans, 80 kHz). After 30 s of measurement, introduce H_2O by changing the gas composition to 2 vol% H_2O /5 vol% O_2/Ar . Save the file as **IR-H2O-ads-O2-Ar-250C**.
13. *Ammonia adsorption in the presence of water*. Record IR spectra every 5 seconds for 10 min (10 scans, 80 kHz). After 30 s of measurement, introduce NH_3 by changing the gas composition to 500 ppm NH_3 /2 vol% H_2O /5 vol% O_2/Ar . Save the file as **IR-NH3-ads-H2O-O2-Ar-250C**.
14. Cool down the cell to room temperature and remove the catalyst sample.

Report

The written report should contain the following parts:

1. Title page including author names
2. Introduction
3. Methods and Materials
4. Results and Discussion
5. Conclusions

The following items must be included and/or discussed in the report:

1. Prior to the experiment, the catalyst sample was heated to 400 °C for 30 min under an oxidative atmosphere. What is the purpose of this step?
2. Plot the last spectrum collected in the **IR-NH3-ads-O2-Ar-250C** dataset. Based on the existing information available in the scientific literature, assign the peaks associated with the adsorbed species. Which adsorbed species can you detect and on which adsorption site? Which of these adsorption sites are associated with V, W, and Ti?
3. In the preceding plot, why are some IR peaks positive and some are negative?
4. Plot the temporal evolution of the signals (normalized area) associated with the adsorption sites for NH₃ in the **IR-NH3-des-O2-Ar-250C** dataset. What can you say about the relative stability of the NH₃ adsorption sites?
5. Plot the temporal evolution of the NH₃ adsorption sites (normalized area) in the **IR-NO-rxn-O2-Ar-250C** dataset. Is there a difference in the NH₃ consumption in the different adsorption sites?
6. Compare the first and the last spectra in the **IR-NO-des-O2-Ar-250C** dataset. What can you say about NO adsorption on the catalyst?
7. Plot the last spectrum collected in the **IR-H2O-ads-O2-Ar-250C** dataset. Based on the existing information available in the scientific literature, assign the peaks associated with the adsorbed species. Which of these adsorption sites are associated with V, W, and Ti?
8. Compare the last spectra collected in the **IR-H2O-ads-O2-Ar-250C** and **IR-NH3-ads-H2O-O2-Ar-250C** datasets. Which species is more strongly adsorbed on the catalyst surface: H₂O or NH₃?
9. How can you use the information you obtained from IR spectroscopy to develop a more active SCR catalyst?

References

- [1] J. H. Seinfeld. Urban air pollution: State of the science. *Science* **1989**, 243, 745-752.
- [2] J. Fengler. Air pollution in the last 50 years – from local to global. *Atmos. Environ.* **2009**, 43, 13-22.
- [3] A. J. Haagen-Smit. Chemistry and physiology of Los Angeles smog. *Ind. Eng. Chem.* **1952**, 44, 1342-1346.
- [4] G. E. Likens, F. H. Bormann, N. M. Johnson. Acid rain. *Environ. Sci. Policy* **1972**, 14, 33-40.
- [5] T.-M. Chen, W. G. Kuschner, J. Gokhale, S. Shofer. Outdoor air pollution: Nitrogen dioxide, sulfur dioxide, and carbon monoxide health effects. *Am. J. Med.* **2007**, 333, 249-256.
- [6] M. Kattan, P. J. Gergen, P. Eggleston, C. M. Visness, H. E. Mitchell. Health effects of indoor nitrogen dioxide and passive smoking on urban asthmatic children. *J. Allergy Clin. Immunol.* **2007**, 120, 618-624.
- [7] M. Takagi, T. Kawai, M. Soma, T. Onishi, K. Tamaru. The mechanism of the reaction between NO_x and NH₃ on V₂O₅ in the presence of oxygen. *J. Catal.* **1977**, 50, 441-446.
- [8] R. Mrad, A. Aissat, R. Cousin, D. Courcot, S. Siffert. Catalysts for NO_x selective catalytic reduction by hydrocarbons (HC-SCR). *Appl. Catal. A* **2015**, 504, 542-548.
- [9] F. Radtke, R. A. Koepfel, A. Baiker. Formation of hydrogen cyanide over Cu/ZSM-5 catalyst used for the removal of nitrogen oxides from exhausts of lean-burn engines. *Environ. Sci. Technol.* **1995**, 29, 2703-2705.
- [10] C. N. Costa, P. G. Savva, J. L. G. Fierro, A. M. Efstathiou. Efstathiou. Industrial H₂-SCR of NO on a novel Pt/MgO–CeO₂ catalyst. *Appl. Catal. B* **2007**, 75, 147-156.
- [11] P. L. T. Gabrielsson. Urea-SCR in automotive applications. *Top. Catal.* **2004**, 28, 177-184.
- [12] M. Koebel, M. Elsener, G. Madia. Reaction pathways in the selective catalytic reduction process with NO and NO₂ at low temperatures. *Ind. Eng. Chem. Res.* **2001**, 40, 52-59.
- [13] M. Koebel, G. Madia, F. Raimondi, A. Wokaun. Enhanced reoxidation of vanadia by NO₂ in the fast SCR reaction. *J. Catal.* **2002**, 209, 159-165.
- [14] A. Kato, S. Matsuda, T. Kamo, F. Nakajima, H. Kuroda, T. Narita. Reaction between nitrogen oxide (NO_x) and ammonia on iron oxide-titanium oxide catalyst. *J. Phys. Chem.* **1981**, 85, 4099-4102.
- [15] G. Madia, M. Koebel, M. Elsener, A. Wokaun. Side reactions in the selective catalytic reduction of NO_x with various NO₂ fractions. *Ind. Eng. Chem. Res.* **2002**, 41, 4008-4015.
- [16] M. Koebel, G. Madia, M. Elsener. Selective catalytic reduction of NO and NO₂ at low temperatures. *Catal. Today* **2002**, 73, 239-247.

-
- [17] M. Amiridis, I. Wachs, G. Deo, J.-M. Jehng, D. Soung Kim. Reactivity of V_2O_5 catalysts for the selective catalytic reduction of NO by NH_3 : Influence of vanadia loading, H_2O , and SO_2 . *J. Catal.* **1996**, *161*, 247–253.
- [18] I. Nova, E. Tronconi. *Urea-SCR Technology for DeNO_x After-treatment of Diesel Exhausts*. Springer: New York, **2014**.
- [19] A. Marberger, M. Elsener, D. Ferri, O. Kröcher. VO_x surface coverage optimization of V_2O_5/WO_3-TiO_2 SCR catalysts by variation of the V loading and by aging. *Catalysts* **2015**, *5*, 1704-1720.
- [20] G. T. Went, L. J. Leu, R. R. Rosin, A. T. Bell. The effects of structure on the catalytic activity and selectivity of V_2O_5/TiO_2 for the reduction of NO by NH_3 . *J. Catal.* **1992**, *134*, 492-505.
- [21] I. E. Wachs. Raman and IR studies of surface metal oxide species on oxide supports: Supported metal oxide catalysts. *Catal. Today* **1996**, *27*, 437-455.
- [22] G. Ramis, G. Busca, F. Bregani, P. Forzatti. Fourier transform-infrared study of the adsorption and coadsorption of nitric oxide, nitrogen dioxide and ammonia on vanadia-titania and mechanism of selective catalytic reduction. *Appl. Catal.* **1990**, *64*, 259-278.
- [23] P. Forzatti, L. Lietti. Recent advances in de-NO_xing catalysis for stationary applications. *Heterogen. Chem. Rev.* **1996**, *3*, 33-51.
- [24] A. Marberger, M. Elsener, R. J. G. Nuguid, D. Ferri, O. Kröcher. Thermal activation and aging of a V_2O_5/WO_3-TiO_2 catalyst for the selective catalytic reduction of NO with NH_3 . *Appl. Catal. A* **2019**, *573*, 64-72.
- [25] C. Cristiani, M. Bellotto, P. Forzatti, F. Bregani. On the morphological properties of tungsta-titania de-NO_xing catalysts. *J. Mater. Res.* **1993**, *8*, 2019-2025.
- [26] T. Yamaguchi, Y. Tanaka, K. Tanabe. Isomerization and disproportionation of olefins over tungsten oxides supported on various oxides. *J. Catal.* **1980**, *65*, 442-447.
- [27] N. R. Jaegers, J.-K. Lai, Y. He, E. Walter, D. A. Dixon, M. Vasiliu, Y. Chen, C. Wang, M. Y. Hu, K. T. Mueller, I. E. Wachs, Y. Wang, J. Z. Hu. Mechanism by which tungsten oxide promotes the activity of supported V_2O_5/TiO_2 catalysts for NO_x abatement: Structural effects revealed by ^{51}V MAS NMR spectroscopy. *Angew. Chem. Int. Ed.* **2019**, *58*, 12609-12616.
- [28] L. J. Alemany, L. Lietti, N. Ferlazzo, P. Forzatti, G. Busca, E. Giamello, F. Bregani. Reactivity and physicochemical characterization of $V_2O_5-WO_3/TiO_2$ de-NO_x catalysts. *J. Catal.* **1995**, *155*, 117-130.
- [29] J. P. Chen, R. T. Yang. Role of WO_3 in mixed $V_2O_5-WO_3/TiO_2$ catalysts for selective catalytic reduction of nitric oxide with ammonia. *Appl. Catal. A* **1992**, *80*, 135-148.
- [30] G. Ramis, G. Busca, C. Cristiani, L. Lietti, P. Forzatti, F. Bregani. Characterization of tungsta-titania catalysts. *Langmuir* **1992**, *8*, 1744-1749.
- [31] M. Inomata, A. Miyamoto, Y. Murakami. Mechanism of the reaction of NO and NH_3 on vanadium oxide catalyst in the presence of oxygen under the dilute gas condition. *J. Catal.* **1980**, *62*, 140-148.
- [32] F. J. J. G. Janssen, F. M. G. Van den Kerkhof, H. Bosch, J. R. H. Ross. Mechanism of the reaction of nitric oxide, ammonia, and oxygen over vanadia catalysts. 1. The role of oxygen studied by way of isotopic transients under dilute conditions. *J. Phys. Chem.* **1987**, *91*, 5921-5927.
- [33] F. J. J. G. Janssen, F. M. G. Van den Kerkhof, H. Bosch, J. R. H. Ross. Mechanism of the reaction of nitric oxide, ammonia, and oxygen over vanadia catalysts. 2.

- Isotopic transient studies with oxygen-18 and nitrogen-15. *J. Phys. Chem.* **1987**, *91*, 6633-6638.
- [34] G. Ramis, L. Yi, G. Busca. Ammonia activation over catalysts for the selective catalytic reduction of NO_x and the selective catalytic oxidation of NH₃. An FT-IR study. *Catal. Today* **1996**, *28*, 373-380.
- [35] G. Busca, L. Lietti, G. Ramis, F. Berti. Chemical and mechanistic aspects of the selective catalytic reduction of NO_x by ammonia over oxide catalysts: A review. *Appl. Catal. B* **1998**, *18*, 1-36.
- [36] N.-Y. Topsøe. Mechanism of the selective catalytic reduction of nitric oxide by ammonia elucidated by in situ on-line Fourier transform infrared spectroscopy. *Science* **1994**, *265*, 1217-1219.
- [37] N. Y. Topsøe, H. Topsoe, J. A. Dumesic. Vanadia/titania catalysts for selective catalytic reduction (SCR) of nitric oxide by ammonia I. Combined temperature programmed in situ FTIR and on-line mass spectroscopy studies. *J. Catal.* **1995**, *151*, 226-240.
- [38] A. Marberger, D. Ferri, M. Elsener, O. Kröcher. The significance of Lewis acid sites for the selective catalytic reduction of nitric oxide on vanadium-based catalysts. *Angew. Chem. Int. Ed.* **2016**, *55*, 11989-11994.
- [39] M. Iwamoto, S. Yokoo, K. Sakai, S. Kagawa. Catalytic decomposition of nitric oxide over copper(II)-exchanged, Y-type zeolites. *J. Chem. Soc., Faraday Trans. 1* **1981**, *77*, 1629-1638.
- [40] W. Held, A. König, T. Richter, L. Puppe. Catalytic NO_x reduction in net oxidizing exhaust gas. *SAE Trans.* **1990**, *99*, 209-216.
- [41] C. Negri, M. Signorile, N. G. Porcaro, E. Borfecchia, G. Berlier, T. V. W. Janssens, S. Bordiga. Dynamic Cu^{II}/Cu^I speciation in Cu-CHA catalysts by in situ diffuse reflectance UV-Vis-NIR spectroscopy. *Appl. Catal. A* **2019**, *578*, 1-9.
- [42] J. H. Kwak, D. Tran, S. D. Burton, J. Szanyi, J. H. Lee, C. H. F. Peden. Effects of hydrothermal aging on NH₃-SCR reaction over Cu/zeolites. *J. Catal.* **2012**, *287*, 203-209.
- [43] B. I. Palella, M. Cadoni, A. Frache, H. O. Pastore, R. Pirone, G. Russo, S. Coluccia, L. Marchese. On the hydrothermal stability of CuAPSO-34 microporous catalysts for N₂O decomposition: A comparison with CuZSM-5. *J. Catal.* **2003**, *217*, 100-106.
- [44] M. Nielsen, A. Hafreager, R. Y. Brogaard, K. De Wispelaere, H. Falsig, P. Beato, V. Van Speybroeck, S. Svelle. Collective action of water molecules in zeolite dealumination. *Catal. Sci. Technol.* **2019**, *9*, 3721-3725.
- [45] M.-C. Silaghi, C. Chizallet, P. Raybaud. Challenges on molecular aspects of dealumination and desilication of zeolites. *Microporous Mesoporous Mater.* **2014**, *191*, 82-96.
- [46] D. Wang, L. Zhang, J. Li, K. Kamasamudram, W. S. Epling. NH₃-SCR over Cu/SAPO-34 – zeolite acidity and Cu structure changes as a function of Cu loading. *Catal. Today* **2014**, *231*, 64-74.
- [47] D. W. Fickel, E. D'Addio, J. A. Lauterbach, R. F. Lobo. The ammonia selective catalytic reduction activity of copper-exchanged small-pore zeolites. *Appl. Catal. B* **2011**, *102*, 441-448.
- [48] B. M. Lok, C. A. Messina, R. L. Patton, R. T. Gajek, T. R. Cannan, E. M. Flanigen. Silicoaluminophosphate molecular sieves: Another new class of microporous crystalline inorganic solids. *J. Am. Chem. Soc.* **1984**, *106*, 6092-6093.
- [49] L. Wang, J. R. Gaudet, W. Li, D. Weng. Migration of Cu species in Cu/SAPO-34 during hydrothermal aging. *J. Catal.* **2013**, *306*, 68-77.

-
- [50] D. Wang, Y. Jangjou, Y. Liu, M. K. Sharma, J. Luo, J. Li, K. Kamasamudram, W. S. Epling. A comparison of hydrothermal aging effects on NH_3 -SCR of NO_x over Cu-SSZ-13 and Cu-SAPO-34 catalysts. *Appl. Catal. B* **2015**, *165*, 438-445.
- [51] K. Leistner, L. Olsson. Deactivation of Cu/SAPO-34 during low-temperature NH_3 -SCR. *Appl. Catal. B* **2015**, *165*, 192-199.
- [52] A. Wang, Y. Chen, E. D. Walter, N. M. Washton, D. Mei, T. Varga, Y. Wang, J. Szanyi, Y. Wang, C. H. F. Peden, F. Gao. Unraveling the mysterious failure of Cu/SAPO-34 selective catalytic reduction catalysts. *Nat. Commun.* **2019**, *10*, 1137.
- [53] A. H. Clark, R. J. G. Nuguid, P. Steiger, A. Marberger, A. W. Petrov, D. Ferri, M. Nachttegaal, O. Kröcher. Selective catalytic reduction of NO with NH_3 on Cu-SSZ-13: Deciphering the low and high-temperature rate-limiting steps by transient XAS experiments. *ChemCatChem* **2019**, *12*, 1429-1435.
- [54] T. V. W. Janssens, H. Falsig, L. F. Lundegaard, P. N. R. Vennestrøm, S. B. Rasmussen, P. G. Moses, F. Giordanino, E. Borfecchia, K. A. Lomachenko, C. Lamberti, S. Bordiga, A. Godiksen, S. Mossin, P. Beato. A consistent reaction scheme for the selective catalytic reduction of nitrogen oxides with ammonia. *ACS Catal.* **2015**, *5*, 2832-2845.
- [55] A. Marberger, A. W. Petrov, P. Steiger, M. Elsener, O. Kröcher, M. Nachttegaal, D. Ferri. Time-resolved copper speciation during selective catalytic reduction of NO on Cu-SSZ-13. *Nat. Catal.* **2018**, *1*, 221-227.
- [56] D. Zhang, R. T. Yang. N_2O formation pathways over zeolite-supported Cu and Fe catalysts in NH_3 -SCR. *Energy Fuels* **2018**, *32*, 2170-2182.
- [57] O. Kröcher, M. Devadas, M. Elsener, A. Wokaun, N. Söger, M. Pfeifer, Y. Demel, L. Musmann. Investigation of the selective catalytic reduction of NO by NH_3 on Fe-ZSM5 monolith catalysts. *Appl. Catal. B* **2006**, *66*, 208-216.
- [58] M. Colombo, I. Nova, E. Tronconi. A comparative study of the NH_3 -SCR reactions over a Cu-zeolite and a Fe-zeolite catalyst. *Catal. Today* **2010**, *151*, 223-230.
- [59] L. Čapek, V. Kreibich, J. Dědeček, T. Grygar, B. Wichterlová, Z. Sobalík, J. A. Martens, R. Brosius, V. Tokarová. Analysis of Fe species in zeolites by UV-Vis-NIR, IR spectra and voltammetry. Effect of preparation, Fe loading and zeolite type. *Microporous Mesoporous Mater.* **2005**, *80*, 279-289.
- [60] S. Brandenberger, O. Kröcher, A. Tissler, R. Althoff. Estimation of the fractions of different nuclear iron species in uniformly metal-exchanged Fe-ZSM-5 samples based on a Poisson distribution. *Appl. Catal. A* **2010**, *373*, 168-175.
- [61] M. S. Kumar, M. Schwidder, W. Grünert, A. Brückner. On the nature of different iron sites and their catalytic role in Fe-ZSM-5 de NO_x catalysts: New insights by a combined EPR and UV/Vis spectroscopic approach. *J. Catal.* **2004**, *227*, 384-397.
- [62] M. Høj, M. J. Beier, J. D. Grunwaldt, S. Dahl. The role of monomeric iron during the selective catalytic reduction of NO_x by NH_3 over Fe-BEA zeolite catalysts. *Appl. Catal. B* **2009**, *93*, 166-176.
- [63] S. Brandenberger, O. Kröcher, A. Tissler, R. Althoff. The state of the art in selective catalytic reduction of NO_x by ammonia using metal-exchanged zeolite catalysts. *Catal. Rev.* **2008**, *50*, 492-531.
- [64] L. Ma, J. Li, Y. Cheng, C. K. Lambert, L. Fu. Propene poisoning on three typical Fe-zeolites for SCR of NO_x with NH_3 : From mechanism study to coating modified architecture. *Environ. Sci. Technol.* **2012**, *46*, 1747-1754.
- [65] P. Boroń, L. Chmielarz, S. Dzwigaj. Influence of Cu on the catalytic activity of FeBEA zeolites in SCR of NO with NH_3 . *Appl. Catal. B* **2015**, *168-169*, 377-384.

-
- [66] O. Kröcher, M. Elsener. Combination of V_2O_5/WO_3-TiO_2 , Fe-ZSM5, and Cu-ZSM5 catalysts for the selective catalytic reduction of nitric oxide with ammonia. *Ind. Eng. Chem. Res.* **2008**, *47*, 8588-8593.
- [67] P. S. Metkar, M. P. Harold, V. Balakotaiah. Selective catalytic reduction of NO_x on combined Fe- and Cu-zeolite monolithic catalysts: Sequential and dual layer configurations. *Appl. Catal. B* **2012**, *111-112*, 67-80.
- [68] J. Liu, Y. Du, J. Liu, Z. Zhao, K. Cheng, Y. Chen, Y. Wei, W. Song, X. Zhang. Design of MoFe/Beta@CeO₂ catalysts with a core-shell structure and their catalytic performances for the selective catalytic reduction of NO with NH₃. *Appl. Catal. B* **2017**, *203*, 704-714.
- [69] M. Iwasaki, K. Yamazaki, H. Shinjoh. NO_x reduction performance of fresh and aged Fe-zeolites prepared by CVD: Effects of zeolite structure and Si/Al₂ ratio. *Appl. Catal. B* **2011**, *102*, 302-309.
- [70] F. Gao, M. Kollár, R. K. Kukkadapu, N. M. Washton, Y. Wang, J. Szanyi, C. H. F. Peden. Fe/SSZ-13 as an NH₃-SCR catalyst: A reaction kinetics and FTIR/Mössbauer spectroscopic study. *Appl. Catal. B* **2015**, *164*, 407-419.
- [71] M. P. Ruggeri, T. Selleri, M. Colombo, I. Nova, E. Tronconi. Identification of nitrites/HONO as primary products of NO oxidation over Fe-ZSM-5 and their role in the standard SCR mechanism: A chemical trapping study. *J. Catal.* **2014**, *311*, 266-270.
- [72] P. S. Metkar, N. Salazar, R. Muncrief, V. Balakotaiah, M. P. Harold. Selective catalytic reduction of NO with NH₃ on iron zeolite monolithic catalysts: Steady-state and transient kinetics. *Appl. Catal. B* **2011**, *104*, 110-126.
- [73] A. Urakawa, T. Bürgi, A. Baiker. Sensitivity enhancement and dynamic behavior analysis by modulation excitation spectroscopy: Principle and application in heterogeneous catalysis. *Chem. Eng. Sci.* **2008**, *63*, 4902-4909.
- [74] S. B. Rasmussen, R. Portela, P. Bazin, P. Ávila, M. A. Bañares, M. Daturi. Transient operando study on the NH₃/NH₄⁺ interplay in V-SCR monolithic catalysts. *Appl. Catal. B* **2018**, *224*, 109-115.
- [75] R. Kopelent, J. A. van Bokhoven, J. Szlachetko, J. Edebeli, C. Paun, M. Nachtegaal, O. V. Safonova. Catalytically active and spectator Ce³⁺ in ceria-supported metal catalysts. *Angew. Chem. Int. Ed.* **2015**, *54*, 8728-8731.
- [76] J. K. Crandall, W. W. Conover, J. B. Komin, W. H. Machleder. Allene epoxidation. Isolation of reactive intermediates from hindered allenes. *J. Org. Chem.* **1974**, *39*, 1723-1729.
- [77] G. Proulx, R. G. Bergman. Synthesis, structures, and kinetics and mechanism of decomposition of terminal metal azide complexes: Isolated intermediates in the formation of imidometal complexes from organic azides. *Organometallics* **1996**, *15*, 684-692.
- [78] J. Grdadolnik. Infrared difference spectroscopy Part I. Interpretation of the difference spectrum. *Vibr. Spectrosc.* **2003**, *31*, 279-288.
- [79] D. Baurecht, U. P. Fringeli. Quantitative modulated excitation Fourier transform infrared spectroscopy. *Rev. Sci. Instrum.* **2001**, *72*, 3782-3792.
- [80] T. Bürgi, A. Baiker. In situ infrared spectroscopy of catalytic solid-liquid interfaces using phase-sensitive detection: Enantioselective hydrogenation of a pyrone over Pd/TiO₂. *J. Phys. Chem. B* **2002**, *106*, 10649-10658.
- [81] A. Urakawa, R. Wirz, T. Bürgi, A. Baiker. ATR-IR flow-through cell for concentration modulation excitation spectroscopy: Diffusion experiments and simulations. *J. Phys. Chem. B* **2003**, *107*, 13061-13068.

-
- [82] R. Caliendo, D. Chernyshov, H. Emerich, M. Milanesio, L. Palin, A. Urakawa, W. van Beek, D. Viterbo. Patterson selectivity by modulation-enhanced diffraction. *J. Appl. Crystallogr.* **2012**, 45, 458-470.
- [83] D. Baurecht, I. Porth, U. P. Fringeli. A new method of phase sensitive detection in modulation spectroscopy applied to temperature induced folding and unfolding of RNase A. *Vib. Spectrosc.* **2002**, 30, 85-92.
- [84] M. Schwarzott, P. Lasch, D. Baurecht, D. Naumann, U. P. Fringeli. Electric field-induced changes in lipids investigated by modulated excitation FTIR spectroscopy. *Biophys. J.* **2004**, 86, 285-295.
- [85] M. Borges Ordoño, S. Yasumura, P. Glatzel, A. Urakawa. Synergistic interplay of Zn and Rh-Cr promoters on Ga₂O₃ based photocatalysts for water splitting. *Phys. Chem. Chem. Phys.* **2018**, 20, 23515-23521.
- [86] W. van Beek, H. Emerich, A. Urakawa, L. Palin, M. Milanesio, R. Caliendo, D. Viterbo, D. Chernyshov. Untangling diffraction intensity: Modulation enhanced diffraction on ZrO₂ powder. *J. Appl. Crystallogr.* **2012**, 45, 738-747.
- [87] N. Maeda, F. Meemken, K. Hungerbühler, A. Baiker. Spectroscopic detection of active species on catalytic surfaces: Steady-state versus transient method. *CHIMIA* **2012**, 66, 664-667.
- [88] F. C. Meunier. The design and testing of kinetically-appropriate operando spectroscopic cells for investigating heterogeneous catalytic reactions. *Chem. Soc. Rev.* **2010**, 39, 4602-4614.
- [89] P. D. Srinivasan, S. R. Nitz, K. J. Stephens, E. Atchison, J. J. Bravo-Suarez. Modified Harrick reaction cell for in situ/operando fiber optics diffuse reflectance UV-visible spectroscopic characterization of catalysts. *Appl. Catal. A* **2018**, 561, 7-18.
- [90] B. S. Patil, P. D. Srinivasan, E. Atchison, H. Zhu, J. J. Bravo-Suárez. Design, modelling, and application of a low void-volume in situ diffuse reflectance spectroscopic reaction cell for transient catalytic studies. *React. Chem. Eng.* **2019**, 4, 667-678.
- [91] G. L. Chiarello, M. Nachtegaal, V. Marchionni, L. Quaroni, D. Ferri. Adding diffuse reflectance infrared Fourier transform spectroscopy capability to extended X-ray-absorption fine structure in a new cell to study solid catalysts in combination with a modulation approach. *Rev. Sci. Instrum.* **2014**, 85, 074102.
- [92] M. M. Schubert, T. P. Häring, G. Bräth, H. A. Gasteiger, R. J. Behm. New DRIFTS cell design for the simultaneous acquisition of IR spectra and kinetic data using on-line product analysis. *Appl. Spectrosc.* **2001**, 55, 1537-1543.
- [93] A. Bansode, G. Guiler, V. Cuartero, L. Simonelli, M. Avila, A. Urakawa. Performance and characteristics of a high pressure, high temperature capillary cell with facile construction for operando X-ray absorption spectroscopy. *Rev. Sci. Instrum.* **2014**, 85, 084105.
- [94] V. Dal Santo, C. Dossi, A. Fusi, R. Psaro, C. Mondelli, S. Recchia. Fast transient infrared studies in material science: Development of a novel low dead-volume, high temperature DRIFTS cell. *Talanta* **2005**, 66, 674-682.
- [95] M. Sridhar, D. Ferri, J. A. van Bokhoven, O. Kröcher. Water-assisted oxygen activation during gold-catalyzed formic acid decomposition under SCR-relevant conditions. *J. Catal.* **2017**, 349, 197-207.
- [96] H. S. Fogler. *Elements of Chemical Reaction Engineering*. 4th Ed. Prentice Hall: Upper Saddle River, **2005**.
- [97] T. Ohsaka, F. Izumi, Y. Fujiki. Raman spectrum of anatase, TiO₂. *J. Raman Spectrosc.* **1978**, 7, 321-324.

-
- [98] O. Frank, M. Zukalova, B. Laskova, J. Kürti, J. Koltai, L. Kavan. Raman spectra of titanium dioxide (anatase, rutile) with identified oxygen isotopes (16, 17, 18). *Phys. Chem. Chem. Phys.* **2012**, *14*, 14567-14572.
- [99] G. T. Went, S. T. Oyama, A. T. Bell. Laser Raman spectroscopy of supported vanadium oxide catalysts. *J. Phys. Chem.* **1990**, *94*, 4240-4246.
- [100] I. E. Wachs, B. M. Weckhuysen. Structure and reactivity of surface vanadium oxide species on oxide supports. *Appl. Catal. A* **1997**, *157*, 67-90.
- [101] E. Tronconi, I. Nova, C. Ciardelli, D. Chatterjee, M. Weibel. Redox features in the catalytic mechanism of the “standard” and “fast” NH_3 -SCR of NO_x over a V-based catalyst investigated by dynamic methods. *J. Catal.* **2007**, *245*, 1-10.
- [102] I. Giakoumelou, C. Fountzoula, C. Kordulis, S. Boghosian. Molecular structure and catalytic activity of $\text{V}_2\text{O}_5/\text{TiO}_2$ catalysts for the SCR of NO by NH_3 : In situ Raman spectra in the presence of O_2 , NH_3 , NO, H_2 , H_2O , and SO_2 . *J. Catal.* **2006**, *239*, 1-12.
- [103] T. Nanba, T. Chino, S. Masukawa, J. Uchisawa, A. Obuchi. Total oxidation of toluene over $\text{Cu}/\text{TiO}_2/\text{SiO}_2$. *Bull. Chem. Soc. Jpn.* **2013**, *86*, 534-539.
- [104] R. Q. Long, R. T. Yang. Characterization of Fe-ZSM-5 catalyst for selective catalytic reduction of nitric oxide by ammonia. *J. Catal.* **2000**, *194*, 80-90.
- [105] M. Schwidder, S. Heikens, A. De Toni, S. Geisler, M. Berndt, A. Brückner, W. Grünert. The role of NO_2 in the selective catalytic reduction of nitrogen oxides over Fe-ZSM-5 catalysts: Active sites for the conversion of NO and of NO/ NO_2 mixtures. *J. Catal.* **2008**, *259*, 96-103.
- [106] F. Roozeboom, M. C. Mittelmeijer-Hazeleger, J. A. Moulijn, J. Medema, V. H. J. De Beer, P. J. Gellings. Vanadium oxide monolayer catalysts. 3. A Raman spectroscopic and temperature-programmed reduction study of monolayer and crystal-type vanadia on various supports. *J. Phys. Chem.* **1980**, *84*, 2783-2791.
- [107] A. A. Akande, A. G. J. Machatine, B. Masina, G. Chimowa, B. Matsoso, K. Roro, M.-M. Duvenhage, H. Swart, J. Bandyopadhyay, S. S. Ray, B. W. Mwakikunga. Blue- and red-shifts of V_2O_5 phonons in NH_3 environment by in situ Raman spectroscopy. *J. Phys. D: Appl. Phys.* **2017**, *51*, 015106.
- [108] C. Julien, G. A. Nazri, O. Bergström. Raman scattering studies of microcrystalline V_6O_{13} . *Phys. Status Solidi B* **1997**, *201*, 319-326.
- [109] M. Zhu, J.-K. Lai, U. Tumuluri, Z. Wu, I. E. Wachs. Nature of active sites and surface intermediates during SCR of NO with NH_3 by supported $\text{V}_2\text{O}_5\text{-WO}_3/\text{TiO}_2$ catalysts. *J. Am. Chem. Soc.* **2017**, *139*, 15624-15627.
- [110] H. Schneider, S. Tschudin, M. Schneider, A. Wokaun, A. Baiker. In situ diffuse reflectance FTIR study of the selective catalytic reduction of NO by NH_3 over vanadia-titania aerogels. *J. Catal.* **1994**, *147*, 5-14.
- [111] L. Lietti, J. L. Alemany, P. Forzatti, G. Busca, G. Ramis, E. Giamello, F. Bregani. Reactivity of $\text{V}_2\text{O}_5\text{-WO}_3/\text{TiO}_2$ catalysts in the selective catalytic reduction of nitric oxide by ammonia. *Catal. Today* **1996**, *29*, 143-148.
- [112] V. Marchionni, D. Ferri, O. Kröcher, A. Wokaun. Increasing the sensitivity to short-lived species in a modulated excitation experiment. *Anal. Chem.* **2017**, *89*, 5801-5809.
- [113] M. D. Amiridis, J. P. Solar. Selective catalytic reduction of nitric oxide by ammonia over $\text{V}_2\text{O}_5/\text{TiO}_2$, $\text{V}_2\text{O}_5/\text{TiO}_2/\text{SiO}_2$, and $\text{V}_2\text{O}_5\text{-WO}_3/\text{TiO}_2$ catalysts: Effect of vanadia content on the activation energy. *Ind. Eng. Chem. Res.* **1996**, *35*, 978-981.

-
- [114] C. Hess, P. Waleska, M. Ratzka, T. V. W. Janssens, S. B. Rasmussen, P. Beato. Hierarchical vanadia model catalysts for ammonia selective catalytic reduction. *Top. Catal.* **2017**, *60*, 1631-1640.
- [115] M. O. Guerrero-Pérez. Supported, bulk and bulk-supported vanadium oxide catalysts: A short review with an historical perspective. *Catal. Today* **2017**, *285*, 226-233.
- [116] H. S. Taylor. Catalysis and catalytic agents in chemical processes. *J. Franklin Inst.* **1922**, *194*, 1-27.
- [117] P. Forzatti. Present status and perspectives in de-NO_x SCR catalysis. *Appl. Catal. A* **2001**, *222*, 221-236.
- [118] I. Song, H. Lee, S. W. Jeon, D. H. Kim. Understanding the dynamic behavior of acid sites on TiO₂-supported vanadia catalysts via operando DRIFTS under SCR-relevant conditions. *J. Catal.* **2020**, *382*, 269-279.
- [119] Y. Inomata, S. Hata, M. Mino, E. Kiyonaga, K. Morita, K. Hikino, K. Yoshida, H. Kubota, T. Toyao, K.-i. Shimizu, M. Haruta, T. Murayama. Bulk vanadium oxide versus conventional V₂O₅/TiO₂: NH₃-SCR catalysts working at a low temperature below 150 °C. *ACS Catal.* **2019**, *9*, 9327-9331.
- [120] C. Resini, T. Montanari, G. Busca, J.-M. Jehng, I. E. Wachs. Comparison of alcohol and alkane oxidative dehydrogenation reactions over supported vanadium oxide catalysts: In situ infrared, Raman and UV-vis spectroscopic studies of surface alkoxide intermediates and of their surface chemistry. *Catal. Today* **2005**, *99*, 105-114.
- [121] M. D. Amiridis, R. V. Duevel, I. E. Wachs. The effect of metal oxide additives on the activity of V₂O₅/TiO₂ catalysts for the selective catalytic reduction of nitric oxide by ammonia. *Appl. Catal. B* **1999**, *20*, 111-122.
- [122] D. S. Kim, M. Ostromecki, I. E. Wachs. Surface structures of supported tungsten oxide catalysts under dehydrated conditions. *J. Mol. Catal. A: Chem.* **1996**, *106*, 93-102.
- [123] T. Kim, A. Burrows, C. J. Kiely, I. E. Wachs. Molecular/electronic structure-surface acidity relationships of model-supported tungsten oxide catalysts. *J. Catal.* **2007**, *246*, 370-381.
- [124] P. Müller, I. Hermans. Applications of modulation excitation spectroscopy in heterogeneous catalysis. *Ind. Eng. Chem. Res.* **2017**, *56*, 1123-1136.
- [125] F. Giraud, C. Geantet, N. Guilhaume, S. Gros, L. Porcheron, M. Kanniche, D. Bianchi. Experimental microkinetic approach of de-NO_x by NH₃ on V₂O₅/WO₃/TiO₂ catalysts. 1. Individual heats of adsorption of adsorbed NH₃ species on a sulfate-free TiO₂ support using adsorption isobars. *J. Phys. Chem. C.* **2014**, *118*, 15664-15676.
- [126] F. Giraud, C. Geantet, N. Guilhaume, S. Loridant, S. Gros, L. Porcheron, M. Kanniche, D. Bianchi. Experimental microkinetic approach of de-NO_x by NH₃ on V₂O₅/WO₃/TiO₂ catalysts. 2. Impact of superficial sulfate and/or V_xO_y groups on the heats of adsorption of adsorbed NH₃ species. *J. Phys. Chem. C.* **2014**, *118*, 15677-15692.
- [127] F. Giraud, C. Geantet, N. Guilhaume, S. Loridant, S. Gros, L. Porcheron, M. Kanniche, D. Bianchi. Experimental microkinetic approach of de-NO_x by NH₃ on V₂O₅/WO₃/TiO₂ catalysts. 3. Impact of superficial WO_z and V_xO_y/WO_z groups on the heats of adsorption of adsorbed NH₃ species. *J. Phys. Chem. C.* **2015**, *119*, 15401-15413.

-
- [128] J.-K. Lai, I. E. Wachs. A perspective on the selective catalytic reduction (SCR) of NO with NH₃ by supported V₂O₅–WO₃/TiO₂ catalysts. *ACS Catal.* **2018**, 8, 6537–6551.
- [129] I. Song, H. Lee, S. W. Jeon, T. Kim, D. H. Kim. Time-resolved observation of V₂O₅/TiO₂ in NH₃-SCR reveals the equivalence of Brønsted and Lewis acid sites. *Chem. Commun.* **2020**, 56, 15450–15453.
- [130] K. Kamasamudram, N. W. Currier, X. Chen, A. Yezerets. Overview of the practically important behaviors of zeolite-based urea-SCR catalysts, using compact experimental protocol. *Catal. Today* **2010**, 151, 212–222.
- [131] R. Nedyalkova, K. Kamasamudram, N. W. Currier, J. Li, A. Yezerets, L. Olsson. Experimental evidence of the mechanism behind NH₃ overconsumption during SCR over Fe-zeolites. *J. Catal.* **2013**, 299, 101–108.
- [132] A. L. Marten, S. C. Newbold. Estimating the social cost of non-CO₂ GHG emissions: Methane and nitrous oxide. *Energy Policy* **2012**, 51, 957–972.
- [133] M. Zhu, J.-K. Lai, I. E. Wachs. Formation of N₂O greenhouse gas during SCR of NO with NH₃ by supported vanadium oxide catalysts. *Appl. Catal. B* **2018**, 224, 836–840.
- [134] A. R. Ravishankara, J. S. Daniel, R. W. Portmann. Nitrous oxide (N₂O): The dominant ozone-depleting substance emitted in the 21st century. *Science* **2009**, 326, 123–125.
- [135] H.-Y. Chen, Z. Wei, M. Kollar, F. Gao, Y. Wang, J. Szanyi, C. H. F. Peden. A comparative study of N₂O formation during the selective catalytic reduction of NO_x with NH₃ on zeolite supported Cu catalysts. *J. Catal.* **2015**, 329, 490–498.
- [136] F. Radtke, R. A. Koeppel, A. Baiker. Hydrogen cyanide formation in selective catalytic reduction of nitrogen oxides over Cu/ZSM-5. *Appl. Catal. A* **1994**, 107, L125–L132.
- [137] I. O. Y. Liu, N. W. Cant, M. Kögel, T. Turek. The formation of HCN during the reduction of NO by isobutane over Fe-MFI made by solid-state ion exchange. *Catal. Lett.* **1999**, 63, 214–244.
- [138] I. Castellanos, O. Marie. An operando FT-IR study of the NO_x SCR over Co-HFER and Fe-HFER using acetylene as a reducing agent. *Catal. Today* **2017**, 283, 54–65.
- [139] I. Castellanos, O. Marie. Fe-HFER and Cu-HFER as catalysts for the NO_x SCR using acetylene as a reducing agent: Reaction mechanism revealed by FT-IR operando study coupled with ¹⁵N isotopic labelling. *Appl. Catal. B* **2018**, 223, 143–153.
- [140] O. Kröcher, M. Elsener, E. Jacob. A model gas study of ammonium formate, methanamide and guanidinium formate as alternative ammonia precursor compounds for the selective catalytic reduction of nitrogen oxides in diesel exhaust gas. *Appl. Catal. B* **2009**, 88, 66–82.
- [141] D. Zengel, P. Koch, B. Torkashvand, J.-D. Grunwaldt, M. Casapu, O. Deutschmann. Emission of toxic HCN during NO_x removal by ammonia SCR in the exhaust of lean-burn natural gas engines. *Angew. Chem. Int. Ed.* **2020**, 59, 14423–14428.
- [142] M. A. Elliott, G. J. Nebel, F. G. Rounds. The composition of exhaust gases from diesel, gasoline and propane powered motor coaches. *J. Air Pollut. Control Assoc.* **1955**, 5, 103–108.
- [143] S. M. Corrêa, G. Arbillá. Formaldehyde and acetaldehyde associated with the use of natural gas as a fuel for light vehicles. *Atmos. Environ.* **2005**, 39, 4513–4518.
- [144] D. B. Olsen, C. E. Mitchell. Formaldehyde formation in large bore engines Part 2: Factors affecting measured CH₂O. *J. Eng. Gas Turbine Power* **1999**, 122, 611–616.

-
- [145] M. Bauer, G. Wachtmeister. Formation of formaldehyde in lean-burn gas engines. *MTZ Worldw.* **2009**, 70, 50-57.
- [146] C. A. Harvey, R. J. Garbe, T. M. Baines, J. H. Somers, K. H. Hellman, P. M. Carey. A study of the potential impact of some unregulated motor vehicle emissions. *SAE Trans.* **1983**, 92, 280-289.
- [147] M. M. Baum, J. A. Moss, S. H. Pastel, G. A. Poskrebyshv. Hydrogen cyanide exhaust emissions from in-use motor vehicles. *Environ. Sci. Technol.* **2007**, 41, 857-862.
- [148] M. Koebel, M. Elsener, M. Kleemann. Urea-SCR: A promising technique to reduce NO_x emissions from automotive diesel engines. *Catal. Today* **2000**, 59, 335-345.
- [149] S. Sun, J. Ding, J. Bao, C. Gao, Z. Qi, C. Li. Photocatalytic oxidation of gaseous formaldehyde on TiO₂: An in situ DRIFTS study. *Catal. Lett.* **2010**, 137, 239-246.
- [150] C. Zhang, H. He, K.-i. Tanaka. Catalytic performance and mechanism of a Pt/TiO₂ catalyst for the oxidation of formaldehyde at room temperature. *Appl. Catal. B* **2006**, 65, 37-43.
- [151] C. Zhang, F. Liu, Y. Zhai, H. Ariga, N. Yi, Y. Liu, K. Asakura, M. Flytzani-Stephanopoulos, H. He. Alkali-metal-promoted Pt/TiO₂ opens a more efficient pathway to formaldehyde oxidation at ambient temperatures. *Angew. Chem. Int. Ed.* **2012**, 51, 9628-9632.
- [152] A. Gremminger, J. Pihl, M. Casapu, J.-D. Grunwaldt, T. J. Toops, O. Deutschmann. PGM based catalysts for exhaust-gas after-treatment under typical diesel, gasoline and gas engine conditions with focus on methane and formaldehyde oxidation. *Appl. Catal. B* **2020**, 265, 118571.
- [153] O. Kröcher, M. Elsener. Hydrolysis and oxidation of gaseous HCN over heterogeneous catalysts. *Appl. Catal. B* **2009**, 92, 75-89.
- [154] P. Bielaczyc, J. Woodburn. Trends in automotive emission legislation: Impact on LD engine development, fuels, lubricants and test methods: A global view, with a focus on WLTP and RDE regulations. *Emiss. Control Sci. Technol.* **2019**, 5, 86-98.
- [155] A. B. Ngo, T. H. Vuong, H. Atia, U. Bentrup, V. A. Kondratenko, E. V. Kondratenko, J. Rabeah, U. Ambruster, A. Brückner. Effect of formaldehyde in selective catalytic reduction of NO_x by ammonia (NH₃-SCR) on a commercial V₂O₅-WO₃/TiO₂ catalyst under model conditions. *Environ. Sci. Technol.* **2020**, 54, 11753-11761.
- [156] M. Misono, Y. Hirao, C. Yokoyama. Reduction of nitrogen oxides with hydrocarbons catalyzed by bifunctional catalysts. *Catal. Today* **1997**, 38, 157-162.
- [157] G. Busca, J. Lamotte, J. C. Lavalley, V. Lorenzelli. FT-IR study of the adsorption and transformation of formaldehyde on oxide surfaces. *J. Am. Chem. Soc.* **1987**, 109, 5197-5202.
- [158] S. Kim, D. C. Sorescu, J. T. Yates. Infrared spectroscopic study of the adsorption of HCN by γ -Al₂O₃: Competition with triethylenediamine for adsorption sites. *J. Phys. Chem. C* **2007**, 111, 5416-5425.
- [159] I. W. M. Smith. Integrated intensities for some infrared absorption bands of HCN. *J. Chem. Soc., Faraday Trans. 2* **1981**, 77, 2357-2363.
- [160] A. A. Tsyganenko, A. M. Chizhik, A. I. Chizhik. A FTIR search for linkage isomerism of CN⁻ ions adsorbed on oxides and zeolites. *Phys. Chem. Chem. Phys.* **2010**, 12, 6387-6395.
- [161] J. Raskó, T. Kecskés, J. Kiss. Adsorption and reaction of formaldehyde on TiO₂-supported Rh catalysts studied by FTIR and mass spectrometry. *J. Catal.* **2004**, 226, 183-191.

-
- [162] G. Busca, A. S. Elmi, P. Forzatti. Mechanism of selective methanol oxidation over vanadium oxide-titanium oxide catalysts: A FT-IR and flow reactor study. *J. Phys. Chem.* **1987**, *91*, 5263-5269.
- [163] T. Chen, G. Wu, Z. Feng, G. Hu, W. Su, P. Ying, C. Li. In situ FT-IR study of photocatalytic decomposition of formic acid to hydrogen on Pt/TiO₂ catalyst. *Chinese J. Catal.* **2008**, *29*, 105-107.
- [164] J. Araña, C. Garriga i Cabo, J. M. Doña-Rodríguez, O. González-Díaz, J. A. Herrera-Melián, J. Pérez-Peña. FTIR study of formic acid interaction with TiO₂ and TiO₂ doped with Pd and Cu in photocatalytic processes. *Appl. Surf. Sci.* **2004**, *239*, 60-71.
- [165] L.-F. Liao, W.-C. Wu, C.-Y. Chen, J.-L. Lin. Photooxidation of formic acid vs formate and ethanol vs ethoxy on TiO₂ and effect of adsorbed water on the rates of formate and formic acid photooxidation. *J. Phys. Chem. B* **2001**, *105*, 7678-7685.
- [166] M. Sridhar, S. Brose, D. Siewert, D. Ferri, J. A. van Bokhoven, O. Kröcher. Mechanistic implications of lanthanum-modification on gold-catalyzed formic acid decomposition under SCR-relevant conditions. *Appl. Catal. B* **2019**, *244*, 709-718.
- [167] L. J. Burcham, I. E. Wachs. The origin of the support effect in supported metal oxide catalysts: In situ infrared and kinetic studies during methanol oxidation. *Catal. Today* **1999**, *49*, 467-484.
- [168] T. Feng, J. M. Vohs. Temperature-programmed desorption study of the selective oxidation of alcohols on silica-supported vanadium oxide. *J. Phys. Chem. B* **2005**, *109*, 2120-2127.
- [169] G. Busca, G. Centi, L. Marchetti, F. Trifiro. Chemical and spectroscopic study of the nature of a vanadium oxide monolayer supported on a high-surface-area TiO₂ anatase. *Langmuir* **1986**, *2*, 568-577.
- [170] X. Yu, Z. Zhang, C. Yang, F. Bebensee, S. Heissler, A. Nefedov, M. Tang, Q. Ge, L. Chen, B. D. Kay, Z. Dohnálek, Y. Wang, C. Wöll. Interaction of formaldehyde with the rutile TiO₂(110) surface: A combined experimental and theoretical study. *J. Phys. Chem. C* **2016**, *120*, 12626-12636.
- [171] G. Y. Popova, T. V. Andrushkevich, Y. A. Chesalov, E. S. Stoyanov. In situ FTIR study of the adsorption of formaldehyde, formic acid, and methyl formate at the surface of TiO₂ (anatase). *Kinet. Catal.* **2000**, *41*, 805-811.
- [172] M. Signorile, C. Salvini, L. Zamirri, F. Bonino, G. Martra, M. Sodupe, P. Ugliengo. Formamide adsorption at the amorphous silica surface: A combined experimental and computational approach. *Life* **2018**, *8*, 42.
- [173] M. M. Dawley, A. M. Scott, F. C. Hill, J. Leszczynski, T. M. Orlando. Adsorption of formamide on kaolinite surfaces: A combined infrared experimental and theoretical study. *J. Phys. Chem. C* **2012**, *116*, 23981-23991.
- [174] H. H. Richmond, G. S. Myers, G. F. Wright. The reaction between formaldehyde and ammonia. *J. Am. Chem. Soc.* **1948**, *70*, 3659-3664.
- [175] C. Chen, S. H. Hong. Oxidative amide synthesis directly from alcohols with amines. *Org. Biomol. Chem.* **2011**, *9*, 20-26.
- [176] M. A. Sprung. A summary of the reactions of aldehydes with amines. *Chem. Rev.* **1940**, *26*, 297-338.
- [177] S. T. Korhonen, D. W. Fickel, R. F. Lobo, B. M. Weckhuysen, A. M. Beale. Isolated Cu²⁺ ions: Active sites for selective catalytic reduction of NO. *Chem. Commun.* **2011**, *47*, 800-802.
- [178] C. Paolucci, A. A. Parekh, I. Khurana, J. R. Di Iorio, H. Li, J. D. Albarracin Caballero, A. J. Shih, T. Anggara, W. N. Delgass, J. T. Miller, F. H. Ribeiro, R.

- Gounder, W. F. Schneider. Catalysis in a cage: Condition-dependent speciation and dynamics of exchanged Cu cations in SSZ-13 zeolites. *J. Am. Chem. Soc.* **2016**, *138*, 6028-6048.
- [179] V. Rizzotto, P. Chen, U. Simon. Mobility of NH₃-solvated Cu^{II} ions in Cu-SSZ-13 and Cu-ZSM-5 NH₃-SCR catalysts: A comparative impedance spectroscopy study. *Catalysts* **2018**, *8*, 162.
- [180] V. Marchionni, A. Kambolis, M. Nachtegaal, O. Kröcher, D. Ferri. High energy X-ray diffraction and IR spectroscopy of Pt/Al₂O₃ during CO oxidation in a novel catalytic reactor cell. *Catal. Struct. React.* **2017**, *3*, 71-78.
- [181] A. H. Clark, J. Imbao, R. Frahm, M. Nachtegaal. ProQEXAFS: A highly optimized parallelized rapid processing software for QEXAFS data. *J. Synchrotron Radiat.* **2020**, *27*, 551-557.
- [182] C. Tyrsted, E. Borfecchia, G. Berlier, K. A. Lomachenko, C. Lamberti, S. Bordiga, P. N. R. Vennestrøm, T. V. W. Janssens, H. Falsig, P. Beato, A. Puig-Molina. Nitrate–nitrite equilibrium in the reaction of NO with a Cu-CHA catalyst for NH₃-SCR. *Catal. Sci. Technol.* **2016**, *6*, 8314-8324.
- [183] G. Lambelle, A. Moen, D. G. Nicholson. Structure of the diamminecopper(I) ion in solution. An X-ray absorption spectroscopic study. *J. Chem. Soc., Faraday Trans.* **1994**, *90*, 2211-2213.
- [184] F. Giordanino, E. Borfecchia, K. A. Lomachenko, A. Lazzarini, G. Agostini, E. Gallo, A. V. Soldatov, P. Beato, S. Bordiga, C. Lamberti. Interaction of NH₃ with Cu-SSZ-13 catalyst: A complementary FTIR, XANES, and XES study. *J. Phys. Chem. Lett.* **2014**, *5*, 1552-1559.
- [185] A. Martini, E. Borfecchia, K. A. Lomachenko, I. A. Pankin, C. Negri, G. Berlier, P. Beato, H. Falsig, S. Bordiga, C. Lamberti. Composition-driven Cu-speciation and reducibility in Cu-CHA zeolite catalysts: A multivariate XAS/FTIR approach to complexity. *Chem. Sci.* **2017**, *8*, 6836-6851.
- [186] L. S. Kau, D. J. Spira-Solomon, J. E. Penner-Hahn, K. O. Hodgson, E. I. Solomon. X-ray absorption edge determination of the oxidation state and coordination number of copper. Application to the type 3 site in *Rhus vernicifera* laccase and its reaction with oxygen. *J. Am. Chem. Soc.* **1987**, *109*, 6433-6442.
- [187] M. Sano, S. Komorita, H. Yamatera. XANES spectra of copper(II) complexes: Correlation of the intensity of the 1s→3d transition and the shape of the complex. *Inorg. Chem.* **1992**, *31*, 459-463.
- [188] C. Prestipino, G. Berlier, F. X. Llabrés i Xamena, G. Spoto, S. Bordiga, A. Zecchina, G. Turnes Palomino, T. Yamamoto, C. Lamberti. An in situ temperature dependent IR, EPR and high resolution XANES study on the NO/Cu⁺-ZSM-5 interaction. *Chem. Phys. Lett.* **2002**, *363*, 389-396.
- [189] J. Rudolph, C. R. Jacob. Revisiting the dependence of Cu K-edge X-ray absorption spectra on oxidation state and coordination environment. *Inorg. Chem.* **2018**, *57*, 10591-10607.
- [190] C. Lamberti, S. Bordiga, A. Zecchina, M. Salvalaggio, F. Geobaldo, C. Otero Areán. XANES, EXAFS and FTIR characterization of copper-exchanged mordenite. *J. Chem. Soc., Faraday Trans.* **1998**, *94*, 1519-1525.
- [191] C. Lamberti, S. Bordiga, F. Bonino, C. Prestipino, G. Berlier, L. Capello, F. D'Acapito, F. X. Llabrés i Xamena, A. Zecchina. Determination of the oxidation and coordination state of copper on different Cu-based catalysts by XANES spectroscopy in situ or in operando conditions. *Phys. Chem. Chem. Phys.* **2003**, *5*, 4502-4509.

-
- [192] J. Chaboy, A. Muñoz-Páez, F. Carrera, P. Merklings, E. S. Marcos. Ab initio X-ray absorption study of copper K-edge XANES spectra in Cu(II) compounds. *Phys. Rev. B* **2005**, *71*, 134208.
- [193] C. Negri, E. Borfecchia, M. Cutini, K. A. Lomachenko, T. V. W. Janssens, G. Berlier, S. Bordiga. Evidence of mixed-ligand complexes in Cu-CHA by reaction of Cu nitrates with NO/NH₃ at low temperature. *ChemCatChem* **2019**, *11*, 3828-3838.
- [194] C. Paolucci, I. Khurana, A. A. Parekh, S. Li, A. J. Shih, H. Li, J. R. Di Iorio, J. D. Albarracin-Caballero, A. Yezerets, J. T. Miller, W. N. Delgass, F. H. Ribeiro, W. F. Schneider, R. Gounder. Dynamic multinuclear sites formed by mobilized copper ions in NO_x selective catalytic reduction. *Science* **2017**, *357*, 898-903.
- [195] K. Kamasamudram, N. Currier, T. Szailer, A. Yezerets. Why Cu- and Fe-zeolite SCR catalysts behave differently at low temperatures. *SAE Int. J. Fuels Lubr.* **2010**, *3*, 664-672.
- [196] B. Guan, R. Zhan, H. Lin, Z. Huang. Review of state of the art technologies of selective catalytic reduction of NO_x from diesel engine exhaust. *Appl. Therm. Eng.* **2014**, *66*, 395-414.
- [197] J. H. Kwak, D. Tran, J. Szanyi, C. H. F. Peden, J. H. Lee. The effect of copper loading on the selective catalytic reduction of nitric oxide by ammonia over Cu-SSZ-13. *Catal. Lett.* **2012**, *142*, 295-301.
- [198] F. Gao, E. D. Walter, N. M. Washton, J. Szanyi, C. H. F. Peden. Synthesis and evaluation of Cu-SAPO-34 catalysts for ammonia selective catalytic reduction. 1. Aqueous solution ion exchange. *ACS Catal.* **2013**, *3*, 2083-2093.
- [199] Y. Cao, S. Zou, L. Lan, Z. Yang, H. Xu, T. Lin, M. Gong, Y. Chen. Promotional effect of Ce on Cu-SAPO-34 monolith catalyst for selective catalytic reduction of NO_x with ammonia. *J. Mol. Catal. A: Chem.* **2015**, *398*, 304-311.
- [200] G. Squires. Francis Aston and the mass spectrograph. *J. Chem. Soc., Dalton Trans.* **1998**, 3893-3900.
- [201] E. Hubble. A relation between distance and radial velocity among extra-galactic nebulae. *Proc. Natl. Acad. Sci. U.S.A.* **1929**, *15*, 168-173.
- [202] G. Nilsson, E. Fok, J. M. Ng, J. Cooke. A web-based spectroscopy tutorial for the inorganic chemistry laboratory. *J. Chem. Educ.* **2010**, *87*, 758-759.
- [203] L. A. Morrill, J. K. Kammeyer, N. K. Garg. Spectroscopy 101: A practical introduction to spectroscopy and analysis for undergraduate organic chemistry laboratories. *J. Chem. Educ.* **2017**, *94*, 1584-1586.
- [204] G. C. Pimentel. Infrared spectroscopy: A chemist's tool. *J. Chem. Educ.* **1960**, *37*, 651-657.
- [205] P. MacCarthy, S. J. Bowman. Undergraduate infrared spectroscopy experiments. *J. Chem. Educ.* **1982**, *59*, 799-801.
- [206] C. W. Alexander, G. L. Asleson, M. T. Doig, F. J. Heldrich. Spectroscopic instruction in introductory organic chemistry: Results of a national survey. *J. Chem. Educ.* **1999**, *76*, 1294-1296.
- [207] M. C. Connor, S. A. Finkenstaedt-Quinn, G. V. Shultz. Constraints on organic chemistry students' reasoning during IR and ¹H NMR spectral interpretation. *Chem. Educ. Res. Pract.* **2019**, *20*, 522-541.
- [208] K. R. Hess, W. D. Smith, M. W. Thomsen, C. H. Yoder. An introductory infrared spectroscopy experiment. *J. Chem. Educ.* **1995**, *72*, 655-656.
- [209] J. Ryczkowski. IR spectroscopy in catalysis. *Catal. Today* **2001**, *68*, 263-381.
- [210] R. P. Eischens. Infrared spectroscopy and catalysis research. *Science* **1964**, *146*, 486-493.

- [211] A. P. Dicks, R. A. Batey. Confchem conference on educating the next generation: Green and sustainable chemistry—greening the organic curriculum: Development of an undergraduate catalytic chemistry course. *J. Chem. Educ.* **2013**, *90*, 519-520.
- [212] J. Andraos, A. P. Dicks. Green chemistry teaching in higher education: A review of effective practices. *Chem. Educ. Res. Pract.* **2012**, *13*, 69-79.

List of Scientific Contributions

Peer-reviewed articles and book chapters

R.J.G. Nuguid, M. Nachtegaal, D. Ferri, O. Kröcher. In situ infrared spectroscopy of NO_x reduction catalysts: A flexible laboratory exercise for in-person and virtual learning. *in preparation*. (**Annex**)

R.J.G. Nuguid, A.H. Clark, M. Nachtegaal, D. Ferri, O. Kröcher. NH₃-mediated inhibition of the SCR reaction over Cu-SSZ-13 at low temperature. *in preparation*. (**Chapter 7**)

R.J.G. Nuguid, L. Ortino Ghini, V.L. Suskevich, J. Yang, D. Ferri, O. Kröcher. Interconversion between Lewis and Brønsted-Lowry acid sites on vanadia-based materials under SCR-relevant conditions. *submitted*. (**Chapter 4**)

A. Bahmanpour, R.J.G. Nuguid, L.M. Saveriede, M.D. Mensi, D. Ferri, J.S. Lutherbacher, O. Kröcher. Restructuring Ni/Al₂O₃ by addition of Ga to shift product selectivity in CO₂ hydrogenation: Studying the role of hydroxyl groups. *submitted*.

O.H. Bjørkedal, S.K. Regli, R.J.G. Nuguid, P.E. Vullum, O. Kröcher, D. Ferri, M. Rønning. One-pot synthesis of highly dispersed mesoporous Cu/ZrO₂ catalysts for NH₃-SCR. *Catal. Today* **2022**, 384-386, 113-121. doi: [10.1016/j.cattod.2021.05.010](https://doi.org/10.1016/j.cattod.2021.05.010)

R.J.G. Nuguid, M. Elsener, O. Kröcher, D. Ferri. Operando diffuse reflectance infrared detection of cyanide intermediate species during the reaction of formaldehyde with ammonia over V₂O₅/WO₃-TiO₂. *Appl. Catal. B* **2021**, 298, 120629. doi: [10.1016/j.apcatb.2021.120629](https://doi.org/10.1016/j.apcatb.2021.120629) (**Chapter 6**)

R.J.G. Nuguid, D. Ferri. Modulated Excitation Spectroscopy of Selective Catalytic Reduction Catalysts. In *Springer Handbook of Advanced Catalyst Characterization. Part*

A: Vibrational Spectroscopy. M. Bañares, Ed. Springer Nature: New York, **2021**. *in press*.
(part of Chapter 1)

D. Ferri, R.J.G. Nuguid, A. Urakawa. Modulated Excitation Spectroscopy. In *Springer Handbook of Advanced Catalyst Characterization. Part A: Vibrational Spectroscopy*. M. Bañares, Ed. Springer Nature: New York, **2021**. *in press*. (part of Chapter 1)

R.J.G. Nuguid, F. Buttignol, A. Marberger, O. Kröcher. Selective Catalytic Reduction of NO_x Emissions. In *Handbook of Biodiesel and Petrodiesel Fuels: Science, Technology, Health, and Environment. Volume 3. Petrodiesel Fuels: Science, Technology, Health, and Environment*. O. Konur, Ed. CRC Press: Boca Raton, **2021**. *in press*. (part of Chapter 1)

M. Elsener, R.J.G. Nuguid, O. Kröcher, D. Ferri. HCN production from formaldehyde during the selective catalytic reduction of NO_x with NH₃ over V₂O₅/WO₃-TiO₂, *Appl. Catal. B* **2021**, 281, 119462. [doi:10.1016/j.apcatb.2020.119462](https://doi.org/10.1016/j.apcatb.2020.119462) (Chapter 5)

A.H. Clark, R.J.G. Nuguid, P. Steiger, A. Marberger, A.W. Petrov, M. Elsener, D. Ferri, M. Nachttegaal, O. Kröcher. Selective catalytic reduction of NO with NH₃ on Cu-SSZ-13: Deciphering the low and high-temperature rate-limiting steps by transient XAS experiments. *ChemCatChem* **2020**, 12, 1429-1435. [doi: 10.1002/cctc.201901916](https://doi.org/10.1002/cctc.201901916)

T.W. Tzeng, C.I. Lin, C.W. Pao, J.L. Chen, R.J.G. Nuguid, C.P.W. Chung. Understanding catalytic hydrogenolysis of 5-hydroxymethylfurfural (HMF) to 2,5-dimethylfuran (DMF) using carbon supported Ru catalysts. *Fuel Process Technol.* **2020**, 199, 10625. [doi: 10.1016/j.fuproc.2019.106225](https://doi.org/10.1016/j.fuproc.2019.106225)

R.J.G. Nuguid, D. Ferri, O. Kröcher. Design of a reactor cell for modulated excitation Raman and diffuse reflectance studies of selective catalytic reduction catalysts. *Emiss. Control Sci. Technol.* **2019**, 5, 307-316. *Special Issue: In Recognition of Professor Wolfgang Grünert's Contributions to the Science and Fundamentals of Selective Catalytic Reduction of NO_x*. [doi: 10.1007/s40825-019-00141-2](https://doi.org/10.1007/s40825-019-00141-2) (Chapter 2)

R.J.G. Nuguid, D. Ferri, A. Marberger, M. Nachtegaal, O. Kröcher. Modulated excitation Raman spectroscopy of V_2O_5/TiO_2 : Mechanistic insights into the selective catalytic reduction of NO by NH_3 . *ACS Catal.* **2019**, 9, 6814-6820. [doi: 10.1021/acscatal.9b01514](https://doi.org/10.1021/acscatal.9b01514)
(Chapter 3)

A. Marberger, M. Elsener, R.J.G. Nuguid, D. Ferri, O. Kröcher. Thermal activation and aging of a V_2O_5/WO_3-TiO_2 catalyst for the selective catalytic reduction of NO with NH_3 . *Appl. Catal. A* **2019**, 573, 64-72. [doi: 10.1016/j.apcata.2019.01.009](https://doi.org/10.1016/j.apcata.2019.01.009)

Invited talk

R.J.G. Nuguid. Environmental Catalysis: From the Liquid Phase to the Gas Phase. *Swiss-Korean Science Club*. Online. April 21, 2021.

Oral presentations

R.J.G. Nuguid. Combined infrared, UV-visible, and Raman spectroscopic investigation of selective catalytic reduction over vanadia-based catalysts. *11th International Conference on Environmental Catalysis*. Online. September 9-6, 2020.

R.J.G. Nuguid. Time-resolved spectroscopy of vanadia-based SCR catalysts under transient conditions. *SCS Fall Meeting 2020*. Online. August 25, 2020.

R.J.G. Nuguid. Mechanistic insights into the selective catalytic reduction of NO with NH_3 using modulated excitation Raman spectroscopy. *XI International Conference: Mechanisms of Catalytic Reactions*. Sochi, Russia. October 7-11, 2019.

R.J.G. Nuguid. Modulated excitation Raman spectroscopy of V_2O_5/TiO_2 catalysts. *8th Asia-Pacific Congress on Catalysis (APCAT-8)*. Bangkok, Thailand. August 4-7, 2019.

R.J.G. Nuguid. Operando spectroscopic investigation of vanadia-based SCR catalysts.
EFCATS School on Catalysis. Liblice, Czech Republic. June 25-29, 2018.

Curriculum Vitae

Name: Rob Jeremiah G. Nuguid

Date of birth: July 25, 1992

Place of birth: Imus, Philippines

Nationality: Filipino

Academic pathway:

**Paul Scherrer Institut & École polytechnique fédérale de
Lausanne, Switzerland**

10.2017 – 09.2021

PhD studies in chemistry

Thesis: Time-resolved spectroscopy of selective catalytic
reduction catalysts under transient conditions

Supervisors: Prof. Oliver Kröcher and Dr. Davide Ferri

Hanyang University, South Korea

10.2020 – 01.2021

Swiss-Korean Young Researchers' Exchange Program

Project: Synthesis of vanadia-based catalysts by atomic layer
deposition

Supervisor: Prof. Tae Joo Park

Academia Sinica, Taiwan

07.2017 – 09.2017

Taiwan International Graduate Program Internship

Project: Effect of carbon support on the hydrogenolysis of 5-hydroxymethylfuran

Supervisor: Prof. Cedric Po-Wen Chung

University College London, United Kingdom

02.2017 – 06.2017

Erasmus Mundus MSc studies in physics/chemistry (4th semester)

Thesis: CuO-CeO₂ catalysts for CO oxidation and Ru/SiO₂ catalysts for biomass conversion

Supervisor: Prof. Ryan Wang

Politechnika Wroclawska, Poland

10.2016 – 01.2017

Erasmus Mundus MSc studies in physics/chemistry (3rd semester)

Project: Enantioselective epoxide ring-opening reactions using chiral zinc organocatalysts

Supervisor: Prof. Jacek Skarzewski

Rice University, United States

07.2016 – 09.2016

Research exchange at the Laboratory for Nanophotonics

Project: Synthesis of aluminum nanocrystals for plasmon-enhanced photocatalysis

Supervisor: Prof. Naomi J. Halas

Universidad Complutense de Madrid, Spain	02.2016 – 06.2016
Erasmus Mundus MSc studies in physics/chemistry (2 nd semester)	
Université Paris-Saclay (ENS Cachan), France	09.2015 – 01.2016
Erasmus Mundus MSc studies in physics/chemistry (1 st semester)	
Petron Corporation – Petroleum Refining and Petrochemicals Division, Philippines	12.2012 – 08.2015
Chemist / Shift Supervisor	
Pamantasan ng Lungsod ng Maynila, Philippines	06.2008 – 03.2012
BSc studies in chemistry	